INVESTIGATION OF HIGH-NONLINEARITY GLASS FIBERS FOR POTENTIAL APPLICATIONS IN ULTRAFAST NONLINEAR FIBER DEVICES

Jong-Kook Kim

Dissertation submitted to the Faculty of the
Virginia Polytechnic Institute and State University
in partial fulfillment of the requirements for the degree of

DOCTOR OF PHILOSOPHY
In
Electrical and Computer Engineering

Dr. Rogers H. Stolen, Chair
Dr. Ahmad Safaai-Jazi, Co-Chair
Dr. T. –C. Poon
Dr. Ioannis M. Besieris
Dr. Dong S. Ha
Dr. James R. Heflin

July 28, 2005
Blacksburg, Virginia

Keywords: Nonlinear Fiber Device, Fiber Nonlinearity, High-Nonlinearity Glass, OTDM/WDM, Demultiplexer, Optical Communication System

INVESTIGATION OF HIGH-NONLINEARITY GLASS FIBERS FOR POTENTIAL APPLICATIONS IN ULTRAFAST NONLINEAR FIBER DEVICES

Jong-Kook Kim

ABSTRACT

Nonlinear fiber devices have been attracting considerable attention in recent years, due to their inherent ultrafast response time and potential applications in optical communication systems. They usually require long fibers to generate sufficient nonlinear phase shifts, since nonlinearities of conventional silica-core silica-clad fibers are too low. These long devices, however, cause the serious problems of pulse walk-off, pulse broadening, and polarization fluctuation which are major limiting factors for response time, switching bandwidth, and maximum transmittable bit-rate. Therefore, short device length is indispensable for achieving ultrafast switching and higher bit-rate data transmission.

To shorten the required device length, fiber nonlinearities should be increased. In this dissertation, as a way of increasing fiber nonlinearities, high-nonlinearity materials of Litharge, Bismite, Tellurite, and Chalcogenide glasses have been considered. Although they have high nonlinearities, they also have high group-velocity dispersion and high losses deteriorating the performance of nonlinear fiber devices seriously. The aim of this work is to investigate how these high-nonlinearity glasses affect the performance of nonlinear fiber devices, taking into consideration both the advantages and disadvantages. To achieve it, the critical properties of various nonlinear fiber devices constructed with the different types of high-nonlinearity glasses and different types of fibers have been evaluated.

It turned out that the required device lengths of nonlinear fiber devices constructed with the high-nonlinearity glasses were significantly reduced and high group-velocity dispersions and losses could not be major problems due to the extremely short device length. As a result, it would be possible to suppress the problems of pulse walk-off, pulse broadening, and polarization fluctuation in nonlinear fiber devices by introducing high-nonlinearity glasses, thus enabling ultrafast switching and higher bit-rate data transmission.

Furthermore, in this dissertation, a new scheme of wavelength-division demultiplexing based on the optical Kerr effect has been proposed for the first time. The new scheme can turn the disadvantage of the extremely high group-velocity dispersion of high-nonlinearity glasses into an advantage of wavelength-division demultiplexing. Finally, it now would be possible to greatly increase maximum transmittable bit-rate in optical communication systems by simultaneously demultiplexing optical time-division-multiplexed signals and wavelength-division-multiplexed signals with an optical Kerr effect-based demultiplexer.

Acknowledgements

First of all, I would like to express my wholehearted gratitude to my advisor, Dr. Rogers H. Stolen who gave me an opportunity to work at his research group. He provided invaluable and consistent guidance, generous advice, financial support, and encouragement during my study at Virginia Tech. His peerless experiences and knowledge in fiber optics, especially nonlinear phenomena, were very helpful to me throughout this entire dissertation. I am indebted to him for everything I have achieved at Virginia Tech. I really respect him and he is my model of the researcher I hope to be. I will never forget about him and my life in Blacksburg for the rest of my life.

I am also particularly grateful to my co-advisor, Dr. Ahmad Safaai-Jazi who presented consistent concern and helpful advices regarding my research. He also reviewed my whole dissertation for a long time and provided invaluable comments and suggestions.

My special thanks should be extended to my committee members, Dr. T. –C. Poon, Dr. Ioannis M. Besieris, Dr. Dong S. Ha, and Dr. James R. Heflin for their worthful comments and suggestions concerning my dissertation. I am really grateful to all of them for favor, concern, and encouragement they provided during my study at Virginia Tech.

My full-hearted thanks should go to my mother for her priceless and unconditional love to me. Although my father is not in the real world, I also would like to express my deep appreciation and heartful love to him. I know well he is always taking care of me in heaven. I will forever remain indebted to my parents. My full-hearted thanks should also go to my parents-in-law for their understanding, love, and faith in me.

I should show my gratitude to my lab-colleagues, Nitin K. Goel, Yuhong Kang, and Harsh M. Sanghvi, for their invaluable help, favor, and friendship.

I also would love to express my gratitude to many Korean associates, who studied together at Virginia Tech and shared a lot of time with me during my life in Blacksburg, for their priceless friendship, encouragement, and help.

Last, but not least, my deepest thanks from the bottom of my heart, of course, must go to my wife, Mi-Young An who let me study abroad willingly, for her love, mental support, encouragement, and patience, and I sincerely would like to express my endless love to my daughter, Seong-Min Kim, who is my wish and always makes me vital, confident, and happy. I love you, baby.

Table of Contents

List of Figures

List of Tables

CHAPTER 1.
INTRODUCTION

This chapter provides the motivation and purpose of this dissertation, the scope of investigations, the general description of fiber nonlinearities, and an overview of the nonlinear effects that are necessary for understanding nonlinear fiber devices discussed in later chapters. This chapter also provides brief discussion of multi-channel lightwave systems using optical time-division multiplexing and wavelength-division multiplexing schemes.

1.1. Background

Due to the advent of sophisticated all-optical amplifiers, notable developments in the area of light sources and detectors, and dramatic reduction in transmission losses, optical fibers have attracted considerable attention for applications in lightwave communication systems.

One of the several impairments limiting the performance of fiber-optic communication systems is the nonlinearity of optical fibers used as transmission medium. Nonlinear effects in optical fibers occur due to intensity dependence of the refractive index. They are primarily governed by the nonlinearities of fiber materials, fiber length, optical power, and effective mode area. Although nonlinear phenomena limit the performance of systems and cause restrictions on designing single-mode lightwave systems[1], they also have useful aspects which form the basis of all-optical ultrafast nonlinear fiber devices such as demultiplexers[2-29], wavelength converters[30-52], optical Kerr shutters[53-58], nonlinear directional couplers[59-73], amplifiers[74-77], and pulse compressors[78-88]. These devices are of great interest due to their inherent ultrafast response time(a few femtoseconds), the high-power density which results from small effective mode area, and simple all-optical features.

Recently, there has been a growing demand for much higher transmission capacity due to the rapid increase of data traffic. To meet this demand, Optical Time-Division Multiplexing (OTDM)[89] and Wavelength-Division Multiplexing(WDM) schemes[90] have been widely used in optical communication systems. However, the transmission capacity of such systems is often restricted by the limited frequency response of the electronic devices used for optical signal processing. Therefore, ultrafast demultiplexing based on all-optical nonlinear fiber devices, in which signal processings are performed optically without the involvement of electronics, are key techniques to the development of ultrafast operation and downconversion of the future ultrahigh bit-rate OTDM or WDM signals to the base rates where electronics can be used. Additionally, wavelength converters have been utilized as a way to enhance routing options and network properties such as reconfigurability, nonblocking capability, and wavelength reuse.

Even though nonlinear fiber devices are capable of ultrafast operation and broad switching bandwidth, conventional silica-core silica-clad fiber devices require either long lengths or high optical powers to achieve the desired nonlinear effects, because the nonlinearities of silica glasses are very small. Typically, a fiber length of 1Km with an optical power of 1W is required to achieve a nonlinear phase shift of π radians in conventional silica-core silica-clad fiber devices. The optical power of 1W is too high for actual devices and, moreover, the long length of fiber leads to the serious problems which limit response time, switching bandwidth, and maximum transmittable bit-rate. These problems include the pulse walk-off between control and signal pulses caused by group-velocity mismatch, the control pulse broadening caused by Group-Velocity Dispersion(GVD), and the polarization sensitivity caused by some external environmental conditions such as temperature variation and stress in nonlinear fiber switching devices. Therefore, short devices are essential for avoiding such serious problems and for exhibiting ultrafast switching and high bit-rate data transmission. Because the nonlinear phase shift induced by the nonlinear phenomena depends on the device length, the nonlinear-index coefficient, the input optical power, and the effective mode area, fiber nonlinearities should be increased in order to shorten the device length while maintaining the same amount of the nonlinear phase shift.

In this dissertation, High-NonLinearity(HNL) glasses of Lead-Oxide(PbO, Litharge)[91-102], Bismuth-Oxide(Bi_2O_3, Bismite)[103-118], Tellurium-Oxide(TeO_2, Tellurite)[119-162], and Chalcogenide glasses[163-196] are considered in order to increase fiber nonlinearities. It is certain that the HNL glasses can increase fiber nonlinearities due to their high nonlinear-index coefficients which enable short length devices. Moreover, the fabrication processes of the HNL glasses are easier because of their low melting temperatures and high glass stability. They, however, exhibit extremely high losses and GVD, causing pulse walk-off and pulse broadening and thus degrading the performance of devices seriously.

Accordingly, the aim of this dissertation is to investigate how the advantages and disadvantages of the HNL glasses affect the performance of nonlinear fiber devices. The nonlinear fiber devices which are discussed and evaluated in this dissertation include (i)OTDM/WDM demultiplexers[2-26] based on the optical Kerr effect[2-5], Nonlinear Optical Loop Mirrors(NOLM)[6-20], Four-Wave Mixing(FWM)[21-26], Asymmetric Twin-Core Fibers(ATCF), or LP_{01}-LP_{11} mode interference, (ii)wavelength converters[30-52] based on the optical Kerr effect[30-32], NOLMs[33-41], or FWM[42-52], (iii)nonlinear noise filters based on LP_{01}-LP_{02} mode interference, and (iv)amplitude modulators and (v)nonlinear optical switches based on LP_{01}-LP_{11} mode interference. To evaluate the performance of those devices, the three types of fibers, HNL glass-core silica-clad fibers, HNL glass-core air-clad (microstructure) fibers, and HNL glass-core HNL glass-clad fibers, are considered. Then, the required device length and the required optical power for the desired nonlinear effect, relative group delay between the control and signal pulses or between the two modes of the signal for the required device length, the properties of GVD and Dispersion Slope(DS), walk-off length for the input pulse width, and output pulse width(pulse broadening) are evaluated for individual nonlinear fiber devices constructed with the three types of fibers. Finally, through the consideration of these all estimations, applicable potentialities as practical nonlinear fiber devices are discussed for individual devices.

1.2. Fiber Nonlinearities

The response of dielectric materials, such as optical fibers, to light becomes nonlinear for intense electromagnetic fields. The electric flux density $\vec{D}$ is related to the electric filed $\vec{E}$ propagating inside a medium through the constitutive relations given by

$$\vec{D} = \varepsilon_0 \vec{E} + \vec{P} = \varepsilon_0 \vec{E} + \varepsilon_0 \chi \vec{E} = \varepsilon_0 \varepsilon_r \vec{E} = \varepsilon \vec{E} \tag{1.1}$$

where ε, ε_0, and ε_r are the permittivity of the medium, the vacuum permittivity, and the relative permittivity of the medium, respectively, χ is the susceptibility, and $\vec{P}$ is the induced electric polarization. Additionally, the total electric polarization $\vec{P}_t$ induced by electric dipoles in electric filed $\vec{E}$ is given by[197]

$$\vec{P}_t = \varepsilon_0 \left(\chi^{(1)} \cdot \vec{E} + \chi^{(2)} : \vec{E}\vec{E} + \chi^{(3)} \vdots \vec{E}\vec{E}\vec{E} + \cdots \right) \tag{1.2}$$

where $\chi^{(1)}$, $\chi^{(2)}$, and $\chi^{(3)}$ are the first-, second-, and third-order susceptibilities, respectively. The first-order susceptibility $\chi^{(1)}$ is related to the linear refractive index representing the dominant contribution to $\vec{P}_t$. The second-order susceptibility $\chi^{(2)}$, which is responsible for the nonlinear effect of Second-Harmonic Generation(SHG), is normally zero for silica glasses since SiO_2 is a symmetric molecule, although the electric-quadrupole and magnetic-dipole moments can generate weak second-order nonlinear effects. Therefore, the lowest-order nonlinear effects in optical fibers originate from the third-order susceptibility $\chi^{(3)}$, which is responsible for nonlinear phenomena such as Third-Harmonic Generation(THG), FWM, and nonlinear refraction.

The third-order susceptibility $\chi^{(3)}$ is positive in most cases and consists of a real part and an imaginary part such that

$$\chi^{(3)} = N_2 + i\beta \tag{1.3}$$

The real part is responsible for the nonlinear-index coefficient N_2 and the imaginary part is responsible for the Two-Photon Absorption(TPA) coefficient β and Raman scattering. Therefore, the total refractive index n and the total absorption coefficient α, including the nonlinear parts of δn and δα, respectively, are expressed as

$$n = n_0 + \delta n = n_0 + N_2 I \tag{1.4}$$

$$\alpha = \alpha_0 + \delta\alpha = \alpha_0 + \beta I \tag{1.5}$$

where n_0 and α_0 are the linear refractive index and the linear absorption coefficient, respectively and I is the optical intensity.

1.2.1. Nonlinear Refraction

Most nonlinear effects in optical fibers originate from nonlinear refraction, a phenomenon referring to the intensity dependence of the refractive index. In optical fibers, the nonlinear refractive index δn, induced by the third-order susceptibility $\chi^{(3)}$, is directly related to the nonlinear-index coefficient N_2 and the optical intensity I as

$$n = n_0 + \delta n = n_0 + N_2 I = n_0 + N_2 \frac{P}{A_{eff}} \tag{1.6}$$

where P is the optical peak power and A_{eff} is the effective mode area defined by[197]

$$A_{eff} = 2\pi \cdot \frac{\left[\int \psi(r)^2 r dr\right]^2}{\int \psi(r)^4 r dr} \tag{1.7}$$

The evaluation of the effective mode area requires the use of modal field distribution ψ(r). The effective mode area clearly depends on fiber parameters such as a core radius, core refractive index, and core-cladding index difference. For step-index fibers, the effective mode area of the fundamental mode can be defined by the Mode Field Radius(MFR) with Gaussian beam approximation, which is slightly larger than the core radius due to the cladding mode contribution. The effective mode area of πw^2 where w is the MFR is nearly same to the core area which is defined by πa^2 where a is the core radius, when the normalized frequency V is the single-mode cutoff frequency of 2.4048. Typically, the effective mode area for single-mode silica fibers can vary in the range of 20~100μm^2 in the 1.5μm region depending on fiber design.

As shown in Equation (1.6), the total refractive index is defined by the sum of the linear refractive index and the nonlinear refractive index affected by the optical intensity. As a result, nonlinearities in optical fibers are highly dependent on the nonlinear-index coefficient, the optical peak power, and the effective mode area.

1.2.2. Nonlinear Phase Shift

One of the most distinct properties in nonlinear fiber optics[198] is the intensity-dependent nonlinear phase shift. Since the maximum nonlinear phase shift occurs at the center of a pulse, it can be given by[197]

$$\phi_{\max} = \frac{L_{eff}}{L_{NL}} = \gamma P L_{eff} = \frac{2\pi L_{eff}}{\lambda}\frac{N_2 P}{A_{eff}} = \frac{2\pi L_{eff}}{\lambda}\delta n \tag{1.8}$$

where L_{eff} is the effective length defined as

$$L_{eff} = \frac{1-\mathrm{e}^{-\alpha L}}{\alpha},\ \alpha = \frac{\alpha_0\left[dB/Km\right]}{10\log_{10} e}[Km^{-1}] \tag{1.9}$$

and L_{NL} is the nonlinear length defined as

$$L_{NL} = \frac{1}{\gamma P},\ \gamma = \frac{2\pi N_2}{\lambda A_{eff}}[W^{-1}\cdot Km^{-1}] \tag{1.10}$$

where γ is the nonlinear parameter. The effective length L_{eff} plays the role of a length that is smaller than the fiber length L because of fiber losses. In the absence of fiber losses, α=0, and L_{eff} =L and when losses are present, L_{eff} =1/α for long fibers and L_{eff} =L for short fibers. Note that the nonlinear phase shift increases with the increase of the effective length. The physical meaning of the nonlinear length L_{NL} is clearly the effective propagation distance at which ϕ_{max} =1. If the nonlinear parameter $\gamma=2W^{-1}\cdot Km^{-1}$, the nonlinear length L_{NL}=50Km at the optical power P=10mW and decreases inversely with P. Typically, the nonlinear parameter γ for a

single-mode silica fiber is in the range of $1\sim10W^{-1}\cdot Km^{-1}$ when the nonlinear-index coefficient $N_2\approx2.6\times10^{-20}m^2/W$.

As shown in Equation (1.8), the nonlinear phase shift is affected by the nonlinear refractive index δn and depends highly on the nonlinear-index coefficient, the optical peak power, the effective mode area, and the effective length.

1.2.3. Self-Phase Modulation and Cross-Phase Modulation

1.2.3.1. Self-Phase Modulation

One of the manifestations of nonlinear effects in optical fibers is Self-Phase Modulation (SPM), a phenomenon that leads to the spectral broadening of an optical pulse[199]. SPM causes a phase shift between the peak and its low-intensity leading and trailing edges of a pulse by itself, resulting in the spectral broadening of the pulse. The SPM-induced spectral broadening has a symmetric spectrum and is accompanied by an oscillatory structure which covers the entire frequency range. Generally, the spectrum has many peaks with the outermost peaks the most intense. The number of peaks and the extent of broadening are dependent on the magnitude of the nonlinear phase shift and increase with it linearly.

With regard to the temporal variation of the pulse, SPM exhibits frequency chirping such that the leading edge of the pulse is down-shifted and the trailing edge of the pulse is up-shifted. This property of SPM and GVD in the anomalous-dispersion regime of an optical fiber can cooperate in such a way that the pulse propagates as an optical soliton. In the normal-dispersion regime which has down-shifted frequency chirping in the leading edge, the combined effects of SPM and GVD can be used for pulse compression. The nonlinear phase shift induced by SPM is given by[197]

$$\delta\phi_{SPM} = \frac{2\pi L_{eff}}{\lambda_s}\frac{N_2 P_s}{A_{eff}} \tag{1.11}$$

where λ_s and P_s are the signal wavelength and the signal peak power, respectively.

1.2.3.2. Cross-Phase Modulation

When two or more optical pulses propagate inside an optical fiber simultaneously, they can interact with each other through fiber nonlinearities. The nonlinear phase shift caused by interaction between two copropagating pulses is called Cross-Phase Modulation(XPM)[200]. XPM is always accompanied by SPM and occurs because the effective refractive index of an optical pulse in a nonlinear medium depends not only on the intensity of that pulse but also on the intensity of the other pulse. In other words, while SPM occurs by itself, XPM occurs by interplay between two copropagating pulses.

Generally, nonlinear interaction between pulses can generate new waves with different frequencies through a variety of nonlinear phenomena such as Stimulated Raman Scattering(SRS), Stimulated Brillouin Scattering(SBS), and FWM. They transfer part of the energy from one pulse to the other, which is referred to as an inelastic effect. However, no energy transfer between pulses occurs through XPM; it is referred to as an elastic effect.

Similar to the case of pure SPM, the spectra of both pulses in XPM are expected to broaden and develop multiple peaks with the outermost peaks the most intense. However, because the spectra of the pulses are governed by the combined contributions of SPM and XPM, each pulse spectrum develops asymmetric spectral broadening. In the absence of the interaction of XPM, the spectrum of each pulse would be symmetric and would exhibit less broadening. It is worth mentioning that the XPM-induced chirp is affected by pulse walk-off and group-velocity mismatch, and depends critically on initial time delay between two pulses.

Actually, XPM can occur between two optical fields of both the same wavelength and different wavelength. It can be used for pulse compression[82-88] through the XPM-induced frequency chirp, optical switching[201-203] through the XPM-induced phase shift, and wavelength shifting[204-205] through the XPM-induced spectral broadening for optical communication systems. Note that in XPM, the nonlinear refractive index is twice as large as that of SPM. As a result, the nonlinear phase shift induced by XPM is given by[197]

$$\delta\phi_{XPM} = \frac{4\pi L_{eff}}{\lambda_s}\frac{N_2 P_p}{A_{eff}} \tag{1.12}$$

where λ_s is the weaker signal wavelength and P_p is the strong pump peak power. For XPM, the effective mode area A_{eff} is defined by both the signal and pump pulses as

$$A_{eff} = 2\pi \cdot \frac{\left[\int \psi_s{}^2 r dr\right]\left[\int \psi_p{}^2 r dr\right]}{\int \psi_s{}^2 \cdot \psi_p{}^2 r dr} \tag{1.13}$$

1.2.4. Stimulated Inelastic Scattering

As briefly mentioned in Section 1.2.3.2, there are two classes of nonlinear effects governed by the third-order susceptibility. The first class includes elastic nonlinear effects such as SPM and XPM in the sense that no energy is exchanged between an optical field and a dielectric medium. The second class includes inelastic nonlinear effects such as SRS, SBS, and FWM in the sense that an optical field transfers its energy to another optical field. Two important stimulated inelastic scatterings are SRS[206-208] and SBS[209] which were among the first nonlinear effects studied in optical fibers. Both effects are related to the vibrational excitation modes of a nonlinear medium. The primary differences between SRS and SBS are that SRS is

associated with molecular vibrations and SBS is associated with acoustic vibrations, and that SBS occurs only in the backward direction whereas SRS can occur in both directions.

1.2.4.1. Stimulated Raman Scattering

Stimulated Raman Scattering(SRS) is one of the most important nonlinear processes and can be used as broadband fiber-based Raman amplifiers and tunable Raman lasers for optical communication systems. In any molecular medium, a small fraction of power can be transferred from one optical field to another optical field through the spontaneous Raman scattering caused by molecular vibration. The newly generated wave is called the Stokes wave and its frequency is downshifted from the incident light by an amount determined by the vibrational modes of the medium. The SRS-generated Stokes wave intensity I_S for a CW or quasi-CW condition is given by[197]

$$I_S(L) = I_S(0)\exp\left(g_R I_P(0) L_{eff} - \alpha_S L\right),\ L_{eff} = \frac{1-\mathrm{e}^{-\alpha_P L}}{\alpha_P} \qquad (1.14)$$

where $I_S(0)$ is the Stokes intensity at L=0, $I_P(0)$ is the pump intensity at L=0, α_S and α_P are the fiber losses at the Stokes and pump frequencies, respectively, L_{eff} is the effective length defined by α_P, and g_R is the Raman-gain coefficient.

In general, g_R depends highly on composition and dopants of fiber core materials, and is inversely proportional to the pump wavelength. For pure silica, g_R exhibits a peak at the frequency that is downshifted from a pump frequency by about 13.2THz(440cm^{-1}) and the Raman-gain spectrum extends over a large frequency range, up to 40THz due to the amorphous nature of silica glasses. When a pump power higher than the Raman threshold given in Equation (1.15) at 1μm is used, the peak Raman-gain coefficient $g_R \approx 1\times10^{-13}$m/W for pure silica[207]. Note that, for the condition of a pulse, the effective length L_{eff} in the Raman

threshold should be replaced by the walk-off length. In Equation (1.15), ψ_S and ψ_P represent modal fields at the Stokes and pump, respectively.

$$P_{th} \approx \frac{16A_{eff}}{g_R L_{eff}},\ A_{eff} = 2\pi \cdot \frac{\left[\int {\psi_P}^2 rdr\right]\left[\int {\psi_S}^2 rdr\right]}{\int {\psi_P}^2 {\psi_S}^2 rdr} \tag{1.15}$$

SRS causes the generation of a Stokes wave whose frequency is determined by the peak Raman-gain coefficient. Once the pump power reaches the Raman threshold, the power is transferred to the Stokes rapidly and finally it is transferred completely. Moreover, this first-order Stokes wave can serve as a pump for the generation of a second-order Stokes wave if its power is still higher than the Raman threshold. The number of multiple Stokes waves generated by the process of cascade SRS depends on the input pump power.

1.2.4.2. Stimulated Brillouin Scattering

The nonlinear phenomenon which occurs at the lowest power, as low as a few mW in the small core of a single-mode fiber, is Stimulated Brillouin Scattering(SBS). It occurs when an optical power reaches the level that can generate acoustic vibration in a nonlinear medium. The acoustic waves generated by the optical power affect the density of a material and thus change its refractive index. This refractive index fluctuation can scatter light; this effect is called the Brillouin scattering. Since the light wave being scattered itself also generates the acoustic waves, this process in a fiber is called SBS. Similar to SRS, SBS also generates a Stokes wave whose frequency is downshifted from an incident light by the amount set by the nonlinear medium. The SBS-generated Stokes wave intensity I_S for a CW or quasi-CW condition is described by[197]

$$I_S(L) = I_S(0)\exp\left(-g_B I_P(0) L_{eff} + \alpha L\right),\ L_{eff} = \frac{1-\mathrm{e}^{-\alpha L}}{\alpha} \tag{1.16}$$

where g_B is the Brillouin-gain coefficient and in this case, the fiber loss α is the same at both the Stokes and pump frequencies due to the small value of the Brillouin shift. The difference from SRS is the reversed sign owing to the counterpropagating nature of the Stokes wave with respect to the pump wave in SBS.

The frequency shift of the Stokes wave in SBS is smaller by three orders of magnitude than that of SRS. For silica-core fibers, g_B develops a peak for the frequency that is downshifted from a pump frequency by about 10GHz and the Brillouin-gain spectrum has an extremely narrow bandwidth of <100MHz. The Brillouin-gain coefficient g_B is larger than g_R by more than two orders of magnitude. For silica-core fibers, $g_B \approx 5\times10^{-11}$m/W[209] and thus the Brillouin threshold can be as low as 1mW.

$$P_{th} \approx \frac{21A_{eff}}{g_B L_{eff}},\ A_{eff} = 2\pi \cdot \frac{\left[\int {\psi_P}^2 rdr\right]\left[\int {\psi_S}^2 rdr\right]}{\int {\psi_P}^2 {\psi_S}^2 rdr} \tag{1.17}$$

SBS is strongest when the pulse width is long and the linewidth of the laser source is very narrow, and it is typically harmful because it reduces signal strength by directing some portion of the light back toward the transmitter, effectively increasing attenuation. However, at the same time, it can be useful for making fiber-based Brillouin amplifiers, Brillouin lasers, and sensors.

1.2.5. Four-Wave Mixing

Nonlinear processes which involve the modulation of a medium parameter such as the refractive index are referred to as parametric processes. They can be classified as the second- and third-order processes depending on whether $\chi^{(2)}$ or $\chi^{(3)}$ is responsible for the process. Generally, the third-order parametric processes involve nonlinear interaction among four optical waves and include Four-Wave Mixing(FWM) often also called four-photon mixing, third-harmonic generation, and parametric amplification. FWM[210-214] occurs when photons from one or more waves are annihilated to create new photons at different frequencies for energy conservation during the parametric process. The primary difference between parametric processes such as FWM and the stimulated scattering processes such as SRS and SBS discussed in the previous sections is related to the condition of phase-matching[215]. It is automatically satisfied in the case of SRS and SBS as a result of active participation of a nonlinear medium. However, in the case of parametric processes, it requires specific choice of frequencies and refractive indices in order to satisfy the phase-matching conditions for efficient occurrence.

There are two types of FWM. The first case occurs when three waves transfer their energies to a single wave at the frequency at $\omega_4=\omega_1+\omega_2+\omega_3$. However, in general, it is difficult to have high efficiency in optical fibers owing to the difficulties in satisfying the phase-matching condition for such processes. The second case occurs when two waves at frequencies ω_1 and ω_2 are annihilated to generate simultaneously two symmetric sidebands at frequencies ω_3(downshifted) and ω_4(upshifted) in frequency such that

$$\omega_3 + \omega_4 = \omega_1 + \omega_2 \tag{1.18}$$

$$\omega_3 = 2\omega_1 - \omega_2 \tag{1.19}$$

$$\omega_4 = 2\omega_2 - \omega_1 \tag{1.20}$$

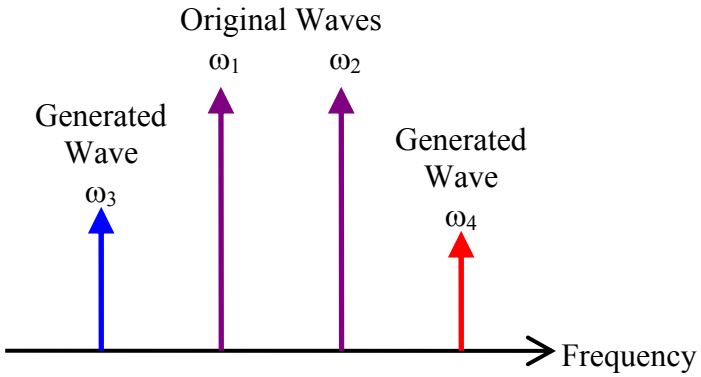

Figure 1-1. 2-Channel Pump Four-Wave Mixing

If the frequencies of the two pump waves are equal, $\omega_1=\omega_2$, it is relatively easy to satisfy the phase-matching requirement given by

$$\Delta\beta = \frac{\left(n_3\omega_3 + n_4\omega_4 - n_1\omega_1 - n_2\omega_2\right)}{c} = 0 \tag{1.21}$$

This specific case is called degenerated FWM or three-wave mixing because only three distinct frequencies are involved in this nonlinear process. It is most relevant for optical fibers and is in direct analogy with SRS in that the low-frequency band is referred to as the Stokes and the high-frequency band is referred to as the anti-Stokes[197].

$$\omega_4 = 2\omega_1 - \omega_3 \tag{1.22}$$

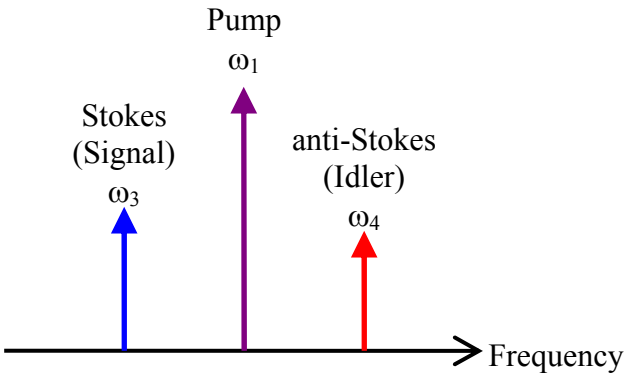

Figure 1-2. 1-Channel Pump Four-Wave Mixing(Degenerated FWM)

If only the pump wave at frequency ω_1 is incident and phase-matching requirement is satisfied, the Stokes and anti-Stokes waves at frequencies ω_3 and ω_4, respectively can be generated. On the other hand, if a weak signal at frequency ω_3 is coupled together into a fiber with the pump, the signal is amplified while a new wave at frequency ω_4 is generated at the same time. When the signal is amplified through such process of FWM, the Stokes and the anti-Stokes are often called the signal and the idler, respectively and the gain caused by such amplification is called the parametric gain.

FWM becomes a serious problem in wavelength-division-multiplexed systems with channels which are separated by equal frequency spacing and operates near Zero-Dispersion Wavelength(ZDW), because the newly generated waves fall on the top of the existing channels, inducing crosstalk and degrading the performance of the systems. Actually, FWM in the ZDW region occurs easily because the phase-matching condition is easily satisfied, resulting in new waves over a wide wavelength range[213]. However, FWM can be avoided using unequal channel spacing or introducing Nonzero-Dispersion-Shifted Fibers(NDSF) with large enough GVD such that the required phase-matching for FWM process does not occur over long length of fibers. Despite this harmful effect, FWM also has useful applications such as optical time-division demultiplexing[21-26], wavelength conversion[42-52], signal amplification, supercontinuum generation, phase conjugation for dispersion compensation, and squeezing for reduction of quantum noise.

1.2.6. Formulas for Third-Order Susceptibility and Nonlinear-Index Coefficient

Various ways to estimate the nonlinear properties of materials have been proposed by many authors. This section summarizes some different ways for estimation of the third-order susceptibility and nonlinear-index coefficient. In this dissertation, some of them are used for estimation of the HNL glasses considered, and the calculated values from some different formulas are compared.

As discussed earlier, the total refractive index is defined by the sum of the linear and nonlinear refractive indices. The nonlinear refractive index can be expressed in terms of the square of the magnitude of the optical electric field $|E|^2$[esu or V^2/m^2][216],

$$n = n_0 + N_2 \left| E \right|^2 \tag{1.23}$$

or in terms of the optical intensity I[W/m^2],

$$n = n_0 + N_2 I \tag{1.24}$$

In Equations (1.23) and (1.24), n_0 is the linear refractive index. The unit of the nonlinear-index coefficient N_2 in Equation (1.23) is [esu](electro-static unit) or [m^2/V^2] and the unit of N_2 in Equation (1.24) is [m^2/W]. For a linearly polarized wave in an isotropic material, the relationship between N_2[esu] and the third-order susceptibility $\chi^{(3)}$[esu] is given by[216-217]

$$N_2[esu] = \frac{12\pi}{n_0} \chi^{(3)}[esu] \tag{1.25}$$

and the relationship between N_2[m^2/V^2] and the third-order susceptibility $\chi^{(3)}$[esu] is given by[179]

$$N_2\left[m^2/v^2\right]=\frac{\pi}{6n_0\times10^8}\chi^{(3)}\left[esu\right] \tag{1.26}$$

In Equations (1.25) and (1.26), n_0 is the linear refractive index.

One of the most convenient ways to estimate the third-order susceptibility $\chi^{(3)}$[esu] is the Miller's rule given by[120].

$$\chi^{(3)}\left[esu\right]=\left(\chi^{(1)}\right)^4\times10^{-10},\ \chi^{(1)}=\frac{\left(n_0{}^2-1\right)}{4\pi} \tag{1.27}$$

where $\chi^{(1)}$ is the linear susceptibility and n_0 is the linear refractive index. According to this rule, high nonlinearity is expected with high linear refractive index.

The nonlinear-index coefficient N_2[esu] can be estimated by using some linear refractive indices at different wavelengths as follows[163, 218].

$$N_2\left[10^{-13}esu\right]=\frac{68\left(n_d-1\right)\left(n_d{}^2+2\right)^2}{v_d\sqrt{1.517+\dfrac{\left(n_d{}^2+2\right)\left(n_d+1\right)v_d}{6n_d}}} \tag{1.28}$$

$$N_2\left[10^{-13}esu\right]=391\frac{\left(n_d-1\right)}{v_d{}^{\frac{5}{4}}},\ v_d=\frac{n_d-1}{n_F-n_C} \tag{1.29}$$

In Equations (1.28) and (1.29), V_d is the Abbe number which is a measure for dispersion and n_d, n_F, and n_C are the linear refractive indices at 0.58756μm, 0.48613μm, and 0.65627μm,

respectively. These equations are useful for crystals, oxide glasses, and fluoride glasses, but they are not useful for chalcogenide glasses. The simpler Equation (1.29) is more accurate than Equation (1.28)[163].

Equation (1.30) is an improved version of Equations (1.28) and (1.29). It is applicable to crystals, oxide glasses, and fluoride glasses, but still not much useful for chalcogenide glasses[163].

$$N_2\left[10^{-13}esu\right]=\frac{\sqrt{3}gS\left(n^2+2\right)^{1.5}\left(n^2-1\right)^2\hbar^2e^2}{12nmE_dE_0{}^2} \tag{1.30}$$

In Equation (1.30), g is the anharmonicity parameter, S is the oscillator strength, n is the linear refractive index, $\hbar$ is Planck's constant divided by 2π, e is the electron charge, m is the electron mass, E_d is the dispersion energy, and E_0 is the oscillator energy.

Equation (1.31) provides a global expression for the nonlinear-index coefficient $N_2[m^2/W]$. The nonlinear-index coefficients calculated from this equation are in reasonable agreement with experimental results for chalcogenide glasses[219].

$$N_2[10^{-20}m^2/W]=\frac{3.4\left(n_0{}^2+2\right)^3\left(n_0{}^2-1\right)d^2}{n_0E_s{}^2} \tag{1.31}$$

In Equation (1.31), d is the nearest-neighbor bond length in 10^{-10}m, E_s is the Sellmeier gap in eV, and n_0 is the linear refractive index given by

$$n_0{}^2=1+\frac{kn_eDZ_A}{E_s} \tag{1.32}$$

where n_e is the number of valence electrons per anion, D is a dimensionless measure of ionic density, Z_A is the magnitude of the formal anionic valency, and k is the empiric energy factor which varies only slightly from material to material.

Equation (1.33) provides an estimation of third-order susceptibility $\chi^{(3)}$[esu], using THG measurements[104].

$$\chi^{(3)}[esu] = \left(\frac{n+1}{n_s+1}\right)^4 \left(\frac{I}{I_s}\right)^{1/2} \chi_s^{(3)} \frac{l_{ch,s}}{l_{ch}} \tag{1.33}$$

In Equation (1.33), l_{ch} and $l_{ch,s}$ are the coherence lengths of sample and fused silica, respectively, I and I_s are the measured peak intensity values in the THG intensity patterns of sample and fused silica, respectively, n and n_s are the linear refractive indices of the sample and fused silica, respectively, and $\chi_s^{(3)}$ is the third-order susceptibility of fused silica.

If three-photon resonance is dominant in the THG as in the case when the optical bandgap E_g is higher than the three-photon energy, the most significant term caused by the three-photon resonance can be obtained as[104]

$$\chi^{(3)}[esu] = \frac{A}{\left(E_g - 1.96\right)\left(E_g - 1.31\right)\left(E_g - E_g{}'\right)}, \; E_g > 1.96 \tag{1.34}$$

where A is a phenomenological constant(1.4×10^{-11}) and $E_g{}'$ is the bandgap energy of the laser beam used(e.g. 0.65eV for 1900nm).

Additionally, Equations (1.35)-(1.37) define the relationship between the third-order susceptibility $\chi^{(3)}$ and the nonlinear-index coefficient N_2[179, 197]. It is quite convenient to estimate one of them from the other. This equation provides nearly exact results for the well-known values of $\chi^{(3)}$ and N_2 of pure silica.

$$\chi^{(3)}\left[m^2/v^2\right] = \frac{4\pi}{9\times10^8}\chi^{(3)}\left[esu\right] \tag{1.35}$$

$$N_2\left[m^2/v^2\right] = \frac{3}{8n_0}\chi^{(3)}\left[m^2/v^2\right] \tag{1.36}$$

$$\begin{aligned} N_2\left[m^2/W\right] &= \left(\frac{1}{cn_0\varepsilon_0}\right)N_2\left[m^2/v^2\right] \\ &\approx \frac{1}{8}\left(\frac{4\pi}{n_0}\right)^2\times10^{-7}\cdot\chi^{(3)}\left[esu\right] \end{aligned} \tag{1.37}$$

In Equations (1.36) and (1.37), n_0 is the linear refractive index, c is the light velocity in vacuum, and ε_0 is the vacuum permittivity.

With respect to the reported values, there is a variation in the nonlinear-index coefficient N_2 and the third-order susceptibility $\chi^{(3)}$. The values of N_2 for fused silica are $0.95\pm0.1\times10^{-13}$[esu] and $2.73\pm0.27\times10^{-20}$[$m^2$/W] with linear polarization at 1.064μm[220]. Typical values of $\chi^{(3)}$ and N_2 for pure silica are around 0.27×10^{-13}[esu] and 2.5×10^{-20}[m^2/W], respectively, with linear polarization at 1.5μm. For silica-core fibers, N_2 is 2.36×10^{-20}[m^2/W] with random polarization at 1.319μm[221]. Measurements of N_2 by various techniques exhibit variation over a 13% range between 2.25 and 2.55×10^{-20}[m^2/W] for Dispersion-Shifted Fibers(DSF) at 1.55μm with random polarization. Well-organized and detailed investigation produces the value of $N_2=2.45\times10^{-20}$[m^2/W](±5%) for DSF at 1.55μm with random polarization[222]. A typical value of N_2 for GeO_2-doped DSF is 2.8×10^{-20}[m^2/W] with linear polarization.

In addition, because refractive index is dependent not only on wavelength but also on the State Of Polarization(SOP), N_2 also varies with the SOP. It has the maximum value for linear polarization and usually drops to 2/3 of maximum for circular polarization. In long non-polarization maintaining fibers, the SOP wanders over all values from linear to circular and produces a lower value of N_2 by a factor of 8/9 of the linearly polarized case.

1.3. Multi-Channel Lightwave Systems

In optical communication systems, the optical carrier frequency is typically on the order of 100THz, in contrast with the microwave carrier frequencies of 1-10GHz. In principle, taking 1% as the limiting value, the signal bandwidth in optical communication systems can exceed 1THz because of such a large carrier frequency associated with the optical signal, thus resulting in the potential of carrying information at bit rates in the order of 1Tb/s[223]. In practice, however, the bit-rate is often limited to tens of Gb/s or less due to fiber impairments, such as losses, dispersion, and nonlinearities, and the slow response time of electronic components required for optical signal processing. Therefore, the development of multi-channel lightwave systems which transmit signal information through multiple optical channels over the same fiber has attracted considerable attention to enhance transmission capacity. Channel multiplexing can mainly be performed in either time or wavelength using optical domain techniques. It is common to refer to the former case as Optical Time-Division Multiplexing(OTDM) to distinguish from Time-Division Multiplexing(TDM) in electrical domain and the latter case as Wavelength-Division Multiplexing(WDM) which is called the Frequency-Division Multiplexing(FDM) in electrical domain. The lightwave systems making use of such techniques are referred to as multi-channel communication systems.

1.3.1. Optical Time-Division Multiplexing Systems

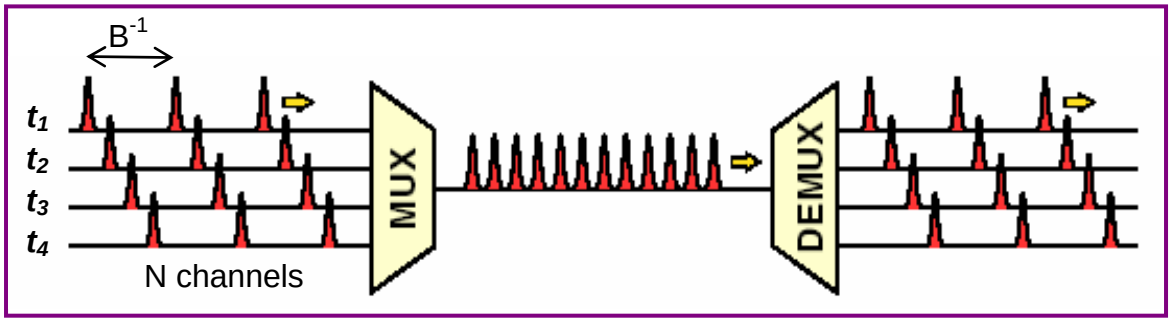

Figure 1-3. Optical Time-Division Multiplexing Systems

In OTDM Systems, as shown in Figure 1-3, optical signals modulated at the bit-rate B in each channel with different delay time are multiplexed optically to form a composite optical signal at the bit-rate NB, where N is the number of multiplexed optical channels. The width of the optical pulse generated by a transmitter should be less than $(NB)^{-1}$ to ensure that the pulse will fit within the allocated time slot. The multiplexing of N channels can be achieved by a delay technique with the fiber segments of controlled lengths, which is optically implemented such that the modulated optical signals in *n*th branch is delayed by an amount (*n*-1)/(NB), where *n*=1, … , N.

The demultiplexing of the individual channels in OTDM systems can be achieved by either electro-optical or all-optical techniques. All-optical techniques are more common because electro-optical techniques require a variety of expensive components and its performance is limited by the speed of modulator. Moreover, all techniques for demultiplexing in OTDM systems require control signals at the same bit-rate of a single channel, requiring an all-optical scheme because of the high bit rates associated with OTDM systems. There are various kinds of all-optical nonlinear demultiplexers for optical time-division-multiplexed signals, based on the optical Kerr effect[2-5], NOLMs[6-20], FWM[21-26], XPM[27-29], Raman amplification, directional coupler, ATCFs, LP_{01}-LP_{11} mode interference, and so forth.

1.3.2. Wavelength-Division Multiplexing Systems

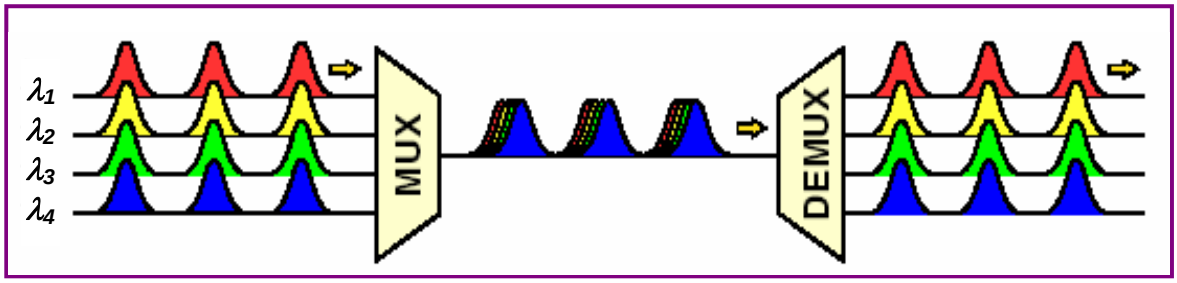

Figure 1-4. Wavelength-Division Multiplexing Systems

Figure 1-4 shows the basic diagram of WDM systems. In WDM systems, multiple optical signals at different wavelengths are modulated and then, the signals at all wavelengths from multiple channels are combined and transmitted over the same fiber. At the end of the transmission link, they are demultiplexed into individual channels by means of optical techniques. These include a tunable bandpass filter, Fiber Bragg Grating(FBG), Arrayed Waveguide Grating(AWG), and all-optical nonlinear wavelength-division demultiplexers based on the optical Kerr effect[5], ATCFs, LP_{01}-LP_{11} mode interference, and so forth. WDM has much higher potential than OTDM for achieving huge transmission capacities. The transmission window near 1.55μm in optical fibers covers a bandwidth of more than 10THz with low-loss. Therefore, in principle, it is possible to transmit hundreds of 10Gb/s signal channels over the same fiber if the channel spacing is reduced to desired level.

CHAPTER 2.
NONLINEAR FIBER DEVICES

This chapter is devoted to the discussion of nonlinear fiber devices operating based on the optical Kerr effect, Nonlinear Optical Loop Mirrors(NOLM), Four-Wave Mixing(FWM), Asymmetric Twin-Core Fibers(ATCF), or mode interference. The characteristic features and principles of operation of the nonlinear fiber devices are examined in some details. Even though nonlinear fiber devices based on FWM are not evaluated, they are also discussed here to understand their operation.

2.1. Optical Kerr Effect

2.1.1. Nonlinear Birefringence

As discussed in the previous chapter, the total refractive index is defined as the sum of the linear and nonlinear refractive indices. When a sufficiently intense optical field is applied to optical fibers, the total refractive indices for two principal axes of x and y axes are given by

$$n_x = n_{0x} + \delta n_x \tag{2.1}$$

$$n_y = n_{0y} + \delta n_y \tag{2.2}$$

$$\Delta n_L = n_{0x} - n_{0y} \tag{2.3}$$

$$\Delta n_{NL} = \delta n_x - \delta n_y \tag{2.4}$$

where n_{0x} and n_{0y} are the linear refractive indices in the directions of the x and y axes, respectively, δn_x and δn_y are the nonlinear index variation along the x and y axes, respectively, and Δn_L and Δn_{NL} are the linear and nonlinear birefringence, respectively.

Ideally, the cores of optical fibers are perfectly circular and uniform along their entire length, so the intrinsic birefringence should be zero along the entire fiber. In practical fibers, however, the shape of the cores can vary randomly due to unintentional variation such as stresses, air bubbles, bends, and twist. This leads to modal birefringence, which means the propagation constants of two orthogonal axes are different. The birefringence can change randomly along the fiber length so that the State Of Polarization(SOP) can also vary randomly.

To avoid this randomly varying SOP in standard fibers, birefringence, which is much higher than the random changes in standard fibers, is built in. Polarization-Maintaining Fibers(PMF) have intentional stresses(or variation of the core shape) and exhibit nearly constant birefringence along the entire length. PMFs have two principal axes, slow and fast axes and are capable of maintaining the state of linear polarization[224] of the incident light. Additionally, since nonlinear interaction between the two orthogonally polarized optical fields changes the refractive index by different amounts for the two axes, the nonlinear contributions δn_x and δn_y are generally unequal, thus creating the nonlinear birefringence Δn_{NL} whose magnitude is dependent on the intensity and SOP of the incident light. As a result, the nonlinear phenomena in birefringent fibers are polarization dependent.

2.1.2. Optical Kerr Shutters

The optical Kerr effect[225-226] uses the nonlinear phase shift induced by the intensity-dependent nonlinear birefringence to change the SOP of a weak signal in a nonlinear medium. Figure 2-1 shows an ideal case when a linearly polarized signal with a 45° angle to both of the two principal axes is launched into a PMF so that the light intensity is equal along the two principal axes. When a pump is not present, the SOP of the signal changes in a periodic way

due to the built-in birefringence and the original SOP is restored by the quarter wave plate. As a result, it is blocked by a crossed polarizer at the fiber end, thus resulting in no output.

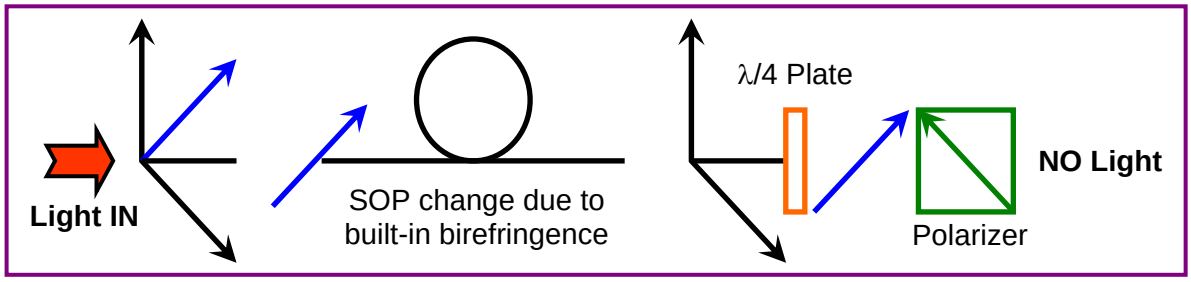

Figure 2-1. State of Polarization of Signals without Pump

However, if a linearly polarized strong pump along one of the two principal axes of the fiber is launched together with the signal, as shown in Figure 2-2, the refractive indices for the parallel and perpendicular components of the signal become slightly different with respect to the direction of the pump polarization due to the pump-induced nonlinear birefringence. This nonlinear birefringence causes a nonlinear phase shift and also changes the SOP of the signal, thus transmitting the signal through the polarizer. The signal transmittivity depends mainly on the pump intensity and can be controlled by adjusting it. Thus, a signal at one wavelength can be passed and modulated only when a pump at a different wavelength is present. This device is referred to as the optical Kerr shutter or the optical Kerr modulator. The optical Kerr effect has a large number of applications[53-58] other than ones discussed in this dissertation, such as optical sampling, and pulse shaping.

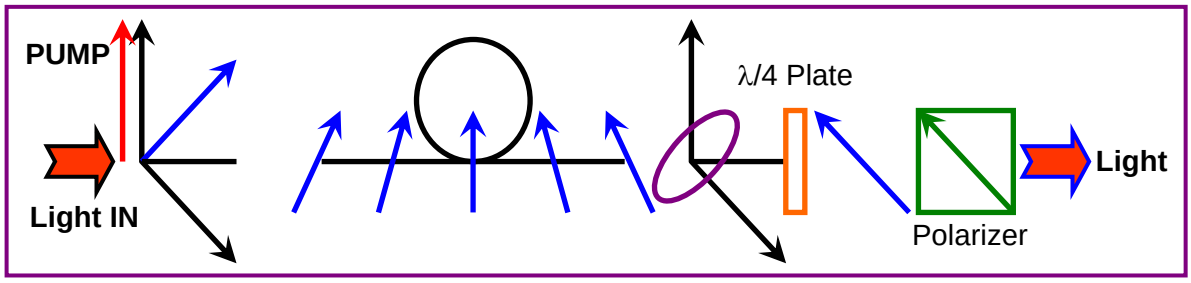

Figure 2-2. State of Polarization of Signals with Pump

The nonlinear phase shift for the signal at the output end of the fiber of length L, when the pump is polarized linearly along the x axis and $n_{0x} > n_{0y}$, can be written as

$$\begin{aligned}\delta\phi \equiv \delta\phi_L + \delta\phi_{NL} &= \frac{2\pi L_{eff}}{\lambda_s}\left(n_x - n_y\right) \\ &= \frac{2\pi L_{eff}}{\lambda_s}\left(\Delta n_L + \Delta n_{NL}\right) = \frac{2\pi L_{eff}}{\lambda_s}\left(\Delta n_L + n_{2B} I\right)\end{aligned} \tag{2.5}$$

where λ_s is the signal wavelength, I is the pump intensity, and n_{2B} is the Kerr coefficient given by[197]

$$\begin{aligned}&n_{2B} \approx 2\left(\delta n'_x - \delta n'_y\right) = 1.5 N_2 \\ &\text{where } \delta n'_x = \frac{9}{8} N_2 \text{ and } \delta n'_y = \frac{1}{3}\delta n'_x\end{aligned} \tag{2.6}$$

In addition, the signal transmittivity T_p is related to the nonlinear phase shift $\delta\phi$ by the simple relation as[197]

$$T_p = \sin^2\left(\frac{\delta\phi}{2}\right) \tag{2.7}$$

The transmittivity will be maximum when $\delta\phi=\pi$ or the an odd multiple integer of π, and the signal will be completely blocked when $\delta\phi=0$ or an even multiple integer of π.

Generally, PMFs are used to ensure that the pump maintains its SOP along the fiber in the optical Kerr shutters. The linear phase shift $\delta\phi_L$, induced by the linear birefringence Δn_L, can be compensated by inserting a quarter-wave plate before the polarizer as shown in Fig 2-2. However, in practical situations, $\delta\phi_L$ fluctuates due to random variation of temperature and

pressure, making it necessary to adjust it continuously. Alternatively, two identical pieces of PMFs which were spliced together such that their fast(or slow) axes are at right angles to each other can be used[2]. Since Δn_L has an opposite sign in the second fiber, the net phase shift induced by the linear birefringence Δn_L is effectively canceled. The phase shift compensation may also be achieved by means of a polarization rotation mirror using a PANDA fiber[4]. As a result, the nonlinear phase shift induced by the optical Kerr shutter can be simplified to

$$\delta\phi = \frac{2\pi L_{eff}}{\lambda_s} 1.5 N_2 \frac{P_p}{A_{eff}} \tag{2.8}$$

where P_p is the pump peak power. The minimum pump peak power for the maximum signal transmission can be obtained by setting $\delta\phi=\pi$. It is given by

$$P_{P\_\min} = \frac{\lambda_s A_{eff}}{3 N_2 L_{eff}} \tag{2.9}$$

Under ideal conditions, the response time of the optical Kerr shutter is limited only by the response time of the Kerr nonlinearity which is less than 10fs for optical fibers. In practice, however, there are some other factors limiting the response time and switching bandwidth. The first one is the group-velocity mismatch between the signal and the pump whose relative group delay is given by

$$\Delta t_g = L\left|\frac{1}{v_{gp}} - \frac{1}{v_{gs}}\right| = \frac{L}{c}\left|n_{gp} - n_{gs}\right| \tag{2.10}$$

where v_{gp} and v_{gs} are the group velocities and n_{gp} and n_{gs} are the group refractive indices for the pump and the signal, respectively. This problem may be solved by choosing the pump and signal wavelengths on opposite sides of the ZDW. The second limiting factor is the built-in birefringence. The two orthogonally polarized components of the signal travel at different speeds due to the linear birefringence Δn_L, resulting in a relative delay given by

$$\Delta t_p = \frac{L\Delta n_L}{c} = \frac{L}{c}\left|n_{0x} - n_{0y}\right| \tag{2.11}$$

This delay may be eliminated by splicing two PMFs together with their fast(or slow) axes at right angles to each other. The last limiting factor is the broadening of the pump pulse caused by GVD. This problem may be reduced by placing the pump wavelength closer to the ZDW. However, it is very difficult to satisfy all requirements simultaneously in order to solve all problems. This dissertation discusses alternative ways for solving them at once.

2.1.3. Optical Time-Division Demultiplexers

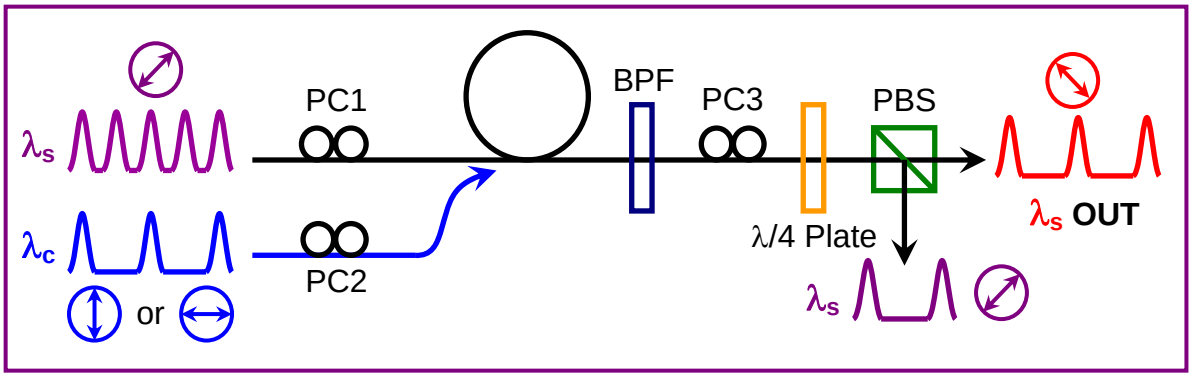

Figure 2-3. An Optical Kerr Optical Time-Division Demultiplexer

Figure 2-3 shows the schematics of an optical Kerr optical time-division demultiplexer[2-4] where λ_s and λ_c are the signal and control wavelengths, respectively, PCs are polarization controllers, BPF is a band pass filter, and PBS is a polarization beam splitter. Usually, PMFs are used to maintain the SOP of the control pulse in optical Kerr demultiplexers. In optical Kerr optical time-division demultiplexers, a strong control pulse causes the variation of refractive indices by different amounts along the two principal axes. This induced nonlinear birefringence changes the SOP of the weaker signal pulse. The extent of change depends on the power and SOP of the control pulse. The BPF is used to separate the control and signal pulses. The waveplate can be adjusted to compensate the intrinsic linear birefringence of PMFs, while active polarization control using the PCs is required to ensure the proper SOP of the signal and control pulses. The PBS is set such that the signal pulse can be detected only when the strong control pulse is present. As a result, the desired signal pulses can be selectively demultiplexed using the optical Kerr effect. The nonlinear phase shift by the nonlinear birefringence shown in Equation (2.8) should be an odd multiple integer of π for maximum switching efficiency. Typically, the required fiber length for a nonlinear phase shift of π is 1Km in conventional silica-core silica-clad fibers for a control power of 1W.

2.1.4. Wavelength-Division Demultiplexers

In the application of demultiplexing, the optical Kerr effect has been efficient only for optical time-division demultiplexing. In this dissertation, a new scheme of optical Kerr wavelength-division demultiplexing, using highly nonlinear MicroStructure Fibers(MSF), is proposed for the first time[5]. Basically, the scheme uses pulse walk-off between a control pulse and undesired signal pulses. The walk-off occurs easily due to the extremely high GVD of HNL glasses and high index difference of MSFs. In optical Kerr wavelength-division demultiplexers, the control and desired signal pulses have the same group velocity at different wavelengths, while other signal pulses with different wavelengths have different group velocities. As a result, the control pulse can affect only the desired signal pulse since others

are easily separated from the control pulse owing to the extremely high group-velocity difference between the control pulse and undesired signal pulses. Thus, wavelength-division-multiplexed signals can be selectively demultiplexed using the optical Kerr effect. The elaboration of the proposed optical Kerr wavelength-division demultiplexer will be discussed in much more detail in Chapter 7.

2.1.5. Wavelength Converters

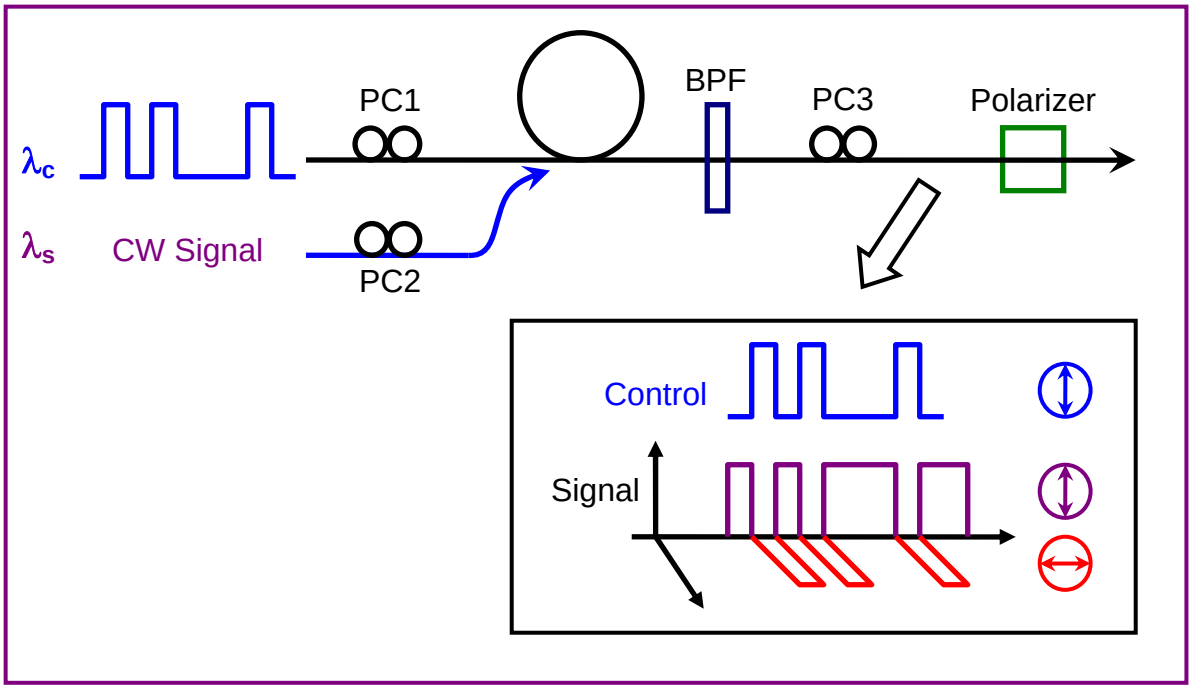

Figure 2-4. An Optical Kerr Wavelength Converter

The optical Kerr effect can also be the basis of operation for wavelength converters[30-32]. Figure 2-4 shows the schematic diagram of an optical Kerr wavelength converter. A strong control pulse changes the SOP of the weaker CW signal. The polarization controllers PC1 and PC2 are included so that both the relative polarization angle between the control and signal could be adjusted to achieve the maximum rotation of SOP and conversion efficiency. The

PC3 placed before a polarizer is adjusted such that the signal is blocked when the control pulse is absent. The inset in Figure 2-4 shows variation of the signal SOPs in the presence of control pulses. The SOP of the CW signal launched initially with the same SOP as that of control pulse is converted to the orthogonal SOP only when the control pulses are present. The wavelength conversion range of the signal depends on the initial pulse width of the control pulse, GVDs at the signal and control wavelengths, and the extent of dispersion flattening(dispersion slope) of optical fibers in the wavelength range of interest.

2.2. Nonlinear Optical Loop Mirrors

2.2.1. Nonlinear Optical Loop Mirrors by SPM

The Nonlinear Optical Loop Mirror(NOLM)[227] is an interferometric ultrafast optical switching device based on the nonlinear phase shift induced by Self-Phase Modulation(SPM). Unlike other interferometric devices, it does not require interferometric alignment, has simple structure, and is immune to external environmental changes since two counterpropagating beams experience exactly the same path.

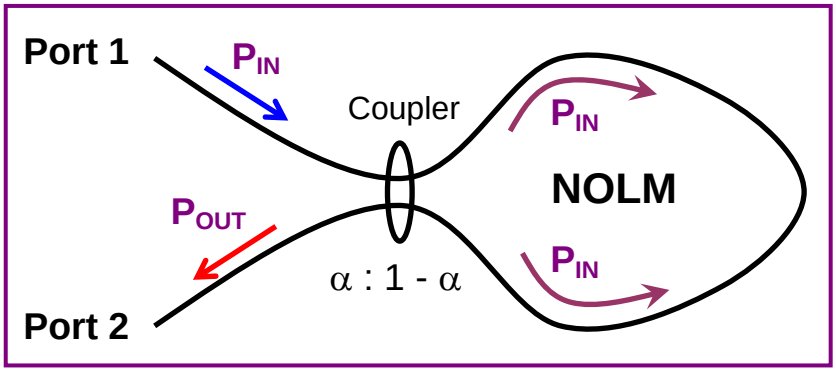

Figure 2-5. Nonlinear Optical Loop Mirrors by SPM

Figure 2-5 shows the basic configuration of the NOLM operating based on SPM. A single input signal is split into two opposite directions by a coupler with a power splitting ratio of α : 1-α. The two counterpropagating signals are recombined again by the coupler. Since they follow the same path but in opposite directions, the optical path length is precisely the same. This device is phase sensitive because it responds to the phase difference between the two counterpropagating signals. The phase difference between them is given by Equation (1.11), the output at port 2 can be expressed as[227]

$$P_{OUT} = P_{IN}\left\{1-2\alpha\left(1-\alpha\right)\left(1+\cos\left[\left(1-2\alpha\right)\times\delta\phi_{SPM}\right]\right)\right\}$$
$$where\ \ \delta\phi_{SPM} = \frac{m\pi}{1-2\alpha} = \frac{2\pi L_{eff}}{\lambda}\frac{N_2 P_{IN}}{A_{eff}} \tag{2.12}$$

This equation indicates that for any value of α≠0.5, when m is an odd integer, all the input power comes out from the port 2 and when m is an even integer, the output at port 2 has the minimum value given by

$$P_{OUT} = P_{IN}\left[1-4\alpha\left(1-\alpha\right)\right] \tag{2.13}$$

Figure 2-6 shows the relationship between the output power and α when m is an even integer[227]. The horizontal axis represents the product of the input power and effective length, the vertical axis represents the ratio of the output power over input power. As α increases, the minimum output power decreases. Therefore, higher α should be applied for higher power extinction ratios. Interestingly, if α=0.5, the output power becomes nearly zero, which means that all input power from port 1 is reflected back into port 1. As a result, it acts as a perfect mirror with 3dB coupler.

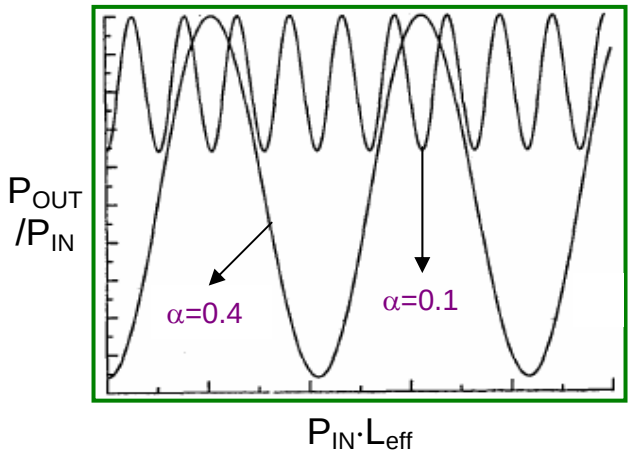

Figure 2-6. Relationship between Output Power and α in Nonlinear Optical Loop Mirrors

2.2.2. Nonlinear Optical Loop Mirrors by XPM

Basically, a NOLM operates based on the nonlinear phase shift induced by SPM. Its operation, however, is affected by Cross-Phase Modulation(XPM) when a strong pump is coupled with the signal. As discussed before, when only a signal is launched into a NOLM with a 3dB coupler, it acts as a perfect mirror. This section now considers the case when a strong pump is present as shown in Figure 2-7.

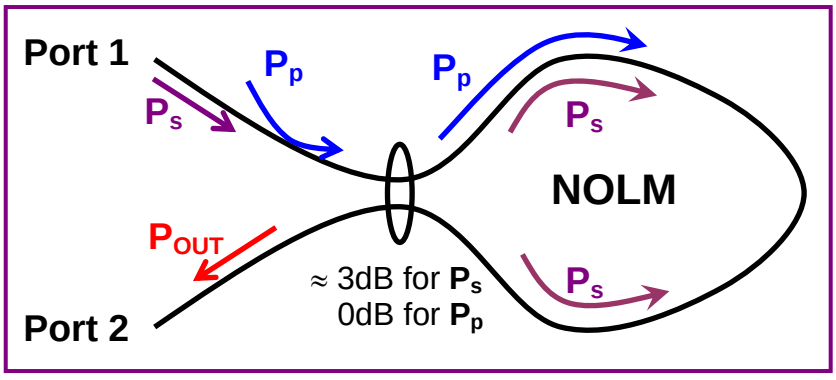

Figure 2-7. Nonlinear Optical Loop Mirrors by XPM

Now, the NOLM operates based on the nonlinear phase shift induced by XPM. When the strong pump is present, it can affect only the clockwise signal and cause the nonlinear phase shift through XPM only between the two copropagating beams, the pump and clockwise signal beams. This XPM-induced nonlinear phase shift of the clockwise signal can break the balance between the two counterpropagating signal beams and thus, they are switched out of the port 2. Therefore, the NOLM can not act as a perfect mirror any more when the pump is present, and the output from the port 2 can easily be controlled by the pump.

In nonlinear fiber devices based on NOLMs, the switched signal power, P_{OUT}, can be expressed as[33]

$$P_{OUT} = \frac{1}{2} P_s \left[1 - \cos \delta\phi\right], \ \delta\phi = 2\gamma P_p L_l \tag{2.14}$$

where P_s is the signal power, P_p is the pump peak power, L_l is the loop length, and γ is the nonlinear parameter defined in Equation (1.10). The output power, P_{OUT}, is maximized when $\delta\phi$ becomes an odd multiple integer of π and thus, the minimum loop length when $\delta\phi=\pi$ is given by

$$L_l = \frac{\pi}{2} \frac{1}{\gamma P_P} = \frac{\pi}{2} L_{NL} = \frac{\lambda_s A_{eff}}{4 N_2 P_p} \tag{2.15}$$

where λ_s is the signal wavelength and L_{NL} is the nonlinear length defined in Equation (1.10).

2.2.3. Optical Time-Division Demultiplexers

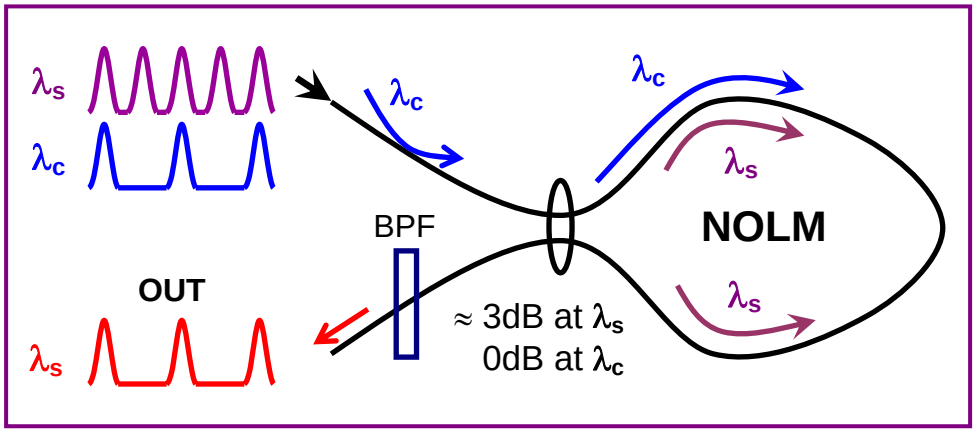

Figure 2-8. A Nonlinear Optical Loop Mirror Optical Time-Division Demultiplexer

Figure 2-8 shows the configuration of a NOLM optical time-division demultiplexer[6-20]. It uses the nonlinear phase shift induced by XPM between the control and clockwise signal pulses to pick up specific signal pulse trains. The coupler should act as a 3dB power divider at the signal wavelength and pass all of the control pulse power in the clockwise direction at the control wavelength. When the control pulse is absent, the signal pulse is reflected back to the input port. If a strong control pulse is introduced, the signal can be extracted from the output port because two counterpropagating signal pulses now experience a phase difference due to the XPM-induced nonlinear phase shift of the clockwise signal pulse. The BPF is required to pass only the switched signal pulses. Consequently, specific signal pulse trains can be selectively demultiplexed using the NOLM. The nonlinear phase shifts induced by XPM given in Equations (1.12) and (2.14) should be odd multiple integers of π in order for the extinction ratio of the demultiplexed signal to be maximized. Typically, the required loop length to achieve a nonlinear phase shift of π is 1Km in conventional silica-core silica-clad fibers when the control power is 1W.

2.2.4. Wavelength Converters

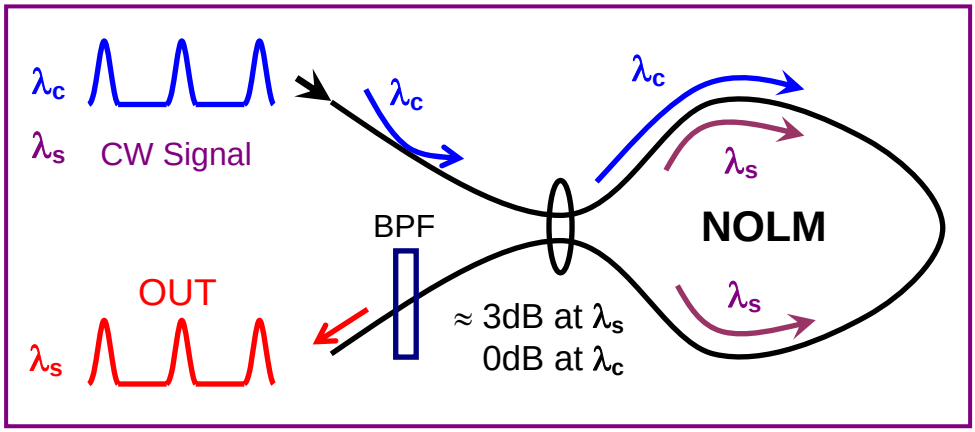

Figure 2-9. A Nonlinear Optical Loop Mirror Wavelength Converter

Figure 2-9 shows the diagram of a NOLM wavelength converter[33-41]. The weak CW signal, to be wavelength converted, can be controlled by XPM caused by the strong control pulses. Only the portions of the CW signal affected by the control pulses can experience a phase difference and thus can be extracted from the output port. As a result, the NOLM can be used for wavelength conversion.

In NOLM wavelength converters, the required minimum loop length for the maximum power of the wavelength-converted signal can be obtained by Equation (2.15). The switching performance depends highly on the initial pulse width of the control pulse and GVDs at the signal and control wavelengths. The dispersion parameter β_2 at the control wavelength λ_c is given by[40]

$$\beta_2 = -\frac{2\pi c \beta_3 \Delta\lambda}{\lambda_c^{\,2}}, \quad \Delta\lambda \equiv \lambda_0 - \lambda_c = \lambda_s - \lambda_0 \tag{2.16}$$

where c is the light velocity in vacuum, β_3 is the dispersion slope parameter, and λ_0 is the ZDW. The dispersion length L_D is given by

$$L_D = \frac{\tau^2}{|\beta_2|} \tag{2.17}$$

where τ is the initial pulse width of the control at FW$\frac{1}{e}$M. If the condition for L_l in Equation (2.15) is satisfied and the signal power P_s is much smaller than the control power P_c, the output pulse characteristics of the wavelength-converted signal is solely dependent on[40]

$$\frac{L_D}{L_l} = \frac{\lambda_c^{\,2}}{\pi^2 c} \cdot \frac{\gamma P_c \tau^2}{|\beta_3||\Delta\lambda|} \tag{2.18}$$

To develop a low control peak power P_c and a broad wavelength conversion range $|\Delta\lambda|$, L_D/L_l should be small when γ and β_3 are given. On the other hand, a smaller value of L_D easily induces pulse broadening due to the short initial pulse width τ and the high dispersion parameter β_2. As a result, it is necessary to consider this trade-off for better wavelength-conversion efficiencies.

2.3. Four-Wave Mixing

The performance efficiency of Four-Wave Mixing(FWM) is highly dependent on the wavelength range of operation[213]. FWM operating near the ZDW exhibits high efficiency and generates new FWM components in a broad wavelength range since the phase-matching condition is easily satisfied with very low GVD. Therefore, the pump of nonlinear devices based on FMW should be placed at the ZDW to maximize the efficiency. In addition, the deviation of the ZDW along a fiber length strongly affects the FWM behavior. FWM

operating around a varying ZDW develops a complicated efficiency pattern, and even the phase-matching condition is not completely satisfied in nonuniform ZDW fibers.

2.3.1. Optical Time-Division Demultiplexers

As discussed in Section 1.2.5, when multiple waves with different frequencies pass through the same fiber, they interact and combine to generate waves at new frequencies due to the nonlinear phenomenon called FWM.

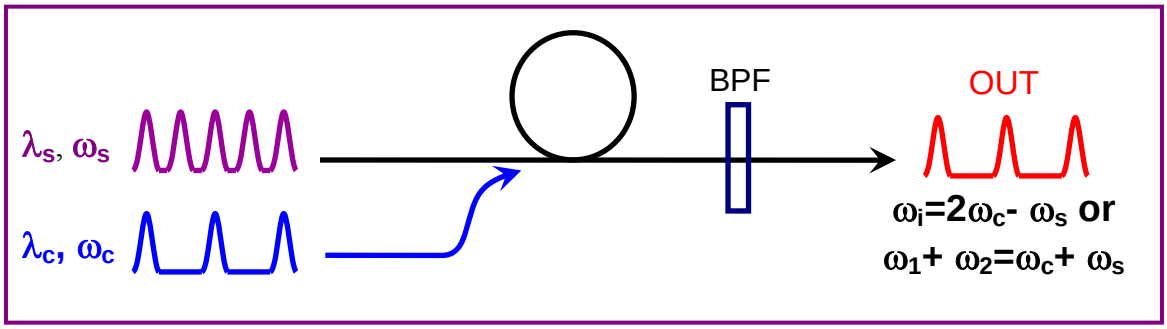

Figure 2-10. A Four-Wave Mixing Optical Time-Division Demultiplexer

Figure 2-10 depicts a simple configuration of an optical time-division demultiplexer based on FWM[21-26]. New FWM components at different frequencies can be generated by the interaction between the control and signal pulses. Only the newly generated FWM components pass through the BPF. In nonlinear fiber devices based on FWM, both of the two types of FWM, namely, four-photon mixing and three-wave mixing(degenerated FWM), can be utilized. When the control pulse power is strong(Pump) and the signal pulse power is weak(Stokes or Signal), only one wave(anti-Stokes or Idler) whose frequency is $\omega_i=2\omega_c-\omega_s$ will be generated(three-wave mixing)[23-25]. On the other hand, if the powers of both the control and signal pulses are strong, there will be two new waves with frequencies such that $\omega_1+\omega_2=\omega_c+\omega_s$(four-photon mixing)[21]. In the latter case, one of the two newly generated waves can be used for demultiplexing through filtering. As a result, the specific signal pulses

can be demultiplexed only when the control pulses are present by creating new frequency components.

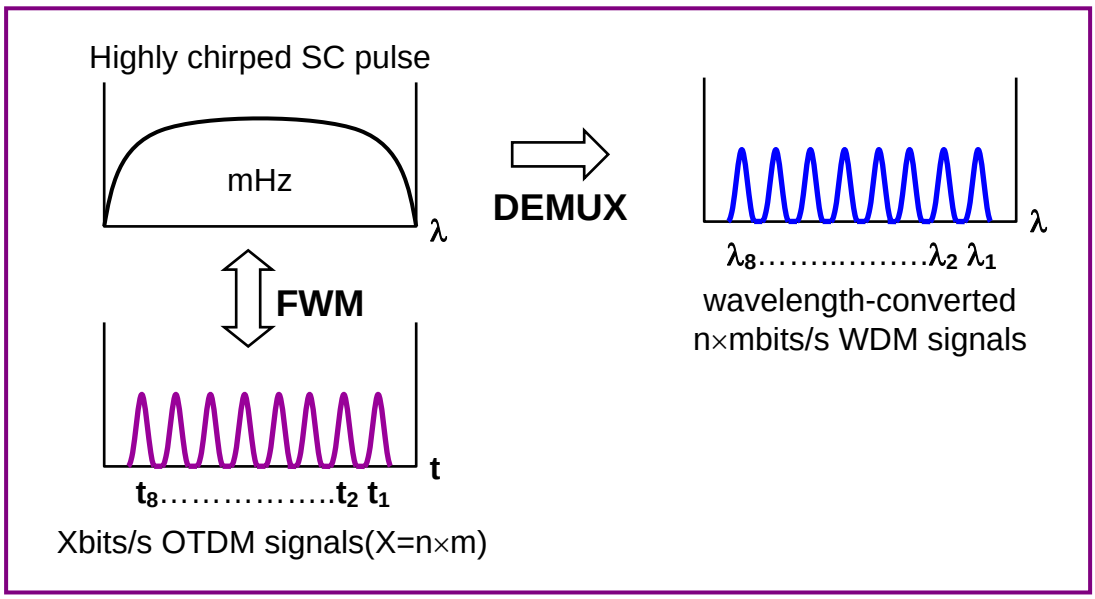

Figure 2-11. An Optical TD Demultiplexer based on OTDM-to-WDM Conversion by FWM

Figure 2-11 shows another scheme for optical time-division demultiplexing capable of simultaneous multichannel operation based on OTDM-to-WDM conversion by FWM[22, 26]. When FWM occurs between a highly chirped rectangular shaped SuperContinuum(SC) pulse(Pump) and OTDM signals(Signal), each of the newly generated waves(Idler) has a different center wavelength corresponding to the time position of the signal pulse, since the center wavelength of the SC pulse differs in its time position. If the bit-rate of the OTDM signals is Xbits/s and a mHz repetition rate of the SC pulse is used, the wavelength-converted new signals become n-channel mbits/s WDM signals because the center wavelength of each idler is different according to the time position of the OTDM signals. Thus, simultaneous multichannel all-optical demultiplexing by OTDM-to-WDM conversion can be achieved. In addition, when the pump SC pulse is placed near ZDW, the conversion and switching efficiency could be maximized.

2.3.2. Wavelength Converters

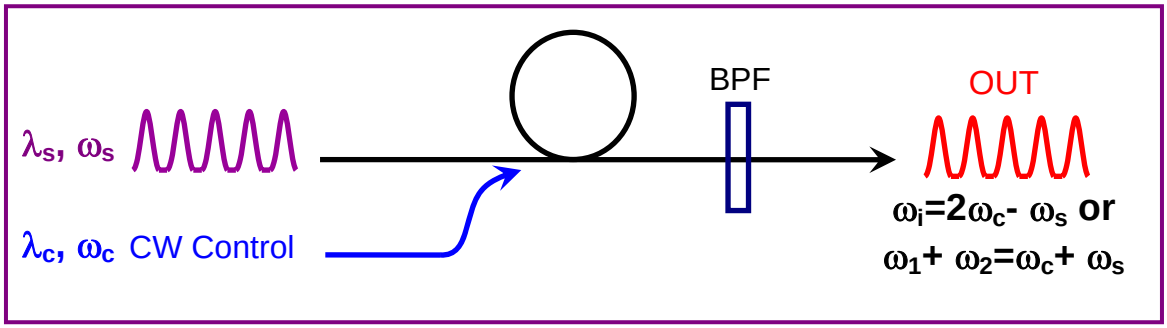

Figure 2-12. A Four-Wave Mixing Wavelength Converter

Figure 2-12 shows a simple configuration of a wavelength converter based on FWM[42-52]. The wavelengths of the input signal pulses are converted by interaction with the CW control wave through FWM. In FWM wavelength converters, the strong powers of both the control and signal are generally used(four-photon mixing, $\omega_1+\omega_2=\omega_c+\omega_s$) for most of cases, in order to increase conversion efficiency and to have simultaneously two wavelength-converted components.

It is also possible to convert the frequencies of multichannel signals simultaneously for more flexible frequency routing systems[43]. Because the phase-matching condition is almost satisfied in a wide frequency range when the control wave is positioned at the ZDW[213], the simultaneous frequency conversion of multichannel signals could be achieved. As a result, the control wave of the FWM wavelength converters should be placed at the ZDW to achieve a wide wavelength conversion range and simultaneous multichannel conversion.

2.4. Asymmetric Twin-Core Fibers

2.4.1. Directional Couplers

Directional couplers are based on the fact that the guided mode field of optical fibers extends far beyond the core-cladding interface. Therefore, when two fiber cores are placed sufficiently close to each other laterally so that their mode fields overlap, then the modes of the two fibers become coupled and their powers can transfer periodically between them. The basic principle of operation of directional couplers is essentially the same as the interference between the LP_{01} and LP_{11} modes[228]. When a system with a pair of identical symmetric planar waveguides, as shown in Figure 2-13, is considered, there will be two modes, the fundamental symmetric mode and the first excited asymmetric mode, according to the super mode theory. If a power is incident in one of the two waveguides, it excites a linear combination of the symmetric and asymmetric modes. Because the two modes have different phase velocities, there will be a phase difference between them as they propagate along the system. When the power is incident in the waveguide 1 and the accumulated phase difference becomes π, the superposition of the two modes will cancel in the waveguide 1 and add in the waveguide 2.

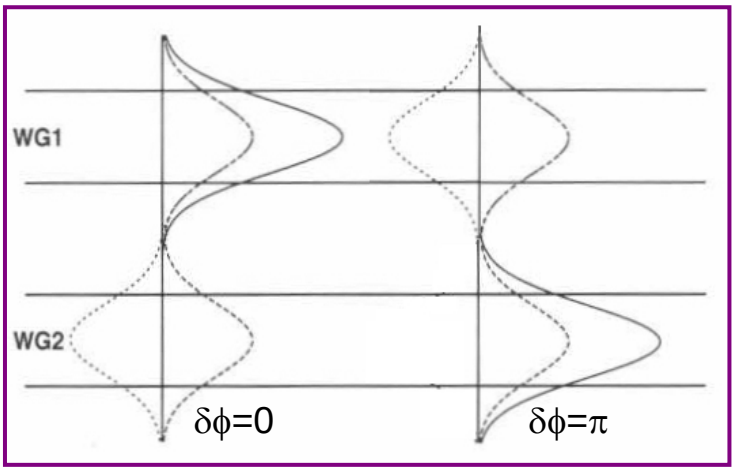

Figure 2-13. Basic Concept of Super Mode Theory

2.4.1.1. Linear Symmetric Directional Couplers

The simplest structure of directional couplers is the Twin-Core Fiber(TCF)[64-73, 229-241]. Figure 2-14 shows a linear symmetric TCF directional coupler[241] with equal core radii(a_1=a_2) and equal core refractive indices(n_1=n_2). That is, in the case of the symmetric directional couplers, the phase difference between the two modes of the cores is always zero regardless of the operating wavelength since all parameters of the two cores are identical.

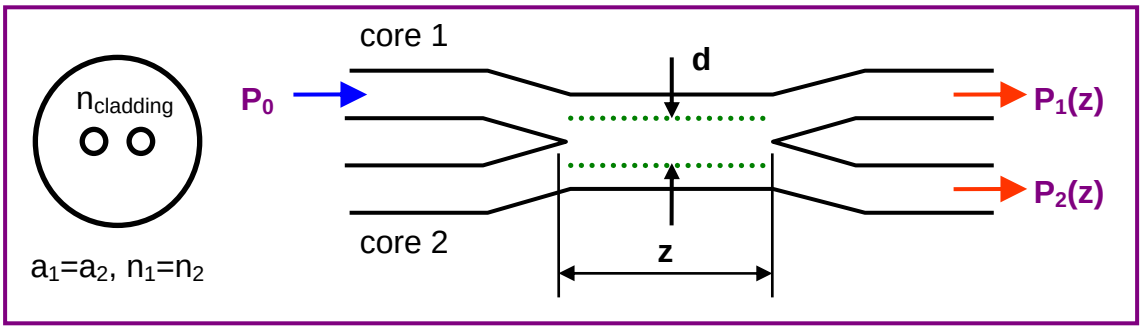

Figure 2-14. A Linear Symmetric Directional Coupler

The output powers of directional couplers can be obtained by the coupled-mode equations [242-243]. In linear symmetric directional couplers[244], when the input power is coupled into the core 1, the output powers from the two cores are given by[242]

$$P_1(z) = P_0\left(1 - \frac{\kappa^2}{\rho^2}\sin^2 \rho z\right) \tag{2.19}$$

$$P_2(z) = P_0 \frac{\kappa^2}{\rho^2}\sin^2 \rho z \tag{2.20}$$

where ρ is the coupling parameter given by

$$\rho = \left[\kappa^2 + \frac{1}{4}\left(\Delta\beta\right)^2 \right]^{\frac{1}{2}} \tag{2.21}$$

$\Delta\beta$ is the phase difference between the two cores which is zero for the symmetric directional couplers,

$$\Delta\beta = \beta_1 - \beta_2 = \frac{2\pi}{\lambda}\left(n_{eff\,1} - n_{eff\,2}\right) \tag{2.22}$$

and κ is the linear symmetric coupling coefficient which is inversely proportional to the distance d between the two cores. By using the LP_{01} mode field of a step-index fiber, for the linear symmetric directional couplers, κ is given by[242]

$$\kappa(d) = \frac{\lambda}{2\pi n}\frac{U^2}{a^2V^2}\frac{K_0\left(Wd/a\right)}{K_1^{\,2}\left(W\right)} \tag{2.23}$$

where λ is the free space wavelength, n is the core refractive index, a is the core radius, d is the distance between the centers of the two cores, and $K_m(\cdot)$ is the modified Bessel function of order m and

$$U = \frac{2\pi a}{\lambda}\sqrt{n_{core}^{\,2} - n_{eff}^{\,2}} \tag{2.24}$$

$$W = \frac{2\pi a}{\lambda}\sqrt{n_{eff}^{\,2} - n_{cladding}^{\,2}} \tag{2.25}$$

$$V = \sqrt{U^2 + W^2} \tag{2.26}$$

Finally, for symmetric couplers since ρ=κ, the output powers can be simplified as

$$P_1(z) = P_0 \cos^2 \kappa z \tag{2.27}$$

$$P_2(z) = P_0 \sin^2 \kappa z \tag{2.28}$$

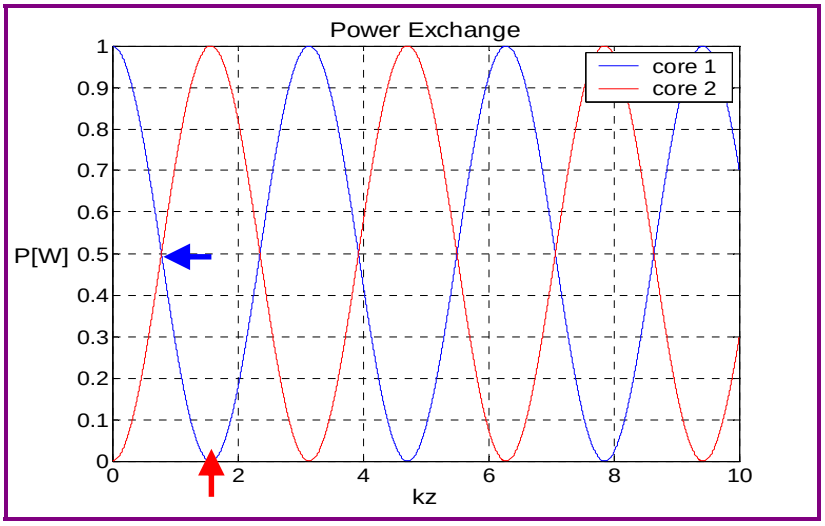

Figure 2-15. Power Exchange in Linear Symmetric Directional Couplers

Figure 2-15 shows power exchange patterns between the two cores in linear symmetric directional couplers. The minimum distance(red arrow) at which the power completely transfers from the input core to the other core is called the Coupling Length(CL) or half-beat length given by

$$z = L_c = \frac{\pi}{2\kappa} \tag{2.29}$$

When the interaction length z=π/4κ(blue arrow), the coupler acts as a 3dB power divider. In addition, since κ depends obviously on the wavelength of the input signal, it can also act as a spectral filter for demultiplexing in WDM systems.

2.4.1.2. Linear Asymmetric Directional Couplers

Figure 2-16 shows a linear Asymmetric Twin-Core Fiber(ATCF)[239-240] directional coupler in which the core radii(aL and aS) and core refractive indices(n_1L and n_1S) are unequal. Typically, asymmetric directional couplers consist of two single-clad fibers which differ in their core radii and/or core refractive indices.

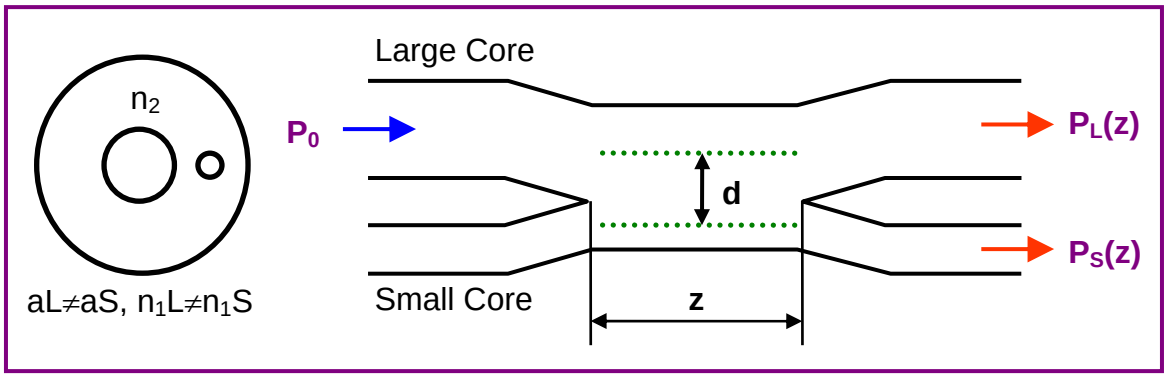

Figure 2-16. A Linear Asymmetric Directional Coupler

In contrast to symmetric directional couplers, the phase difference between the two modes of the cores in asymmetric directional couplers is not zero except at a specific wavelength. This phase difference is zero only at the wavelength where the propagation constants of the two modes of the cores are equal. As a result, the coupling process in asymmetric directional couplers occurs in a complicated manner due to the phase mismatch between the two cores.

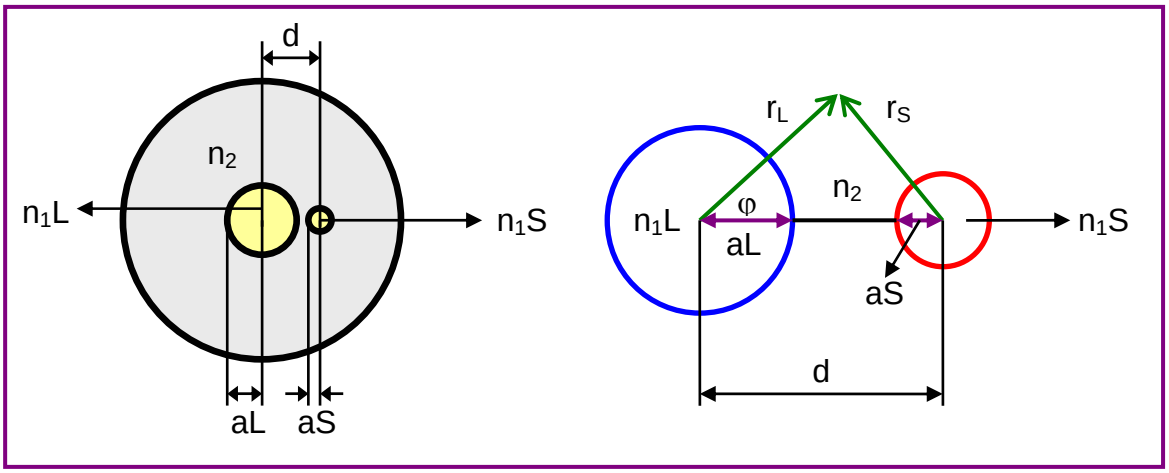

Figure 2-17. Geometry and Coordinates of Asymmetric Twin-Core Fibers

Figure 2-17 shows the cross-sectional geometry and coordinates of an ATCF. Assuming that each core guides only the fundamental LP_{01} mode and the two cores interact weakly with each other, the total field of each core can be expressed as[236]

$$\Psi_L = A_L(z)\psi_L(r_L)\exp(-j\beta_L z) \tag{2.30}$$

$$\Psi_S = A_S(z)\psi_S(r_S)\exp(-j\beta_S z) \tag{2.31}$$

where A_S and A_L are the z-dependent amplitude coefficients responsible for power transfer between the two cores, ψ_S and ψ_L are the transverse mode fields of the LP_{01} mode, r_S and r_L are the radial coordinates referred to the axis of the core, and β_S and β_L are the propagation constants of the modes. Also, the subscripts S and L refer to the small and large cores, respectively. According to the theory of weakly-coupled parallel waveguides, A_L and A_S are governed by the following coupled-mode differential equations[243].

$$\frac{dA_L}{dz} = -j\left[\kappa'_{LL}A_L + \kappa'_{LS}\exp\left(j\Delta\beta z\right)A_S\right] \tag{2.32}$$

$$\frac{dA_S}{dz} = -j\left[\kappa'_{SS}A_S + \kappa'_{SL}\exp\left(-j\Delta\beta z\right)A_L\right] \tag{2.33}$$

where $\Delta\beta$ is the phase difference between the fundamental modes of the large and small cores and κ' is the linear asymmetric coupling coefficient defined by an overlap integral as[236]

$$\kappa'_{ij} = \frac{\omega\varepsilon_0}{4}\left(n_2{}^2 - n_i{}^2\right)\int_{S_i}\psi_i\left(r_i\right)\psi_j\left(r_j\right)dS_i,\ i \text{ and } j = L,S$$

$$\begin{aligned}\kappa'_{LS} &= \frac{\omega\varepsilon_0}{4}\left(n_2{}^2 - n_1L^2\right)\int_{S_L}\psi_L\left(r_L\right)\psi_S\left(r_S\right)dS_L \\ &= \frac{\omega\varepsilon_0}{4}\left(n_2{}^2 - n_1L^2\right)\int_{-aL}^{aL}\int_0^{2\pi}\psi_L\left(r_L\right)\psi_S\left(r_S\right)adad\varphi\end{aligned} \tag{2.34}$$

$$\begin{aligned}\kappa'_{SL} &= \frac{\omega\varepsilon_0}{4}\left(n_2{}^2 - n_1S^2\right)\int_{S_S}\psi_S\left(r_S\right)\psi_L\left(r_L\right)dS_S \\ &= \frac{\omega\varepsilon_0}{4}\left(n_2{}^2 - n_1S^2\right)\int_{-aS}^{aS}\int_0^{2\pi}\psi_S\left(r_S\right)\psi_L\left(r_L\right)adad\varphi\end{aligned} \tag{2.35}$$

where ω is the angular frequency, ε_0 is the vacuum permittivity, and S is the cross-section of the coupler. Assuming that the entire input power is launched into the large core at z=0, that is, $A_S(0)=0$, the solutions of Equations (2.32) and (2.33) can be expressed as

$$P_L(z) \sim \left|A_L(z)\right|^2 = \frac{P_0}{\rho^2}\left[\frac{1}{4}\left(\Delta\beta + \kappa'_{LL} - \kappa'_{SS}\right)^2 \cdot \sin^2(\rho z) + \rho^2 \cdot \cos^2(\rho z)\right] \quad (2.36)$$

$$P_S(z) \sim \left|A_S(z)\right|^2 = \frac{P_0}{\rho^2}\left[\kappa'^{\,2}_{LS} \cdot \sin^2(\rho z)\right] \quad (2.37)$$

where ρ is the coupling parameter given by

$$\rho = \left[\frac{1}{4}\left(\Delta\beta + \kappa'_{LL} - \kappa'_{SS}\right)^2 + \kappa'_{LS}\kappa'_{SL}\right]^{\frac{1}{2}} \quad (2.38)$$

Equations (2.36) and (2.37) describe the output powers at the output of the large and small cores. As the phase difference Δβ increases, the power transferred to the small core, $P_S(z)$, decreases. It should be noted that complete power transfer occurs at the particular wavelength where Δβ=0(phase-matching) and ρz=π/2+mπ(m=integer). In other words, power transfer in asymmetric directional couplers is always incomplete except at a specific wavelength. This wavelength is referred to as the Maximum Coupling Wavelength(MCW). The input power launched into the large core will be completely transferred to the small core at the MCW when the length of the coupler L=π/2ρ(the coupling length). At wavelengths far away from the MCW, the transferred power decreases because Δβ increases. As a result, the asymmetric directional coupler can function as a spectral filter with peak transmission at MCW.

The self-coupling coefficients κ'_{LL} and κ'_{SS} represent corrections to the propagation constants of the modes of each individual core due to the presence of the other core; they are much smaller than κ'_{LS} and κ'_{SL} and are often neglected. In addition, at MCW, because Δβ=0 and $\kappa'_{LS}=\kappa'_{SL}$, the output powers at MCW can be simplified as

$$P_L(z) = P_0 \cos^2(\rho z) \tag{2.39}$$

$$P_S(z) = P_0 \sin^2(\rho z) \tag{2.40}$$

$$\rho = \sqrt{\kappa'_{LS}\kappa'_{SL}} = \kappa'_{LS} = \kappa'_{SL} \tag{2.41}$$

2.4.1.3. Nonlinear Directional Couplers

The intensity-dependent nonlinear refractive index δn affects the coupling process in the nonlinear directional couplers[59-73]. As shown in Figure 2-18, when input power P_{IN} is much lower than critical power P_{CR}, namely, $P_{IN} << P_{CR}$, it behaves just as a linear directional coupler. Therefore, all input power can be completely transferred to the other guide at the CL.

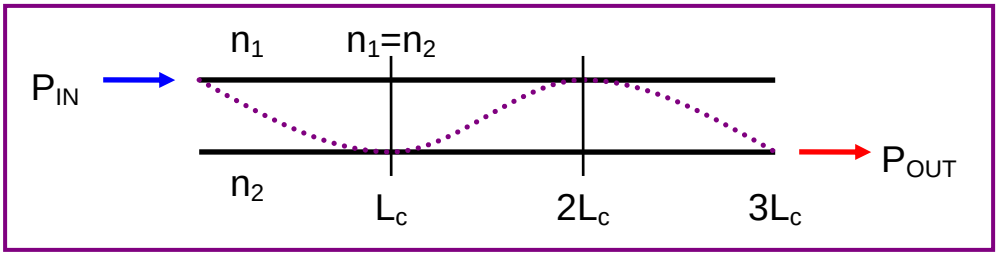

Figure 2-18. A Linear Symmetric Directional Coupler($P_{IN} << P_{CR}$)

However, as the input power increases, the refractive index of the input guide increases due to its intensity-dependence. This intensity-dependent variation of the nonlinear refractive index δn destroys the condition of phase-matching(δϕ=0). As a result, it blocks the complete power transfer due to the induced phase difference given by

$$\delta\phi = \phi_1 - \phi_2 = \frac{2\pi L_{eff}}{\lambda}\left(\delta n_1 - \delta n_2\right) \neq 0 \tag{2.42}$$

As shown in Figure 2-19, at critical power[64] which is defined as

$$P_{CR} = \frac{A_{eff}\lambda}{N_2 L_c}, \tag{2.43}$$

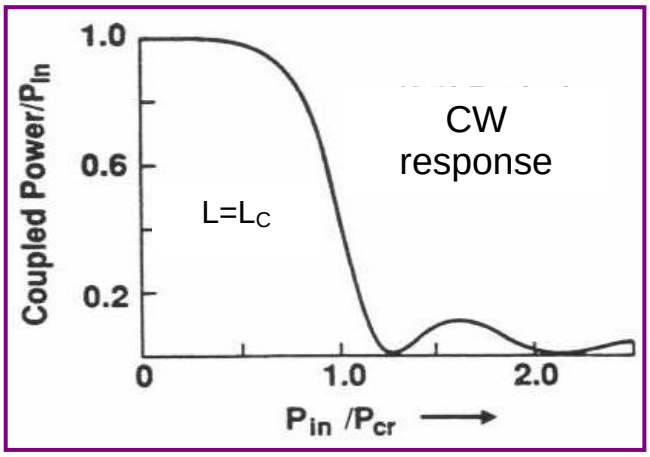

Figure 2-19. Relationship between Input Power and Critical Power

only half of the input power can be transferred to the other guide. As the input power exceeds the critical power, the transferred power decreases more and more and finally becomes 0. Therefore, as shown in Figure 2-20, all input power stays in the input guide and no power is transferred to the other guide when $P_{IN} >> P_{CR}$. The intensity-dependent change in refractive index blocks the normal power transfer between the guides.

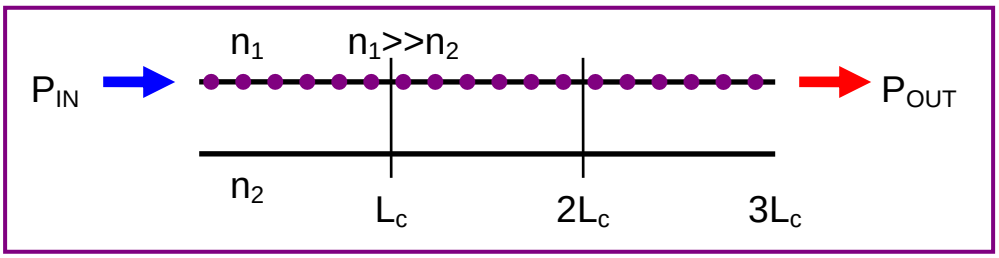

Figure 2-20. A Nonlinear Symmetric Directional Coupler($P_{IN} >> P_{CR}$)

Accordingly, in the nonlinear directional couplers, when the input power is much smaller than the critical power, all input power can be transferred to the other guide at the CL. On the other hand, when the input power is much larger than the critical power, all input power stays in the input guide, thus resulting in no power transfer. Therefore, the extent of the input power transfer to the other guide can be controlled by adjusting the input power in nonlinear directional couplers. One of the obvious applications of such couplers is a nonlinear optical switch. Figure 2-21 shows the basic concept of the nonlinear optical switch. When the pump is not incident, the input signal can come out from the other guide at the CL. If the strong pump is present, it causes a phase mismatch between the two guides, thus resulting in blocking the power transfer. As a result, the position of the output power can be selected by controlling the pump power.

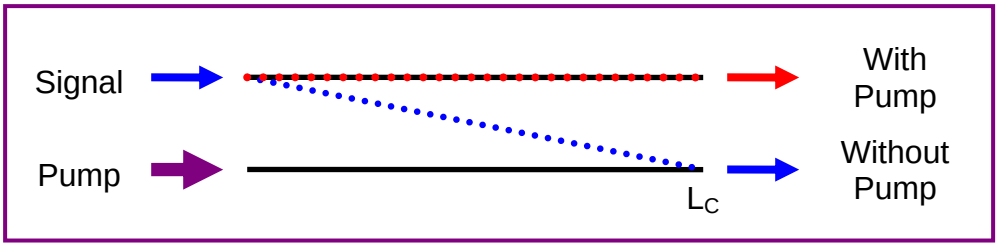

Figure 2-21. A Nonlinear Optical Switch

For the case of symmetric couplers, $\delta\phi=0$ at any wavelength in the linear region($P_{IN} << P_{CR}$) while for the case of asymmetric couplers, $\delta\phi=0$ only at one particular wavelength even in the linear region. Therefore, in nonlinear symmetric directional couplers[59-61, 64-71] described so far, complete transfer of power is possible for any signal wavelength at the corresponding CL by adjusting signal(self) or pump powers. However, in the nonlinear asymmetric directional couplers[62-63, 72-73], the signal should be placed at MCW where $\delta\phi=0$ to transfer the input power completely. This MCW can be modified by the strong pump due to the intensity-dependence of refractive index. Using this property of the nonlinear asymmetric directional couplers, they can be used as demultiplexers for wavelength-division-multiplexed signals. It will be described in the next section in more detail.

2.4.2. Structures and Properties of Asymmetric Twin-Core Fibers

Figures 2-22 and 2-23 show the structures and refractive index profile of the ATCF considered in this dissertation, respectively. The ATCF consists of two cores sharing the same cladding, but their core radii and core refractive indices are different. The small core is highly doped with GeO_2, thus resulting in much higher refractive index.

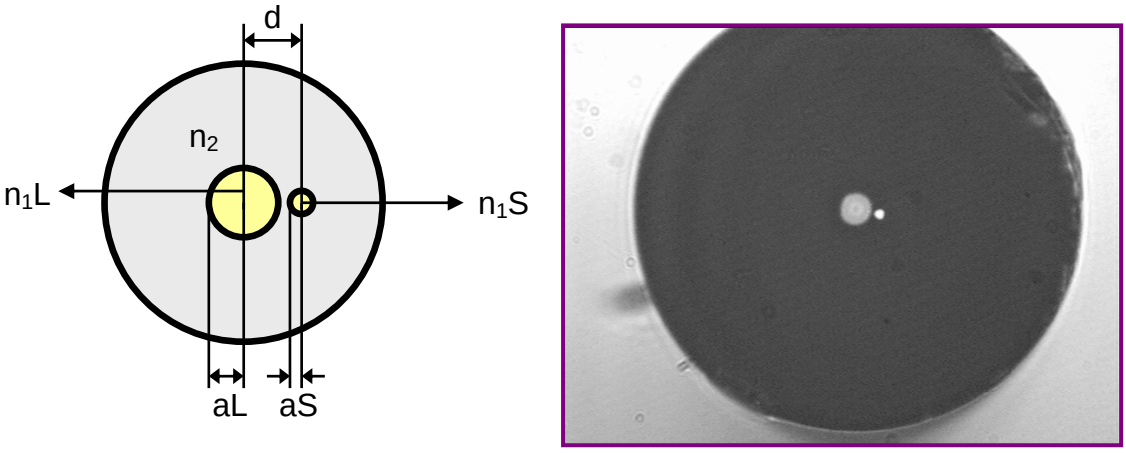

Figure 2-22. Structures of the Asymmetric Twin-Core Fiber

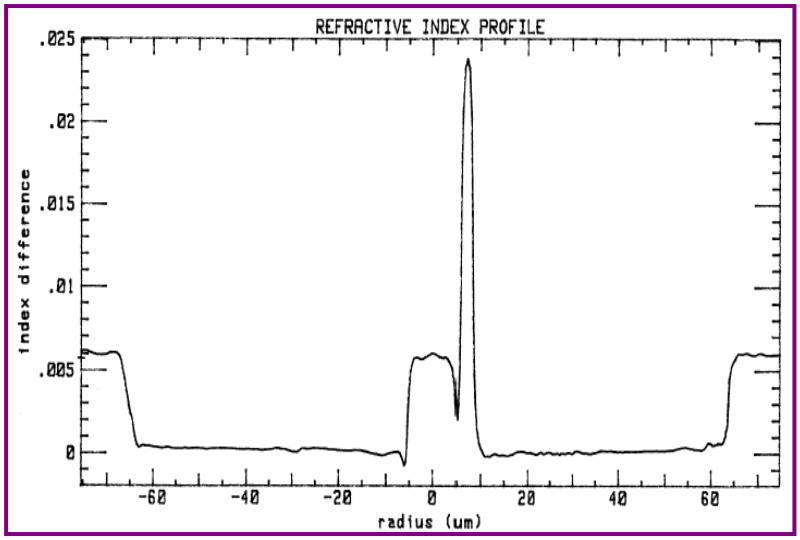

Figure 2-23. Measured Refractive Index Profile of the Asymmetric Twin-Core Fiber

The measured parameters of the ATCF are listed below.

$$aL = 4.2\mu m,\ aS = 1.15\mu m,\ d = 6.85\mu m$$
$$n_1L = 1.451,\ n_1S = 1.469,\ n_2 = 1.445\ \ at\ 1.55\mu m$$

The index difference Δn between the large core and the cladding is 0.006 and Δn between the small core and the cladding is 0.024. For the large core fiber, since $n_1L \approx n_2$, the scalar wave approximation(weakly guiding approximation) can be used. However, for the small core fiber, since $n_1S >> n_2$, the vector wave equation should be used to achieve accurate results. As a result, to analyze this ATCF, the vector wave equation is used for both small core and even large core fibers for best analysis.

The difference between the effective refractive index and the cladding refractive index for each core has been calculated using vector wave analysis with the measured parameters as shown in Figure 2-24. The single-mode cutoff wavelengths are 1.447μm and 0.795μm for the large and small cores, respectively and the MCW is 1.5216μm. Maximum transfer of power between the two cores occurs only at the MCW of 1.5216μm in this ATCF directional coupler.

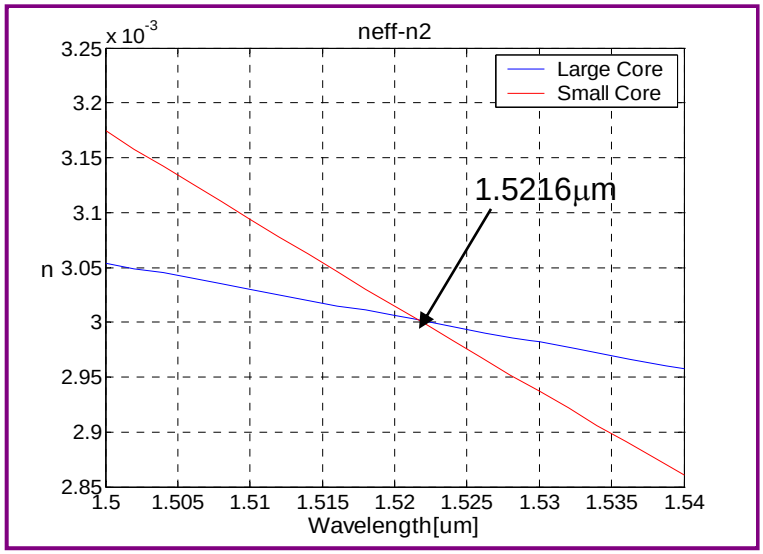

Figure 2-24. Variation of Effective Refractive Indices

The MCW of the ATCF depends on the variation of the refractive indices and the core radii of the two cores. The MCW variation caused by slightly different refractive index or core radius of each core has been simulated to examine how the MCW is sensitive to the core properties.

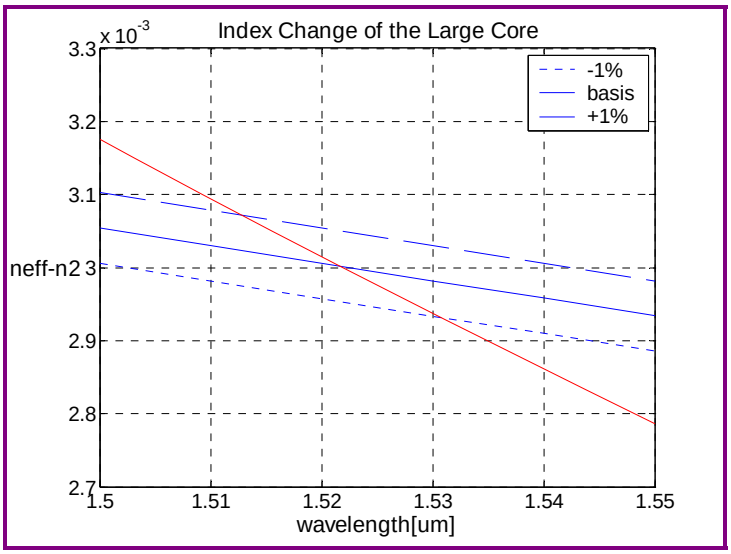

Figure 2-25. Range of MCW Variation due to Refractive Index Change of the Large Core

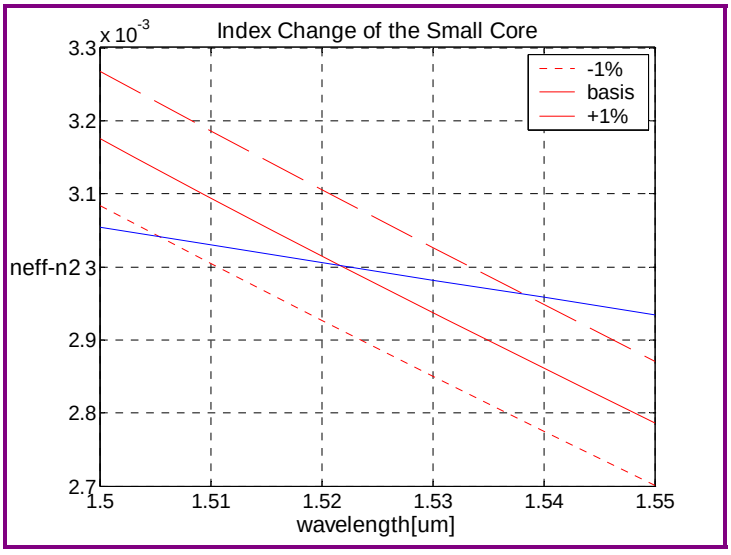

Figure 2-26. Range of MCW Variation due to Refractive Index Change of the Small Core

Figures 2-25 and 2-26 show the range of variation of the MCW caused by the refractive index change of the large core and the small core, respectively, leaving the radii of the two cores and the cladding refractive index unchanged. It was found that when the refractive indices were changed by the same percent amount, the extent of the range of MCW variation was higher for the case of the small core refractive index change.

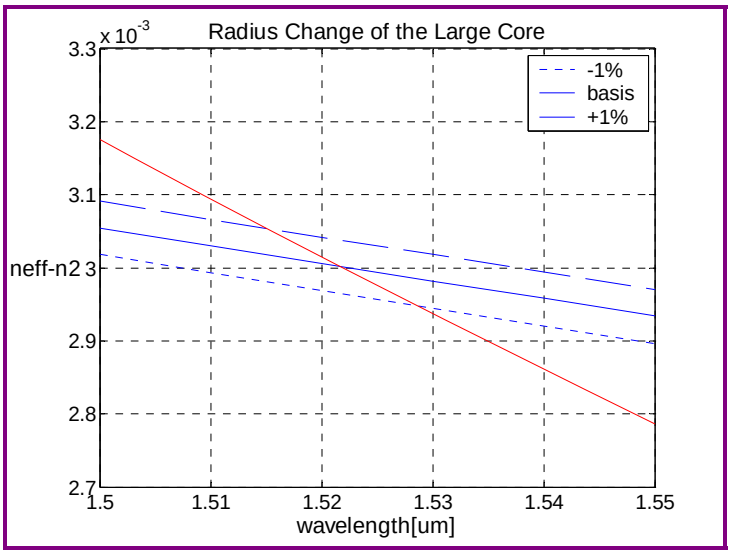

Figure 2-27. Range of MCW Variation due to Radius Change of the Large Core

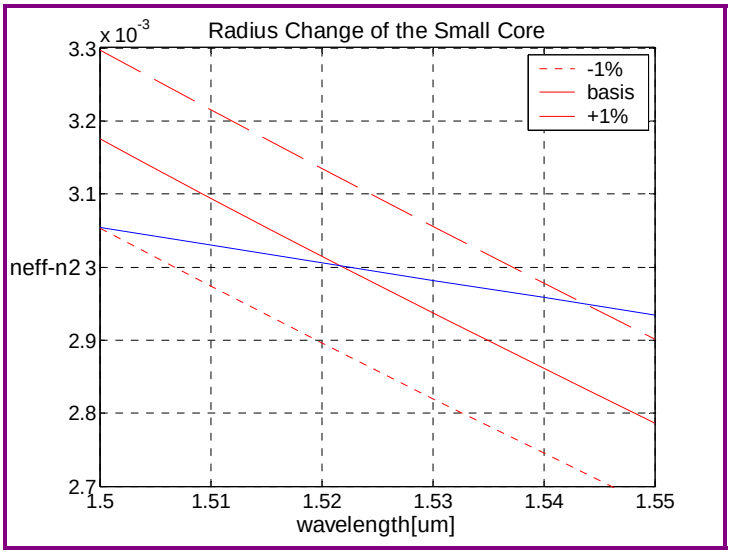

Figure 2-28. Range of MCW Variation due to Radius Change of the Small Core

Figures 2-27 and 2-28 show the range of variation of the MCW caused by the core radius change of the large core and the small core, respectively, leaving the refractive indices of the two cores and the cladding refractive index unchanged. It was found that when the core radii were changed by the same percent amount, the extent of the range of MCW variation was higher for the case of the small core radius change.

The coupling coefficients in asymmetric directional couplers are defined by Equations (2.34) and (2.35), and their coupling processes are governed by Equations (2.36) and (2.37). Power exchange and variation patterns have been simulated with the measured parameters of the ATCF. Figure 2-29 shows power exchange between the two cores as a function of length at the MCW when input power is launched into the large core. It is clearly seen that the input power in the large core is totally transferred to the small core at the MCW of 1.5216μm for the CL of 165mm.

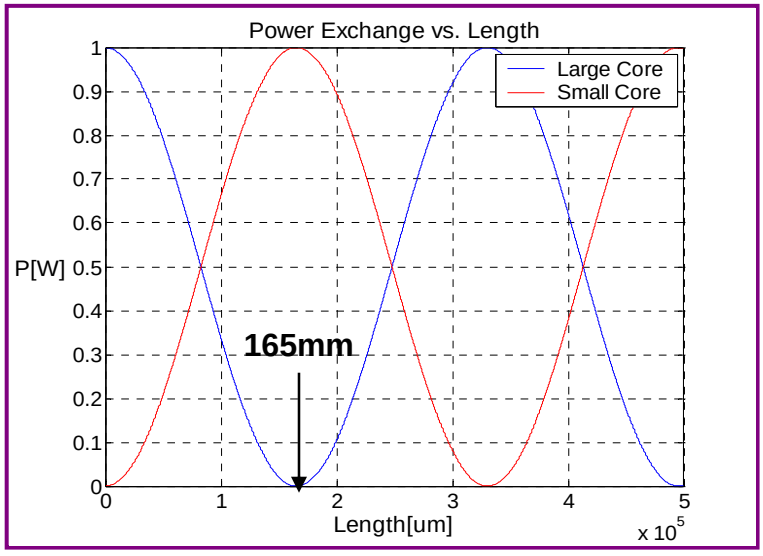

Figure 2-29. Power Exchange vs. Length at the Maximum Coupling Wavelength

Figure 2-30 shows power exchange between the two cores as a function of wavelength at the CL of 165mm. In Figure 2-31, the power variation of the small core is expressed in dB scale in order to better see the power levels away from MCW. In both figures, it is clear that the input power in the large core is completely transferred to the small core only at the MCW

of 1.5216μm and the spectral width is 1.6nm. Note that for ATCF directional couplers, as the separation between the two cores increases, the CL increases while the spectral width $\Delta\lambda$ decreases. In addition, $\Delta\lambda$ becomes smaller when the CL is a multiple integer of the CL.

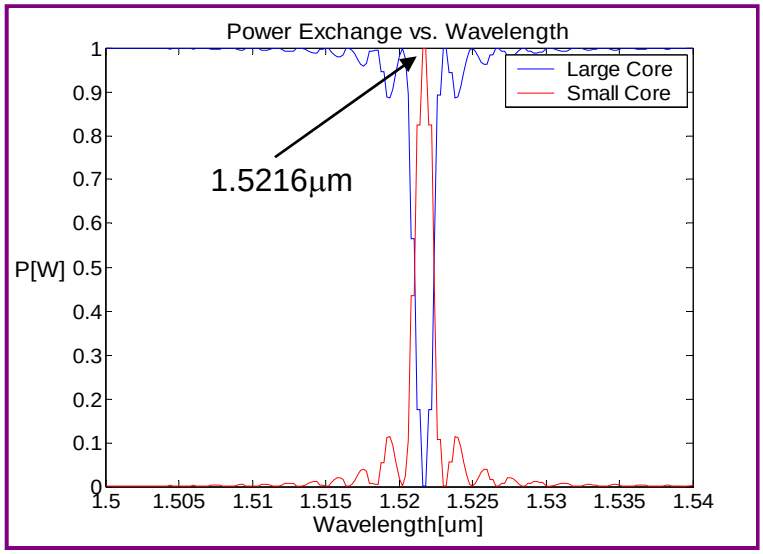

Figure 2-30. Power Exchange vs. Wavelength at the Coupling Length

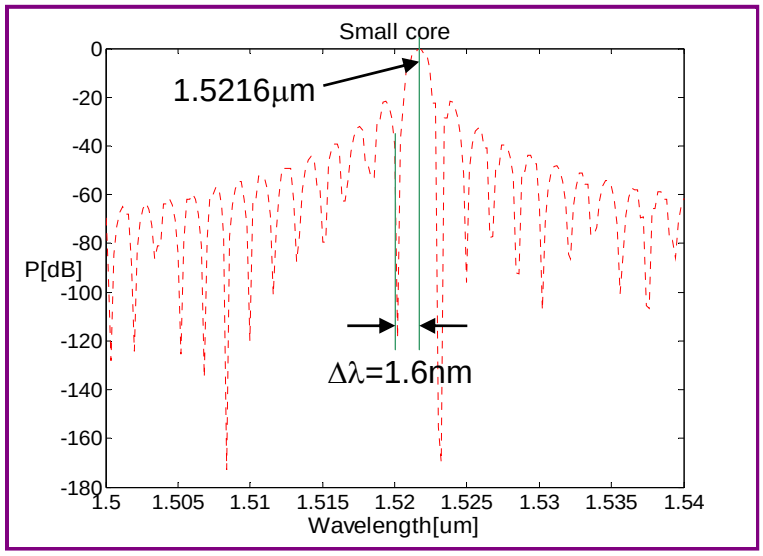

Figure 2-31. Power Variation of the Small Core vs. Wavelength at the Coupling Length

2.4.3. Optical Time-Division Demultiplexers

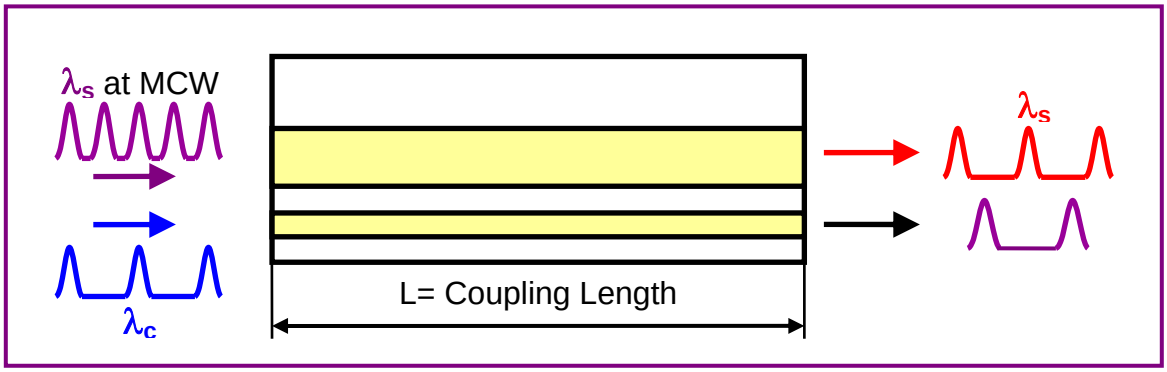

Figure 2-32. An ATCF Optical Time-Division Demultiplexer(A Signal-Pass Scheme)

Figure 2-32 describes the basic concept of an ATCF optical time-division demultiplexer(A signal-pass scheme). All signal pulses at the MCW which are coupled into the large core come out from the small core when the control pulses are not present. However, if the strong control pulses are introduced into the small core, the refractive index of the small core changes, thus causing phase mismatch between the two cores. As a result, the specific desired signal pulses affected by the control pulses stay in the large core while other signal pulses come out from the small core. Finally, the specific signal pulses could be selectively demultiplexed by adjusting the control pulses. The control pulse wavelength should be far away from the MCW in order to block power exchange by the control power.

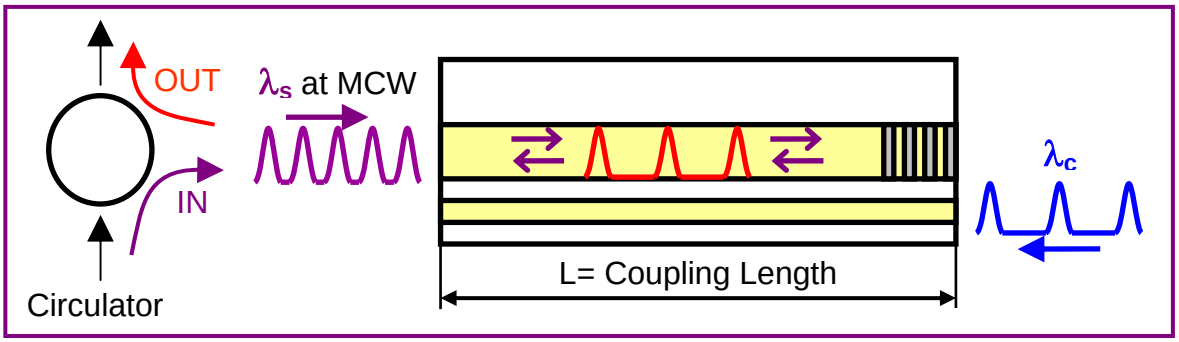

Figure 2-33. An ATCF Optical Time-Division Demultiplexer(A Signal-Reflection Scheme)

In ATCFs, it is quite difficult to launch the signal and control pulses at the same end due to a geometrical restriction of ATCFs. Figure 2-33 presents another scheme an ATCF optical time-division demultiplexer(a signal-reflection scheme) to make it easier. In this scheme, the signal pulses are launched into the large core at one end of the ATCF with a circulator while the control pulses are launched into the small core at the other end. The desired signal pulses affected by the control pulses stay in the large core due to the phase mismatch between the two cores, and they are reflected by the grating. These desired signal pulses come out from one port of the circulator while the undesired signal pulses come out from the other port.

2.4.4. Wavelength-Division Demultiplexers

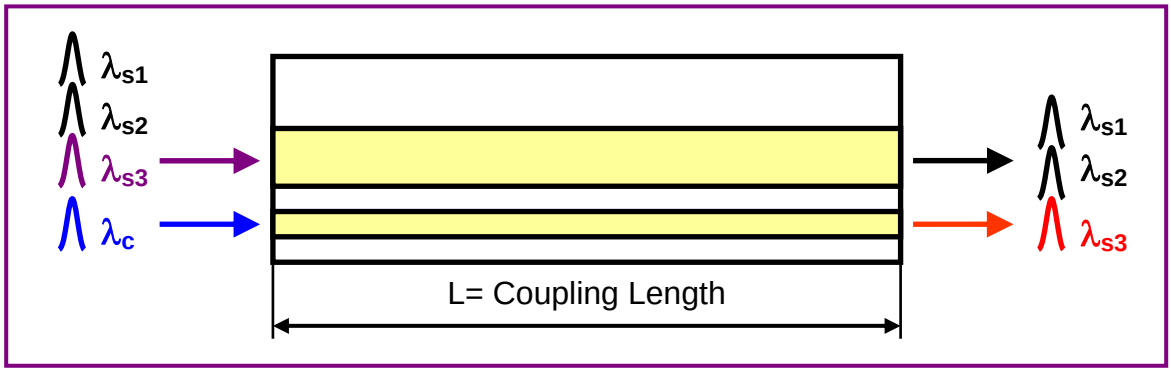

Figure 2-34. An Asymmetric Twin-Core Fiber Wavelength-Division Demultiplexer

Figure 2-34 shows the configuration of an ATCF wavelength-division demultiplexer. As discussed in Section 2.4.2, the MCW of the ACTF is highly dependent on the refractive index difference between the small core(higher-index core) and cladding. In addition, since the nonlinear refractive index δn of the small core is affected by the strong pump power, the MCW can be tuned by controlling δn which can be adjusted by the control power. When a number of signal pulses with different wavelengths are coupled simultaneously into the large core, the magnitude of the control power is adjusted and launched into the small core in order to shift the MCW to the same wavelength of the desired signal pulse. As a result, the desired signal pulse with the particular wavelength selected by the control pulse will come out from the small core while others continue to stay in the large core.

2.5. Mode Interference

2.5.1. Fiber Modes in Step-Index Fibers

The propagation characteristics of optical fibers play an extremely important role in the design of optical communication systems. Therefore, a detailed modal analysis of a step-index fiber is essential to the understanding of propagation characteristics of optical fibers. A step-index fiber is characterized by its refractive index profile shown in Figure 2-35.

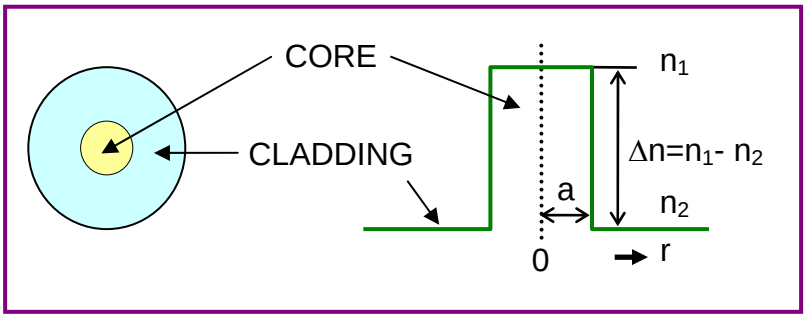

Figure 2-35. Schematic Illustration of Step-Index Fibers

2.5.1.1. Scalar Wave Analysis

In conventional silica-core silica–clad fibers, the core refractive index is nearly equal to the cladding refractive index. This enables the use of the so-called scalar wave analysis based on the weakly guiding approximation. In this analysis, by superimposing transverse components(e_r and e_ϕ) of appropriate nearly degenerate modes, the resultant field is polarized in only one Cartesian direction. These linearly polarized modes are usually referred to as the LP modes.

Under the weakly guiding approximation, the transverse Cartesian component of the electric field satisfies the scalar wave equation given by

$$\nabla^2\Psi = \frac{n^2}{c^2}\frac{\partial^2\Psi}{\partial t^2},\ \Psi(r,\phi,z,t) = \psi(r,\phi)e^{j(\omega t-\beta z)} \tag{2.44}$$

where ω is the angular frequency and β is the propagation constant. After solving this scalar wave equation, it is found that the general solutions for ψ(r,ϕ) are expressed in terms of the J Bessel function $J_l(\cdot)$ and the modified K Bessel function $K_l(\cdot)$ as[245]

$$\psi(r,\phi) = AJ_l\left(\frac{Ur}{a}\right)\begin{bmatrix}\cos(l\phi)\\ \sin(l\phi)\end{bmatrix}, \quad r \le a \tag{2.45}$$

$$\psi(r,\phi) = CK_l\left(\frac{Wr}{a}\right)\begin{bmatrix}\cos(l\phi)\\ \sin(l\phi)\end{bmatrix}, \quad r \ge a \tag{2.46}$$

where U and W are the parameters defined in Equations (2.24) and (2.25), respectively. The field solution in the core region where r is smaller than the core radius can be represented by $J_l(\cdot)$ and the field in the cladding region where r is larger than the core radius can be represented by $K_l(\cdot)$.

Through the imposition of boundary conditions, namely that ψ and its derivative $\frac{\partial\psi}{\partial r}$ are continuous at the boundary r=a, the characteristic(eigenvalue) equation can be derived as

$$\frac{UJ_{l-1}(U)}{J_l(U)} = -\frac{WK_{l-1}(W)}{K_l(W)} \tag{2.47}$$

In the scalar wave analysis, the modes are classified as LP_{lm}(*l*=0, 1, 2..., m=1, 2, 3…). For example, when *l*=0 and m=1, *l*=0 and m=2, and *l*=1 and m=1, the modes are LP_{01}, LP_{02}, and LP_{11}, respectively.

2.5.1.2. Vector Wave Analysis

The scalar wave analysis of fiber modes is valid only when index difference between core and cladding is much smaller than 1. For the HNL glass-core fibers which have extremely high core refractive indices, vector wave analysis should be considered. Therefore, the properties of the highly nonlinear fiber devices examined in this dissertation are evaluated by vector wave analysis in order to obtain more accurate results. Solutions of the vector wave equations for fiber modes are discussed in Appendix in more detail.

2.5.2. Modal Properties of Step-Index Fibers

The fiber modes described in this section are obtained from the scalar wave analysis for weakly guiding standard step-index fibers. Figures 2-36, 2-37, and 2-38 show the electric field and intensity patterns of the LP_{01}, LP_{02}, and LP_{11} modes, respectively.

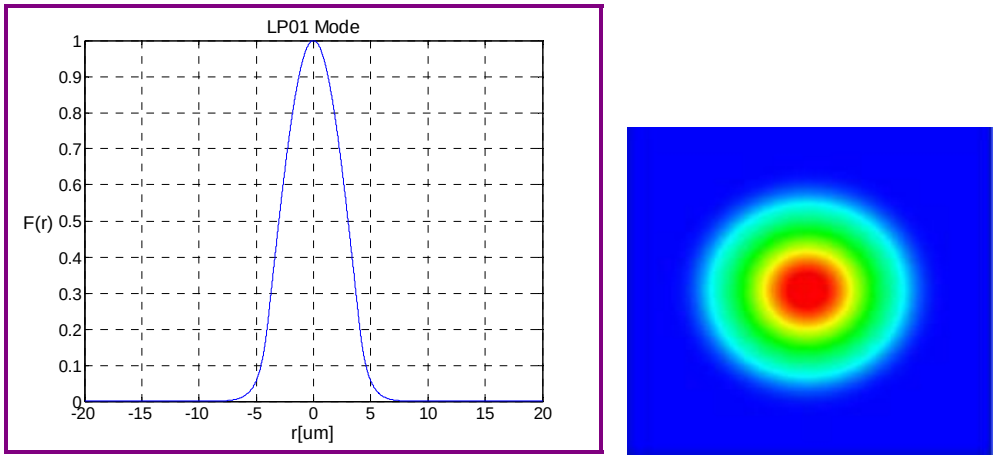

Figure 2-36. Electric Field and Intensity Patterns of the LP_{01} Mode

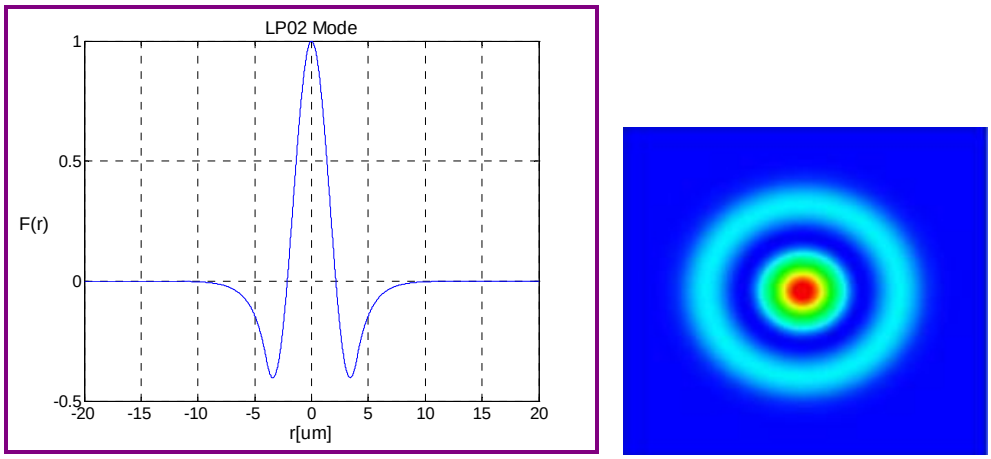

Figure 2-37. Electric Field and Intensity Patterns of the LP_{02} Mode

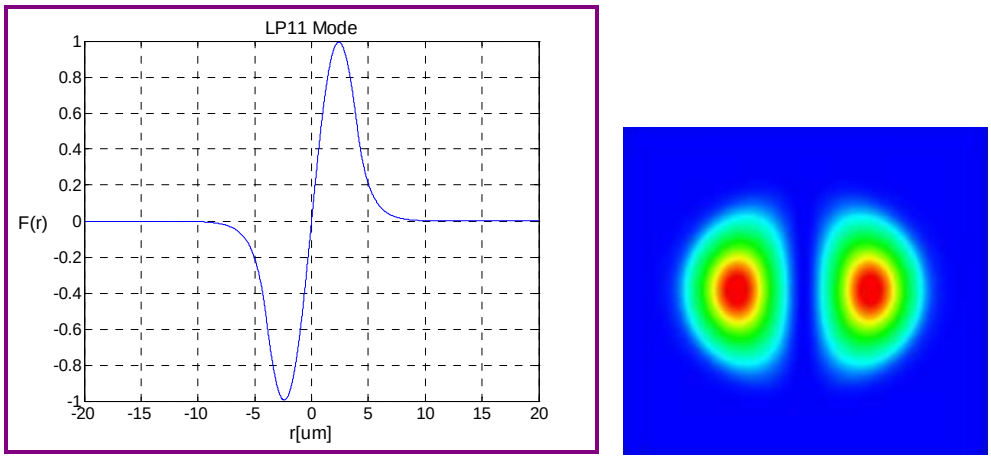

Figure 2-38. Electric Field and Intensity Patterns of the LP_{11} Mode

Figure 2-39 presents variation of the effective refractive index as a function of normalized frequency for fiber modes. If $V < 2.4048$, a fiber supports only the fundamental LP_{01} mode and the value $V_c=2.4048$ is referred to as the single-mode cutoff frequency. Note that at higher V, most of the power propagates in the core and the effective refractive index approaches the core refractive index while at lower V, most of the power is in the cladding and the effective refractive index approaches the cladding refractive index.

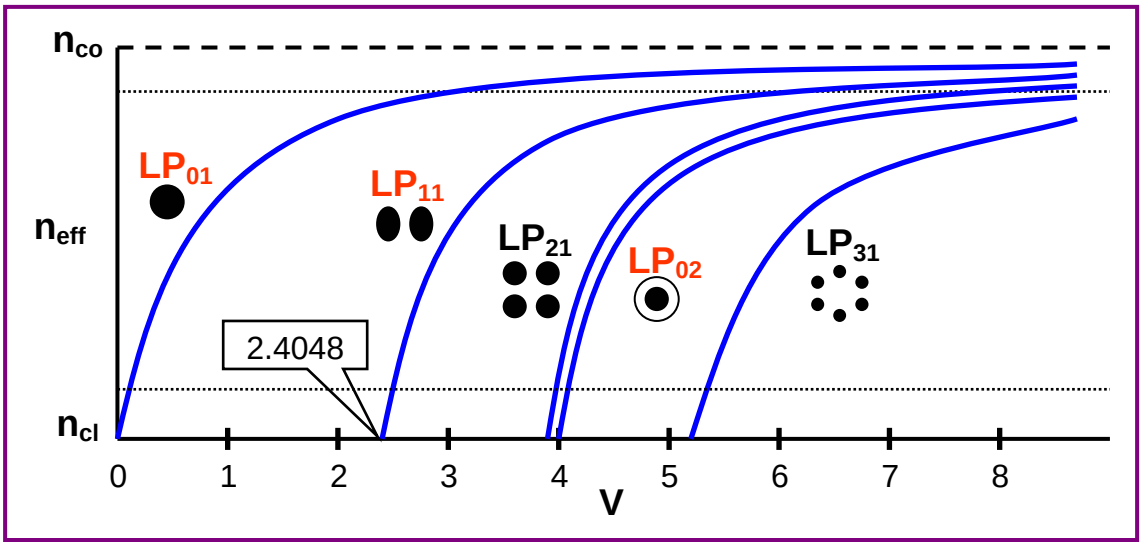

Figure 2-39. Effective Refractive Index vs. Normalized Frequency

In addition, the number of modes in step-index fibers is determined by the normalized frequency given by

$$V = \frac{2\pi a}{\lambda}\sqrt{n_{core}{}^2 - n_{cladding}{}^2} \tag{2.48}$$

As can be seen in Figure 2-36, the electric field pattern of the LP_{01} mode in fact closely fits a Gaussian function and the Mode Field Radius(MFR) defined as the radial distance from the center to the 1/e point is given by the following empirical formula[242].

$$\frac{w}{a} \approx 0.65 + \frac{1.619}{V^{3/2}} + \frac{2.879}{V^6} \tag{2.49}$$

As expected, as V increases, the MFR decreases, thus reflecting the tighter mode confinement for higher V. In addition, the MFR is always larger than the core radius under single-mode operation(V<2.4048).

2.5.3. LP_{01}-LP_{02} Mode Interference

2.5.3.1. Concepts

As shown in Figure 2-39, fiber modes have different effective refractive indices. It means that they have different propagation constants. Due to this phase-velocity mismatch of fiber modes, there will be a phase difference between two different modes when they propagate along the fiber. Figures 2-40 and 2-41 show the intensity distributions due to interference when the LP_{01} and LP_{02} modes with equal peaks are in phase and when they are out of phase by π, respectively. When the two modes are in phase, they interfere constructively, so resultant intensity pattern will be maximized. This intensity pattern is called SPOT. On the other hand, when they are out of phase by π, they interfere destructively, so resultant intensity pattern will be minimized. This intensity pattern is called RING, which means there is no power at the center.

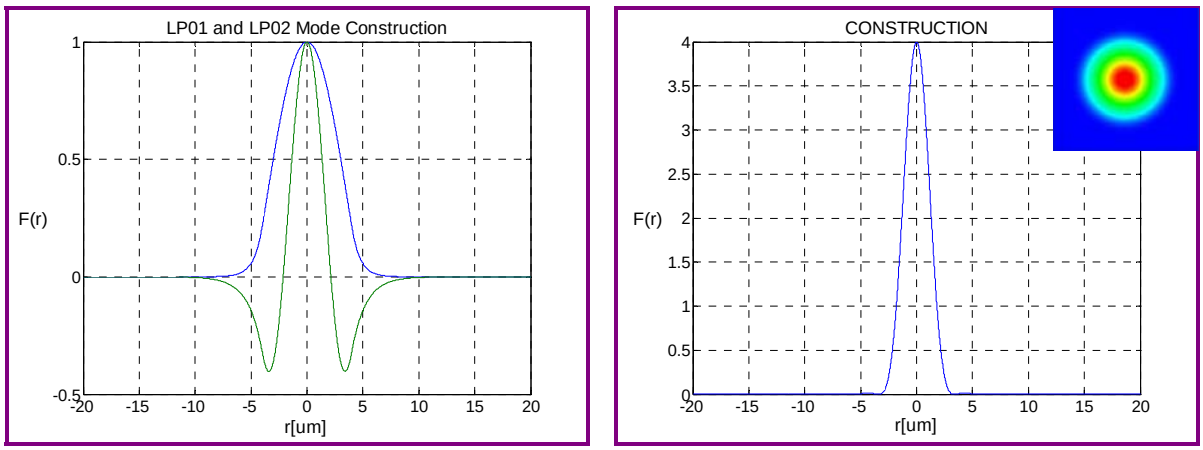

Figure 2-40. LP_{01}-LP_{02} Mode Interference Patterns(In Phase)

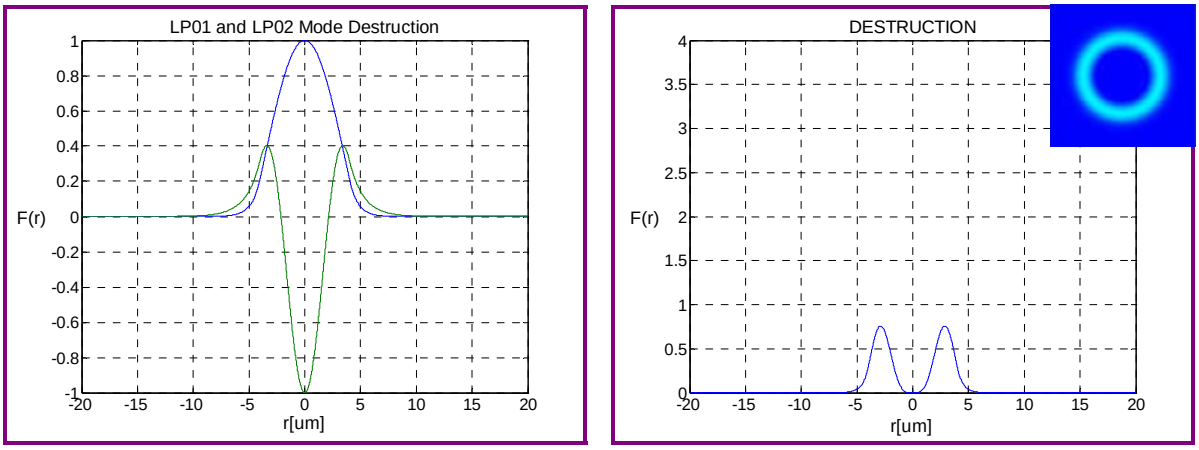

Figure 2-41. LP_{01}-LP_{02} Mode Interference Patterns(Out of Phase by π)

Figure 2-42 shows the experimental setup used to examine the effect of mode interference between the LP_{01} and LP_{02} modes[246-249]. The fiber used supports four modes at the wavelength of operation, namely, LP_{01}, LP_{11}, LP_{21}, and LP_{02} modes. Among them, only the LP_{01} and LP_{02} modes are circularly symmetric and thus can be selectively coupled into the fiber. After launching the LP_{01} and LP_{02} modes equally, the fiber glued on a movable plate is strained. As the length of the fiber varies due to strain, a phase difference between the two modes develops. As a result, far-field mode constructive and destructive intensity patterns occur periodically.

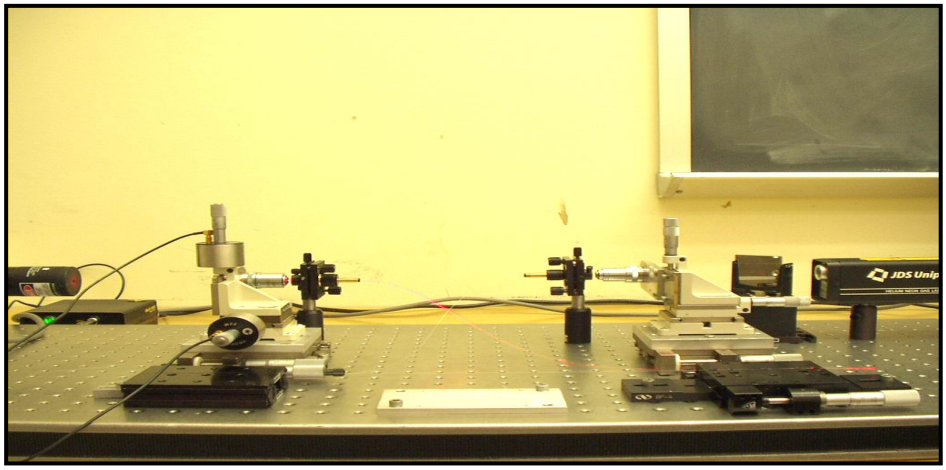

Figure 2-42. Experimental Setup for Demonstration of LP_{01}-LP_{02} Mode Interference

This intensity variation can be measured by placing a pinhole in front of the detector which is positioned at the center of the far-field pattern. Table 2-1 presents the measured power of the far-field pattern. As can be seen, maximum powers are detected when the two modes are in phase(Spot), while almost no powers are detected when they are out of phase by π(Ring). It is noted that a better agreement is achieved for the shorter fiber with the same sensing length. The interference properties of the LP_{01} and LP_{02} modes can be used for sensing of strain, temperature, and pressure[247-249].

Table 2-1. Power Variation at the Center of the Pattern due to LP_{01}-LP_{02} Mode Interference

Fiber Length	Sensing Length	Far-field Pattern	Power
10m	45cm	Spot	17μW
		Ring	3μW
2m	45cm	Spot	19μW
		Ring	1μW

2.5.3.2. Nonlinear Filters

In optical communication systems, signals always suffer intrinsic and extrinsic noise, thus causing bit-detection errors. As a way of removing the low-power background noise of signals, a nonlinear fiber device named nonlinear filter was proposed[250]. Figure 2-43 shows the basic concept of the nonlinear filter based on LP_{01}-LP_{02} mode interference. The basic idea is to use the intensity-dependent nonlinear phase shift induced by self-interaction between the LP_{01} and LP_{02} modes. According to the variation of the input power, there will be intensity dependence on the beat period because of the nonlinear refractive index. This device adjusts the input power to make the output power SPOT or RING by exploiting the interference of the LP_{01} and LP_{02} modes. To make a filter, it is necessary to determine the required power for making the output RING at a low power or SPOT at a higher power for a chosen fiber length.

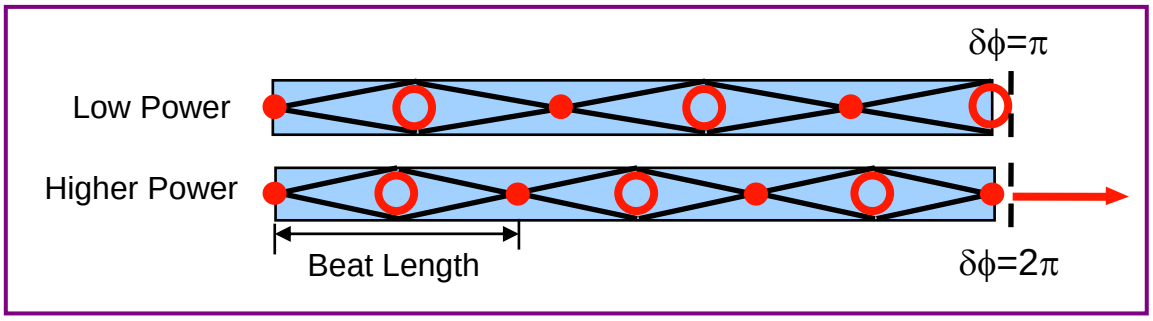

Figure 2-43. Basic Concept of Nonlinear Filter based on LP_{01}-LP_{02} Mode Interference[250]

The intensity-dependent nonlinear phase shifts of the LP_{01} and LP_{02} modes in the signal induced by self-interaction between them can be defined as

$$\delta\phi(01) = \frac{2\pi L_{eff}}{\lambda_s}\left[\delta n(01) + \delta n(02)\right]$$
$$\delta n(01) = \delta n_{01} = \frac{N_2 P_{01}}{A_{eff\_01}},\ \delta n(02) = \frac{2N_2 P_{01}}{A_{eff\_01\_02}} \tag{2.50}$$

$$\delta\phi(02) = \frac{2\pi L_{eff}}{\lambda_s}\left[\delta n(02) + \delta n(01)\right]$$
$$\delta n(02) = \delta n_{02} = \frac{N_2 P_{02}}{A_{eff\_02}},\ \delta n(01) = \frac{2N_2 P_{02}}{A_{eff\_01\_02}} \tag{2.51}$$

where

$$A_{eff\_01\_02} = 2\pi \cdot \frac{\left[\int \psi_{01}{}^2 r dr\right]\left[\int \psi_{02}{}^2 r dr\right]}{\int \psi_{01}{}^2 \cdot \psi_{02}{}^2 r dr} \tag{2.52}$$

As a result, the total nonlinear phase shift induced by self-interaction between the LP_{01} and LP_{02} modes, can be expressed as

$$\delta\phi(01)-\delta\phi(02)=\left|\frac{2\pi L_{eff}}{\lambda_s}\left[\frac{N_2P_{01}}{A_{eff\_01}}+\frac{2N_2P_{01}}{A_{eff\_01\_02}}-\frac{N_2P_{02}}{A_{eff\_02}}-\frac{2N_2P_{02}}{A_{eff\_01\_02}}\right]\right| \quad (2.53)$$

Assuming that the LP_{01} and LP_{02} modes have the same power in the device, that is, $P_{01}=P_{02}$, the required optical power for a phase shift of π can be obtained from

$$P_{01}=P_{02}=\frac{\lambda_s}{2N_2L_{eff}\left|\frac{1}{A_{eff\_01}}-\frac{1}{A_{eff\_02}}\right|} \quad (2.54)$$

Therefore, the output will be RING when each mode is launched into the device with this power. If the power is doubled, then the output will be SPOT.

In nonlinear fiber devices based on mode interference, there are two categories according to the way of operation. When the signal power is itself strong and no pump is present, the induced nonlinear phase shift depends on self-interaction between the modes carrying the signal. This kind of device is referred to as SPM-induced device. The nonlinear filter based on LP_{01}-LP_{02} mode interference, discussed before, and an amplitude modulator based on LP_{01}-LP_{11} mode interference belong to this category. However, when the signal power is much weaker than the pump power and the field distribution of the waveguide mode is independent of its intensity, the differential phase shift between the modes of the signal is induced by the pump power. This kind of device is referred to as XPM-induced device. The nonlinear optical switch[56, 246, 251] based on LP_{01}-LP_{11} mode interference, which will be discussed later, belongs to this category.

Even though XPM-induced nonlinear fiber devices based on LP_{01}-LP_{02} mode interference have never been experimentally demonstrated, it is useful to investigate their operations by numerical simulation. Under the assumption that the strong pump operates at a single-mode

wavelength, the total nonlinear phase shift, induced by the strong pump in the XPM-induced nonlinear fiber devices based on LP_{01}-LP_{02} mode interference, can be defined as

$$\delta\phi(01) - \delta\phi(02) = \left| \frac{2\pi L_{eff}}{\lambda_s} \left[\frac{2N_2 P_p}{A_{eff\_01S\_01P}} - \frac{2N_2 P_p}{A_{eff\_02S\_01P}} \right] \right| \tag{2.55}$$

where

$$A_{eff\_01S\_01P} = 2\pi \cdot \frac{\left[\int {\psi_{01S}}^2 r dr\right]\left[\int {\psi_{01P}}^2 r dr\right]}{\int {\psi_{01S}}^2 \cdot {\psi_{01P}}^2 r dr} \tag{2.56}$$

$$A_{eff\_02S\_01P} = 2\pi \cdot \frac{\left[\int {\psi_{02S}}^2 r dr\right]\left[\int {\psi_{01P}}^2 r dr\right]}{\int {\psi_{02S}}^2 \cdot {\psi_{01P}}^2 r dr} \tag{2.57}$$

In Equations (2.55)-(2.57), 01S and 02S refer to the LP_{01} mode and the LP_{02} mode of the signal, respectively, and 01P refers to the LP_{01} mode of the pump. As a result, the required optical pump power for a phase shift of π can be obtained from

$$P_p = \frac{\lambda_s}{4N_2 L_{eff} \left| \frac{1}{A_{eff\_01S\_01P}} - \frac{1}{A_{eff\_02S\_01P}} \right|} \tag{2.58}$$

2.5.4. LP_{01}-LP_{11} Mode Interference

2.5.4.1. Concepts

In a similar manner, the LP_{01} and LP_{11} modes can interfere each other due to the phase-velocity difference between the two modes. However, LP_{01}-LP_{11} mode interference[56, 60, 228, 246, 251-255] has quite different characteristics because of the asymmetric field pattern of the LP_{11} mode. Figures 2-44 and 2-45 show the intensity distributions due to interference when the LP_{01} and LP_{11} modes are in phase and when they are out of phase by π, respectively. Since the LP_{01} mode is symmetric about the fiber axis and the LP_{11} mode is asymmetric, interference is constructive on one side of the axis and destructive on the other, thus resulting in an asymmetric intensity distribution.

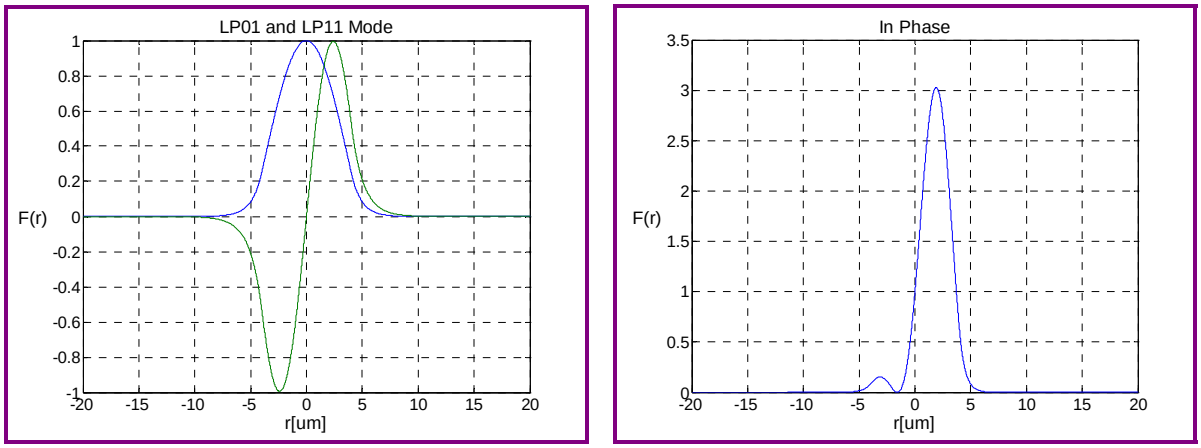

Figure 2-44. LP_{01}-LP_{11} Mode Interference Patterns(In Phase)

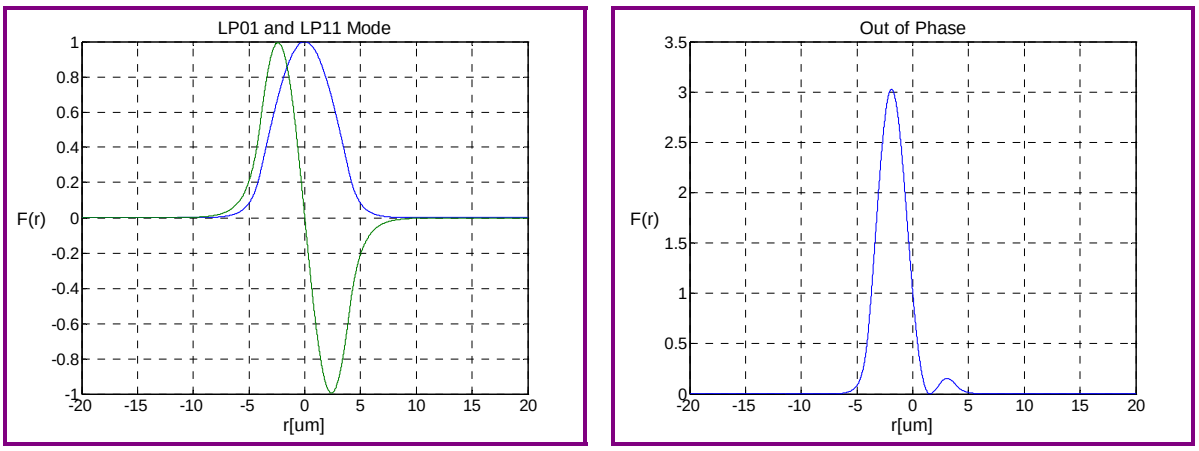

Figure 2-45. LP_{01}-LP_{11} Mode Interference Patterns(Out of Phase by π)

Figure 2-46 illustrates intensity patterns for several values of the phase difference Δϕ between the LP_{01} and LP_{11} modes[228]. Note that the intensity distribution has a minor lobe due to the asymmetry of the LP_{11} mode and there is always a finite intensity on the fiber axis. As the phase difference increases, the power moves to the other side more and more and when Δϕ=π/2, the power is distributed equally on both sides.

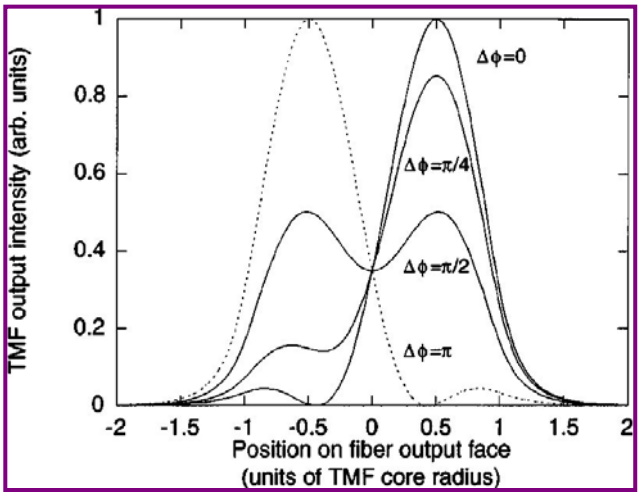

Figure 2-46. Intensity Patterns for Different Phase Differences between LP_{01} and LP_{11} Modes

2.5.4.2. Amplitude Modulators

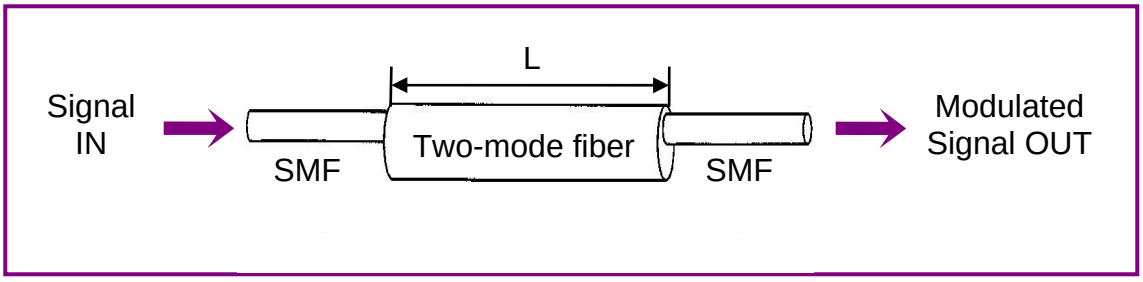

Figure 2-47. An Amplitude Modulator based on LP_{01}-LP_{11} Mode Interference

Figure 2-47 describes an amplitude modulator based on LP_{01}-LP_{11} mode interference. The input Single-Mode Fiber(SMF) is aligned slightly off the Two-Mode Fiber(TMF) axis so that its power is coupled equally into the LP_{01} and LP_{11} modes of the TMF. Similarly, the output SMF is aligned off axis so that it picks up the power from only one of the two lobes of the LP_{01}-LP_{11} mode interference pattern. The maximum intensity position of the interference pattern in the TMF will vary according to the nonlinear phase shift which is affected by the input powers of the LP_{01} and LP_{11} modes. If the input powers of the two modes are chosen such that the nonlinear phase shift, induced by self-interaction between the two modes, becomes 0 or π, the intensity from the output SMF can be modulated.

The intensity-dependent nonlinear phase shifts of the LP_{01} and LP_{11} modes in the signal induced by self-interaction between them can be defined as

$$\delta\phi(01) = \frac{2\pi L_{eff}}{\lambda_s}\left[\delta n(01) + \delta n(11)\right]$$
$$\delta n(01) = \delta n_{01} = \frac{N_2 P_{01}}{A_{eff\_01}},\ \delta n(11) = \frac{2N_2 P_{01}}{A_{eff\_01\_11}} \tag{2.59}$$

$$\delta\phi(11) = \frac{2\pi L_{eff}}{\lambda_s}\left[\delta n(11) + \delta n(01)\right]$$
$$\delta n(11) = \delta n_{11} = \frac{N_2 P_{11}}{A_{eff\_11}},\ \delta n(01) = \frac{2N_2 P_{11}}{A_{eff\_01\_11}} \tag{2.60}$$

where

$$A_{eff\_01\_11} = 2\pi \cdot \frac{\left[\int {\psi_{01}}^2 r dr\right]\left[\int {\psi_{11}}^2 r dr\right]}{\int {\psi_{01}}^2 \cdot {\psi_{11}}^2 r dr} \tag{2.61}$$

As a result, the total nonlinear phase shift induced by self-interaction between the LP_{01} and LP_{11} modes, can be expressed as

$$\delta\phi(01) - \delta\phi(11) = \left| \frac{2\pi L_{eff}}{\lambda_s}\left[\frac{N_2 P_{01}}{A_{eff\_01}} + \frac{2N_2 P_{01}}{A_{eff\_01\_11}} - \frac{N_2 P_{11}}{A_{eff\_11}} - \frac{2N_2 P_{11}}{A_{eff\_01\_11}} \right] \right| \tag{2.62}$$

Assuming that the LP_{01} and LP_{11} modes have the same power in the device, that is, $P_{01}=P_{11}$, the required optical power for a phase shift of π can be obtained from

$$P_{01} = P_{11} = \frac{\lambda_s}{2N_2 L_{eff}\left| \frac{1}{A_{eff\_01}} - \frac{1}{A_{eff\_11}} \right|} \tag{2.63}$$

Therefore, supposing that the maximum power is first in the upper position, it will be shifted to the lower position when each mode is launched into the device with this power. If the power is doubled, the maximum power will be back to the upper position.

2.5.4.3. Nonlinear Optical Switches

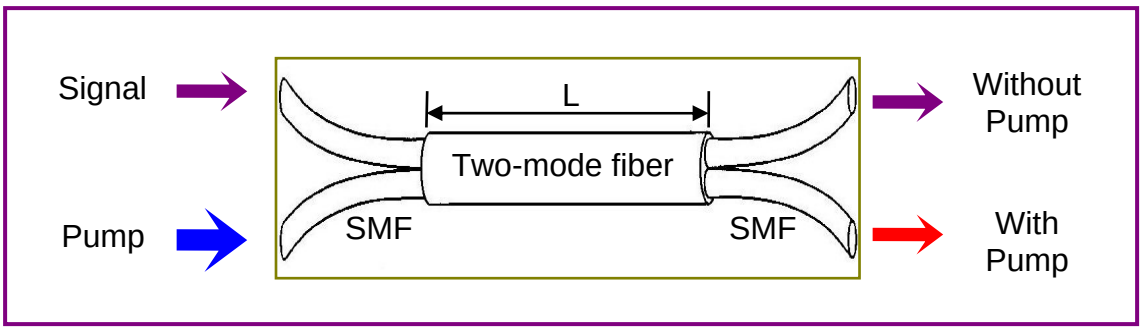

Figure 2-48. A Nonlinear Optical Switch based on LP_{01}-LP_{11} Mode Interference

Figure 2-48 presents the schematics of a 2×2 nonlinear optical switch based on LP_{01}-LP_{11} mode interference. The TMF is butt coupled at both ends to two side-by-side SMFs. The input SMFs are positioned such that one of the SMFs carries in the signal and excites equal amounts of the LP_{01} and LP_{11} modes of the TMF, while the other carries the pump. At the output end of the TMF, the output SMFs are positioned such that each fiber picks up the signal power contained in one of the two lobes. When weak signal powers of the LP_{01} and LP_{11} modes are launched, mode interference patterns between them are now affected by the strong pump power. As a result, the signal can be switched by adjusting the strong pump. The pump should have the same polarization as the signal and it may propagate in either or both of the two modes.

Under the assumption that the strong pump operates at a single-mode wavelength, the total nonlinear phase shift, induced by the strong pump in the XPM-induced nonlinear fiber devices based on LP_{01}-LP_{11} mode interference, can be defined as

$$\delta\phi(01) - \delta\phi(11) = \left| \frac{2\pi L_{eff}}{\lambda_s} \left[\frac{2N_2 P_p}{A_{eff\_01S\_01P}} - \frac{2N_2 P_p}{A_{eff\_11S\_01P}} \right] \right| \tag{2.64}$$

where $A_{eff\_01S\_01P}$ is the effective mode area given in Equation (2.56) and

$$A_{eff\_11S\_01P} = 2\pi \cdot \frac{\left[\int {\psi_{11S}}^2 rdr\right]\left[\int {\psi_{01P}}^2 rdr\right]}{\int {\psi_{11S}}^2 \cdot {\psi_{01P}}^2 rdr} \tag{2.65}$$

In Equations (2.64) and (2.65), 01S and 11S refer to the LP_{01} mode and the LP_{11} mode of the signal, respectively, and 01P refers to the LP_{01} mode of the pump. As a result, the required optical pump power for a phase shift of π can be obtained from

$$P_p = \frac{\lambda_s}{4N_2 L_{eff}\left|\frac{1}{A_{eff\_01S\_01P}} - \frac{1}{A_{eff\_11S\_01P}}\right|} \tag{2.66}$$

2.5.4.4. Optical Time-Division Demultiplexers

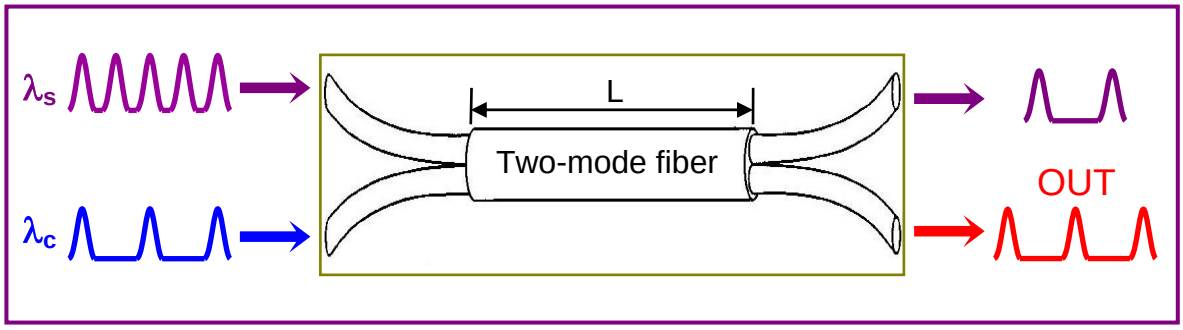

Figure 2-49. An Optical Time-Division Demultiplexer based on LP_{01}-LP_{11} Mode Interference

Figure 2-49 shows the schematic diagram of an optical time-division demultiplexer based on the LP_{01}-LP_{11} mode interference. When no control pulses are incident, all signal pulses go through the upper single-mode pick-up fiber. If a strong control pulse is introduced such that the nonlinear phase shift between the LP_{01} and LP_{11} modes of the signal pulse becomes π, the

maximum intensity of the specific signal pulse affected by the control pulse shifts to the other side and thus come out from lower single-mode pick-up fiber. As a result, the desired signal pulses are selectively demultiplexed using LP_{01}-LP_{11} mode interference. The control pulse should have the same polarization as the signal pulse and it may propagate in either or both of the two modes. In contrast to the previous time-independent applications, in this kind of time-dependent applications, group-velocity difference between the two modes will be the critical factor for proper operation.

CHAPTER 3.
ISSUES IN NONLINEAR FIBER DEVICES

This chapter focuses on critical issues in nonlinear fiber devices. The critical issues in nonlinear fiber devices include the relationship between device length, optical power, the nonlinear-index coefficient, effective mode area, and nonlinear phase shift, the pulse walk-off caused by group-velocity mismatch, the pulse broadening caused by GVD, and the polarization fluctuation caused by environmental disturbances.

3.1. Required Device Length and Required Optical Power

As shown in Equations (1.11) and (1.12), the operation of nonlinear fiber devices is directly related to the nonlinear phase shift. The nonlinear phase shift is dependent on the nonlinear-index coefficient, the optical power, the device length, and the effective mode area. For conventional silica-core silica-clad fibers in which nonlinear-index coefficients are small, the nonlinear fiber devices using them usually require substantially long fiber length to generate a sufficient amount of phase shift. For typical parameters of silica fibers, the required device length to acquire a nonlinear phase shift of π with an optical power of 1W is about 1Km as shown below.

$$\delta\phi_{SPM} = \pi,\ P_s = 1W,\ \lambda_s = 1.5\mu m$$
$$A_{eff} = 35\mu m^2,\ N_2 = 2.5\times 10^{-20}\, m^2/W$$
$$L_\pi^{SPM} = \frac{\lambda_s A_{eff}}{2N_2 P_s} = 1[Km]$$

This long device length causes some serious problems which are the major limiting factors for response time and switching bandwidth. The problems include the pulse walk-off between control and signal pulses caused by group-velocity mismatch, the control pulse broadening caused by GVD, and the polarization sensitivity caused by external environmental disturbances such as temperature drift and stresses. Therefore, fibers with high nonlinearities are essential in nonlinear fiber devices to shorten the device length required for acquiring sufficient nonlinear phase shifts. In addition, the effective mode area should be smaller for a given optical power to shorten the device length. High Non-Linearity(HNL) glasses can satisfy these requirements since they have both high nonlinear-index coefficients and high linear refractive indices. A high linear refractive index of the core allows smaller core radius, while maintaining single-mode operation at the desired wavelength, and thus, the effective mode area decreases.

Additionally, the Two-Photon Absorption(TPA) discussed in Chapter 1 can be a factor which degrades the performance of all-optical nonlinear switching devices. Since the TPA is manifested by an intensity-dependent nonlinear absorption, it limits the transmittable power and thereby limits the obtainable nonlinear phase shift. This negatively affects the switching behavior. Therefore, the following criterion should be satisfied to avoid significant TPA-induced effects[256].

$$\frac{2\beta\lambda}{N_2} < 1 \tag{3.1}$$

where N_2 is the nonlinear-index coefficient and β is the TPA coefficient given in Equation (1.5).

3.2. Pulse Walk-Off and Pulse Broadening

3.2.1. Group-Velocity Dispersion

In a dielectric medium such as an optical fiber, the response of an electromagnetic wave depends on the optical frequency. This property of the frequency dependence of the effective refractive index is referred to as chromatic dispersion. Chromatic dispersion in optical fibers consists of two components, material dispersion and waveguide dispersion. The material dispersion originates from the characteristic resonance frequencies at which the dielectric medium absorbs the electromagnetic radiation through oscillation of bound electrons.

The refractive index as a function of wavelength is well approximated by the Sellmeier equation defined as[197]

$$n^2 = 1 + \sum_{j=1}^{m} \frac{A_j \omega_j{}^2}{\omega_j{}^2 - \omega^2} = 1 + \sum_{j=1}^{m} \frac{A_j \lambda^2}{\lambda^2 - \lambda_j{}^2}, \ \lambda_j = \frac{2\pi c}{\omega_j} \tag{3.2}$$

where ω_j is the *j*th resonance frequency and A_j is the strength of *j*th resonance. The parameters of A_j and ω_j depend on composition of dielectric materials and m=3 for the case of optical fibers. In addition, the group refractive index is given by

$$n_g = \frac{d\left[\omega n(\omega)\right]}{d\omega} = n(\omega) + \omega \frac{dn(\omega)}{d\omega} = n(\lambda) - \lambda \frac{dn(\lambda)}{d\lambda} \tag{3.3}$$

Different spectral components of pulses in optical fibers travel at different group velocities given by

$$v_g = \frac{c}{n_g(\lambda)} \tag{3.4}$$

due to the wavelength dependence of the refractive index. This wavelength dependence of the group velocity leads to pulse broadening because different spectral components of pulses in optical fibers spread as they propagate along the fiber and arrive at the fiber end at different times. This phenomenon is referred to as the Group-Velocity Dispersion(GVD).

To assess the effects of GVD on pulse spreading, the propagation constant β is expanded in a Taylor series about the center frequency ω_0 of the pulse spectrum.

$$\beta(\omega) = n(\omega)\frac{\omega}{c} = \beta_0 + \beta_1(\omega-\omega_0) + \frac{1}{2}\beta_2(\omega-\omega_0)^2 + \frac{1}{6}\beta_3(\omega-\omega_0)^3 + \cdots \tag{3.5}$$

where

$$\beta_m = \left(\frac{d^m\beta}{d\omega^m}\right)_{\omega=\omega_0} \quad (m = 0, 1, 2, 3, \ldots) \tag{3.6}$$

The parameter β_1 given by

$$\beta_1 = \frac{d\beta}{d\omega} = \frac{1}{v_g} = \frac{n_g}{c} = \frac{1}{c}\left(n + \omega\frac{dn}{d\omega}\right) \tag{3.7}$$

represents the group velocity of the pulse, while the parameter β_2 given by

$$\beta_2 = \frac{d\beta_1}{d\omega} = \frac{d^2\beta}{d\omega^2} = \frac{1}{c}\left(2\frac{dn}{d\omega} + \omega\frac{d^2n}{d\omega^2}\right) \tag{3.8}$$

represents the GVD which is responsible for pulse broadening. The parameter β_3 given by

$$\beta_3 = \frac{d\beta_2}{d\omega} = \frac{d^3\beta}{d\omega^3} = \frac{1}{c}\left(3\frac{d^2n}{d\omega^2} + \omega\frac{d^3n}{d\omega^3}\right) \tag{3.9}$$

represents the Dispersion Slope(DS) or Third-Order Dispersion(TOD) which is responsible for asymmetry.

The most notable feature is that the dispersion parameter β_2 for bulk-fused silica becomes zero at the wavelength of about 1.27μm. This particular wavelength λ_D is referred to as the Zero-Dispersion Wavelength(ZDW). In addition, the dispersion slope parameter β_3, also referred to as the TOD parameter, is required to be included when wavelength approaches the ZDW to within a few nanometers for accurate evaluation of ultrashort pulse propagation.

The ZDW of actual silica glass fibers deviates from that of bulk-fused silica. The reasons are as follows. First, the fiber core may be slightly doped with dopants such as GeO_2. Second, due to the structure of dielectric waveguide, the effective refractive index is slightly lower than the material refractive index of the core. More specifically, the change in mode confinement with optical frequency adds an additional refractive index variation which shifts the ZDW from the silica value to longer wavelengths. This waveguide contribution should be added to the material contribution to achieve the total GVD. Therefore, the total GVD is defined as the sum of the material dispersion and the waveguide dispersion as[197]

$$D_{MAT} = \frac{d\beta_1}{d\lambda} = -\frac{2\pi c}{\lambda^2}\beta_2 = \frac{1}{c}\frac{dn_g}{d\lambda} = -\frac{\lambda}{c}\frac{d^2n}{d\lambda^2} \tag{3.10}$$

$$D_{WG} = \frac{1}{c}\frac{dn_{g\_WG}}{d\lambda} = -\frac{\Delta n}{c}\frac{V}{\lambda}\frac{d^2[bV]}{dV^2} \tag{3.11}$$

$$D_{TOTAL} = D_{MAT} + D_{WG} = -\frac{\lambda}{c}\frac{d^2 n}{d\lambda^2} - \frac{\Delta n}{c}\frac{V}{\lambda}\frac{d^2[bV]}{dV^2} \tag{3.12}$$

where Δn is the core-cladding index difference, V is the normalized frequency given in Equation (2.48) and b is the normalized propagation constant defined by the effective refractive index n_{eff} as[242]

$$b = \frac{n_{eff}^{\ 2} - n_{cladding}^{\ 2}}{n_{core}^{\ 2} - n_{cladding}^{\ 2}} \tag{3.13}$$

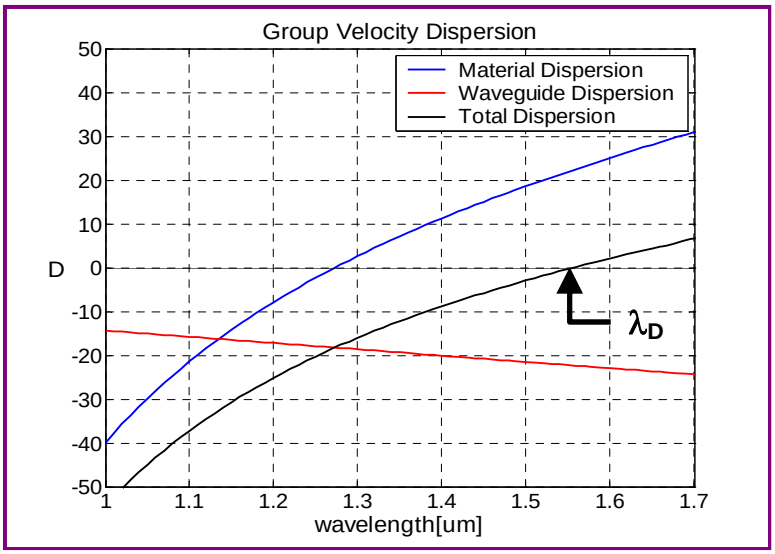

Figure 3-1. Waveguide Contribution for Dispersion-Shifted Fibers

Figure 3-1 shows the waveguide contribution for Dispersion-Shifted Fibers(DSF). The primary effect of the waveguide contribution is to shift ZDW toward longer wavelengths. This waveguide contribution can be controlled by adjusting fiber-design parameters such as

core radius and core-cladding index difference. $\lambda_D \approx 1.55\mu m$ for DSFs and $\lambda_D \approx 1.31\mu m$ for standard step-index fibers.

Actually, Equation (3.12) is valid only when the core-cladding index difference Δn is wavelength independent(a constant). Most generally, the effective refractive index is used with the varying core and/or cladding refractive indices to get the total GVD as

$$D_{TOTAL} = \frac{1}{c}\frac{dn_{geff}}{d\lambda} = -\frac{\lambda}{c}\frac{d^2 n_{eff}}{d\lambda^2} \tag{3.14}$$

where n_{geff} is the group effective refractive index. This total GVD represents pulse broadening in time[ps] by a fiber length of L[Km] for a pulse with a spectral width of $\delta\lambda$[nm] as follows.

$$\Delta t[ps] = L[Km] \cdot \delta\lambda[nm] \cdot D\left[\frac{ps}{nm \cdot Km}\right] \tag{3.15}$$

The effect of GVD on the bit-rate B can be estimated by

$$B \cdot \Delta t = B \cdot L \cdot \delta\lambda \cdot |D| < 1 \tag{3.16}$$

Therefore, the BL product of single-mode fibers can be increased by operating at the ZDW and using a pulse with narrow spectral width. However, the dispersive effects do not disappear completely even at the ZDW. Optical pulses still experience broadening due to the higher-order dispersive effects and these higher-order dispersion effects are governed by the DS D_λ which can be defined by the dispersion parameter β_2[ps^2/Km] and the TOD parameter β_3[ps^3/Km] as[197]

$$D_\lambda \left[\frac{ps}{nm^2 \cdot Km} \right] = \frac{dD}{d\lambda} = \left(\frac{2\pi c}{\lambda^2} \right)^2 \beta_3 + \left(\frac{4\pi c}{\lambda^3} \right) \beta_2 \tag{3.17}$$

In particular, $\beta_2 = 0$ at the ZDW, so D_λ is now only affected by β_3 as

$$D_\lambda = \frac{4\pi^2 c^2}{\lambda^4} \beta_3 \tag{3.18}$$

More specifically, although β_2 dominates in most cases of practical interest, β_3 can provide the dominant contribution when pulses operates near the ZDW where $\beta_2 \approx 0$. It is also necessary to consider β_3 even when $\beta_2 \neq 0$ for ultrashort pulses. As a result, the limiting BL product can also be estimated by

$$B \cdot L \cdot (\delta\lambda)^2 \cdot |D_\lambda| < 1 \tag{3.19}$$

Additionally, the GVD $D(\lambda)$ is related to the DS D_λ by the relation

$$D(\lambda) = \frac{D_\lambda}{4} \left(\lambda - \frac{\lambda_D{}^4}{\lambda^3} \right) \tag{3.20}$$

Figure 3-2 shows the properties of pulse broadening by GVD. For the wavelengths smaller than the ZDW, the low-frequency components(red-shifted) of pulses travel faster than the high-frequency components(blue-shifted) of the same pulses. As a result, pulses spread with the red side of the spectrum leading. This region is often called ‘Normal’ or ‘Negative’ dispersion regime. On the other hand, for the wavelengths longer than the ZDW, the opposite occurs. This region is often called ‘Anomalous’ or ‘Positive’ dispersion regime. This

anomalous-dispersion regime is of considerable interest because in this regime, optical fibers support solitons through interplay between GVD and SPM.

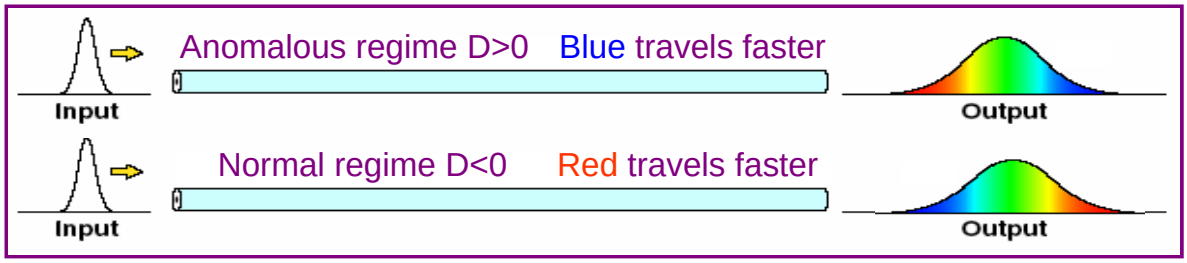

Figure 3-2. Illustration of Pulse Broadening by Group-Velocity Dispersion

The pulse broadening by GVD is also affected by the position of the pump and signal wavelengths[257]. When the pump is in the normal regime and the signal is in the anomalous regime, the signal pulse is less broadened than it would be if the pump and signal pulses were in the opposite regimes. The reason is that when the pump is in the anomalous regime, its peak is increased and compressed and this high peak-compressed pump affects the signal pulse to create chirp. As a result, the signal is broken and broadened more.

3.2.2. Pulse Walk-Off

As discussed in the previous section, the important feature of GVD is that pulses at different wavelengths propagate at different speed due to the group-velocity differences. It causes pulse walk-off that plays a central role in nonlinear fiber switching devices involving two or more closely spaced pulses. In nonlinear fiber switching devices, they, in general, use different wavelengths for control and signal pulses to separate them easily after switching. Therefore, the effect of pulse walk-off between control and signal pulses seriously affects the switching performance. The interaction between the two pulses terminates when the fast moving pulse completely walks through the slower moving pulse. More specifically, when walk-off exceeds one time slot of OTDM signal pulses, the control pulse interacts with many

other different signal pulses, making it hard to select only one channel of the signals. Finally, it limits the bit-rate of the signal and switching bandwidth. This feature is governed by the walk-off parameter d_w given by

$$d_w = \left|\beta_1(\lambda_1) - \beta_1(\lambda_2)\right| = \left|\frac{1}{v_g(\lambda_1)} - \frac{1}{v_g(\lambda_2)}\right| \tag{3.21}$$

The walk-off length for the initial pulse width of τ can be defined as

$$L_w = \frac{\tau}{d_w} \tag{3.22}$$

As the walk-off parameter increases and the initial pulse width decreases, the walk-off length decreases, thus making it hard to achieve high bit-rate and broad switching bandwidth.

3.2.3. Pulse Broadening

Another issue in nonlinear fiber devices is the temporal broadening of the control pulse caused by GVD. Even though the control and signal pulses have the same group velocities, if the control pulse has high GVD, the temporal broadening of the control pulse reduces the switching time of the devices. A shorter control pulse width exhibits faster response time, but it is often limited due to GVD.

The dispersion length L_D is defined as given in Equation (2.17) and the critical pulse width τ_c is defined as[191]

$$\tau_c^{\,2} = 4\ln\left(2\left|\beta_2\right|L\right) \tag{3.23}$$

where β_2 is the dispersion parameter and L is the fiber length. Over a propagating length L, an optical pulse broadens by a factor of 2 when $L=L_D$. Therefore, to avoid the pulse broadening effect, the following condition should be satisfied.

$$\frac{L}{L_D} << 1 \tag{3.24}$$

and the output pulse width τ_o given by

$$\tau_o^{\,2} = \tau_i^{\,2}\left[1+\left(\frac{\tau_c}{\tau_i}\right)^2\right] \tag{3.25}$$

should be nearly equal to the input pulse width τ_i.

Usually, nonlinear fiber devices require long device lengths to induce a sufficient nonlinear phase shift at lower optical powers due to the low nonlinearities of silica fibers. Furthermore, since the minimum switching time is limited by the control pulse width, a short control pulse is required to achieve much faster switching. These requirements of long device length, which increases the walk-off parameter and GVD, and short control pulse in nonlinear fiber devices make the switching performance much worse because a short pulse is broadened even more for a given fiber length. Therefore, the device length should be short enough to minimize the walk-off parameter and pulse broadening due to GVD. This can be achieved by introducing HNL glasses since they can increase the nonlinear-index coefficient and decrease the effective mode area, thus resulting in extremely short devices.

3.3. Polarization

3.3.1. Polarization-Mode Dispersion

Single-mode fibers, in fact, support two modes that are linearly polarized in two orthogonal directions. Under the ideal conditions of perfect cylindrical symmetry and no asymmetric stresses, the two linearly polarized modes would not couple to each other and their propagation constants are the same. However, in practical fibers, due to the variation of core shape caused by stresses, bubbles, bends, twist, and so forth, fibers become slightly birefringent and the propagation constants of the two orthogonal modes become slightly different. This property of optical fibers is referred to as modal birefringence defined by

$$\delta n = \frac{\left|\beta_x - \beta_y\right|}{k_0} = \left|n_x - n_y\right| \tag{3.26}$$

where x and y represent the two orthogonal directions. This small difference between the propagation constants leads to the mixing of the two orthogonally polarized modes even under the smallest external perturbations. Therefore, for such fibers, the SOP of the linearly polarized input signal varies randomly as it propagates inside the fiber. Although this random variation of SOP is typically harmless for a continuous wave, it can be a problem when a short pulse is transmitted over long length in optical communication systems. As the short pulse propagates, its SOP changes randomly and finally it becomes broader at the output end because the group velocities of the two orthogonal modes are different. This phenomenon is referred to as the Polarization Mode Dispersion(PMD). The extent of the pulse broadening can be estimated from the time delay Δt between the two orthogonal modes as

$$\Delta t = L\left|\frac{1}{v_{gx}} - \frac{1}{v_{gy}}\right| = \frac{L}{c}\left|n_{gx} - n_{gy}\right| \tag{3.27}$$

Consequently, for Polarization-Maintaining Fibers(PMF)(δn=constant), PMD is defined as

$$PMD\left[\frac{ps}{Km}\right] = \frac{\left|n_{gx} - n_{gy}\right|}{c} = \frac{\delta n_g}{c} = \frac{1}{c}\left[\delta n - \lambda\frac{d(\delta n)}{d\lambda}\right] = \frac{\delta n}{c} \tag{3.28}$$

However, δn varies randomly for non-PMFs(δn≠constant), and PMD is defined as

$$PMD\left[\frac{ps}{\sqrt{Km}}\right] = \frac{\delta n_g}{c}\sqrt{L_{co}} \tag{3.29}$$

where L_{co} is the correlation length defined by the length over which the two polarization components remain correlated. Typically, for L > 0.1Km, L_{co} << L. Note that since the time delay Δt for non-PMFs depends on $\sqrt{L}$ as

$$\Delta t = \frac{\delta n_g}{c}\sqrt{L_{co}}\cdot\sqrt{L} \tag{3.30}$$

This PMD-induced pulse broadening is relatively small compared with the GVD-induced pulse broadening. However, PMD becomes a limiting factor for the system designed to operate over a long distance at high bit rates near the ZDW. PMFs can be used to overcome the randomly varying SOP. In PMFs, the input signal which is linearly polarized in either one of the two principal axes, maintains the SOP during propagation along the fiber. If the linearly polarized input signal makes an angle with the two principal axes, the SOP of the two modes

varies continuously as they propagate inside the fiber in a periodic manner with the period called the beat length given by

$$L_B = \frac{2\pi}{\left|\beta_x - \beta_y\right|} = \frac{\lambda}{\delta n} \tag{3.31}$$

3.3.2. Polarization Sensitivity

The fluctuation of SOP seriously degrades the performance of nonlinear fiber devices because SOP is very critical to the operation of almost all nonlinear fiber devices. Therefore, polarization controllers or PMFs are usually used in order to control the SOP of an optical pulse, since the SOP in standard fibers changes randomly as the pulse propagates along the fiber. However, it is not efficient to adjust the polarization controllers continuously whenever required, and moreover, huge built-in stress birefringence in conventional low-index cladding PMFs depends highly on temperature variation.

In particular, nonlinear fiber devices based on the optical Kerr effect always use PMFs to ensure that the control pulse which is linearly polarized in either one of the two principal axes maintains its SOP along the fiber, because the optical Kerr effect operates based on the variation of SOP. In such devices, since the direction of the linearly polarized signal pulse makes a 45° angle with the two principal axes, the signal pulse will suffer PMD by the built-in birefringence. Moreover, this intentional non-varying built-in birefringence in PMFs is much higher than the varying birefringence in standard fibers. As a result, the use of PMFs also brings serious problems which cause the limitation of the response time and bit-rate of signals. The problems include the signal pulse broadening caused by PMD and the pulse walk-off between the control and signal pulses caused by the birefringence-induced group-velocity mismatch. Additionally, for the nonlinear fiber devices based on mode interference,

SOPs of the two modes should be maintained and remain the same during operation for better performance, but it is hard to achieve due to the temperature dependence of the SOP.

Short lengths of devices are able to solve these problems of the signal pulse broadening caused by PMD and the pulse walk-off caused by the birefringence-induced group-velocity mismatch. Moreover, short devices are hardly affected by environmental disturbances. Therefore, the use of HNL glasses for short devices would be the best way to effectively reduce polarization sensitivity.

CHAPTER 4.
MICROSTRUCTURE FIBERS

In this dissertation, the three types of high-nonlinearity glass fibers, HNL glass-core silica-clad fibers, HNL glass-core air-clad(microstructure) fibers, and HNL glass-core HNL glass-clad fibers, are considered in studying the effect of HNL glasses. More specifically, when HNL glasses are used for the three types of fibers, the performance of highly nonlinear fiber devices operating based on different principles are evaluated. This chapter describes the structures, properties, and applications of the MicroStructure Fibers(MSF). This chapter also compares structures and some critical properties, which are related to nonlinear operations, of different types of optical fibers.

4.1. Structures

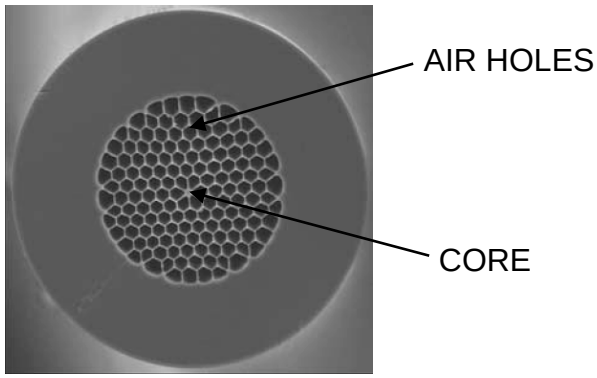

Figure 4-1. Structures of a Microstructure Fiber[258]

Figure 4-1 shows the structures of one kind of MSF[258]. The most distinct feature of MSFs[259] compared with conventional fibers is that the low-index cladding region is

replaced by holes which are usually air holes. That is, the cladding region consists of both glass and air, so the average refractive index of the cladding falls somewhere between glass and air.

Because MSFs can be made from a single material, it is possible to eliminate the problems caused by the core-cladding interface of two different glasses. The characteristics of MSFs are affected by the diameter of a hole and the pitch which is the length from center of a hole to center of an adjacent hole. Additionally, the combination of small hole-to-hole pitch and large air-filling fraction, defined by the ratio of hole area to total cladding area, results in tight mode confinement due to the high glass/air index contrast and thus, a small effective mode area.

The MSFs can be classified according to their structural geometries, determined by the arrangement, number, size, pitch, and shape of air holes. Fibers with structures, as that shown in Figure 4-1, in which a central core is supported by a spider web of glass are called "Cobweb" fibers[260] and fibers with structures in which air holes fill only a small fraction of glass in the cladding are often referred to as "Endless Single-Mode" fibers[261]. In addition, when holes are arranged in a periodic manner, a photonic bandgap is introduced where light is coherently reflected back into the core. Such fibers are referred to as "Photonic Bandgap Fibers"(PBF)[262]. The guidance mechanisms of PBFs are different from those of Cobweb and Endless Single-Mode fibers, which are similar to the conventional way of light guiding. For the PBFs, the core refractive index can be lower than the average cladding refractive index. It, in fact, can be hollow. In contrast, the exact position of the holes does not make much difference for the Cobweb fibers.

4.2. Properties

One of the attractive features of MSFs is the greater tolerance in tailoring various fiber properties. There are some unique and interesting properties in MSFs. It is possible to design a single-mode fiber with an extremely small spot size to enhance nonlinear effects[263] or with a very large spot size to carry high optical power without nonlinear interactions or optical damage[264-265].

4.2.1. Group-Velocity Dispersion

The dispersion properties of MSFs are quite different from those of the conventional fibers. As discussed in Section 3.2.1, the ZDW can be shifted from a shorter wavelength to a longer wavelength in the conventional silica-core silica-clad fibers due to the waveguide contribution. Note that it is impossible to shift the ZDW to a shorter wavelength in the conventional fibers. In the MSFs in which the core region is surrounded by air, the waveguide dispersion dominates over material dispersion due to high index difference and small core radius. This can increase the flexibility in controlling the total dispersion as well as the location of ZDW[260].

As shown in Figure 4-2, the Cobweb MSF can have two ZDWs and it is possible to place the ZDW anywhere in the visible or infrared spectral regions. This ability to control the ZDW plays an important role in nonlinear fiber devices, since they usually require anomalous or near-zero dispersion at 1550nm where most HNL glasses show high normal material dispersion. It is also shown in Figure 4-2 how the dispersion varies with the silica-core diameter surrounded by air. As the core size increases, the dispersion will eventually match the material dispersion.

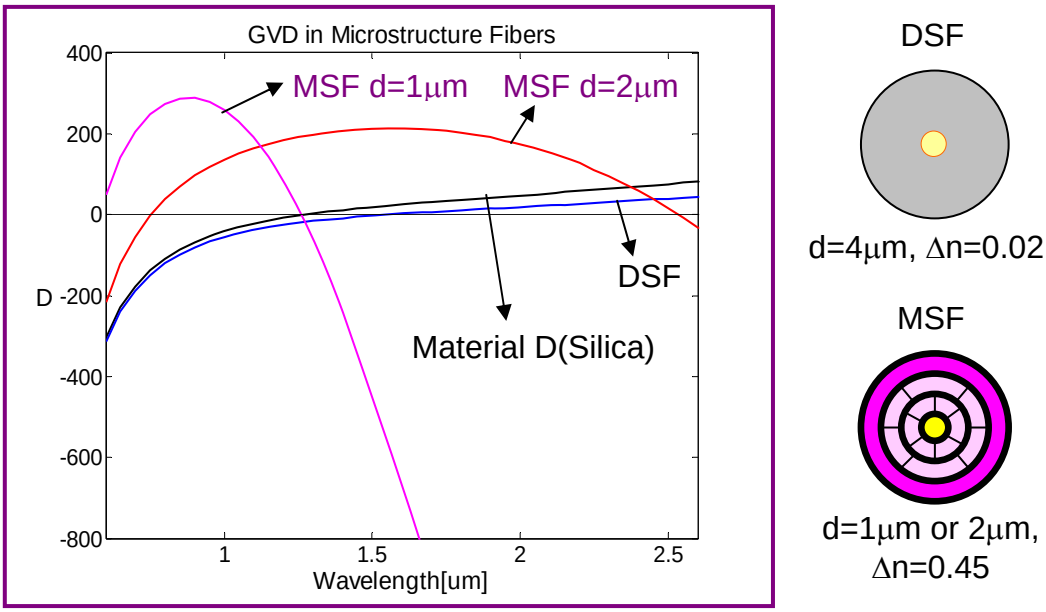

Figure 4-2. Group-Velocity Dispersion of Microstructure Fibers for Different Core Diameters

In addition, the careful design of the Endless Single-Mode MSFs allows a constant dispersion over a relatively broad spectral range[266-267]. The net dispersion can be close to zero which is useful for wideband continuum generation. The basic idea is to try to balance the slopes of the material and waveguide dispersions over some wavelength band. In MSFs, it is possible to shift the ZDW to a shorter wavelength[268], to have two ZDWs which can give flattened region by modifying air holes, to have very large negative dispersion for dispersion compensation[269], and to have anomalous dispersion in the visible range[270]. The applications of these properties will be discussed in Section 4.3.3.

4.2.2. Birefringence

It is relatively easy to obtain high birefringence in the design of MSFs, which can facilitate control over the SOP for device applications. As discussed in Section 3.3, no fiber can be perfectly circular, which means that there will always be some local birefringence. The birefringence is usually linear so there will be orthogonal directions of maximum and

minimum effective refractive index. Because the birefringence can vary in magnitude and direction, the SOP of optical waves will vary as they travel along the fiber. This randomly varying SOP can be avoided by using Polarization-Maintaining Fibers(PMF). In PMFs, a large birefringence, which increases the resistance to the cross-coupling of the two orthogonal SOPs from internal and external perturbations, is deliberately introduced.

The maximum birefringence in conventional low-index cladding PMFs is around 4×10^{-4}. However, a birefringence of 10^{-4} can arise unintentionally in MSFs from small asymmetries [271-272]. The reported maximum intentional birefringence($\sim4\times10^{-3}$) in MSFs is an order of magnitude larger than that of the conventional PMFs[273]. The simplest way to introduce birefringence is making the core noncircular. The key point is to take a large ellipticity to achieve high birefringence and the birefringence can also be introduced by applying air holes on each side of the core in MSFs. Conventional PMFs usually rely on stress introduced by differential thermal expansion from Boron-doped regions near the core.

Geometrical form birefringence of the MSFs can have fairly stable polarization properties while stress birefringence of the conventional low-index cladding fibers is highly temperature dependent, thus resulting in huge changes with temperature variation.

4.2.3. Photonic Bandgap

PBFs can guide light in a lower-index core, which means that the core region can be filled with liquids such as water or can be even hollow(air). The transmission of a hollow-core light guide can be improved by adding reflecting layers around the hollow core as shown in Figure 4-3. The coherent reflections from multiple layers can be viewed as reflection from a photonic bandgap.

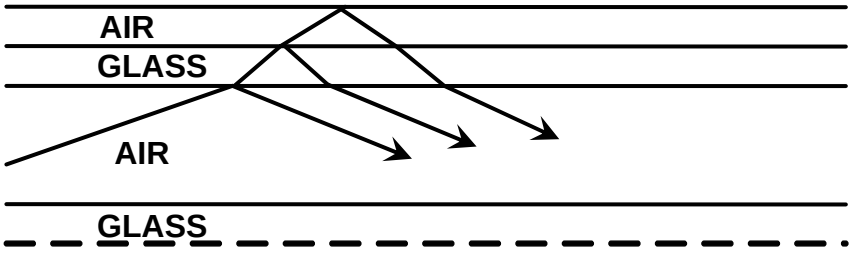

Figure 4-3. Basic Concept of Light Propagation in Hollow-Core

Early PBFs had hole spacings(pitch) around 5μm and air filling fractions less than 50%. More recent PBFs have air filling fractions greater than 90% so the hollow core is surrounded by a thin cylinder of silica[274]. Also, the PBF in which air holes are arranged in a hexagonal pattern has been developed with an extremely low loss of 1.72dB/Km at 1565nm[275].

4.3. Applications

4.3.1. Supercontinuum Generation

The most simple and ubiquitous application of MSFs is continuum generation[276-278]. The principle is that a short intense optical pulse coupled into a fiber is spectrally broadened by nonlinear effects. The evident characteristic of nonlinear effects is a generation of new frequencies and the magnitude of nonlinear effects increases with high optical intensity, long interaction length, and small effective mode area. The core diameters of MSFs can be less than 1μm giving the effective mode area $A_{eff} \approx 1\mu m^2$. While, the effective mode areas for standard fibers and specially-designed highly nonlinear conventional fibers are around $60\mu m^2$ and $20\mu m^2$, respectively. The supercontinuum can be used for ultrafast spectroscopy, spectrum slicing, optical pulse compression, and optical coherence tomography.

4.3.2. Nonlinear Fiber Devices

The nonlinear phenomena discussed in Chapter 1 can occur easily in MSFs due to the extremely small effective mode area[279-281] and a demultiplexer based on XPM for optical time-division-multiplexed signals[282] can be implemented using MSFs. As discussed in Section 3.1, a general rule for nonlinear switching is that 1KW of optical power is typically required with 1m of device length for a phase shift of π in standard fibers. This is about three orders of magnitude away from the most practical applications. Specially-designed highly nonlinear fibers utilizing high GeO_2 doping can lower the required power by about a factor of five. For silica-core cobweb MSFs, the power requirement drops to 10W for 1m of device length. Furthermore, if HNL glasses are used as the cores of the MSFs, the required power can be further reduced to practical levels.

4.3.3. Applications of Dispersion Shifting

The increased ability to tailor the magnitude and sign of the dispersion in MSFs brings new applications and extends the capabilities of existing applications. Many lightwave systems utilize Dispersion Compensating Fibers(DCF) to correct the dispersive broadening of optical pulses. DCFs are designed to maximize the normal or negative dispersion to cancel the pulse broadening. Figure 4-4 shows the extremely high negative GVD of a Cobweb MSF. It can have the negative dispersion which is 20 times larger than that of a conventional DCF. As a result, it is possible to use a shorter length of DCF for dispersion compensation[269]. Also, MSFs can have greater ability in compensating dispersion over a wide bandwidth[270].

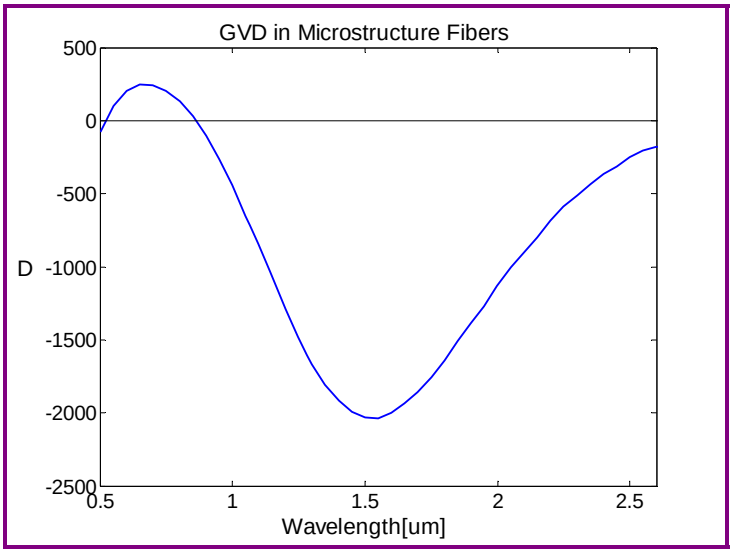

Figure 4-4. High Negative Group-Velocity Dispersion of Cobweb Microstructure Fibers

While dispersion compensation restores a temporally broadened optical pulse to its original pulse width, optical pulse compression produces a pulse much shorter than an input pulse. The spectrally-broadened chirped pulse is produced with large optical nonlinearity as discussed under the application of supercontinuum generation. For compression of this chirped pulse, the required dispersive delay must be obtained by the anomalous or positive dispersion. This can be achieved using the high anomalous dispersion shown in Figure 4-4.

Soliton pulses propagate without spreading by balancing chirp from SPM with anomalous dispersion. In conventional fibers, solitons are only observed at the wavelength greater than 1300nm, because anomalous dispersion in conventional fibers can not be developed at the wavelength shorter than 1300nm. However, as also shown in Figure 4-4, MSFs can be designed with anomalous dispersion at any wavelength[270]. This makes it possible to produce solitons in the visible range as well as in the infrared range[283].

4.4. Comparison

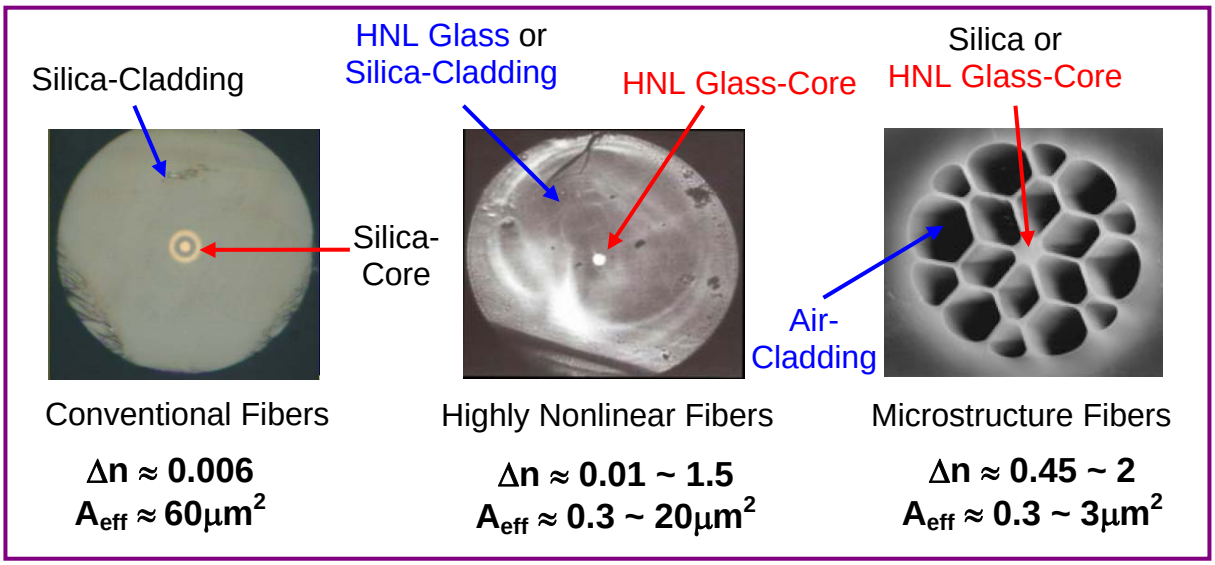

Figure 4-5. Comparison of Structures and Properties for Different Fiber Types[260]

Figure 4-5 compares the structures and properties of different types of fibers. The conventional silica-core silica-clad fibers have very small index difference and large effective mode area, while highly nonlinear fibers with silica-cladding have high index difference and small effective mode area, thus resulting in high nonlinearity. In MSFs, because the core is surrounded by air holes, they can develop much higher index difference and much smaller effective mode area. These properties enable extremely small spot size and thus much higher nonlinearity for nonlinear applications. Therefore, it is highly likely that the required device length for nonlinear fiber devices can be considerably reduced further by introducing HNL glasses as the cores of the MSFs.

Highly nonlinear fibers with lower-index cladding have usually been fabricated using similar glasses with slightly different compositions for both the core and cladding. As a result, they have lower index differences and larger effective mode areas compared to the highly nonlinear fibers with silica-cladding.

CHAPTER 5.
HIGH-NONLINEARITY GLASSES

Optical glasses with fast response times and high third-order nonlinearities are very promising materials for ultrafast nonlinear fiber devices[219, 284]. The third-order optical nonlinearity is the most important property for realization of ultrafast all-optical switching. This chapter addresses the general properties of the High-NonLinearity(HNL) Glasses of Lead-Oxide(PbO, Litharge), Bismuth-Oxide(Bi_2O_3, Bismite), Tellurium-Oxide(TeO_2, Tellurite), and Chalcogenide glasses with a focus on their nonlinear properties such as the third-order susceptibility and nonlinear-index coefficient. This chapter also discusses the characteristics of the conventional and microstructure fibers made of those HNL glasses.

5.1. Litharge(PbO) Glasses

Lead reacts easily with silica to form low melting lead-silicates of high gloss and quality. It is the heaviest oxide that produces incredible colors and surface characteristics. It promotes low expansion, decreases the viscosity, but has a tendency to devitrify. In addition, it is often used in combination with boric oxide which improves crazing problems and resistance to chemical attacks. Problems with lead include toxic nature of many forms, volatilization, loss of gloss during higher firing, and less abrasion resistance.

The glasses containing lead-oxide(PbO) are called Litharge glasses. Litharge glass has a high refractive index making it bright and a relatively soft surface making it easy to decorate by grinding, cutting and engraving. Its ability to refract light more efficiently than standard glass makes it an excellent material for prisms, decorative objects, and artificial jewelry. It is also favored for electrical applications because of excellent electrical insulating characteristics,

and the concave or diverging half on an achromatic lens is usually made of litharge glass. It can not withstand high temperatures or sudden changes in temperature.

Lead-silicate glasses are especially promising materials for highly nonlinear fibers due to their suitable combination of properties. Although their material nonlinearities are lower than those of bismite, tellurite, and chalcogenide glasses, they provide higher thermal and crystallization stability and less steep viscosity-temperature-curves, while exhibiting low softening temperatures. The properties of PbO-based glasses are summarized below.

- High linear refractive index(1.75~2.46)
- High nonlinear-index coefficient(22~286×10^{-20}[m^2/W])
- Wide transmission range(0.4μm~3μm)
- Transition temperature(~700°C) and melting temperature(~1100°C)
- Soft, toxic, heavy, and ductile
- Highly malleable
- Poor electrical conductivity
- High corrosion resistance
- Highest atomic number of all stable elements

Hereafter, for all tables of the linear and nonlinear properties for different HNL glasses,

1. Numbers with asterisk(*) mean the references placed on the bottom of tables.
2. The values of $\chi^{(3)}$ and N_2 in separate columns were obtained from references. Since most references present only one value of either $\chi^{(3)}$ or N_2, the other value was estimated using the most accurate formulas given in Equations (1.35)-(1.37).
3. The number in the parenthesis next to N_2 indicates how many times it is larger than the N_2 value of silica glass. For pure silica glasses, $\chi^{(3)}$ and N_2 are 0.27×10^{-13}[esu] and 2.5×10^{-20}[m^2/W], respectively at a wavelength of about 1500nm, and $\chi^{(3)}$ and N_2 are 0.28×10^{-13}[esu] and 2.6×10^{-20}[m^2/W], respectively at a wavelength of about 633nm with linear polarization.

4. The value of $\chi^{(3)}$ in the parenthesis next to the linear refractive index n_0 was simply calculated only with the n_0 through the Miller's rule given in Equation (1.27) for comparison. These values of $\chi^{(3)}$ obtained from the Miller's rule showed quite large difference with those obtained from references or Equations (1.35)-(1.37). It seems that the Miller's rule might not be useful for compositions of different glasses. This is why many people have proposed the more complicated formulas, shown in section 1.2.6, for more accurate nonlinear properties of various types of glasses.

Table 5-1 summarizes the linear refractive index n_0, the third-order susceptibility $\chi^{(3)}$, and the nonlinear-index coefficient N_2 for PbO-based glasses[91-102]. The largest value of N_2 is 114 times larger than that of silica glass.

Table 5-1. Linear and Nonlinear Properties of PbO-based Glasses

Glass Compositions	n_0 and $\chi^{(3)}[10^{-13}esu]$	$\chi^{(3)}$ $[10^{-13}esu]$	N_2 $[10^{-20}m^2/W]$
[*1]	(635nm)		
$67PbO{\cdot}33GaO_{1.5}$	2.260 (11.42)	7.7	30(11)
$10TiO_2{\cdot}60PbO{\cdot}30GaO_{1.5}$	2.301 (13.64)	8.5	32(12)
$10NbO_{2.5}{\cdot}60PbO{\cdot}30GaO_{1.5}$	2.280 (12.46)	7.5	28(11)
$10WO_3{\cdot}60PbO{\cdot}30GaO_{1.5}$	2.258 (11.32)	6.7	26(10)
$PbO{\cdot}TiO_2{\cdot}SiO_2$ [*2]			286(114) (1064nm)
SF : Lead-Silicate Glasses [*3]	(1060nm)		
SF59	1.91 (1.97)	13	68(27)
SF58	1.88 (1.65)	8.8	49(20)
SF57	1.81 (1.08)	6.8	41(16)
SF56	1.75 (0.73)	4	26(10)
SF : Lead-Silicate Glasses [*4]	(546nm)	(1060nm)	
SF6	1.81 (1.08)	3.7	22(9)
SF66	1.93 (2.21)		
$PbO{\cdot}SiO_2$ [*5]	(1060nm)		
	1.774 (0.85)	3.5	22(9)
$PbO{\cdot}SiO_2$ [*6]	(633nm)		
	1.846 (1.35)	5.5	32(12)
[*7]	(589.3nm)		
$60PbO{\cdot}40SiO_2$	2.06 (4.44)		
$57PbO{\cdot}25BiO_3{\cdot}18Ga_2O_3$	2.46 (26.11)		
$70PbO{\cdot}12Ga_2O_3{\cdot}6Tl_2O{\cdot}12CdO$	2.31 (14.18)		
$57PbO{\cdot}18Bi_2O_3{\cdot}18Ga_2O_3{\cdot}7Tl_2O$	2.30 (13.58)		
$48PbO{\cdot}14Bi_2O_3{\cdot}10Ga_2O_3{\cdot}14Tl_2O{\cdot}14CdO$	2.27 (11.93)		

References : [*1][91], [*2][92], [*3][219], [*4]: Schott Glass Catalog, [*5][94], [*6][96], [*7][216]

As discussed in Chapter 4, MSF technology has enabled considerable progress in the development of fibers with high nonlinearity. This can be achieved by combining a small core with a high numerical aperture to develop tight mode confinement. When HNL glasses are used for such MSFs, a further dramatic increase of the fiber nonlinearity can be obtained. While Table 5-1 shows the properties of PbO-based glasses, Table 5-2 presents the properties of highly nonlinear fibers which have actually been fabricated with PbO-based glasses[94-102].

Hereafter, for all tables of the properties of actual highly nonlinear fibers made of different HNL glasses,

1. Numbers with asterisk(*) mean the references placed on the bottom of tables.
2. CF represents Conventional Fiber in which both the core and cladding are made of glasses, and MSF represents MicroStructure Fiber which has a glass-core and air-cladding.
3. γ is the nonlinear parameter given in Equation (1.10), d is the core diameter, A_{eff} is the effective mode area given in Equation (1.7), and GVD is the Group-Velocity Dispersion.

Table 5-2. Properties of Highly Nonlinear Fibers with PbO-based Glasses

Fiber Compositions	γ [$W^{-1}Km^{-1}$]	d [μm]	A_{eff} [μm^2]	GVD [ps/nm·Km]	Loss [dB/m]
CF[*1] : Δn=0.046 core(n=1.774) & clad(n=1.728) $PbO{\cdot}SiO_2$		0.45	7 ± 1	-207 (1060nm)	2 (1071nm)
CF[*2] : core: $PbO{\cdot}GeO_2$ clad: SF57		7			2
MSF[*3] : SF57		2	2 (1550nm)		3 (633nm) 10 (1550nm)
MSF[*4] : SF57	550 (1550nm)	2	3.0 ± 0.3 (1550nm)		4 (1550nm)
MSF[*5] : SF6		2.6		50 (1550nm)	4.5 (1550nm) min. 2 (1200nm)
MSF[*6] : SF57	640 ± 60 (1550nm)	1.7	2.6 ± 0.3 (1550nm)	80 (1550nm)	2.6 (1550nm)
MSF[*7] : SF6 (LMAF)			40 ± 2 (800nm)		

LMAF : Large Mode Area Fiber

References : [*1][94], [*2][95], [*3][96], [*4][97], [*5][98], [*6][99-100], [*7][101]

5.2. Bismite(Bi_2O_3) Glasses

Bismite is derived from the ignition of bismuth nitrate which in turn is obtained from the heavy metal bismuth. Bismuth is very similar to lead, however there is no evidence of toxicity, and it has been used in low temperature frits, as a flux in conductive glazes, and in metal enamels. Bismite has been used instead of litharge in amounts up to 50% in optical glasses to improve durability and increase the specific gravity and the refractive index. Arsenic is often used with it to prevent a tendency toward grey coloration. Bismite is a very effective substitute for litharge, providing the same high gloss, flow, bubble clearance characteristics, high refractive index, surface tension, viscosity, and resistance to aggressive dishwasher detergents. Bismite melts at a lower temperature than litharge and thus glazes can be even more fluid. The properties of Bi_2O_3-based glasses are summarized below.

- High linear refractive index(1.87~2.6)
- High nonlinear-index coefficient(32~1810×10^{-20}[m^2/W])
- Very wide transmission range(0.45μm~5μm)
- Transition temperature(~500°C) and melting temperature(~900°C)
- Fusion-spliceable to SiO_2-based glasses
  : Easy integration to silica-based systems
- High mechanical, chemical, and thermal durability
  : Simple and easy fabrication process
- No toxicity

Table 5-3 summarizes the transition temperature TT, the linear refractive index n_0, the third-order susceptibility $\chi^{(3)}$, and the nonlinear-index coefficient N_2 for Bi_2O_3-based glasses [103-118]. The largest value of N_2 is 696 times larger than that of silica glass.

Table 5-3. Linear and Nonlinear Properties of Bi_2O_3-based Glasses

Glass Compositions	TT [°C]	n_0 and $\chi^{(3)}$[10^{-13}esu]	$\chi^{(3)}$ [10^{-13}esu]	N_2 [$10^{-20}m^2/W$]
*1		(633nm)		
$25.5Bi_2O_3 \cdot 51.0SiO_2 \cdot 15.7B_2O_3 \cdot 7.8BaO$		1.87 (1.56)	58	327(126)
$42.5Bi_2O_3 \cdot 28.4SiO_2 \cdot 28.4B_2O_3 \cdot 0.7CeO_2$		2.05 (4.22)	93	436(168)
$Bi_2O_3 \cdot B_2O_3 \cdot SiO_2$ *2		(633nm)		
Bi_2O_3 : 84.2 wt.%		2.04 (4.01)	53	251(97)
Bi_2O_3 : 89.0 wt.%		2.13 (6.28)	75	326(125)
Bi_2O_3 : 92.0 wt.%		2.21 (9.13)	93	375(144)
Er^{3+}-doped $Bi_2O_3 \cdot B_2O_3 \cdot SiO_2$ *3		(970nm)		
Bi_2O_3 : 25 mol.%		1.908 (1.95)		
Bi_2O_3 : 35 mol.%		2.005 (3.34)		
Bi_2O_3 : 45 mol.%		2.093 (5.24)		
Bi_2O_3 : 55 mol.%		2.165 (7.41)		
$(100-x)Bi_2O_3 \cdot xB_2O_3$ *4		(643.85nm)		
x=60	432	2.0153 (3.52)		
x=65	449	1.9593 (2.61)		
x=70	459	1.8997 (1.86)		
x=75	465	1.8359 (1.27)		
x=80	460	1.7657 (0.81)		
$(30-x)Li_2O \cdot xK_2O \cdot 20Bi_2O_3 \cdot 50B_2O_3$ *5		(633nm)		
x=5		2.22 (9.55)		
x=10		2.42 (22.31)		
x=20		2.55 (36.76)		

$Bi_2O_3 \cdot B_2O_3 \cdot SiO_2$ [*6]		(633nm)	(753nm)	
Bi_2O_3 : 44.0 mol.%		2.10 (5.42)	60	268(103)
Bi_2O_3 : 56.0 mol.%		2.22 (9.55)	260	1040(400)
Bi_2O_3 : 65.5 mol.%		2.31 (14.18)	490 (748nm)	1810(696) (748nm)
$78Bi_2O_3 \cdot 22SiO_2$ [*7]		(1550nm)		
		2.02 (3.61)	6.6	32(13)

References : [*1][103], [*2][104], [*3][105], [*4][106], [*5][107], [*6][108], [*7][110]

Table 5-4 presents the properties of highly nonlinear fibers which have actually been fabricated with Bi_2O_3-based glasses[110-118].

Table 5-4. Properties of Highly Nonlinear Fibers with Bi_2O_3-based Glasses

Fiber Compositions	γ [$W^{-1}Km^{-1}$]	d [μm]	A_{eff} [μm^2]	GVD [ps/nm·Km]	Loss [dB/m]
CF[*1] : Δn=0.01 core(n=2.02) & clad(n=2.01) $78Bi_2O_3 \cdot 22SiO_2$	64.2 (1550nm)		20.4 (1550nm)	-130 (1550nm)	0.8
CF[*2] : Δn=0.07 core(n=2.099)&clad(n=2.029) Er^{3+}-doped Bi_2O_3-based		4.9			0.7 (1310nm)
CF[*3] : Δn=0.09 core(n=2.22) & clad(n=2.13) $Bi_2O_3 \cdot B_2O_3$	1360 (1550nm)	1.72	3.3 (1550nm)	-280 (1550nm)	1.9 (1310nm)
MSF[*4] : $Bi_2O_3 \cdot SiO_2$	460 ± 40 (1550nm)	2.1	2.8 ± 0.3 (1550nm)	40 (1550nm)	3.8 ± 0.5 (1550nm)
MSF[*5] : $Bi_2O_3 \cdot SiO_2$	1100 (1550nm)	1.8			3.4 (1550nm)
	735 (1550nm)	2.1			2.8 (1550nm)
	460 ± 50 (1550nm)	2.7	2.8 ± 0.3 (1550nm)		3.8 (1550nm)

References : [*1][110], [*2][111], [*3][112-113], [*4][114], [*5][115]

5.3. Tellurite(TeO_2) Glasses

Tellurite glasses, compared to silicate and fluoride glasses, have a reasonably wide transmission region, the lowest phonon energy among the common oxide glasses, large refractive indices, and high nonlinear-index coefficients. Their large refractive index and the small phonon energy are desirable for radiative transitions of rare-earth ions(Er^{3+}, Tm^{3+}, Nd^{3+}, Pr^{3+}, Yb^{3+}, and so on) and the application of fiber lasers and amplifiers. The lower phonon energy leads to lower nonradiative transition rate(high fluorescence quantum efficiency) between adjacent rare earth energy levels, causing new fluorescence transitions and laser emission from additional energy levels.

Under normal conditions, tellurium-dioxide(TeO_2) has no vitrification ability without modifiers. Thus, glass-modifiers and/or secondary glass-formers are necessary in order to obtain tellurite glasses. Incorporation of a second component to tellurite glasses is expected to extend the Te-O interatomic distance, which should increase the mobility of the polyhedra and thereby provide a favorable condition for tellurite vitrification.

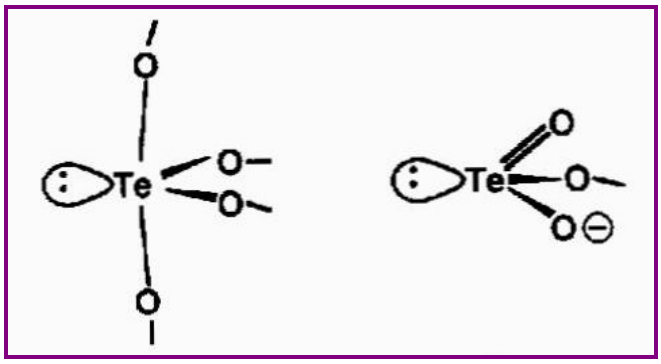

Figure 5-1. Structures of TeO_4 tbp and TeO_3 tp

Tellurite glasses have been found to be composed mainly of low symmetric structural units like TeO_4 trigonal bipyramid(tbp) and TeO_3 trigonal pyramid(tp) which are shown in Figure 5-1. They differ from conventional glass-forming systems like silicate and phosphates, in which symmetrical SiO_4 and PO_4 tetrahedra, respectively, are the main structural units. The

coordination state of tellurium atom changes from TeO_4 tbp through TeO_{3+1} polyhedron to TeO_3 tp with increasing alkali oxide. In the TeO_4 tbp, one equatorial site of the Te sp^3d hybrid orbital is occupied by a lone pair of electrons and the other two equatorial and axial sites are occupied by oxygen atoms. In the TeO_3 tp, one of the Te sp^3 hybrid orbital is occupied by a lone pair of electrons. The irregular connection of these units has been proposed as a structure model for a variety of binary TeO_2-based glasses. The properties of TeO_2-based glasses are summarized below.

- High linear refractive index(1.82~2.27)
- High nonlinear-index coefficient($16\sim210\times10^{-20}[m^2/W]$)
- Very wide transmission range(0.35μm~6μm)
- Low transition temperature(250~400°C) and melting temperature(450~800°C)
- Good glass stability, strength, and corrosion resistance
- Good rare-earth ion solubility
- Relatively low phonon energy for oxide glasses($600\sim850cm^{-1}$) to minimize nonradiative losses
- High electrical conductivity
- High resistance to devitrification and atmospheric moisture
- Good chemical durability
- High homogeneity
- Highly capable of incorporating large concentrations of rare-earth ions into the matrix

Table 5-5 summarizes the transition temperature TT, the melting temperature MT, the linear refractive index n_0, the third-order susceptibility $\chi^{(3)}$, and the nonlinear-index coefficient N_2 for TeO_2-based glasses[119-162]. The largest one is 81 times larger than that of silica glass.

Table 5-5. Linear and Nonlinear Properties of TeO_2-based Glasses

Glass Compositions	TT [°C]	MT [°C]	n_0 and $\chi^{(3)}$[10^{-13}esu]	$\chi^{(3)}$ [10^{-13}esu]	N_2 [$10^{-20}m^2$/W]
$(100-x)TeO_2 \cdot xZnO$ [*1, *3]			(643.8nm)		
x=17.4 [*1]			2.1099 (5.7)		
x=24.6 [*1]	315		2.0807 (4.9)		
x=36.4 [*1]			2.0297 (3.8)		
			(840nm)		
x=25 [*3]	326		2.13 (6.28)	35	153(59)
x=30 [*3]	329		2.11 (5.70)	33	147(57)
$(100-x-y)TeO_2 \cdot xTiO_2 \cdot yLi_2O$ [*2, *4]			(633nm)		
x=5, y=20 [*2]			2.1 (5.42)	4.3	19(8)
x=10, y=10 [*2]			2.2 (8.72)	8.0	33(13)
			(1900nm)		
x=10, y=5 [*4]	340		2.145 (6.74)	3.729	16(6)
x=15, y=5 [*4]	333		2.223 (9.68)	4.111	16(6)
$(100-x-y)TeO_2 \cdot xTiO_2 \cdot yPbO$ [*2]			(633nm)		
x=5, y=20			2.13 (6.28)	36	156(60)
x=10, y=20			2.2 (8.72)	28	114(44)
x=10, y=25			2.27 (11.93)	37	142(54)
$(100-x-y)TeO_2 \cdot xTiO_2 \cdot yNb_2O$ [*2]			(633nm)		
x=10, y=10			2.18 (7.95)	12	50(19)
x=10, y=15			2.27 (11.93)	9.6	37(14)

$(100-x)TeO_2 \cdot xNb_2O_5$ [*3]			(840nm)		
x=5	326		2.23 (9.99)	53	210(81)
x=10	357		2.24 (10.45)	47	185(71)
x=20	427		2.26 (11.42)	47	180(69)
$(100-x-y)TeO_2 \cdot xLi_2O \cdot yNb_2O_5$ [*3]			(840nm)		
x=10, y=5	308		2.17 (7.59)	36	150(58)
x=15, y=5	296		2.15 (6.91)	34	146(56)
x=10, y=10	330		2.17 (7.59)	38	158(61)
$(100-x-y)TeO_2 \cdot xK_2O \cdot yNb_2O_5$ [*3]			(840nm)		
x=10, y=10	353				
x=15, y=5	298		2.07 (4.67)	28	127(49)
$xTeO_2 \cdot (63-x)GeO_2 \cdot 27PbO \cdot 10CaO$ [*5]			(546.1nm)		
x=20	420		1.86 (1.47)		
x=30	385	600	1.91 (1.97)		
x=40	365	610	1.95 (2.47)		
$(100-x)TeO_2 \cdot xWO_3$ [*6, *7]	[*7]		(632.8nm) [*6]		
x=10			2.166 (7.45)	14.2	60(23)
x=15	362	607			
x=20			2.169 (7.55)	14.8	62(24)
x=30	398	622	2.172 (7.66)	15.9	66(26)
$(100-x)TeO_2 \cdot xPbO$ [*8, *9]	[*9]		(632.8nm) [*8]		
x=10	289		2.12 (5.98)		
x=30	262		2.17 (7.59)		
x=40			2.18 (7.95)		
x=50	231				
$xTeO_2 \cdot (65-x)GeO_2 \cdot 5Nb_2O_5 \cdot 30BaO$ [*10]			(589.3nm)		
x=10			1.8235 (1.2)		

x=30			1.9235 (2.1)		
x=50			2.0235 (3.7)		
$(100-x-y)TeO_2 \cdot xK_2O \cdot yWO_3$ [*11]			(632.8nm)		
x=5, y=5	306	687	2.11 (5.70)		
x=10, y=10	308	619	2.04 (4.01)		
x=25, y=15	252	454	1.86 (1.47)		
x=20, y=40	363	630	1.92 (2.09)		
x=30, y=50	325	550	1.62 (0.28)		
$(100-x)TeO_2 \cdot xLi_2O$ [*12]			(633nm)		
x=7.5			2.141 (6.62)	12.81	55(21)
x=20			2.040 (4.01)	5.86	28(11)
x=25			1.997 (3.20)	4.21	21(8)
$(100-x)TeO_2 \cdot xNa_2O$ [*12]			(633nm)		
x=5			2.135 (6.43)	7.26	31(12)
x=10			2.085 (5.03)	5.86	27(10)
x=20			1.994 (3.15)	4.82	24(9)
$(100-x)TeO_2 \cdot xK_2O$ [*12, *13]	[*13]		(633nm) [*12]		
x=7.5			2.105 (5.56)	7.31	33(13)
x=15	249	442	1.990 (3.08)	5.15	26(10)
x=20	230	464	1.928 (2.19)	3.78	20(8)
$(90-x)TeO_2 \cdot xZnF_2 \cdot 10Na_2O$ [*14]			(632.8nm)		
x=10	256	494	1.990 (3.08)		
x=20	241	466	1.914 (2.02)		
x=30	235	467	1.850 (1.38)		
$85TeO_2 \cdot 15WO_3$ [*15]			2.17 (7.59) (800nm)	18	76(29)
$(100-x)TeO_2 \cdot xScO_{1.5}$ [*16]			(633nm)		
x=5			2.121 (6.01)	8.2	36(14)
x=10			2.085 (5.03)	5.6	25(10)

$(100-x)TeO_2 \cdot xTiO_2$ [*16]			(633nm)		
x=5			2.190 (8.33)	14.2	58(22)
x=10			2.214 (9.29)	15.8	64(24)
x=15			2.227 (9.86)	16.6	66(25)
$90TeO_2 \cdot 10VO_{2.5}$ [*16]			2.141 (6.62)	36	155(60)
$(100-x)TeO_2 \cdot xNbO_{2.5}$ [*16]			(633nm)		
x=10			2.172 (7.66)	14.1	59(23)
x=20			2.182 (8.03)	16.1	67(26)
x=30			2.192 (8.41)	16.9	69(27)
$(100-x)TeO_2 \cdot xMoO_3$ [*16]			(633nm)		
x=10			2.115 (5.84)	6.7	29(11)
x=20			2.132 (6.34)	7.1	31(12)
x=30			2.092 (5.21)	6.9	31(12)
$(100-x)TeO_2 \cdot xTaO_{2.5}$ [*16]			(633nm)		
x=5			2.164 (7.38)	12.2	51(20)
x=10			2.154 (7.04)	10.1	43(17)
x=15			2.137 (6.49)	8.0	35(13)
$(100-x)TeO_2 \cdot xMgO$ [*17]			(632.8nm)		
x=5			2.01 (3.43)		
x=25			1.96 (2.62)		
$(100-x)TeO_2 \cdot xLa_2O_3$ [*18]					
x=10	620			1.19	
x=20				1.04	
$(100-2x)TeO_2 \cdot xBaO \cdot xZnO$ [*19]			(589.3nm)		
x=7.5			2.17 (7.59)		
x=20			2.02 (3.61)		

References : [*1][119], [*2][120], [*3][121], [*4][122], [*5][123], [*6][124], [*7][125], [*8][126], [*9][127], [*10][128], [*11][129], [*12][130], [*13][131], [*14][132], [*15][133], [*16][124], [*17][126], [*18][285], [*19][216]

Table 5-6 presents the properties of highly nonlinear fibers which have actually been fabricated with TeO_2-based glasses[154-162]. TeO_2-based fibers have been extensively used in rare-earth ion-doped, especially erbium, fiber amplifiers[157-161].

Table 5-6. Properties of Highly Nonlinear Fibers with TeO_2-based Glasses

Fiber Compositions	γ [$W^{-1}Km^{-1}$]	d [μm]	A_{eff} [μm^2]	Cutoff λ [μm]	Loss [dB/m]
CF[*1] : TeO_2-based		5			0.9 (1350nm)
MSF[*2] : $75TeO_2 \cdot 20ZnO \cdot 5Na_2CO_3$	47.8 (1550nm)	7	21.2		min. 2.3 (1055nm)
CF[*3] : Δ=2.2% TeO_2-based	55			1.3	0.02 (1560nm)
CF[*4] : Δ=1.5% Er^{3+}-doped TeO_2-based				1.15	0.054 (1200nm)
CF[*5] : Δ=1.5% Er^{3+}-doped TeO_2-based				1.3	1
CF[*6] : Δ=1.5% Er^{3+}-doped TeO_2-based				1.2	0.2 (1300nm)
CF[*7] : Δ=1.5% Er^{3+}-doped TeO_2-based				1.4	0.035 (1230nm)
CF[*8] : Tm^{3+}-doped TeO_2-based		5			6.5 (1400nm)

References : [*1][154], [*2][155], [*3][156], [*4][157], [*5][158], [*6][159], [*7][160], [*8][161]

Table 5-7 compares the properties of pure SiO_2 and pure TeO_2 glasses.

Table 5-7. Comparison of Properties of Pure SiO_2 and Pure TeO_2 Glasses

Glasses	TT [°C]	MT [°C]	n_0	$\chi^{(3)}$ [10^{-13}esu]	N_2 [$10^{-20}m^2/W$]	GVD [ps/nm·Km]	ZDW [μm][*1]	Abbe #[*2]
			(633nm)			(1550nm)		
SiO_2	1100	1700	1.457	0.28	2.6(1)	21.7	1.273	69
TeO_2	400	733	2.239	14	55(21)	-35.7	1.688	17.7
Ref.	285		120			134		

[*1]: Zero-Dispersion Wavelength by Material Contribution Only, [*2]: Equation (1.29)

5.4. Chalcogenide Glasses

The chalcogenide glasses are composed of one or more of the chalcogenide elements such as S, Se, and Te, with other elements such as As, Ga, Ge, In, and Sb to form a stable glasses. Other elements such as P, I, Cl, Br, Cd, Br, Ba, Si, or Tl can be added to these glasses for tailoring their thermal, mechanical, and optical properties. The chalcogenide elements are covalent in nature and can exhibit chain, ring and/or network structures. In contrast to oxide glasses, they can depart from atomic stoichiometry through the partial segregation of chalcogens and/or redox adjustments of the nonchalcogen constituents.

Chalcogenide glasses are melted in closed systems due to the chalcogens volatility. Therefore, it is required, typically, to seal the batch components in an evacuated silica ampoule and to increase temperatures slowly with rocking motion to promote mixing. The glass components are often individually prepurified to remove oxide and hydride impurities which can impair the mid-IR transmission. The most distinct characteristics of chalcogenide glasses are high refractive indices and ZDWs in the mid-IR range.

It has been confirmed that Se-based chalcogenide glasses possess higher nonlinearity than S-based chalcogenide glasses, and it seems that Te-based chalcogenide glasses are not suitable for optical communications at wavelengths of 1.3μm or 1.5μm because their bandgap wavelengths become longer than the operating wavelengths. Additionally, the chalcogenide glasses based on Ga-La-S are of great interest, particularly due to their low toxicity, high transition temperature, and excellent rare-earth solubility, and the chalcogenide glasses based on As-S are suitable candidates for passive and active fiber applications due to their crystallization stability and their mechanical and chemical stability. The properties of Chalcogenide glasses are summarized below.

- High linear refractive index(2.03~3.23)
- High nonlinear-index coefficient(101~9000×10^{-20}[m^2/W])
- Ultra wide transparency region from near IR to far IR(0.7μm~16μm)

- Low transition temperature(150~250°C) and melting temperature(300~400°C)
- High chemical durability
- Low phonon energy (200~300cm^{-1})
- Wide glass-forming region
- Can be fabricated into low-loss fiber
- Can be doped by rare-earth elements

Table 5-8 summarizes the transition temperature TT, the linear refractive index n_0, the third-order susceptibility $\chi^{(3)}$, and the nonlinear-index coefficient N_2 for chalcogenide glasses [163-196]. The largest one is 3600 times larger than that of silica glass.

Table 5-8. Linear and Nonlinear Properties of Chalcogenide Glasses

Glass Compositions	TT [°C]	n_0 and $\chi^{(3)}[10^{-13}$esu]	$\chi^{(3)}$ $[10^{-13}$esu]	N_2 $[10^{-20}m^2/W]$
*1		(1500nm)		
45As·55S		2.270 (11.93)	50	191(77)
33Ge·67S		2.027 (3.75)	24	115(46)
20As·60S·20Ge		2.112 (5.75)	40	177(71)
*2				(1500nm)
40As·45S·15Se	207			475(190)
40As·30S·30Se	202			263(105)
40As·15S·45Se	196			193(77)
24As·38S·38Se	135			1015(406)
*3		(1500nm)		
25Ge·75Se		2.4 (20.59)	88	300(120)
25Ge·65Se·10Te		2.5 (30.47)	174	550(220)
28Ge·60Se·12Sb		2.61 (45.76)	311	900(360)
40As·60Se		2.78 (82.19)	490	1250(500)
*4				(1064nm)
10Ge·90Se	102			1500(600)
30Ge·70Se	324			2100(840)
10Ge·10As·80Se	128			2200(880)
15Ge·10As·75Se	153			1200(480)
*2, *5	*2	(1550nm)*5		
40As·60S	215	2.45 (25.11)	168	550(220)
40As·60Se	191	2.81 (90.69)	931	2325(930)

40As·40S·20Se		2.55 (36.76)	247	750(300)
40As·10S·50Se		2.76 (76.91)	541	1400(560)
40As·55Se·5Cu		2.93 (132.73)	926	2125(850)
25As·55S·20Te		2.52 (32.86)	376	1175(470)
*6		(1520nm)		
$65Ga_2S_3 \cdot 32La_2S_3 \cdot 3La_2O_3$		2.41 (21.43)	64	216(86)
$70Ga_2S_3 \cdot 30La_2O_3$		2.25 (10.92)	46	177(71)
$70Ga_2S_3 \cdot 15La_2O_3 \cdot 15LaF_3$		2.26 (11.42)	36	139(56)
$68Ga_2S_3 \cdot 32Na_2S$		2.14 (6.58)	24	101(40)
*7				(1060nm)
$(As_2S_3)_{50}(Sb_2S_3)_{30}(PbI_2)_{20}$				700(280)
$(As_2S_3)_{45}(Sb_2S_3)_{45}(Bi_2S_3)_{10}$				800(320)
$(As_2S_3)_{35}(Sb_2S_3)_{35}(Bi_2S_3)_{10}(PbI_2)_{20}$				1300(520)
$(As_2S_3)_{25}(Sb_2S_3)_{25}(Bi_2S_3)_{10}(PbI_2)_{40}$				1600(640)
xAg·(100-x)(0.4As·0.6Se)*8		(1050nm)		
x=20		3.1 (220.38)	4388	9000(3600)
x=30		3.23 (317.50)		
*9		(2μm)		
40As·60S		2.43 (23.21)		
15As·25Ge·60Se		2.22 (9.55)		
12As·33Ge·55Se		2.53 (34.12)		
28Ge·12Sb·60Se		2.63 (49.15)		
*10		(633nm)		
Ge-As-S		2.22 (9.55)	37	148(59)
Ge-As-S-Se		2.36 (17.49)	70	248(99)
As-S-Se		2.55 (36.76)	140	424(170)

References : *1[163], *2[164], *3[165], *4[166], *5[167], *6[168], *7[169], *8[170], *9[216], *10[120]

Table 5-9 presents the properties of highly nonlinear fibers which have actually been fabricated with chalcogenide glasses[179-196].

Table 5-9. Properties of Highly Nonlinear Fibers with Chalcogenide Glasses

Fiber Compositions	N_2 [$10^{-20}m^2/W$]	d [μm]	A_{eff} [μm^2]	GVD [ps/nm·Km]	Loss [dB/m]
CF[*1] :					
40As·60S-unclad					0.035 (2.44μm)
38As·5Ge·57Se-unclad					0.182 (2.12μm)
20Ge·80S-unclad					0.148 (1.68μm)
CF[*2] : Δ=0.4% core : 38As·62S clad : 37.4As·62.6S	170		24.6		3 (1319nm)
CF[*3] :					(1536nm)
Δ=0.4% core : 38As·62S clad: 37.4As·62.6S	93	5.4			0.9
Δ=0.8% core : 38As·62S clad : 36.8As·63.2S	230	3.6			2.1
Δ=1.3% core : 40As·60S clad : 38As·62S	200	3			3.0
CF[*4] : Δn=0.157 core : 38As·62S(n=2.6) clad:37.4As·62.6S(n=2.443)	390		27.8		2.0
CF[*5] : core : 38As·62S clad : 37.4As·62.6S	(1552nm)				
	93		23.3	-410	0.88

CF[*6] : As_2S_3-based			8.6 (1.55μm)		0.6-3.0
CF[*7] :					
core : 40As·58S·2Se clad : 40As·60S		200			0.6 (4.8μm)
core: 30Ge·10As·30Se·30Te clad: 25Ge·10As·40Se·25Te		140			0.7 (6.56μm)
CF[*8] :					
70Ga_2S_3·30La_2S_3-unclad					4.8 (4.75μm)
72.5Ga_2S_3·27.5La_2O_3-unclad					3.8 (3.9μm)
CF[*9] : core : 40As·58S·2Se clad : 40As·60S		12			1 (2.7μm)
CF[*10] : Δn=0.032 core : (n=2.426) Pr^{3+}-doped 37.8As·1.3Ge·0.5Ga·60.4S clad : (n=2.394) 36.6As·3.2Ge·60.2S		2.5			6.7 (1020nm) 3.3 (1300nm)
MSF[*11] Ga·Ga·S-based		10		10 (1500nm)	
CF[*12] : core : 38As·62Se clad : 39As·61S		7			0.7 (1560nm)
CF[*13] : core : 39As·61Se clad : 38As·62Se	(1550nm)				
	2340 γ = 2450	7	40	-670	1

References : [*1][179], [*2][180], [*3][181], [*4][182], [*5][183], [*6][184], [*7][185], [*8][186], [*9][187], [*10][188], [*11][189], [*12][190], [*13][191]

5.5. Estimation of Losses

With the actual losses from fabricated fibers given in the previous sections, it would be useful to see the way of loss estimation for predictions of losses of HNL glasses. This section provides useful formulas for loss estimation[286-287].

The major scattering absorption losses are caused by density, Raman, and (for multi-component systems) concentration mechanisms and contribute to total loss $\alpha=\alpha_0$(in dB/Km) at minimum dispersion wavelength λ_0 as follows.

$$\alpha_{0\_Density} = 7.0\times10^{-6} E_0 E_d E_l^2 \left(1-\Lambda\right)^2 TK_T \tag{5.1}$$

$$\alpha_{0\_Concentration} = 0.084 E_0 E_d E_l^2 VF \tag{5.2}$$

$$\alpha_{0\_Raman} = \frac{1.4 E_0 E_d E_l^2 V d^2 \Lambda^2}{z_R l^2 m\omega} \coth\left(\frac{0.72\omega}{T}\right) \tag{5.3}$$

In addition, the minimum dispersion vacuum wavelength can be defined in terms of the three Sellmeier energies[288] of the average electronic energy gap E_0, the dispersion energy E_d, and the lattice oscillator strength E_l(all in eV) as

$$\lambda_0[\mu m] = 1.63\left(\frac{E_d}{E_0^3 E_l^2}\right)^{\frac{1}{4}} \tag{5.4}$$

It is presumed that one particular local motion with a number Z_R of such independent modes per molecular unit, which involves a highly polarizable bond type of bond length *l*, dominates both bond-dependent density and Raman scattering mechanisms. In Equations (5.1)-(5.3), d is the local structural dimensionality, K_T is the static isothermal compressibility in 10^{-}

^{12}cm^2/dyne, T is the temperature in Kelvin, V is the molar volume in cm^3, *l* is the bond length in Angstroms, m is the effective mass of the dominant Raman mode in atomic mass units which has a frequency ω in cm^{-1}, F is a dimensionless parameter which is zero for single component materials. The dimensionless quantity Λ is related to d and to other physical characteristics of the bond.

Under the assumption in Equations (5.1) and (5.2) that at minimum dispersion, the electronic contribution to the dielectric constant is dominant and closely equal to its long wavelength limit of $1+E_d/E_0$, the three major contributions to scattering loss in this region vary with wavelength as λ^{-4}. For wavelengths which are not too far from λ_0, the wavelength-dependent absorption contributions can be given

$$\alpha_{Density} = \frac{5.0\times10^{-5} E_d^2 \left(1-\Lambda\right)^2 TK_T}{E_0^2 \lambda^4} \tag{5.5}$$

$$\alpha_{Concentration} = \frac{0.6 E_d^2 VF}{E_0^2 \lambda^4} \tag{5.6}$$

$$\alpha_{Raman} = \frac{10.0 E_d^2 V d^2 \Lambda^2}{E_0^2 \lambda^4 z_R l^2 m\omega} \coth\left(\frac{0.72\omega}{T}\right) \tag{5.7}$$

5.6. Comparison

Table 5-10 compares the properties for different glasses of Pure Silica, Litharge, Bismite, Tellurite, and Chalcogenide glasses.

Table 5-10. Comparison of Properties for Different Glasses

Properties	**Pure Silica**	**Litharge**	**Bismite**	**Tellurite**	**Chalcogenide**
n_0	**1.4441 (1.5μm)**	**1.75~2.46**	**1.87~2.6**	**1.82~2.27**	**2.03~3.23**
N_2 [10^{-20} m^2/W]	**2.5 (1.5μm)**	**22~286**	**32~1810**	**16~210**	**101~9000**
Transmission Range [μm]	**0.2~2.5**	**0.4~3**	**0.45~5**	**0.35~6**	**0.7~16**
Melting Temp. [°C]	**1700 [pyrex: 820]**	**1100**	**900**	**450~800**	**300~400**
Best Fiber Loss [dB/m]	**0.0002 (1.5μm)**	**2 (1.2μm)**	**0.7 (1.31μm)**	**0.035 (1.23μm)**	**0.7 (1.56μm)**
Transition Temp. [°C]	1100 [pyrex: 560]	700	500	250~400	150~250
Thermal Expansion Coefficient [10^{-6}/°C]	0.55	29	13	12~20	13~24
Density [g/cm^3]	2.2 [pyrex: 3.25]	9.5	9.4	6	4

CHAPTER 6.
EVALUATION METHODOLOGY

This chapter describes how the properties of nonlinear fiber devices, constructed with the HNL glasses of litharge, bismite, tellurite, and chalcogenide glasses, are evaluated. At first, representative glasses for each of the HNL glasses are selected and used in each of the nonlinear fiber devices operating based on the optical Kerr effect, NOLMs, ATCFs, or mode interference. To evaluate the performance of those devices, the three types of fibers, HNL glass-core silica-clad fibers, HNL glass-core air-clad(microstructure) fibers, and HNL glass-core HNL glass-clad fibers, are considered. Then, the required device length and the required optical power for the desired nonlinear effect, relative group delay between the control and signal pulses or between the two modes of the signal for the required device length, the properties of GVD and Dispersion Slope(DS), walk-off length for the input pulse width, and output pulse width(pulse broadening) are evaluated for individual nonlinear fiber devices constructed with the three types of fibers.

6.1. Glass Selection

To evaluate the properties of highly nonlinear fiber devices, representative types of HNL glasses are chosen with careful consideration of both linear and nonlinear properties. The selected glasses include SF57(lead-silicate, Schott glass), $55Bi_2O_3{\cdot}45B_2O_3$, $75TeO_2{\cdot}25ZnO$, and 40As·60Se for litharge, bismite, tellurite, and chalcogenide glasses, respectively. Table 6-1 presents the linear and nonlinear properties of selected glasses as well as the silica glass. The number in the parenthesis for N_2 indicates how many times it is larger than the N_2 value of silica glass.

Table 6-1. Linear and Nonlinear Properties of Selected Representative Glasses

Properties (at 1.55μm)	Silica SiO_2	Litharge SF57	Bismite $55Bi_2O_3{\cdot}45B_2O_3$	Tellurite $75TeO_2{\cdot}25ZnO$	Chalcogenide $40As{\cdot}60Se$
n_0	1.4554 pure:1.4441	1.8017	2.1009	2.0278	2.7555
N_2 $[10^{-20}\ m^2/W]$	2.5(1)	40(16)	1000(400)	148(59)	1250(500)
$\chi^{(3)}$ $[10^{-13}esu]$	0.27	6.6	224	31	481

6.2. Required Device Length and Required Optical Power

For conventional silica-core silica-clad fiber devices, usually, a fiber length of 1Km with an optical power of 1W is required to obtain a phase shift of π. To assess the reduction in the required device length and optical power when the HNL glasses are used, the required lengths are calculated for nonlinear fiber devices based on the optical Kerr effect, NOLMs, or mode interference, while the required optical powers are calculated for wavelength-division demultiplexers based on ATCFs.

The required device lengths for nonlinear fiber devices based on the optical Kerr effect or NOLMs to achieve a nonlinear phase shift of π are obtained from followings.

Nonlinear Fiber Devices based on the Optical Kerr Effect

$$\delta\phi_{XPM} = \frac{2\pi L}{\lambda_S} 1.5 N_2 \frac{P_C}{A_{eff}} = \pi$$

$$L_\pi^{XPM} = \frac{\lambda_S A_{eff}}{3 N_2 P_C} \tag{6.1}$$

Nonlinear Fiber Devices based on Nonlinear Optical Loop Mirrors

$$\delta\phi_{XPM} = \frac{2\pi L}{\lambda_S} 2N_2 \frac{P_C}{A_{eff}} = \pi$$

$$L_\pi^{XPM} = \frac{\lambda_S A_{eff}}{4N_2 P_C} \tag{6.2}$$

In Equations (6.1) and (6.2), λ_S is the signal wavelength, P_C is the control peak power, and

$$A_{eff} = 2\pi \cdot \frac{\left[\int \psi_S{}^2 r dr\right]\left[\int \psi_C{}^2 r dr\right]}{\int \psi_S{}^2 \cdot \psi_C{}^2 r dr} \tag{6.3}$$

The required device lengths for SPM-induced and XPM-induced nonlinear fiber devices based on LP_{01}-LP_{02} mode interference to achieve a nonlinear phase shift of π can be obtained from Equations (2.53) and (2.55), respectively as follows.

SPM-Induced Nonlinear Fiber Devices based on LP_{01}-LP_{02} Mode Interference When $P_S=P_{01}=P_{02}$

$$\delta\phi_{SPM} = \left|\frac{2\pi L N_2 P_S}{\lambda_S}\left[\frac{1}{A_{eff\_01}} - \frac{1}{A_{eff\_02}}\right]\right| = \pi$$

$$L_\pi^{SPM} = \frac{\lambda_S}{2N_2 P_S \left|\frac{1}{A_{eff\_01}} - \frac{1}{A_{eff\_02}}\right|} \tag{6.4}$$

XPM-Induced Nonlinear Fiber Devices based on LP_{01}-LP_{02} Mode Interference When $P_P >> P_S$ (P_P >> P_S (Pump is in LP_{01} Mode))

$$\delta\phi_{XPM} = \left| \frac{4\pi L N_2 P_P}{\lambda_S} \left[\frac{1}{A_{eff\_01S\_01P}} - \frac{1}{A_{eff\_02S\_01P}} \right] \right| = \pi$$

$$L_\pi^{XPM} = \frac{\lambda_S}{4 N_2 P_P \left| \frac{1}{A_{eff\_01S\_01P}} - \frac{1}{A_{eff\_02S\_01P}} \right|} \tag{6.5}$$

where $A_{eff\_01S\_01P}$ and $A_{eff\_02S\_01P}$ are the effective mode areas given in Equations (2.56) and (2.57), respectively.

The required device lengths for SPM-induced and XPM-induced nonlinear fiber devices based on LP_{01}-LP_{11} mode interference to achieve a nonlinear phase shift of π can be obtained from Equations (2.62) and (2.64), respectively as follows.

SPM-Induced Nonlinear Fiber Devices based on LP_{01}-LP_{11} Mode Interference When P_S=P_{01}=P_{11}

$$\delta\phi_{SPM} = \left| \frac{2\pi L N_2 P_S}{\lambda_S} \left[\frac{1}{A_{eff\_01}} - \frac{1}{A_{eff\_11}} \right] \right| = \pi$$

$$L_\pi^{SPM} = \frac{\lambda_S}{2 N_2 P_S \left| \frac{1}{A_{eff\_01}} - \frac{1}{A_{eff\_11}} \right|} \tag{6.6}$$

XPM-Induced Nonlinear Fiber Devices based on LP_{01}-LP_{11} Mode Interference

When $P_P >> P_S$ (Pump is in LP_{01} Mode)

$$\delta\phi_{XPM} = \left| \frac{4\pi L N_2 P_P}{\lambda_S} \left[\frac{1}{A_{eff\_01S\_01P}} - \frac{1}{A_{eff\_11S\_01P}} \right] \right| = \pi$$

$$L_{\pi}^{XPM} = \frac{\lambda_S}{4 N_2 P_P \left| \frac{1}{A_{eff\_01S\_01P}} - \frac{1}{A_{eff\_11S\_01P}} \right|} \tag{6.7}$$

where $A_{eff\_01S\_01P}$ and $A_{eff\_11S\_01P}$ are the effective mode areas given in Equations (2.56) and (2.65), respectively.

In addition, the required optical powers for wavelength-division demultiplexers based on ATCFs are obtained by

Wavelength-Division Demultiplexers based on Asymmetric Twin-Core Fibers

$$\delta n = N_2 I = N_2 \frac{P_C}{A_{eff}}$$

$$P_C = \frac{A_{eff} \cdot \delta n}{N_2} \tag{6.8}$$

6.3. Relative Group Delay, Group-Velocity Dispersion, and Dispersion Slope

The refractive index as a function of wavelength for each selected glass is first obtained by the following Sellmeier(or a similar) equation and accompanying coefficients.

For Slightly GeO_2-doped Silica(core), Pure Silica(cladding), and Litharge(SF57) Glasses

$$n^2 = 1 + \frac{B_1\lambda^2}{\lambda^2 - \lambda_1^2} + \frac{B_2\lambda^2}{\lambda^2 - \lambda_2^2} + \frac{B_3\lambda^2}{\lambda^2 - \lambda_3^2} \tag{6.9}$$

Table 6-2. Coefficients for $GeO_2 \cdot SiO_2$, Pure SiO_2, and SF57 Glasses

	$GeO_2 \cdot SiO_2$(core)	Pure SiO_2(cladding)	SF57
B_1	0.68698290	0.6961663	1.81651732
B_2	0.44479505	0.4079426	0.428893631
B_3	0.79073512	0.8974794	1.07186278
λ_1	0.078087582	0.0684043	0.0143704198
λ_2	0.11551840	0.1162414	0.0592801172
λ_3	10.436628	9.896161	121.419942

For Bismite Glass($55Bi_2O_3 \cdot 45B_2O_3$)[109]

$$n^2 = A_0 + A_1 \cdot x + A_2 \cdot x^2 + \frac{B_1 \cdot x}{\lambda^2 - C_0 - C_1 \cdot x} - D_0 \cdot \lambda^2 \tag{6.10}$$

Table 6-3. Coefficients for $55Bi_2O_3 \cdot 45B_2O_3$ Glass

x	A_0	A_1	A_2	B_1	C_0	C_1	D_0
0.55	1.90598	5.78900	-2.22010	0.16995	0.02116	0.09230	0.01857

For Tellurite Glass($75TeO_2 \cdot 25ZnO$)[134]

$$n^2 = A + \frac{B\lambda^2}{\lambda^2 - C} + \frac{D\lambda^2}{\lambda^2 - E} \tag{6.11}$$

Table 6-4. Coefficients for $75TeO_2 \cdot 25ZnO$ Glass

A	B	C	D	E
2.4843245	1.6174321	0.053715551	2.4765135	225

For Chalcogenide Glass(40As·60Se)[191]

$$n^2 = 1 + \frac{E_d E_s}{E_s^{\,2} - \left(\frac{hc}{\lambda q}\right)^2} \tag{6.12}$$

where E_d is the electronic oscillator energy, E_s is the Sellmeier gap energy, h is the Planck's constant, c is the light velocity in vacuum, and q is the electron charge.

Table 6-5. Coefficients for 40As·60Se Glass

E_d[eV]	E_s[eV]	h[J·s]	q[C]
26	4.1	6.626×10^{-34}	1.602×10^{-19}

After determining the refractive indices of these glasses, the effective refractive indices for fiber modes are obtained by using vector wave analysis. Then, the RGD, between the control and signal pulses for nonlinear fiber devices based on the optical Kerr effect, NOLMs, and ATCFs[Equation (6.13)] or between two different modes of the signal pulse for nonlinear fiber devices based on mode interference[Equation (6.14)], for the required device length is estimated by

$$\Delta t_g = L\left|\frac{1}{v_{g\_s}} - \frac{1}{v_{g\_c}}\right| = \frac{L}{c}\left|n_{geff\_s} - n_{geff\_c}\right| \tag{6.13}$$

$$\Delta t_g = L\left|\frac{1}{v_{g\_01}} - \frac{1}{v_{g\_02\ or\ 11}}\right| = \frac{L}{c}\left|n_{geff\_01} - n_{geff\_02\ or\ 11}\right| \tag{6.14}$$

where n_{geff_s} and n_{geff_c} are the group effective refractive indices of the signal and control pulses, respectively, n_{geff_01} and $n_{geff\_02\ or\ 11}$ are the group effective refractive indices of the LP_{01} and LP_{02}(or LP_{11}) modes of the signal pulse, respectively, and L is the device length.

Additionally, the GVD and DS are evaluated by using Equations (3.14) and (3.17), respectively to examine the effects of pulse broadening.

6.4. Walk-Off Length and Output Pulse Width

The most critical point regarding the nonlinear fiber devices made of HNL glasses is the extremely high GVD. It is certain that high GVDs cause the serious problems of pulse walk-off and pulse broadening. To examine the effects caused by group-velocity mismatch, the walk-off length between the control and signal pulses for nonlinear fiber devices based on the optical Kerr effect, NOLMs, and ATCFs[Equation (6.15)] or between two different modes of the signal pulse for nonlinear fiber devices based on mode interference[Equation (6.16)] is estimated by

$$L_w = \frac{\tau \cdot c}{\left|n_{geff\_s} - n_{geff\_c}\right|} \tag{6.15}$$

$$L_w = \frac{\tau \cdot c}{\left| n_{geff\_01} - n_{geff\_02\ or\ 11} \right|} \tag{6.16}$$

where n_{geff_s} and n_{geff_c} are the group effective refractive indices of the signal and control pulses, respectively, n_{geff_01} and $n_{geff\_02\ or\ 11}$ are the group effective refractive indices of the LP_{01} and LP_{02}(or LP_{11}) modes of the signal pulse, respectively, τ is the initial pulse width, and c is the light velocity in vacuum.

Additionally, the propagation of the input pulse down the nonlinear fiber devices is simulated to observe the extent of pulse broadening caused by GVD. Since nonlinear fiber devices operate on the basis of nonlinear phenomena, both GVD and nonlinear effects should be considered to accurately simulate propagation of the input pulse. To this end, the nonlinear Schrödinger equation, which is the wave equation for a dispersive nonlinear medium and covers both linear and nonlinear properties of optical fibers, is used. Using the nonlinear Schrödinger equation, the effect of pulse distortion by SPM can also be accounted for. The nonlinear Schrödinger equation is expressed as

$$\frac{\partial A}{\partial z} + \beta_1 \frac{\partial A}{\partial t} + \frac{i}{2}\beta_2 \frac{\partial^2 A}{\partial t^2} - \frac{1}{6}\beta_3 \frac{\partial^3 A}{\partial t^3} = i\gamma \left| A \right|^2 A - \frac{\alpha}{2} A \tag{6.17}$$

where γ is the nonlinear parameter defined in Equation (1.10) and α is the fiber loss. In this equation, β_1, β_2, β_3, and γ account for the group velocity, GVD, DS, and nonlinearity, respectively. This equation is quite accurate for describing the evolution of optical pulses as short as 5ps. The input pulse width considered in the simulation is 10ps.

Furthermore, the extent of pulse broadening is also estimated by considering both GVD and PMD in the linear regime. Since polarization is a very critical factor in the performance of nonlinear fiber devices, in most devices, PMFs are used. Therefore, nonlinear fiber devices should have a high index difference between the two principal axes due to the high built-in

birefringence. Moreover, MSFs easily exhibit extremely high birefringence due to their structural properties. This high index difference leads to high PMD and thus spreading of the input pulse. Thus, it is useful to examine the extent of pulse broadening by high PMD and high GVD in nonlinear fiber devices. The output pulse width can be estimated by

$$\Delta t_{OUT}{}^2 = \Delta t_{IN}{}^2 + \delta t^2 \tag{6.18}$$

$$\delta t^2 = \delta t_{GVD}{}^2 + \delta t_{PMD}{}^2 \tag{6.19}$$

$$\delta t_{GVD}[ps] = L[Km] \times \delta\lambda[nm] + GVD[ps/nm \cdot Km] \tag{6.20}$$

$$\delta t_{PMD}[ps] = L[Km] \times PMD[ps/Km] \tag{6.21}$$

where Δt_{IN} is the initial input pulse width and δt is the factor representing the extent of pulse broadening by GVD(δt_{GVD}) and PMD(δt_{PMD}). For the estimation of the output pulse width Δt_{OUT}, 10ps transform limited pulse defined as

$$\Delta\nu \cdot \Delta t = 0.44 \tag{6.22}$$

is considered as the input pulse. In Equation (6.22), $\Delta\nu$ is the Full-Width at Half Maximum (FWHM) bandwidth and Δt is the FWHM pulses width. The almost maximum values of index differences δn of 10^{-4} and 10^{-3} are used for silica-clad fiber and MSF devices, respectively for the rigorous condition of evaluation.

6.5. Modal Solutions by Vector Wave Analysis

As previously described in Section 2.5, there are two ways for analyzing the mode distribution patterns of optical fibers. For the case of high index difference between the core and the cladding of optical fibers, vector wave analysis should be utilized. Therefore, the properties of the highly nonlinear fiber devices studied in this dissertation must be evaluated by the vector wave analysis for accurate results. It should be noted that although, in this dissertation, they have been referred to as LP_{01}, LP_{02}, and LP_{11} modes, strictly speaking, the LP_{01} and the LP_{02} modes are the HE_{11} and the HE_{12} modes, respectively, and the LP_{11} mode is the combination of either the nearly degenerate TE_{01} and HE_{21} modes or TM_{01} and HE_{21} modes. The solutions of the vector wave equation for fiber modes are described in Appendix in some detail

CHAPTER 7.
IMPACT OF HIGH-NONLINEARITY GLASSES ON NONLINEAR FIBER DEVICES

This chapter is devoted to describing the effects of the HNL glasses of litharge, bismite, tellurite, and chalcogenide glasses on the performance of highly nonlinear fiber devices based on the optical Kerr effect, NOLMs, ATCFs, or mode interference. The required device length, the required optical power, Effective Refractive Index(ERI), Group Effective Refractive Index(GERI), Relative Group Delay(RGD), Group-Velocity Dispersion(GVD), Dispersion Slope(DS), walk-off length, and output pulse width (pulse broadening) have been evaluated for individual nonlinear fiber devices made of HNL glass-core silica-clad fibers or HNL glass-core air-clad(microstructure) fibers.

As summarized in Chapter 5, HNL glass fibers with lower-index cladding have usually been fabricated using similar glasses with slightly different compositions for both the core and cladding. Moreover, chalcogenide glasses have never been used as cores in silica-clad fibers due to the high melting temperature difference between silica and chalcogenide glasses. Thus, it is useful to compare this type of devices with the two different types of devices described above. As a result, the required device length for individual nonlinear fiber devices made of such HNL glass-core HNL glass-clad fibers has also been evaluated using actual parameters of the specific fibers which were fabricated with litharge glasses[94], bismite glasses[112], tellurite glasses[156], and chalcogenide glasses[182].

7.1. Nonlinear Fiber Devices based on the Optical Kerr Effect

7.1.1. Required Device Length

This section provides the required device length for nonlinear fiber devices based on the optical Kerr effect. The required device length was calculated from Equation (6.1) with a control power of 1W for a nonlinear phase shift of π due to XPM. For all nonlinear fiber devices constructed with different glasses, the same normalized frequency V of 2.25 at 1.55μm was selected for reasonable comparison. Thus, the devices operate in a single-mode regime at wavelengths larger than 1.45μm. It is assumed that the wavelengths of the signal and control pulses are 1.55μm and 1.54μm, respectively.

For Nonlinear Fiber Devices based on the Optical Kerr Effect

$$\lambda_s = 1.55\mu m,\ \lambda_c = 1.54\mu m,\ P_c = 1W,\ V = 2.25(at\,1.55\mu m),\ \lambda_{cutoff} = 1.45\mu m$$

SILICA-CORE

$$n_{core} = 1.4554,\ N_2 = 2.5\times10^{-20}\,m^2/W\ \ at\,1.55\mu m$$

Silica-Clad Devices

$$n_{cladding} = 1.4441(at\,1.55\mu m),\ a = 3.07\mu m$$

$$n_{eff\_s} = 1.4496,\ n_{eff\_c} = 1.4497,\ A_{eff} = 37.67\mu m^2$$

$$L_\pi^{XPM} = \frac{\lambda_s A_{eff}}{3N_2P_c} = \frac{1.55\times10^{-6}\times37.67\times10^{-12}}{3\times2.5\times10^{-20}\times1} = 780[m]$$

Microstructure Devices

$$n_{cladding} = 1,\ a = 0.53\mu m$$

$$n_{eff\_s} = 1.1982,\ n_{eff\_c} = 1.2005,\ A_{eff} = 1.44\mu m^2$$

$$L_\pi^{XPM} = \frac{\lambda_s A_{eff}}{3N_2P_c} = \frac{1.55\times10^{-6}\times1.44\times10^{-12}}{3\times2.5\times10^{-20}\times1} = 30[m]$$

LITHARGE-CORE

$$n_{core} = 1.8017,\ N_2 = 40\times10^{-20}\,m^2/W\ \ at\,1.55\,\mu m$$

Silica-Clad Devices

$$n_{cladding} = 1.4441(at\,1.55\,\mu m),\ a = 0.52\,\mu m$$

$$n_{eff\_s} = 1.6087,\ n_{eff\_c} = 1.6103,\ A_{eff} = 1.21\,\mu m^2$$

$$L_{\pi}^{XPM} = \frac{\lambda_s A_{eff}}{3N_2 P_c} = \frac{1.55\times10^{-6}\times1.21\times10^{-12}}{3\times40\times10^{-20}\times1} = 1.56[m]$$

Microstructure Devices

$$n_{cladding} = 1,\ a = 0.37\,\mu m$$

$$n_{eff\_s} = 1.3186,\ n_{eff\_c} = 1.3234,\ A_{eff} = 0.88\,\mu m^2$$

$$L_{\pi}^{XPM} = \frac{\lambda_s A_{eff}}{3N_2 P_c} = \frac{1.55\times10^{-6}\times0.88\times10^{-12}}{3\times40\times10^{-20}\times1} = 1.14[m]$$

Litharge-Clad Devices

$$n_{core} = 1.774,\ n_{cladding} = 1.728,\ a = 1.38\,\mu m$$

$$n_{eff\_s} = 1.7504,\ n_{eff\_c} = 1.7506,\ A_{eff} = 7.70\,\mu m^2$$

$$L_{\pi}^{XPM} = \frac{\lambda_s A_{eff}}{3N_2 P_c} = \frac{1.55\times10^{-6}\times7.70\times10^{-12}}{3\times40\times10^{-20}\times1} = 9.95[m]$$

BISMITE-CORE

$$n_{core} = 2.1009,\ N_2 = 1000 \times 10^{-20}\, m^2/W \ \ at 1.55\,\mu m$$

Silica-Clad Devices

$$n_{cladding} = 1.4441 (at 1.55\,\mu m),\ a = 0.36\,\mu m$$

$$n_{eff\_s} = 1.7301,\ n_{eff\_c} = 1.7334,\ A_{eff} = 0.70\,\mu m^2$$

$$L_{\pi}^{XPM} = \frac{\lambda_s A_{eff}}{3 N_2 P_c} = \frac{1.55 \times 10^{-6} \times 0.70 \times 10^{-12}}{3 \times 1000 \times 10^{-20} \times 1} = 3.62[cm]$$

Microstructure Devices

$$n_{cladding} = 1,\ a = 0.30\,\mu m$$

$$n_{eff\_s} = 1.4058,\ n_{eff\_c} = 1.4132,\ A_{eff} = 0.66\,\mu m^2$$

$$L_{\pi}^{XPM} = \frac{\lambda_s A_{eff}}{3 N_2 P_c} = \frac{1.55 \times 10^{-6} \times 0.66 \times 10^{-12}}{3 \times 1000 \times 10^{-20} \times 1} = 3.41[cm]$$

Bismite-Clad Devices

$$n_{core} = 2.22,\ n_{cladding} = 2.13,\ a = 0.89\,\mu m$$

$$n_{eff\_s} = 2.1737,\ n_{eff\_c} = 2.1741,\ A_{eff} = 3.19\,\mu m^2$$

$$L_{\pi}^{XPM} = \frac{\lambda_s A_{eff}}{3 N_2 P_c} = \frac{1.55 \times 10^{-6} \times 3.19 \times 10^{-12}}{3 \times 1000 \times 10^{-20} \times 1} = 16.48[cm]$$

TELLURITE-CORE

$$n_{core} = 2.0278,\ N_2 = 148\times10^{-20}\,m^2/W\ \ at\,1.55\mu m$$

Silica-Clad Devices

$$n_{cladding} = 1.4441(at\,1.55\mu m),\ a = 0.39\mu m$$

$$n_{eff\_s} = 1.7017,\ n_{eff\_c} = 1.7046,\ A_{eff} = 0.77\mu m^2$$

$$L_{\pi}^{XPM} = \frac{\lambda_s A_{eff}}{3N_2 P_c} = \frac{1.55\times10^{-6}\times0.77\times10^{-12}}{3\times148\times10^{-20}\times1} = 26.88[cm]$$

Microstructure Devices

$$n_{cladding} = 1,\ a = 0.31\mu m$$

$$n_{eff\_s} = 1.3857,\ n_{eff\_c} = 1.3925,\ A_{eff} = 0.70\mu m^2$$

$$L_{\pi}^{XPM} = \frac{\lambda_s A_{eff}}{3N_2 P_c} = \frac{1.55\times10^{-6}\times0.70\times10^{-12}}{3\times148\times10^{-20}\times1} = 24.44[cm]$$

Tellurite-Clad Devices

$$n_{core} = 2.028,\ n_{cladding} = 1.983,\ a = 1.31\mu m$$

$$n_{eff\_s} = 2.0049,\ n_{eff\_c} = 2.0052,\ A_{eff} = 6.86\mu m^2$$

$$L_{\pi}^{XPM} = \frac{\lambda_s A_{eff}}{3N_2 P_c} = \frac{1.55\times10^{-6}\times6.86\times10^{-12}}{3\times148\times10^{-20}\times1} = 2.40[m]$$

CHALCOGENIDE-CORE

$$n_{core} = 2.7555,\ N_2 = 1250 \times 10^{-20} m^2/W\ \ at 1.55\mu m$$

Silica-Clad Devices

$$n_{cladding} = 1.4441 (at 1.55\mu m),\ a = 0.24\mu m$$

$$n_{eff\_s} = 1.9513,\ n_{eff\_c} = 1.9595,\ A_{eff} = 0.38\mu m^2$$

$$L_{\pi}^{XPM} = \frac{\lambda_s A_{eff}}{3N_2 P_c} = \frac{1.55 \times 10^{-6} \times 0.38 \times 10^{-12}}{3 \times 1250 \times 10^{-20} \times 1} = 1.57[cm]$$

Microstructure Devices

$$n_{cladding} = 1,\ a = 0.21\mu m$$

$$n_{eff\_s} = 1.5545,\ n_{eff\_c} = 1.5699,\ A_{eff} = 0.37\mu m^2$$

$$L_{\pi}^{XPM} = \frac{\lambda_s A_{eff}}{3N_2 P_c} = \frac{1.55 \times 10^{-6} \times 0.37 \times 10^{-12}}{3 \times 1250 \times 10^{-20} \times 1} = 1.53[cm]$$

Chalcogenide-Clad Devices

$$n_{core} = 2.6,\ n_{cladding} = 2.443,\ a = 0.62\mu m$$

$$n_{eff\_s} = 2.5188,\ n_{eff\_c} = 2.5195,\ A_{eff} = 1.60\mu m^2$$

$$L_{\pi}^{XPM} = \frac{\lambda_s A_{eff}}{3N_2 P_c} = \frac{1.55 \times 10^{-6} \times 1.60 \times 10^{-12}}{3 \times 1250 \times 10^{-20} \times 1} = 6.61[cm]$$

Table 7-1 summarizes the required device length with a control power of 1W for nonlinear fiber devices based on the optical Kerr effect when the signal pulse operates at 1.55μm and the control pulse operates at 1.54μm.

Table 7-1. The Required Device Length with 1W Control Power for Nonlinear Fiber Devices based on the Optical Kerr Effect (Signal at 1.55μm and Control at 1.54μm)

Device Length[m]	Silica	Litharge	Bismite	Tellurite	Chalcogenide
Silica-Cladding	780	1.56	0.0362	0.2688	0.0157
MSF	30	1.14	0.0341	0.2444	0.0153
HNL Glass-Cladding	-	9.95	0.1648	2.40	0.0661

7.1.2. Relative Group Delay, Group-Velocity Dispersion, and Dispersion Slope

This section provides the Effective Refractive Index(ERI), the Group Effective Refractive Index(GERI), the Group-Velocity Dispersion(GVD), and the Dispersion Slope(DS) of the devices. In addition, the Effective Mode Area(EMA) and the Required Device Length(RDL), which vary according to the signal and control wavelengths, are provided with the signal pulse fixed at 1.55μm for control pulses at different wavelengths. Furthermore, graphs of the Relative Group Delay(RGD) between the signal wavelength fixed at 1.55μm and different control wavelengths for the different required device lengths.

SILICA-CORE

$$n_{core} = slightly\ GeO_2 - doped\ \ silica$$

Silica-Clad Devices

$$n_{cladding} = silica,\ a = 3.07\,\mu m$$

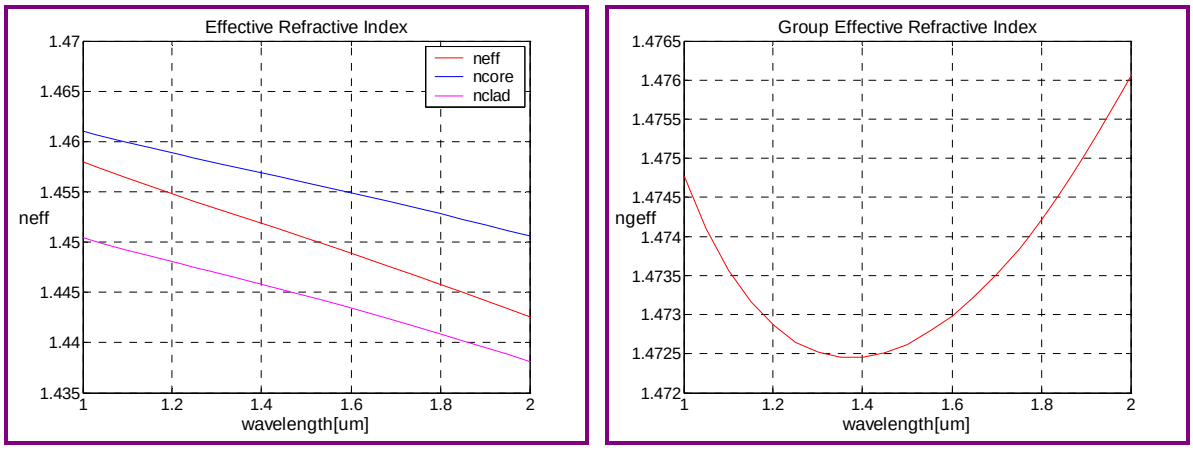

Figure 7-1. ERI and GERI of Silica-Core Silica-Clad Devices

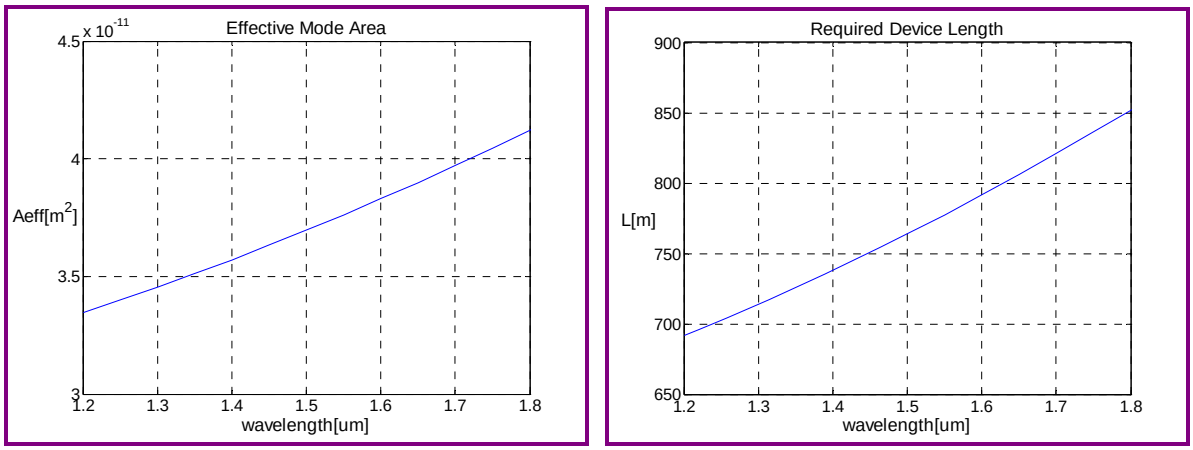

Figure 7-2. EMA and RDL of Silica-Core Silica-Clad Devices

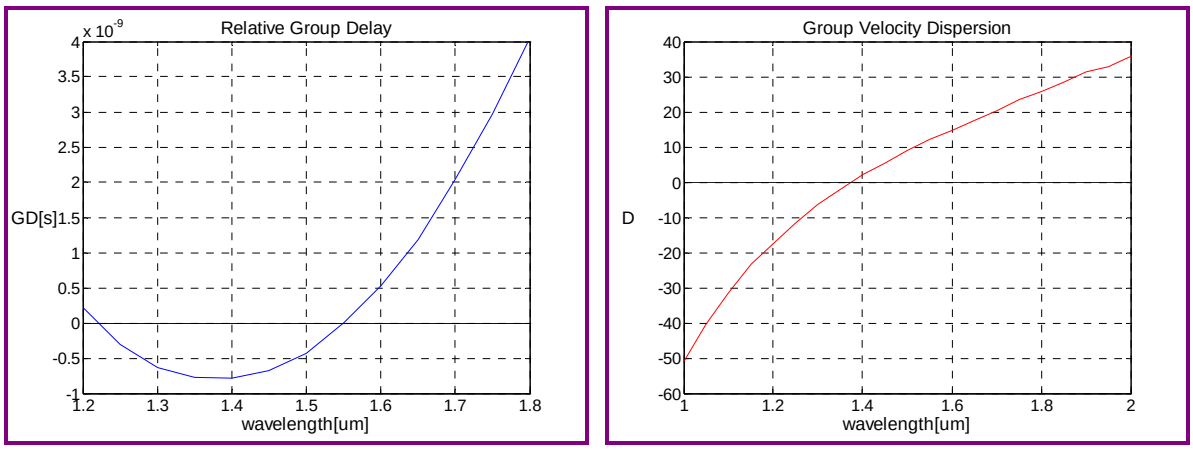

Figure 7-3. RGD and GVD of Silica-Core Silica-Clad Devices

The RGD between the signal pulse at 1.55μm and the control pulse at 1.54μm for the required device length of 780m is 78ps, the GVD at 1.55μm is 12[ps/nm-km], and the DS at 1.55μm is 0.057[ps/nm^2-km].

Microstructure Devices

$$n_{cladding} = air,\ a = 0.53\mu m$$

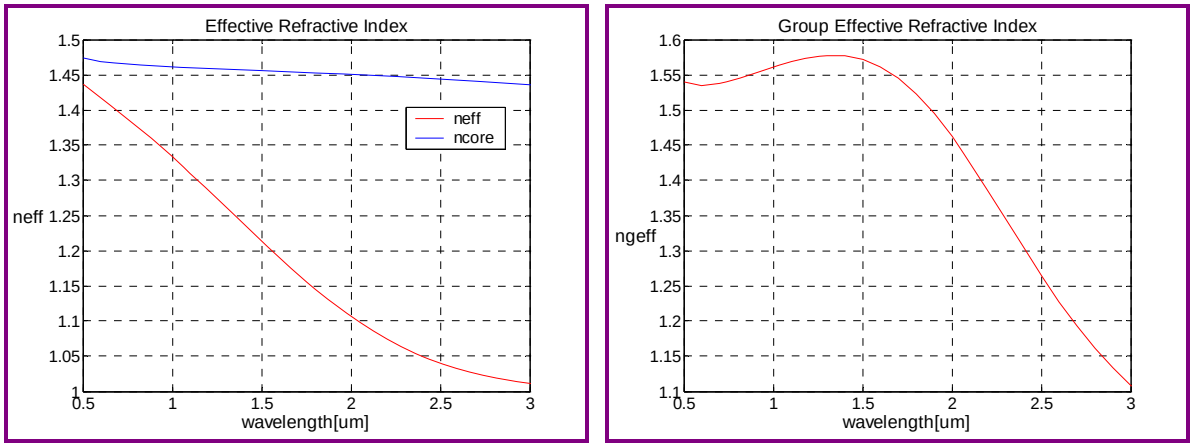

Figure 7-4. ERI and GERI of Silica-Core Microstructure Devices

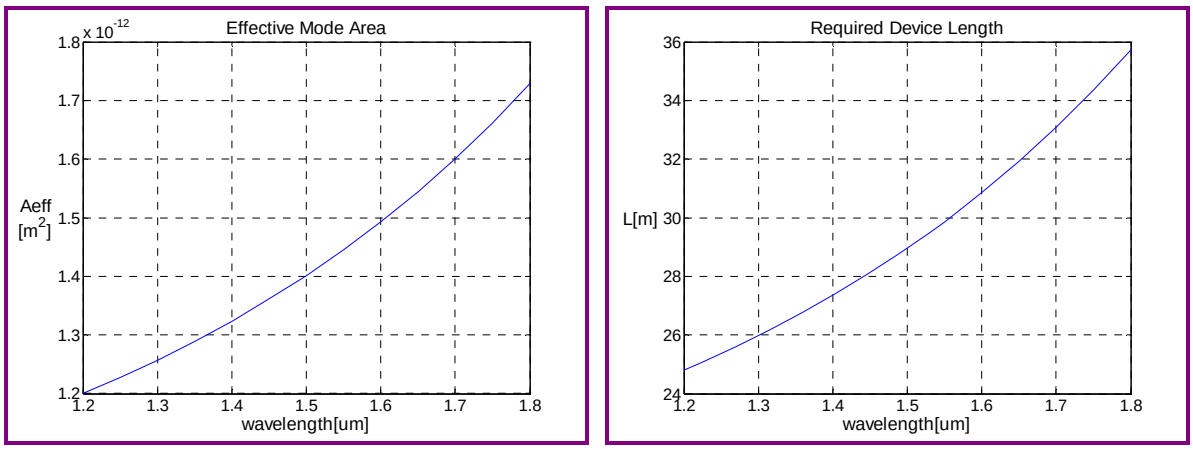

Figure 7-5. EMA and RDL of Silica-Core Microstructure Devices

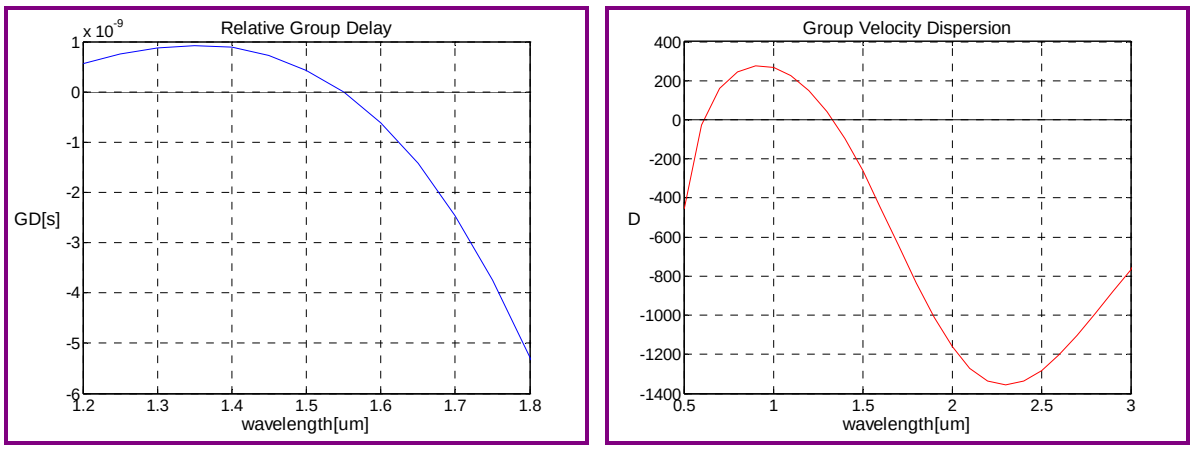

Figure 7-6. RGD and GVD of Silica-Core Microstructure Devices

The RGD between the signal pulse at 1.55μm and the control pulse at 1.54μm for the required device length of 30m is 110ps, the GVD at 1.55μm is -355[ps/nm-km], and the DS at 1.55μm is -1.836[ps/nm^2-km].

LITHARGE-CORE

$$n_{core} = SF57$$

Silica-Clad Devices

$$n_{cladding} = silica,\ a = 0.52\mu m$$

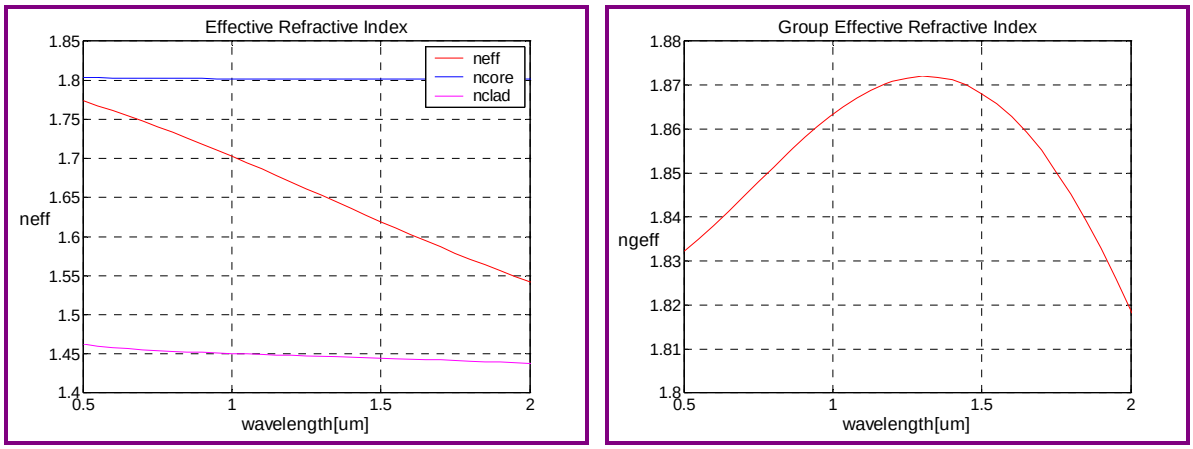

Figure 7-7. ERI and GERI of Litharge-Core Silica-Clad Devices

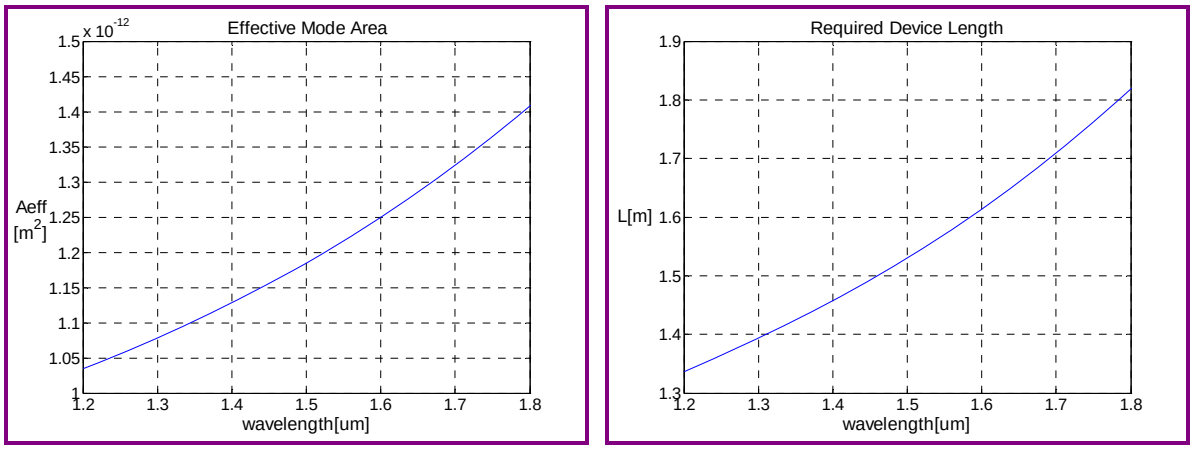

Figure 7-8. EMA and RDL of Litharge-Core Silica-Clad Devices

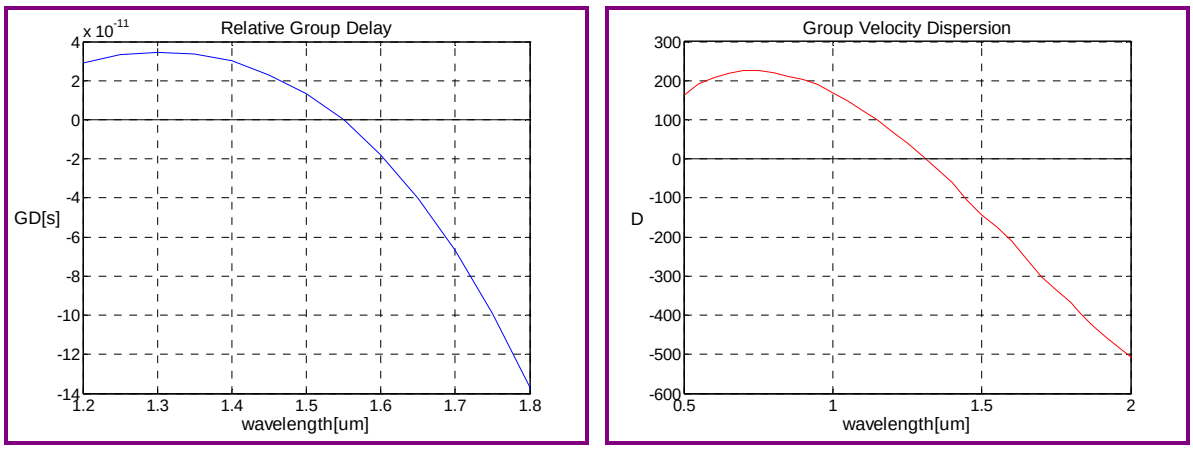

Figure 7-9. RGD and GVD of Litharge-Core Silica-Clad Devices

The RGD between the signal pulse at 1.55μm and the control pulse at 1.54μm for the required device length of 1.56m is 2.50ps, the GVD at 1.55μm is -174[ps/nm-km], and the DS at 1.55μm is -0.676[ps/nm^2-km].

Microstructure Devices

$$n_{cladding} = air,\ a = 0.37\,\mu m$$

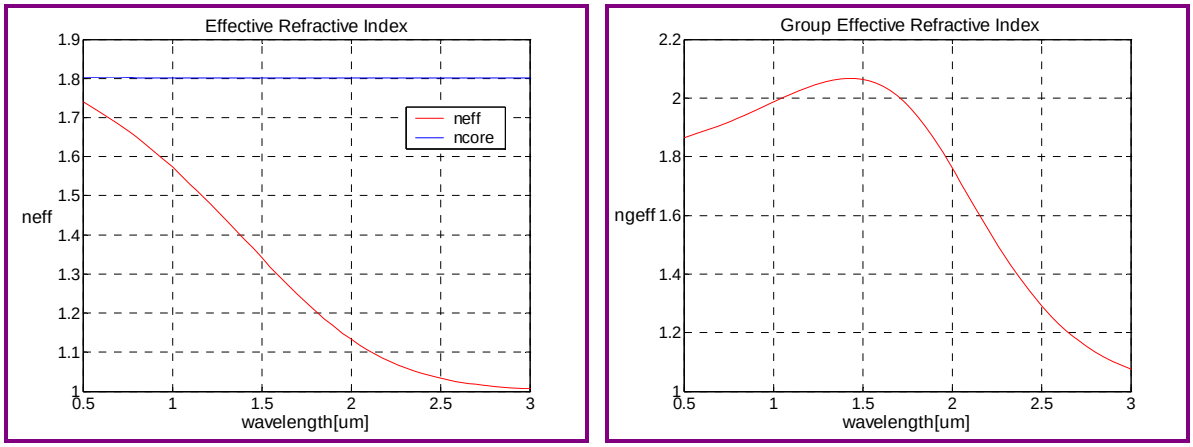

Figure 7-10. ERI and GERI of Litharge-Core Microstructure Devices

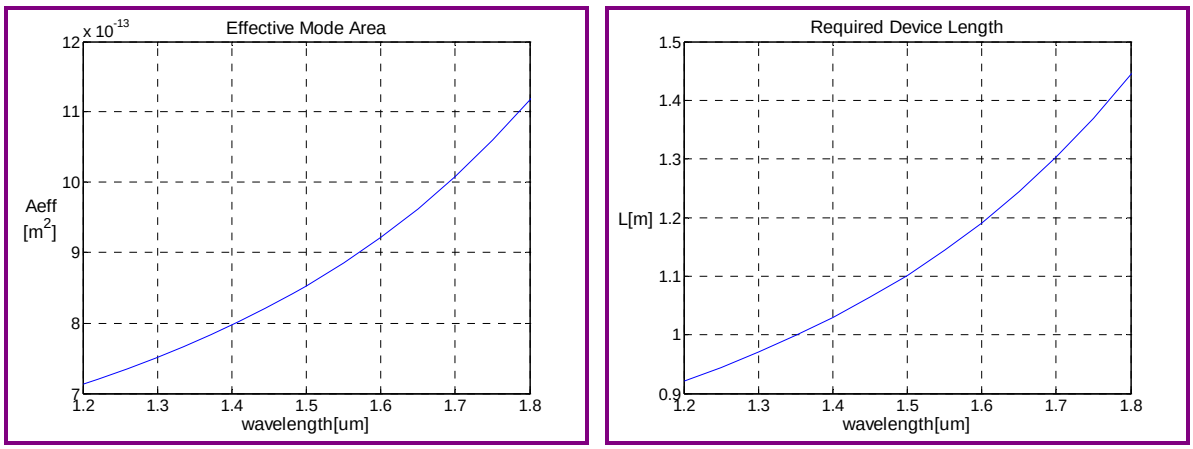

Figure 7-11. EMA and RDL of Litharge-Core Microstructure Devices

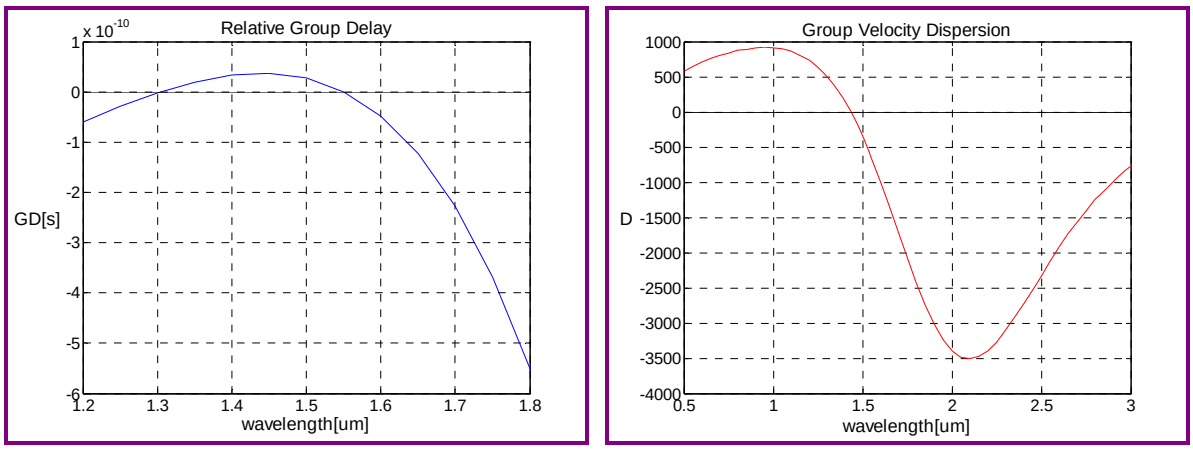

Figure 7-12. RGD and GVD of Litharge-Core Microstructure Devices

The RGD between the signal pulse at 1.55μm and the control pulse at 1.54μm for the required device length of 1.14m is 5.32ps, the GVD at 1.55μm is -653[ps/nm-km], and the DS at 1.55μm is -6.356[ps/nm^2-km].

BISMITE-CORE

$$n_{core} = 55Bi_2O_3 \cdot 45B_2O_3$$

Silica-Clad Devices

$$n_{cladding} = silica,\ a = 0.36\mu m$$

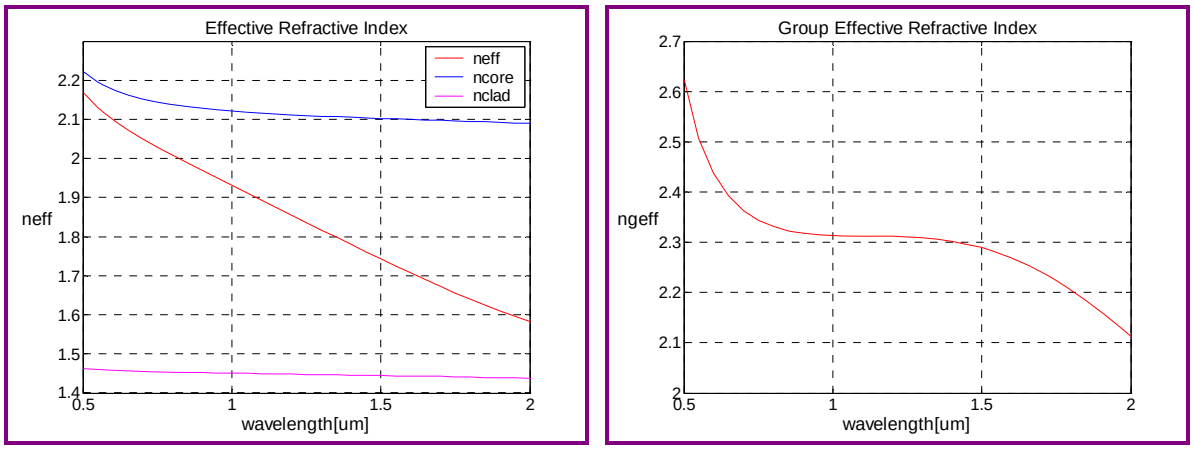

Figure 7-13. ERI and GERI of Bismite-Core Silica-Clad Devices

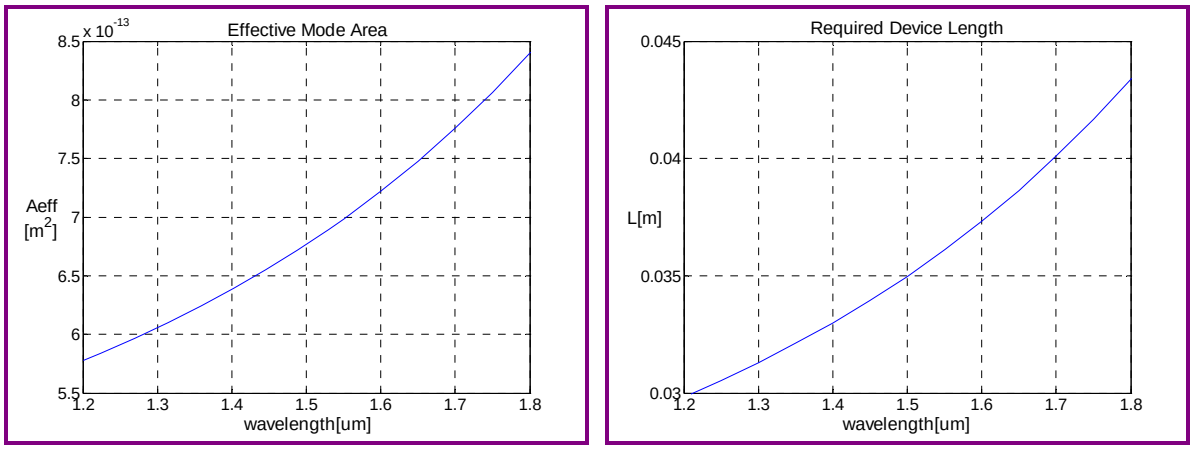

Figure 7-14. EMA and RDL of Bismite-Core Silica-Clad Devices

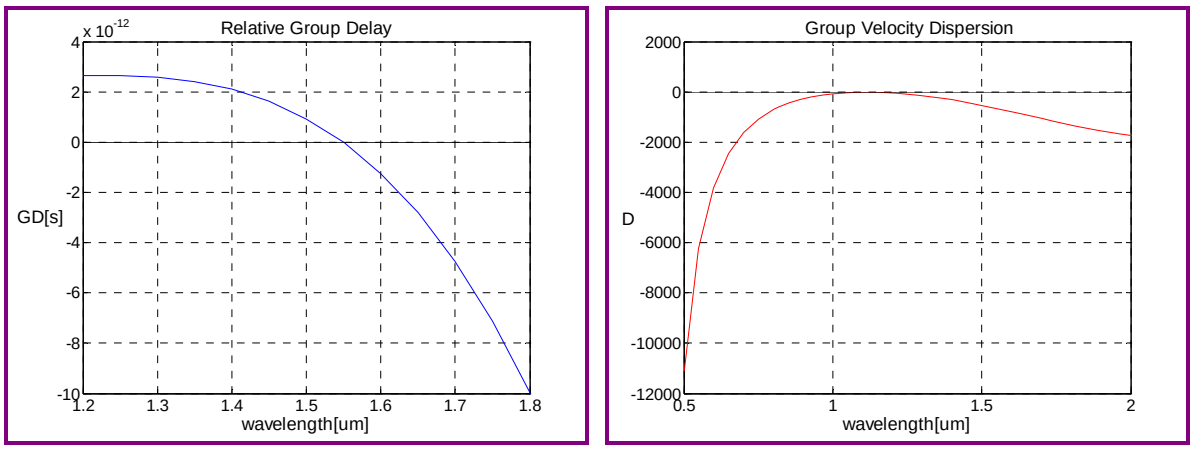

Figure 7-15. RGD and GVD of Bismite-Core Silica-Clad Devices

The RGD between the signal pulse at 1.55μm and the control pulse at 1.54μm for the required device length of 0.0362m is 0.22ps, the GVD at 1.55μm is -667[ps/nm-km], and the DS at 1.55μm is -2.549[ps/nm^2-km].

Microstructure Devices

$$n_{cladding} = air,\ a = 0.30\mu m$$

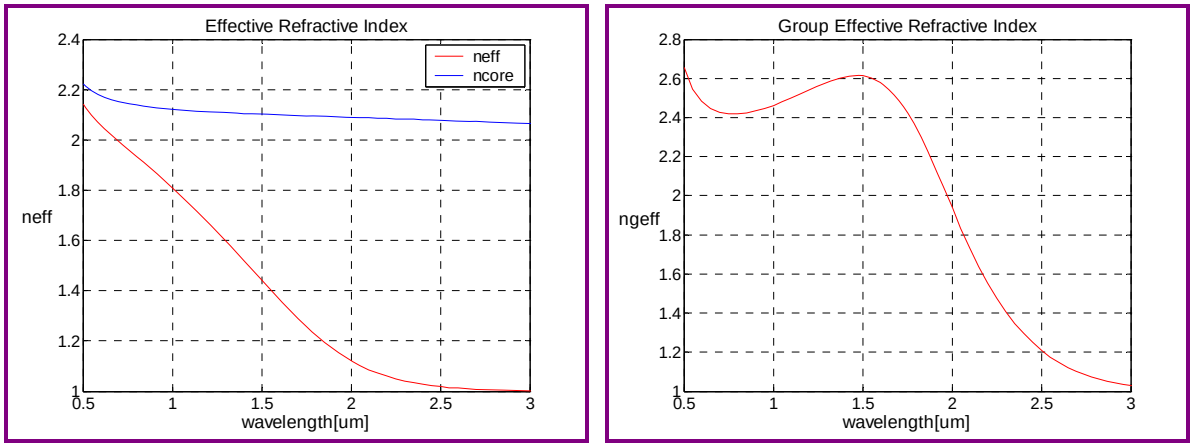

Figure 7-16. ERI and GERI of Bismite-Core Microstructure Devices

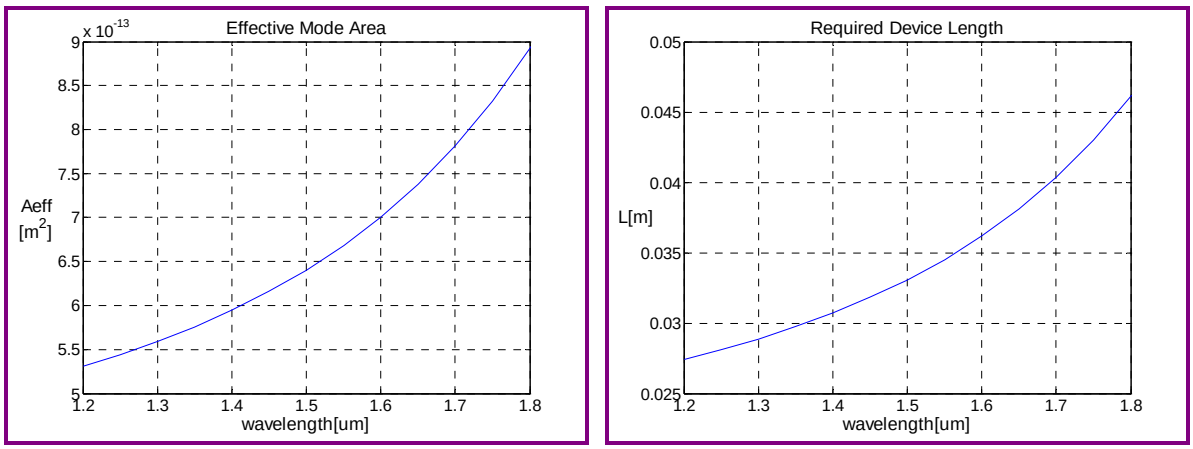

Figure 7-17. EMA and RDL of Bismite-Core Microstructure Devices

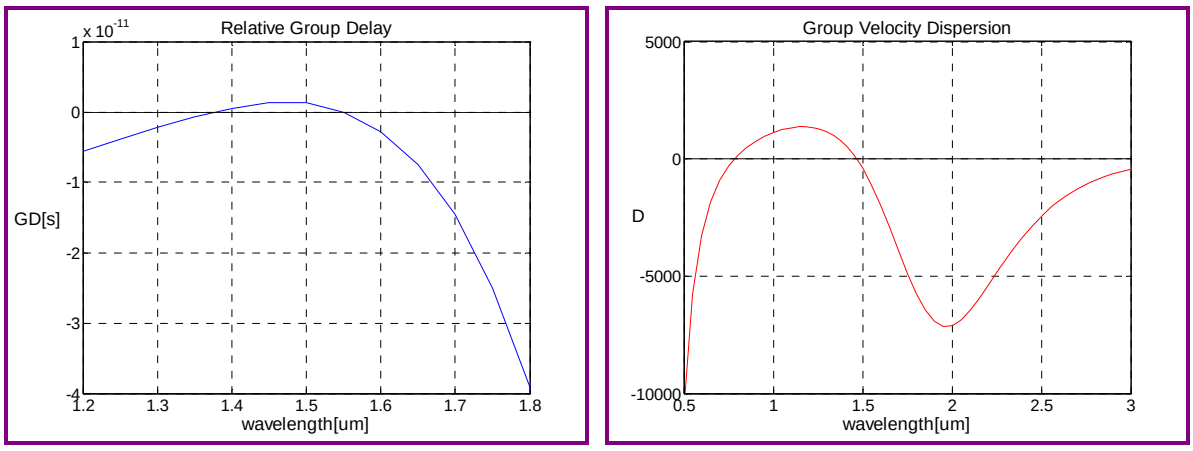

Figure 7-18. RGD and GVD of Bismite-Core Microstructure Devices

The RGD between the signal pulse at 1.55μm and the control pulse at 1.54μm for the required device length of 0.0341m is 0.25ps, the GVD at 1.55μm is -1110[ps/nm-km], and the DS at 1.55μm is -15.537[ps/nm^2-km].

TELLURITE-CORE

$$n_{core} = 75TeO_2 \cdot 25ZnO$$

Silica-Clad Devices

$$n_{cladding} = silica,\ a = 0.39\mu m$$

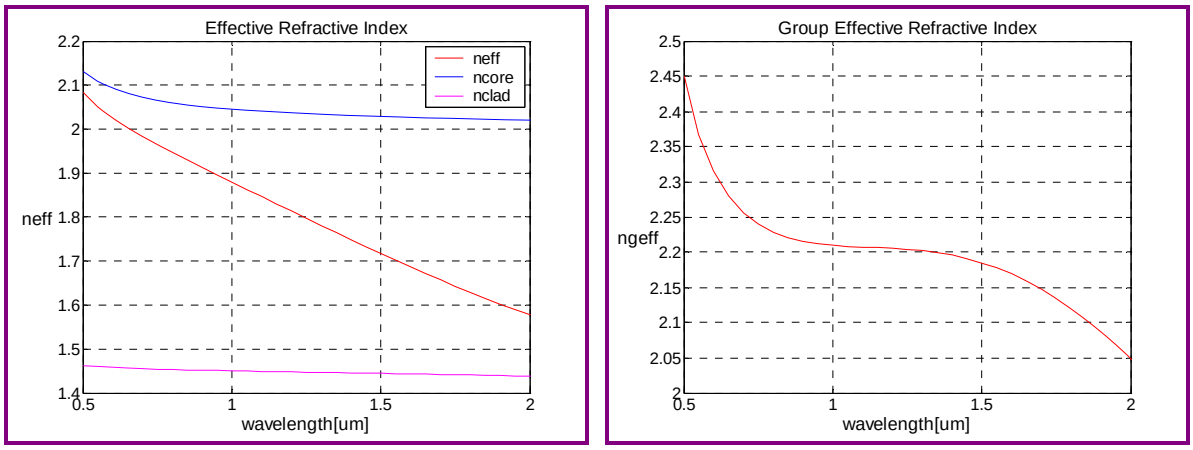

Figure 7-19. ERI and GERI of Tellurite-Core Silica-Clad Devices

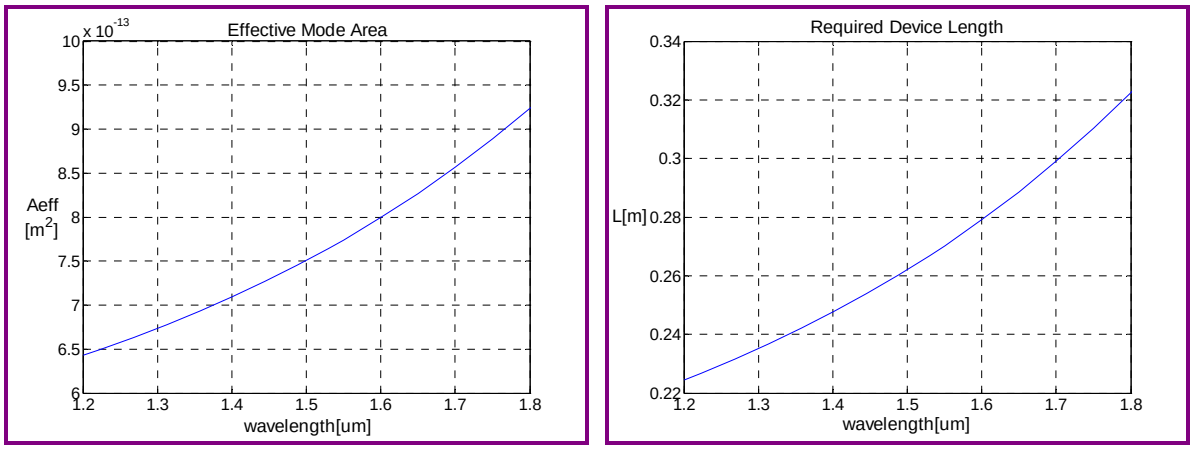

Figure 7-20. EMA and RDL of Tellurite-Core Silica-Clad Devices

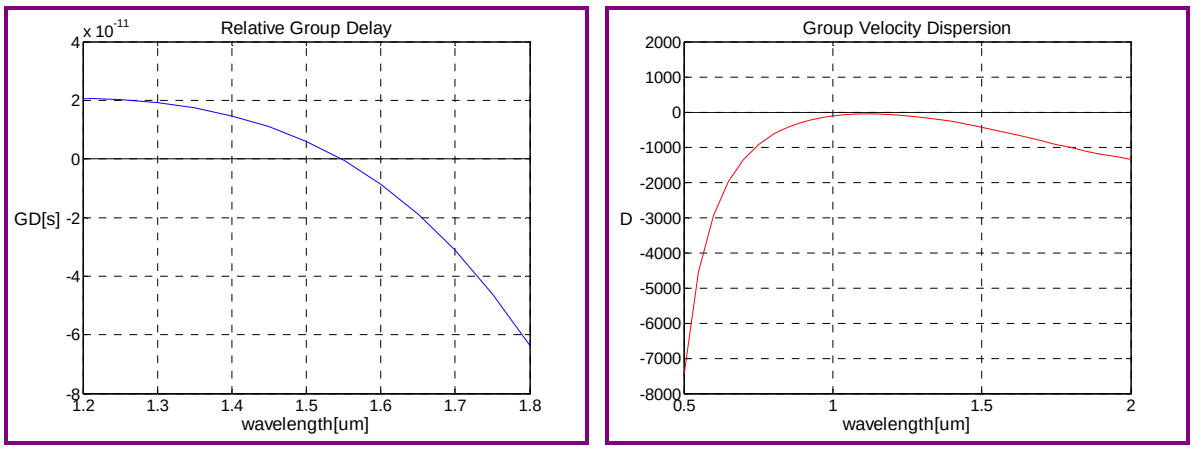

Figure 7-21. RGD and GVD of Tellurite-Core Silica-Clad Devices

The RGD between the signal pulse at 1.55μm and the control pulse at 1.54μm for the required device length of 0.2688m is 1.25ps, the GVD at 1.55μm is -529[ps/nm-km], and the DS at 1.55μm is -1.865[ps/nm^2-km].

Microstructure Devices

$$n_{cladding} = air,\ a = 0.31\mu m$$

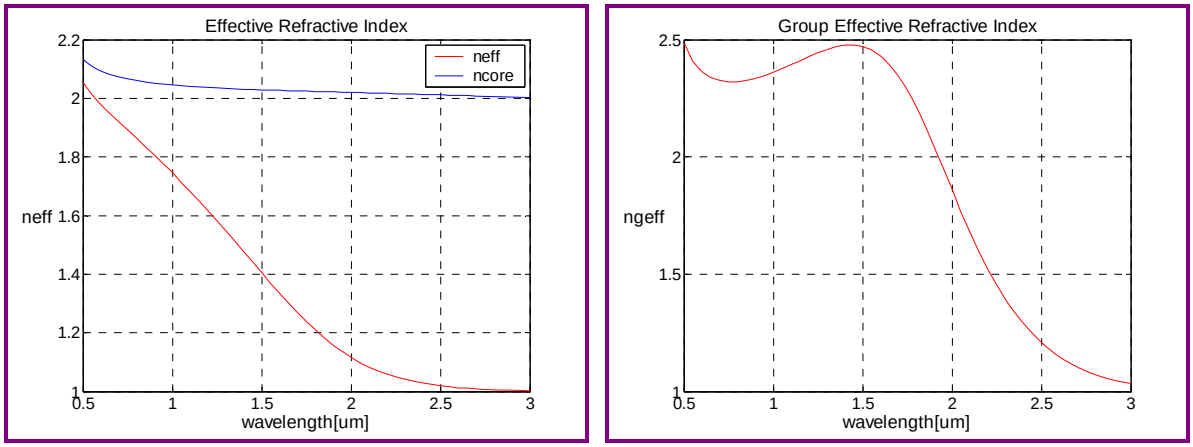

Figure 7-22. ERI and GERI of Tellurite-Core Microstructure Devices

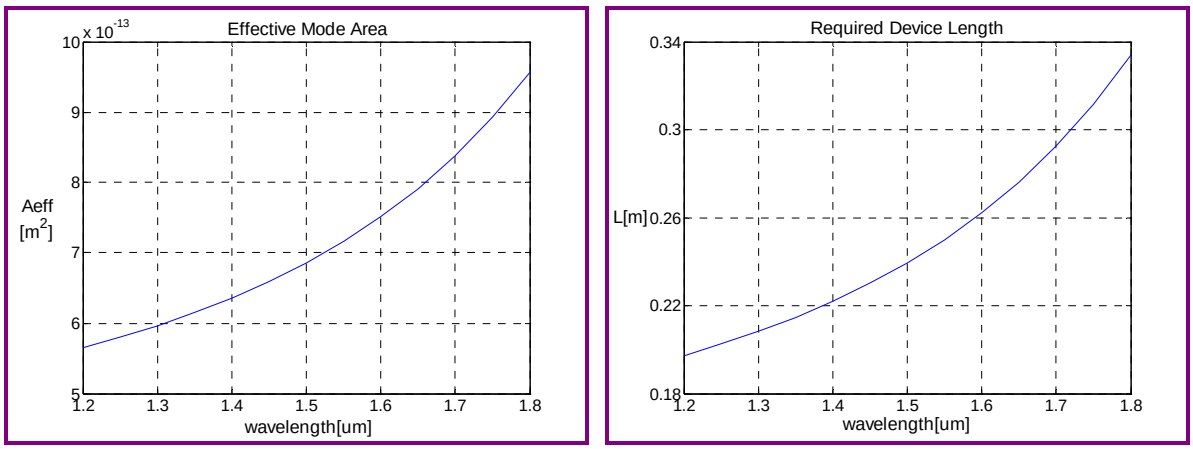

Figure 7-23. EMA and RDL of Tellurite-Core Microstructure Devices

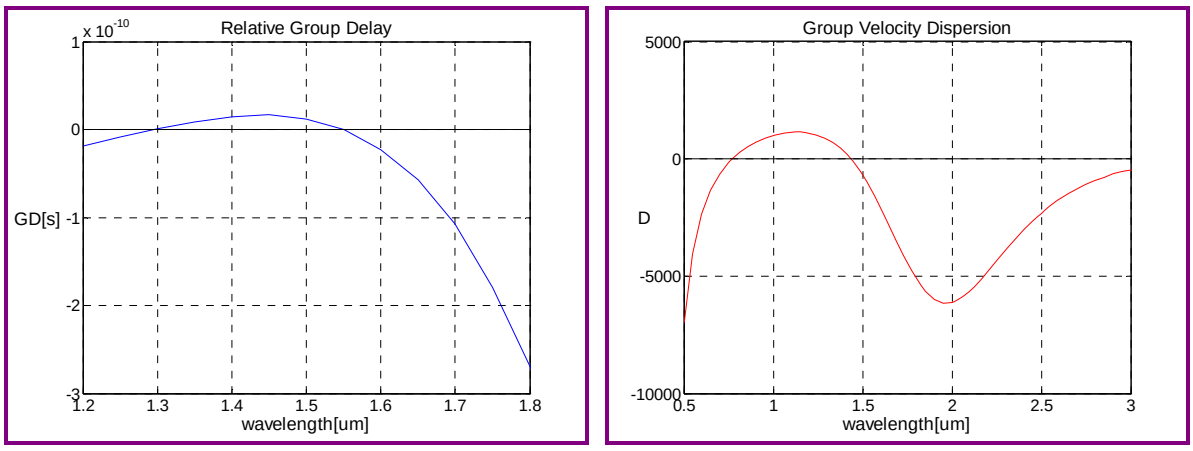

Figure 7-24. RGD and GVD of Tellurite-Core Microstructure Devices

The RGD between the signal pulse at 1.55μm and the control pulse at 1.54μm for the required device length of 0.2444m is 2.44ps, the GVD at 1.55μm is -1329[ps/nm-km], and the DS at 1.55μm is -13.665[ps/nm^2-km].

CHALCOGENIDE-CORE

$$n_{core} = 40As \cdot 60Se$$

Silica-Clad Devices

$$n_{cladding} = silica,\ a = 0.24\mu m$$

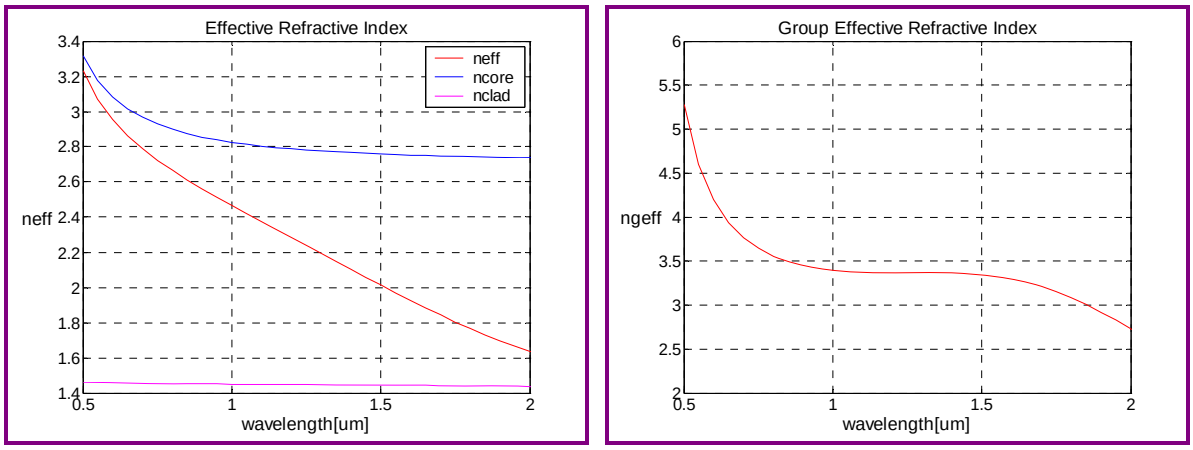

Figure 7-25. ERI and GERI of Chalcogenide-Core Silica-Clad Devices

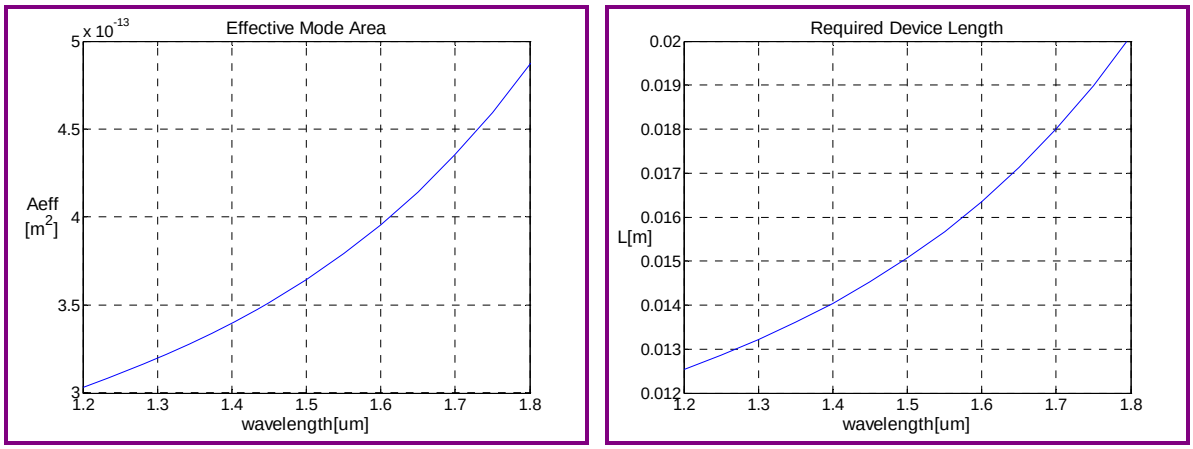

Figure 7-26. EMA and RDL of Chalcogenide-Core Silica-Clad Devices

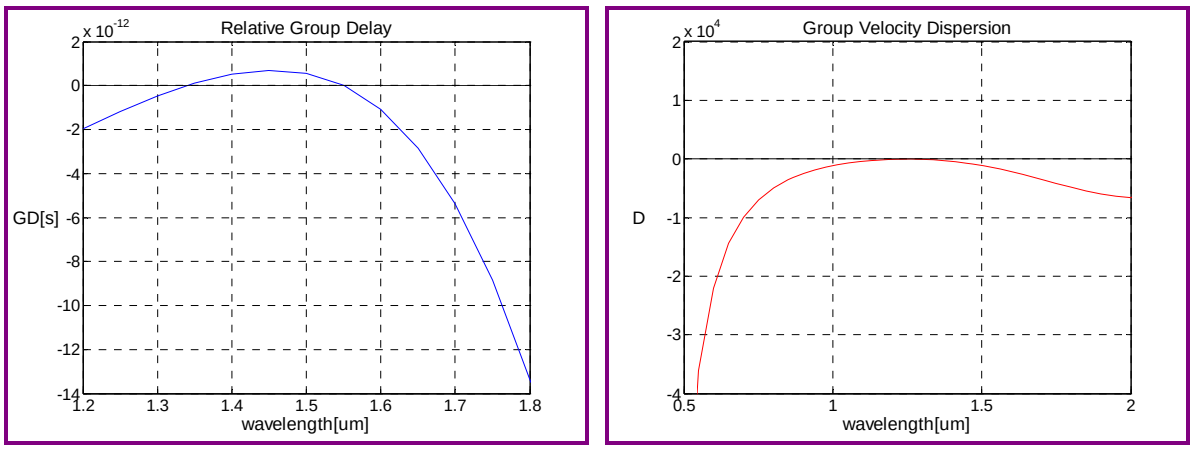

Figure 7-27. RGD and GVD of Chalcogenide-Core Silica-Clad Devices

The RGD between the signal pulse at 1.55μm and the control pulse at 1.54μm for the required device length of 0.0157m is 0.20ps, the GVD at 1.55μm is -1590[ps/nm-km], and the DS at 1.55μm is -10.602[ps/nm^2-km].

Microstructure Devices

$$n_{cladding} = air,\ a = 0.21\mu m$$

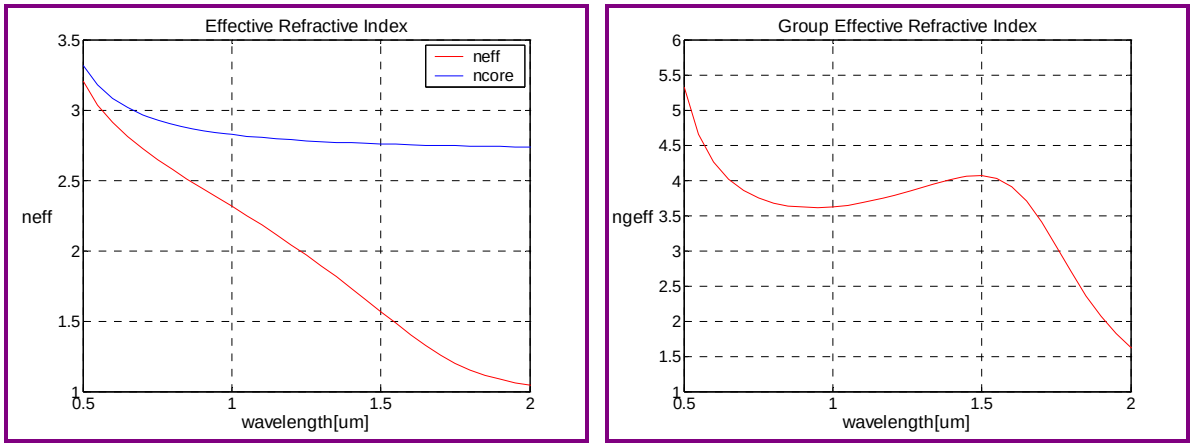

Figure 7-28. ERI and GERI of Chalcogenide-Core Microstructure Devices

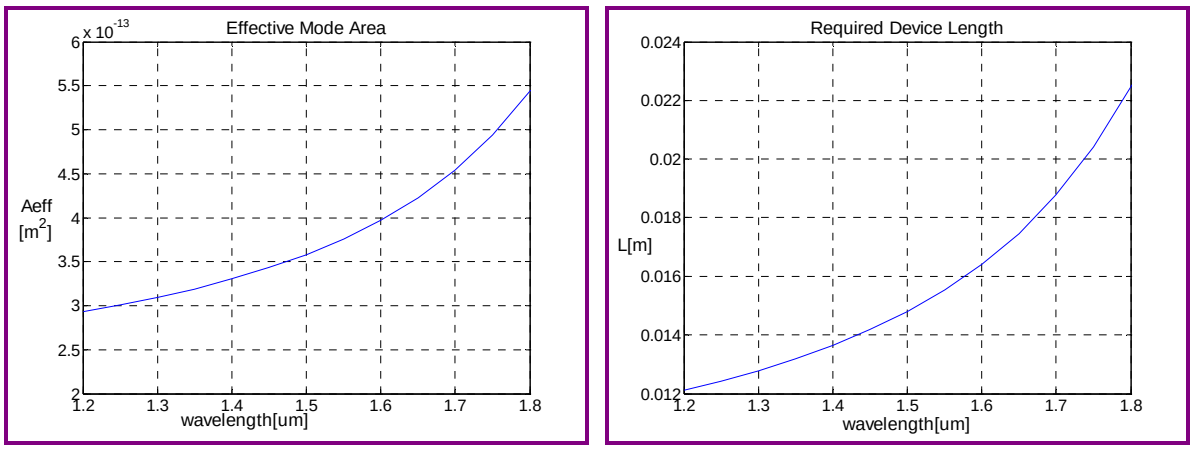

Figure 7-29. EMA and RDL of Chalcogenide-Core Microstructure Devices

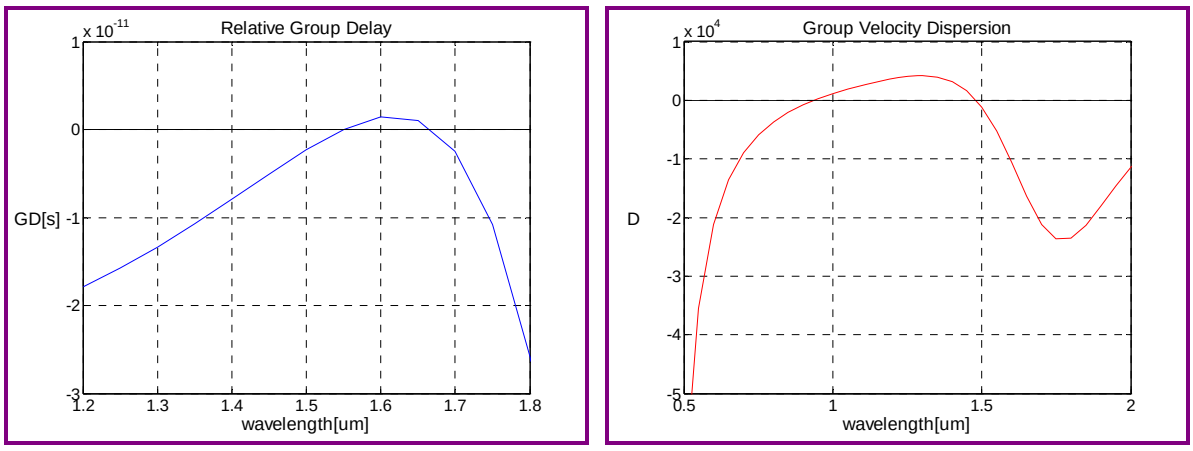

Figure 7-30. RGD and GVD of Chalcogenide-Core Microstructure Devices

The RGD between the signal pulse at 1.55μm and the control pulse at 1.54μm for the required device length of 0.0153m is 0.44ps, the GVD at 1.55μm is -5316[ps/nm-km], and the DS at 1.55μm is -95[ps/nm^2-km].

Table 7-2 summarizes the RGD, calculated from Equation (6.13), between the signal pulse at 1.55μm and the control pulse at 1.54μm for the required device length shown in Table 7-1, the GVD at 1.55μm, and the DS at 1.55μm for nonlinear fiber devices based on the optical Kerr effect.

Table 7-2. RGD between Signal at 1.55μm and Control at 1.54μm, GVD at 1.55μm, and DS at 1.55μm for Nonlinear Fiber Devices based on the Optical Kerr Effect

Properties		Silica	Litharge	Bismite	Tellurite	Chalcogenide
RGD [ps]	Silica-Cladding	78	2.50	0.22	1.25	0.20
	MSF	110	5.32	0.25	2.44	0.44
GVD [ps/nm-km] at 1.55μm	Silica-Cladding	12	-174	-667	-529	-1590
	MSF	-355	-653	-1110	-1329	-5316
DS [ps/nm^2-km] at 1.55μm	Silica-Cladding	0.057	-0.676	-2.549	-1.865	-10.602
	MSF	-1.836	-6.356	-15.537	-13.665	-95

This consideration of the control pulse at 1.54μm with the signal pulse at 1.55μm is the best case. A reasonable comparison between the different glasses would be to evaluate the RGD for a worst case in the applicable wavelength range. For example, in Figure 7-3, the range for control wavelengths would be between 1.22μm and 1.55μm for the silica-core silica-clad devices. In the range, the worst case is when the control pulse is at 1.4μm. At this control wavelength, the RGD is 782ps. Similar evaluations from Figures 7-6, 7-9, 7-12, 7-15, 7-18, 7-21, 7-24, 7-27, and 7-30 were performed for the different types of devices. Table 7-3 presents the RGD between the signal pulse at 1.55μm and the control pulse at different wavelengths of the worse case for the required device lengths at different control wavelengths.

Table 7-3. RGD between Signal at 1.55μm and Control at Different Wavelengths for Nonlinear Fiber Devices based on the Optical Kerr Effect

Properties		Silica	Litharge	Bismite	Tellurite	Chalcogenide
Control Wavelength [μm]	Silica-Cladding	1.40	1.30	1.22	1.04	1.45
	MSF	1.35	1.45	1.48	1.45	1.60
RDL at Control Wavelength [m]	Silica-Cladding	738	1.39	0.0301	0.2102	0.0145
	MSF	27	1.06	0.0326	0.2301	0.0164
RGD [ps]	Silica-Cladding	782	34.61	2.65	21.56	0.69
	MSF	917	36.86	1.31	16.64	1.45

7.1.3. Walk-Off Length and Output Pulse Width

Table 7-4 presents the walk-off length, calculated from Equation (6.15), between the signal pulse at 1.55μm and the control pulse at 1.54μm with 10ps pulse width for nonlinear fiber devices based on the optical Kerr effect.

Table 7-4. Walk-Off Length between Signal at 1.55μm and Control at 1.54μm with 10ps Pulse Width for Nonlinear Fiber Devices based on the Optical Kerr Effect

Walk-Off Length [m]	Silica	Litharge	Bismite	Tellurite	Chalcogenide
Silica-Cladding	100	6	1.67	2.14	0.77
MSF	3	2.14	1.36	1	0.34

Table 7-5 presents the walk-off length, between the signal pulse at 1.55μm and the control pulse at different wavelengths of the worse case, shown in Table 7-3, with 10ps pulse width.

Table 7-5. Walk-Off Length between Signal at 1.55μm and Control at Different Wavelengths with 10ps Pulse Width for Nonlinear Fiber Devices based on the Optical Kerr Effect

Walk-Off Length [m]	Silica	Litharge	Bismite	Tellurite	Chalcogenide
Silica-Cladding	9.44	0.40	0.11	0.10	0.21
MSF	0.29	0.29	0.25	0.13	0.11

Table 7-6 shows the output control pulse width for nonlinear fiber devices based on the optical Kerr effect simulated using the nonlinear Schrödinger equation for the input control pulse at 1.54μm with 10ps pulse width and 1W peak power.

Table 7-6. Output Control Pulse Width by the Nonlinear Schrödinger Equation for Nonlinear Fiber Devices based on the Optical Kerr Effect

Pulse Width [ps]	Silica	Litharge	Bismite	Tellurite	Chalcogenide
Silica-Cladding	16.1420	10.1053	10.0787	10.0981	10.0686
MSF	15.4628	10.0943	10.0695	10.0762	10.0357

Table 7-7 presents the output control pulse width for nonlinear fiber devices based on the optical Kerr effect calculated from Equations (6.18)-(6.21) with the consideration of both GVD and PMD for a 10ps transform limited input pulse at 1.54μm. The spectral width $\delta\lambda$ for this input pulse calculated from Equation (6.22) is 0.348nm and the index differences δn used are 10^{-4} and 10^{-3} for silica-clad fiber and MSF devices, respectively

Table 7-7. Output Control Pulse Width by GVD and PMD
for Nonlinear Fiber Devices based on the Optical Kerr Effect

Output Pulse Width [ps]	**Silica**		**Litharge**		**Bismite**		**Tellurite**		**Chalcogenide**	
	Si-C	MSF	Si-C	MSF	Si-C	MSF	Si-C	MSF	Si-C	MSF
P[W]	**Device Length[m]**									
1	780	30	1.56	1.14	0.0362	0.0341	0.2688	0.2444	0.0157	0.0153
0.1	1560	60	3.12	2.28	0.0724	0.0682	0.5376	0.4888	0.0314	0.0306
0.01	7800	300	15.6	11.4	0.362	0.3410	2.688	2.444	0.157	0.153
δn	10^{-4}	10^{-3}	10^{-4}	10^{-3}	10^{-4}	10^{-3}	10^{-4}	10^{-3}	10^{-4}	10^{-3}
PMD[ps/m]	0.333	3.333	0.333	3.333	0.333	3.333	0.333	3.333	0.333	3.333
P[W]	**δt_{PMD}[ps] = PMD[ps/m] × L[m]**									
1	260	100	0.52	3.8	0.012	0.114	0.09	0.815	0.005	0.051
0.1	520	200	1.04	7.6	0.024	0.227	0.179	1.629	0.01	0.102
0.01	2600	1000	5.2	38	0.121	1.137	0.896	8.147	0.052	0.51
GVD	**11.6**	**-336**	**-168**	**-653**	**-642**	**-968**	**-511**	**-1200**	**-1491**	**-4486**
δλ[nm]	**0.348**									
P[W]	**δt_{GVD}[ps] = L[Km] × δλ[nm] × GVD[ps/nm-Km]**									
1	3.15	-3.51	-0.09	-0.26	-0.01	-0.01	-0.05	-0.10	-0.01	-0.02
0.1	6.30	-7.02	-0.18	-0.52	-0.02	-0.02	-0.10	-0.20	-0.02	-0.05
0.01	31.49	-35.08	-0.91	-2.59	-0.08	-0.11	-0.48	-1.02	-0.08	-0.24
P[W]	**δt^2[ps] = δt_{GVD}^2[ps] + δt_{PMD}^2[ps]**									
1	260	100	0.528	3.809	0.015	0.114	0.102	0.821	0.010	0.056
0.1	520	200	1.056	7.618	0.029	0.228	0.203	1.642	0.019	0.113
0.01	2600	1000	5.279	38.088	0.145	1.142	1.016	8.210	0.097	0.563
P[W]	**Δt_{OUT}^2[ps] = Δt_{IN}^2[ps] + δt^2[ps]**									
1	**260**	**100**	**10.01**	**10.70**	**10.00**	**10.00**	**10.00**	**10.03**	**10.00**	**10.00**
0.1	**520**	**200**	**10.06**	**12.57**	**10.00**	**10.00**	**10.00**	**10.13**	**10.00**	**10.00**
0.01	**2600**	**1000**	**11.31**	**39.38**	**10.00**	**10.07**	**10.05**	**12.94**	**10.00**	**10.02**

7.1.4. All-Optical Kerr Wavelength-Division Demultiplexers

In the application to demultiplexers, the optical Kerr effect has been used only for optical time-division-multiplexed signals. In this dissertation, a new scheme of wavelength-division demultiplexing based on the optical Kerr effect has been proposed for the first time[5]. As shown in the previous results, highly nonlinear fiber devices using HNL glasses have extremely high GVD which causes pulse walk-off between the control and signal pulses due to group-velocity mismatch. The new scheme utilizes this extremely high GVD to easily separate the control pulse and undesired signal pulses. To confirm the reliability of the scheme, a calculation has been performed using a MSF constructed with S-LAH79(Ohara Glass) glass. It was found that a specific signal pulse separated in wavelength by 0.8nm(ITU Standard) can be selectively demultiplexed by a 10ps control pulse in just 2m propagation distance.

Figure 7-31 shows the refractive index of S-LAH79 glass and the ERI of the all-optical Kerr wavelength-division demultiplexer.

S-LAH79 Glass-Core Microstructure Devices

$$V = 1.84\,(at\,1.55\,\mu m),\ \lambda_{cutoff} = 1.2\,\mu m,\ a = 0.27\,\mu m$$

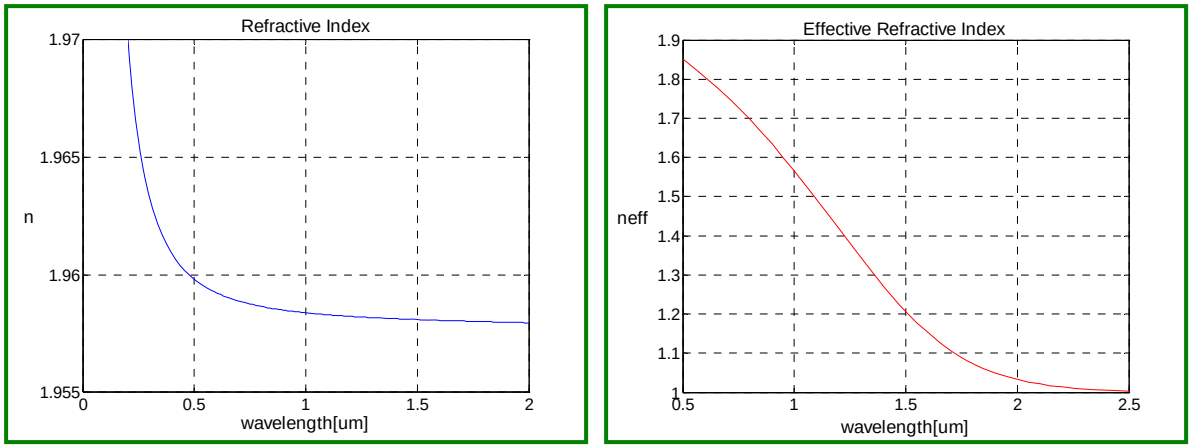

Figure 7-31. R/Index of SLAH-79 and ERI of Kerr Wavelength-Division Demultiplexers

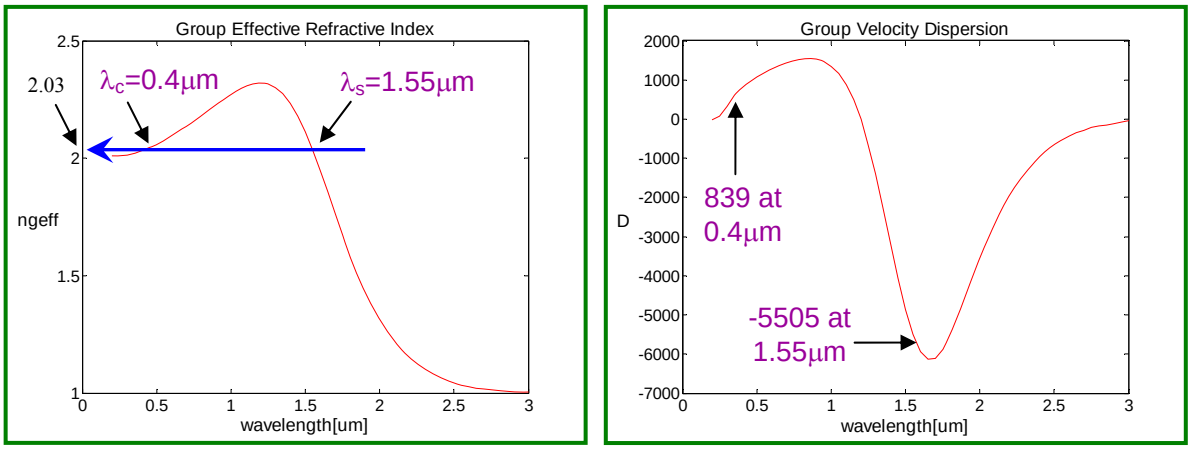

Figure 7-32. GERI and GVD of Optical Kerr Wavelength-Division Demultiplexers

Figure 7-32 shows the GERI and the GVD of the all-optical Kerr wavelength-division demultiplexer as a function of wavelength. As shown in the figure, group velocities are matched for the control pulse at 0.4μm and the desired signal pulse at 1.55μm while signal pulses at other wavelengths will easily walk-off from the 0.4μm control pulse due to the high group-velocity difference between the control and undesired signal pulses. The pulse walk-off length between the 0.4μm control pulse and the closest adjacent 1.5492μm signal pulse was just 2m when a control pulse of 10ps was used.

However, although the power of the 1.5492μm signal pulse will be less than that of the 1.55μm signal pulse after propagation of one walk-off length, it will not be zero. If there are many WDM channels, the desired signal will sit on a huge background. As a result, it is necessary to eliminate undesired signals completely. To achieve that, a two-control-pulse scheme has been devised as shown in Figure 7-33. A second control pulse is coupled into the orthogonal principal axis with a delay of one pulse width to remove the undesired signals completely. The change in SOP induced by the first control pulse is canceled by the opposite change induced by the orthogonal second control pulse. The 1.55μm desired signal pulse is matched to the first control pulse and is thus unaffected by the orthogonal second control pulse. If the first adjacent signal channel(1.5492μm) is suppressed, all other signal channels

will also be suppressed because those pulses will experience more than one pass through both control pulses.

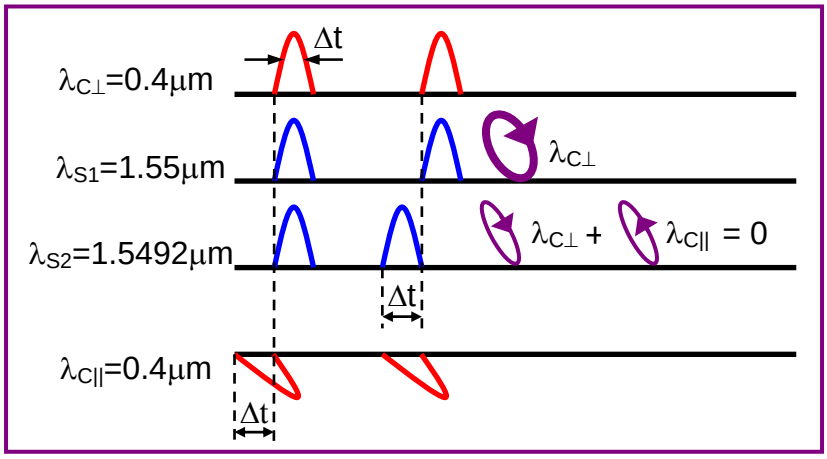

Figure 7-33. A Two-Control-Pulse Scheme

In the all-optical Kerr wavelength-division demultiplexer, the control pulse wavelength should vary according to the desired signal pulse wavelength. The control pulse selects the wavelength where its group velocity is the same as that of the desired signal pulse. With the parameters used in this dissertation, the device would require a laser source capable of being tuned over 170nm and producing 10ps pulses at 400-570nm if we use 40 wavelength signal channels with 0.8nm spacing(1518nm~1550nm). It is possible to develop a narrower tuning range by adjusting fiber parameters to make a slope of the GERI near the control wavelength region steeper.

In this application, higher GVD is desirable for more rapid pulse walk-off. However, high GVD causes pulse broadening which limits the maximum transmittable bit-rate. To examine the effect of pulse broadening, the output signal pulse width was also calculated. Although the signal pulse has an extremely high GVD of around -5500[ps/nm-km], the output signal pulse width after propagation of the pulse walk-off length of 2m was just 10.6ps when a 10ps transform limited input signal pulse was considered. As a result, all-optical wavelength-division demultiplexers based on the optical Kerr effect can be realized by using the property of high GVD in HNL glasses.

With this scheme, it now would be possible to demultiplex simultaneously optical Time-Division(TD)-multiplexed signals and Wavelength-Division(WD)-multiplexed signals using an optical Kerr effect-based demultiplexer. Figure 7-34 shows an example of systems in which 40Gb/s optical TD-multiplexed signals(4channels×10Gb/s) and 40 channels of WD-multiplexed signals are transmitted together. The apparent disadvantage of high GVD in HNL glasses is actually advantageous in that an optical Kerr effect-based demultiplexer can select optical TD-multiplexed and WD-multiplexed signals simultaneously.

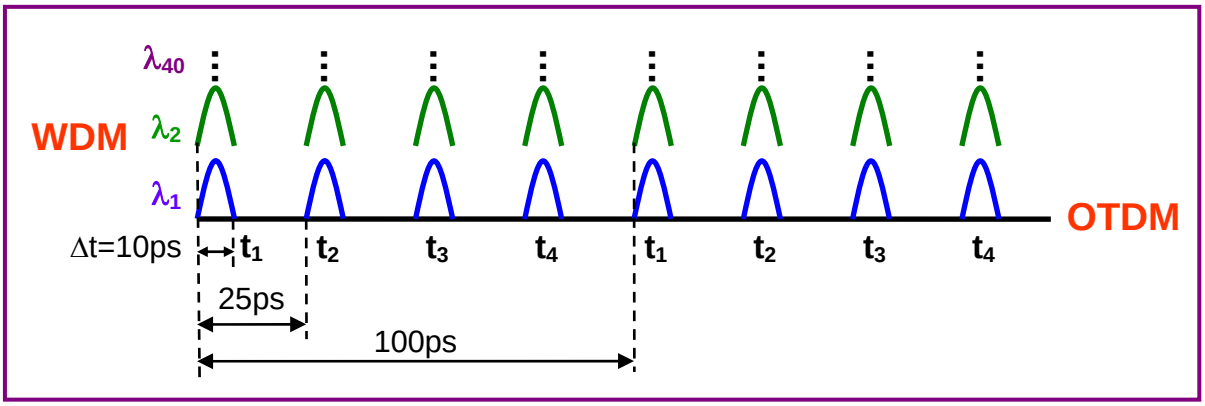

Figure 7-34. 1.6Tb/s OTDM-WDM Systems

7.2. Nonlinear Fiber Devices based on Nonlinear Optical Loop Mirrors

7.2.1. Required Device Length

Similarly, this section provides the required device length for nonlinear fiber devices based on NOLMs. The required device length was calculated from Equation (6.2) with a control power of 1W for a nonlinear phase shift of π due to XPM. The conditions and parameters are the same as those of devices based on the optical Kerr effect.

For Nonlinear Fiber Devices based on Nonlinear Optical Loop Mirrors

$$\lambda_s = 1.55\mu m,\ \lambda_c = 1.54\mu m,\ P_c = 1W,\ V = 2.25(at\,1.55\mu m),\ \lambda_{cutoff} = 1.45\mu m$$

SILICA-CORE

Silica-Clad Devices

$$L_{\pi}^{XPM} = \frac{\lambda_s A_{eff}}{4N_2 P_c} = \frac{1.55\times10^{-6}\times37.67\times10^{-12}}{4\times2.5\times10^{-20}\times1} = 584[m]$$

Microstructure Devices

$$L_{\pi}^{XPM} = \frac{\lambda_s A_{eff}}{4N_2 P_c} = \frac{1.55\times10^{-6}\times1.44\times10^{-12}}{4\times2.5\times10^{-20}\times1} = 22[m]$$

LITHARGE-CORE

Silica-Clad Devices

$$L_{\pi}^{XPM} = \frac{\lambda_s A_{eff}}{4 N_2 P_c} = \frac{1.55\times10^{-6}\times1.21\times10^{-12}}{4\times40\times10^{-20}\times1} = 1.17[m]$$

Microstructure Devices

$$L_{\pi}^{XPM} = \frac{\lambda_s A_{eff}}{4 N_2 P_c} = \frac{1.55\times10^{-6}\times0.88\times10^{-12}}{4\times40\times10^{-20}\times1} = 0.85[m]$$

Litharge-Clad Devices

$$L_{\pi}^{XPM} = \frac{\lambda_s A_{eff}}{4 N_2 P_c} = \frac{1.55\times10^{-6}\times7.70\times10^{-12}}{4\times40\times10^{-20}\times1} = 7.46[m]$$

BISMITE-CORE

Silica-Clad Devices

$$L_{\pi}^{XPM} = \frac{\lambda_s A_{eff}}{4 N_2 P_c} = \frac{1.55\times10^{-6}\times0.70\times10^{-12}}{4\times1000\times10^{-20}\times1} = 2.71[cm]$$

Microstructure Devices

$$L_{\pi}^{XPM} = \frac{\lambda_s A_{eff}}{4 N_2 P_c} = \frac{1.55\times10^{-6}\times0.66\times10^{-12}}{4\times1000\times10^{-20}\times1} = 2.56[cm]$$

Bismite-Clad Devices

$$L_{\pi}^{XPM} = \frac{\lambda_s A_{eff}}{4 N_2 P_c} = \frac{1.55\times10^{-6}\times3.19\times10^{-12}}{4\times1000\times10^{-20}\times1} = 12.36[cm]$$

TELLURITE-CORE

Silica-Clad Devices

$$L_{\pi}^{XPM} = \frac{\lambda_s A_{eff}}{4 N_2 P_c} = \frac{1.55\times10^{-6}\times0.77\times10^{-12}}{4\times148\times10^{-20}\times1} = 20.16[cm]$$

Microstructure Devices

$$L_{\pi}^{XPM} = \frac{\lambda_s A_{eff}}{4 N_2 P_c} = \frac{1.55\times10^{-6}\times0.70\times10^{-12}}{4\times148\times10^{-20}\times1} = 18.33[cm]$$

Tellurite-Clad Devices

$$L_{\pi}^{XPM} = \frac{\lambda_s A_{eff}}{4 N_2 P_c} = \frac{1.55\times10^{-6}\times6.86\times10^{-12}}{4\times148\times10^{-20}\times1} = 1.80[m]$$

CHALCOGENIDE-CORE

Silica-Clad Devices

$$L_{\pi}^{XPM} = \frac{\lambda_s A_{eff}}{4 N_2 P_c} = \frac{1.55\times10^{-6}\times0.38\times10^{-12}}{4\times1250\times10^{-20}\times1} = 1.18[cm]$$

Microstructure Devices

$$L_{\pi}^{XPM} = \frac{\lambda_s A_{eff}}{4 N_2 P_c} = \frac{1.55\times10^{-6}\times0.37\times10^{-12}}{4\times1250\times10^{-20}\times1} = 1.15[cm]$$

Chalcogenide-Clad Devices

$$L_{\pi}^{XPM} = \frac{\lambda_s A_{eff}}{4 N_2 P_c} = \frac{1.55\times10^{-6}\times1.60\times10^{-12}}{4\times1250\times10^{-20}\times1} = 4.96[cm]$$

Table 7-8 summarizes the required device length with a control power of 1W for nonlinear fiber devices based NOLM when the signal pulse operates at 1.55μm and the control pulse operates at 1.54μm.

Table 7-8. The Required Device Length with 1W Control Power for Nonlinear Fiber Devices based on Nonlinear Optical Loop Mirrors (Signal at 1.55μm and Control at 1.54μm)

Device Length[m]	Silica	Litharge	Bismite	Tellurite	Chalcogenide
Silica-Cladding	584	1.17	0.0271	0.2016	0.0118
MSF	22	0.85	0.0256	0.1833	0.0115
HNL Glass-Cladding	-	7.46	0.1236	1.80	0.0496

7.2.2. Relative Group Delay, Group-Velocity Dispersion, and Dispersion Slope

Table 7-9 presents the RGD, calculated from Equation (6.13), between the signal pulse at 1.55μm and the control pulse at 1.54μm for the required device length shown in Table 7-8, for nonlinear fiber devices based on NOLMs. The GVD and DS are the same as those of the devices based on the optical Kerr effect.

Table 7-9. RGD between Signal at 1.55μm and Control at 1.54μm
for Nonlinear Fiber Devices based on Nonlinear Optical Loop Mirrors

Properties		Silica	Litharge	Bismite	Tellurite	Chalcogenide
RGD [ps]	Silica-Cladding	59	1.88	0.17	0.94	0.15
	MSF	83	3.99	0.19	1.83	0.33

Similarly, for a reasonable comparison between different glasses, the same evaluations as the case of the optical Kerr effect were performed. Table 7-10 presents the RGD between the signal pulse at 1.55μm and the control pulse at different wavelengths of the worse case for the required device lengths at different control wavelengths.

Table 7-10. RGD between Signal at 1.55μm and Control at Different Wavelengths for Nonlinear Fiber Devices based on Nonlinear Optical Loop Mirrors

Properties		Silica	Litharge	Bismite	Tellurite	Chalcogenide
Control Wavelength [μm]	Silica-Cladding	1.40	1.30	1.22	1.04	1.45
	MSF	1.35	1.45	1.48	1.45	1.60
RDL at Control Wavelength [m]	Silica-Cladding	554	1.04	0.0226	0.1577	0.0109
	MSF	20	0.80	0.0245	0.1726	0.0123
RGD [ps]	Silica-Cladding	587	25.96	1.99	16.17	0.52
	MSF	688	27.65	0.98	12.48	1.09

7.2.3. Walk-Off Length and Output Pulse Width

The results for the walk-off length are the same as those of the devices based on the optical Kerr effect with the same conditions. Table 7-11 shows the output control pulse width for nonlinear fiber devices based on NOLMs simulated using the nonlinear Schrödinger equation for the input control pulse at 1.54μm with 10ps pulse width and 1W peak power.

Table 7-11. Output Control Pulse Width by the Nonlinear Schrödinger Equation for Nonlinear Fiber Devices based on Nonlinear Optical Loop Mirrors

Output Pulse Width [ps]	Silica	Litharge	Bismite	Tellurite	Chalcogenide
Silica-Cladding	14.9399	10.0879	10.0642	10.0730	10.0502
MSF	13.2122	10.0692	10.0529	10.0613	10.0322

Table 7-12 presents the output control pulse width for nonlinear fiber devices based on NOLMs calculated from Equations (6.18)-(6.21) with the consideration of both GVD and PMD for a 10ps transform limited input pulse at 1.54μm. The spectral width $\delta\lambda$ for this input pulse calculated from Equation (6.22) is 0.348nm and the index differences δn used are 10^{-4} and 10^{-3} for silica-clad fiber and MSF devices, respectively.

Table 7-12. Output Control Pulse Width by GVD and PMD
for Nonlinear Fiber Devices based on Nonlinear Optical Loop Mirrors

Output Pulse Width [ps]	**Silica**		**Litharge**		**Bismite**		**Tellurite**		**Chalcogenide**	
	Si-C	MSF	Si-C	MSF	Si-C	MSF	Si-C	MSF	Si-C	MSF
P[W]	**Device Length[m]**									
1	584	22	1.17	0.85	0.0271	0.0256	0.2016	0.1833	0.0118	0.0115
0.1	1168	44	2.34	1.7	0.0542	0.0512	0.4032	0.3666	0.0236	0.0230
0.01	5840	220	11.7	8.5	0.2710	0.2560	2.0160	1.8330	0.1180	0.1150
δn	10^{-4}	10^{-3}	10^{-4}	10^{-3}	10^{-4}	10^{-3}	10^{-4}	10^{-3}	10^{-4}	10^{-3}
PMD[ps/m]	0.333	3.333	0.333	3.333	0.333	3.333	0.333	3.333	0.333	3.333
P[W]	**δt_{PMD}[ps] = PMD[ps/m] × L[m]**									
1	194	73	0.39	2.83	0.009	0.085	0.067	0.611	0.004	0.038
0.1	389	146	0.78	5.67	0.018	0.171	0.134	1.222	0.008	0.077
0.01	1946	733	3.9	28.33	0.090	0.853	0.672	6.110	0.039	0.383
GVD	**11.6**	**-336**	**-168**	**-653**	**-642**	**-968**	**-511**	**-1200**	**-1491**	**-4486**
δλ[nm]	**0.348**									
P[W]	**δt_{GVD}[ps] = L[Km] × δλ[nm] × GVD[ps/nm-Km]**									
1	2.36	-2.57	-0.07	-0.19	-0.01	-0.01	-0.04	-0.08	-0.01	-0.02
0.1	4.71	-5.14	-0.14	-0.39	-0.01	-0.02	-0.07	-0.15	-0.01	-0.04
0.01	23.57	-25.72	-0.68	-1.93	-0.06	-0.09	-0.36	-0.77	-0.06	-0.18
P[W]	**δt^2[ps] = δt_{GVD}^2[ps] + δt_{PMD}^2[ps]**									
1	194	73	0.4	2.84	0.011	0.086	0.076	0.616	0.007	0.042
0.1	389	146	0.79	5.68	0.022	0.172	0.152	1.232	0.015	0.085
0.01	1946	733	3.96	28.4	0.109	0.858	0.762	6.158	0.073	0.423
P[W]	**Δt_{OUT}^2[ps] = Δt_{IN}^2[ps] + δt^2[ps]**									
1	**194**	**74**	**10.01**	**10.40**	**10.00**	**10.00**	**10.00**	**10.02**	**10.00**	**10.00**
0.1	**389**	**147**	**10.03**	**11.50**	**10.00**	**10.00**	**10.00**	**10.08**	**10.00**	**10.00**
0.01	**1946**	**734**	**10.76**	**30.11**	**10.00**	**10.04**	**10.03**	**11.74**	**10.00**	**10.01**

7.3. Nonlinear Fiber Devices based on Asymmetric Twin-Core Fibers

7.3.1. Coupling Properties

This section describes the coupling properties of nonlinear fiber devices based on single silica-clad ATCFs in which slightly GeO_2-doped silica glass is in the large core and one of HNL glasses is in the small core. The Maximum Coupling Wavelengths(MCW), the Coupling Lengths(CL) at the MCW, power exchange patterns between the two cores, coupling power variation patterns in the small core at the CL, and the spectral width of the devices are provided. In the simulations, the parameters of the devices were chosen such that their MCWs have the same wavelength of 1.5496μm for reasonable comparison. In addition, for all cases, the input power is launched into the larger core at z=0 and the separation between the two cores is 1.5μm(from boundary to boundary). In the following parameters, L refers to the large core, S refers to the small core, and n_2 is the cladding refractive index.

$$aL = 3\mu m,\ n_1 L = 1.4554,\ n_2 = 1.4441\ at\ 1.55\mu m,\ \lambda_{cutoff} L = 1.42\mu m$$

LITHARGE GLASSES in the Small Core

$$aS = 0.2254\mu m,\ n_1 S = 1.8017\,(at 1.55\mu m),\ \lambda_{cutoff} S = 0.63\mu m$$

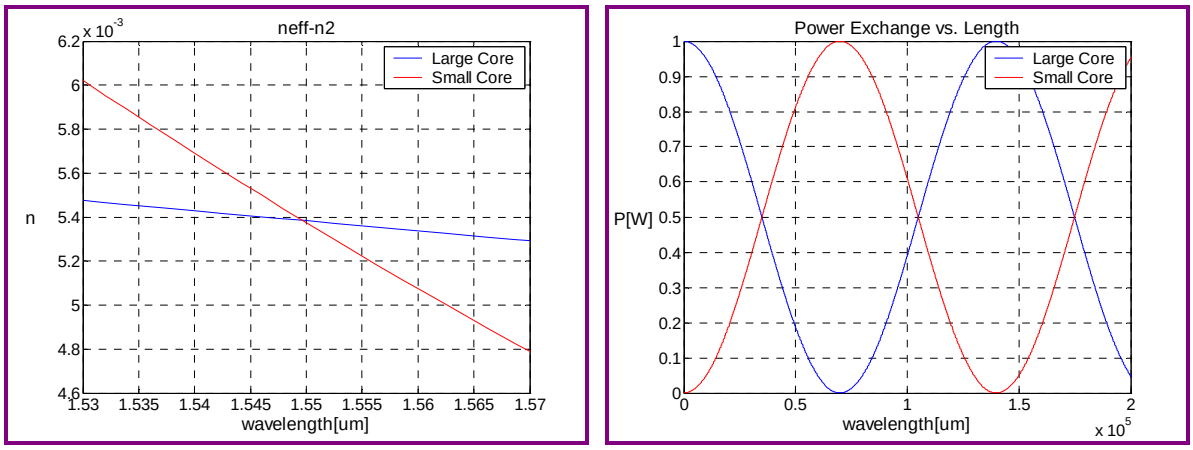

Figure 7-35. MCW(1.5496μm) and CL(70.0mm) at the MCW for Litharge Glasses

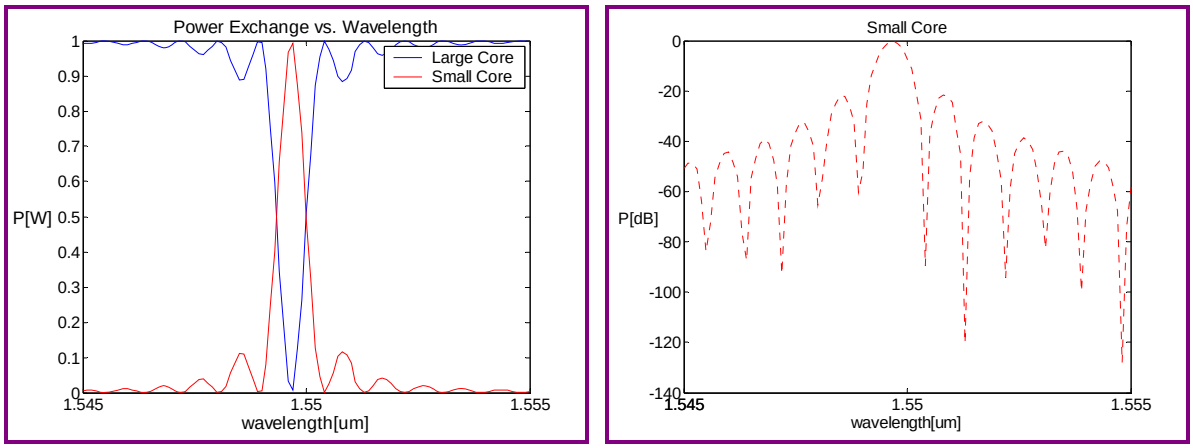

Figure 7-36. Power Exchange between the Cores and Power Variation in the Small Core at the CL(Δλ=0.73nm) for Litharge Glasses

BISMITE GLASSES in the Small Core

$$aS = 0.164\mu m,\ n_1 S = 2.1009\,(at\,1.55\mu m),\ \lambda_{cutoff} S = 0.65\mu m$$

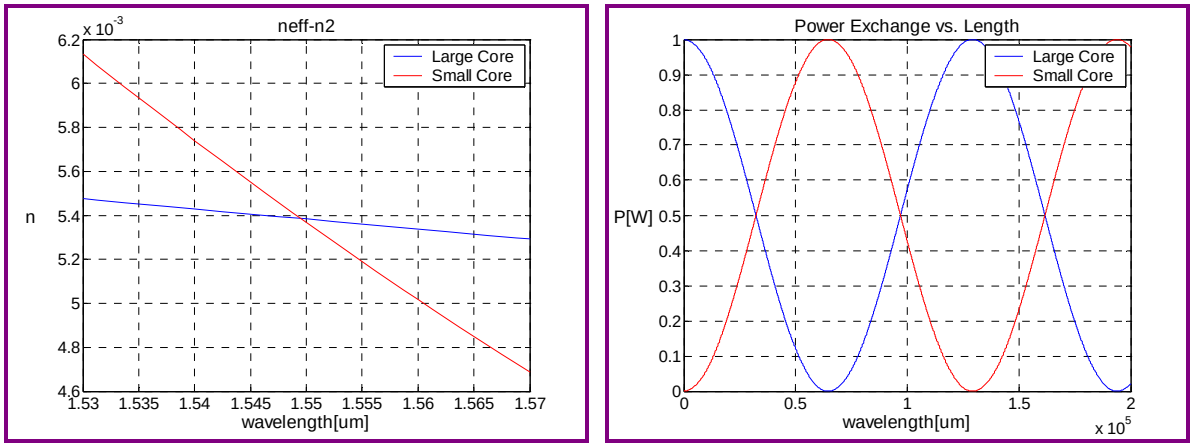

Figure 7-37. MCW(1.5496μm) and CL(64.7mm) at the MCW for Bismite Glasses

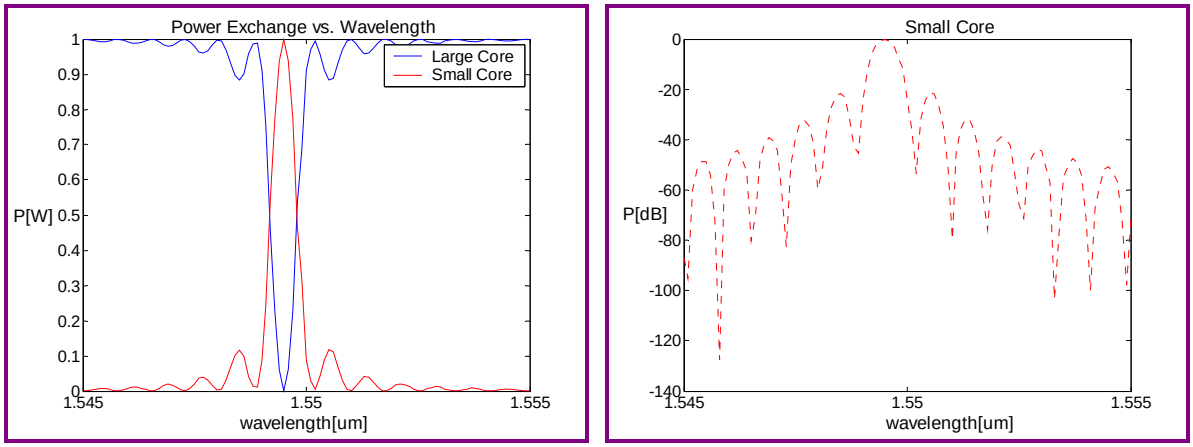

Figure 7-38. Power Exchange between the Cores and Power Variation in the Small Core at the CL(Δλ=0.65nm) for Bismite Glasses

TELLURITE GLASSES in the Small Core

$$aS = 0.174\mu m,\ n_1 S = 2.0278 (at 1.55\mu m),\ \lambda_{cutoff} S = 0.64\mu m$$

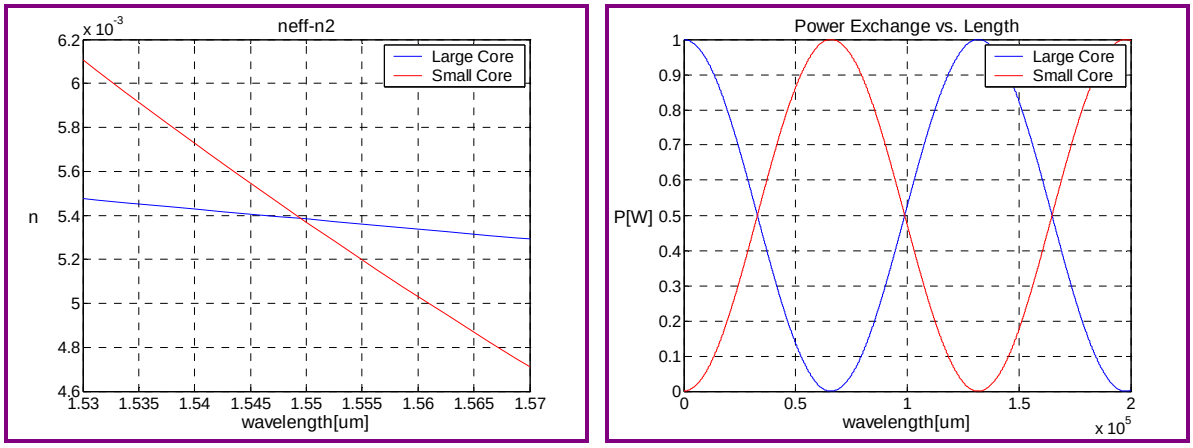

Figure 7-39. MCW(1.5496μm) and CL(65.9mm) at the MCW for Tellurite Glasses

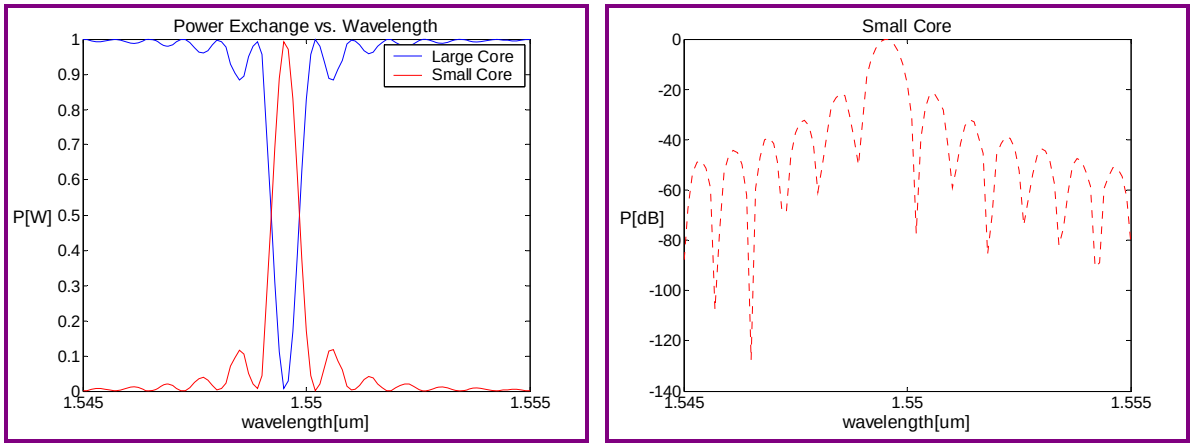

Figure 7-40. Power Exchange between the Cores and Power Variation in the Small Core at the CL(Δλ=0.70nm) for Tellurite Glasses

CHALCOGENIDE GLASSES in the Small Core

$$aS = 0.1203\mu m,\ n_1 S = 2.7555\,(at\,1.55\mu m),\ \lambda_{cutoff} S = 0.74\mu m$$

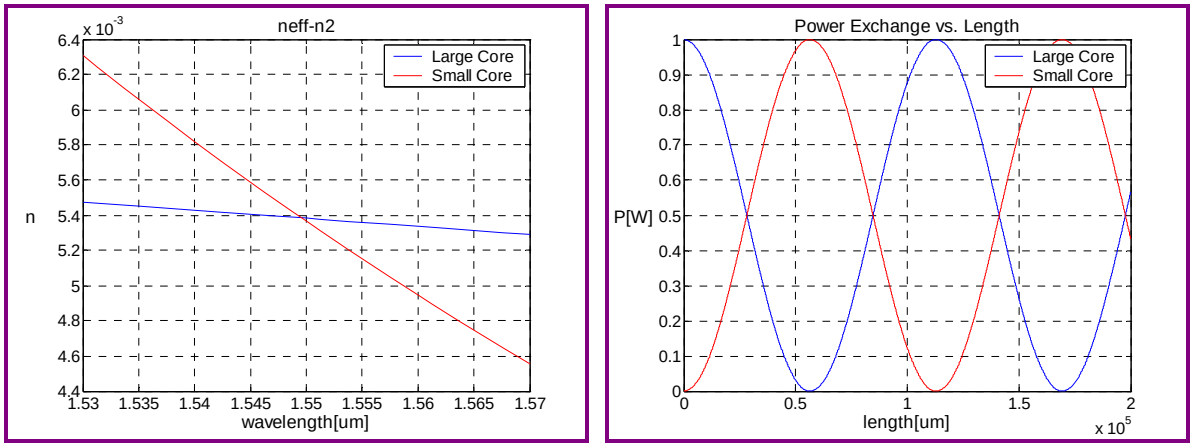

Figure 7-41. MCW(1.5496μm) and CL(56.5mm) at the MCW for Chalcogenide Glasses

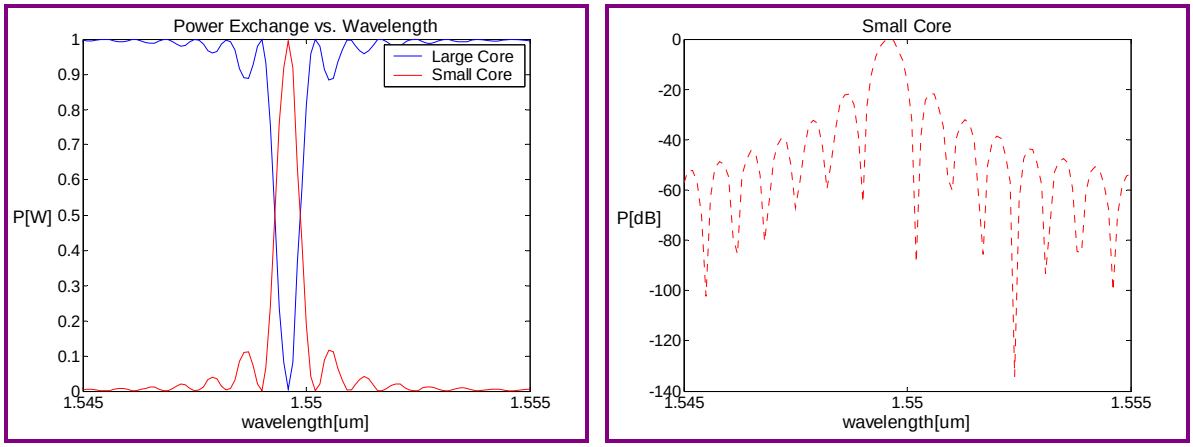

Figure 7-42. Power Exchange between the Cores and Power Variation in the Small Core at the CL(Δλ=0.61nm) for Chalcogenide Glasses

Table 7-13 compares the MCW, CL, spectral width, and effective mode area of the small core for nonlinear fiber devices based on ATCFs in which different HNL glasses are used in the small core.

Table 7-13. Comparison of the Properties of Nonlinear Fiber Devices based on ATCFs

Properties	GeO_2-doped*	Litharge	Bismite	Tellurite	Chalcogenide
MCW [μm]	1.5216	1.5496	1.5496	1.5496	1.5496
CL [mm]	165	70.0	64.7	65.9	56.5
$\Delta\lambda$ [nm]	1.6	0.73	0.65	0.70	0.61
A_{eff} [μm^2]	12.2	2.12	1.84	1.92	1.19

* : The results from Section 2.4.2

7.3.2. Required Optical Power for Wavelength-Division Demultiplexers

As discussed in Section 2.4.4, MCWs of ATCFs are highly dependent on refractive index difference between the small core and cladding, and the refractive index of the small core is affected by strong pump power. As a result, the MCW can be adjusted by controlling the pump power to choose a specific wavelength of the signal pulses in wavelength-division demultiplexers based on ATCFs. This section presents the required optical pump power at 1.3μm, calculated from Equation (6.8), for shifting the MCW by an amount of the spectral width to select the adjacent wavelength channel. It should be noted that the pump wavelength should be far away from the MCW in order to block power exchange of the pump power.

GeO_2-doped GLASSES in the Small Core

$$\lambda_{MCW} = 1.5216\mu m,\ N_2 = 2.8\times10^{-20} m^2/W,\ A_{eff} = 12.2\mu m^2$$

For shifting the MCW by $\Delta\lambda = 1.6nm,\ \delta n = 2.316\times10^{-5}$

$$P_{1.3\mu m} = \frac{A_{eff}\cdot\delta n}{N_2} = \frac{12.2\times10^{-12}\times2.316\times10^{-5}}{2.8\times10^{-20}} = 10[KW]$$

LITHARGE GLASSES in the Small Core

$$\lambda_{MCW} = 1.5496\mu m,\ N_2 = 40\times10^{-20} m^2/W,\ A_{eff} = 2.12\mu m^2$$

For shifting the MCW by $\Delta\lambda = 0.73nm,\ \delta n = 2.517\times10^{-4}$

$$P_{1.3\mu m} = \frac{A_{eff}\cdot\delta n}{N_2} = \frac{2.12\times10^{-12}\times2.517\times10^{-4}}{40\times10^{-20}} = 1.33[KW]$$

BISMITE GLASSES in the Small Core

$$\lambda_{MCW} = 1.5496\mu m,\ N_2 = 1000\times10^{-20} m^2/W,\ A_{eff} = 1.84\mu m^2$$

For shifting the MCW by $\Delta\lambda = 0.65nm,\ \delta n = 5\times10^{-4}$

$$P_{1.3\mu m} = \frac{A_{eff}\cdot\delta n}{N_2} = \frac{1.84\times10^{-12}\times5\times10^{-4}}{1000\times10^{-20}} = 92[W]$$

TELLURITE GLASSES in the Small Core

$$\lambda_{MCW} = 1.5496\mu m,\ N_2 = 148\times10^{-20} m^2/W,\ A_{eff} = 1.92\mu m^2$$

For shifting the MCW by $\Delta\lambda = 0.70nm,\ \delta n = 5.385\times10^{-4}$

$$P_{1.3\mu m} = \frac{A_{eff}\cdot\delta n}{N_2} = \frac{1.92\times10^{-12}\times5.385\times10^{-4}}{148\times10^{-20}} = 0.7[KW]$$

CHALCOGENIDE GLASSES in the Small Core

$$\lambda_{MCW} = 1.5496\mu m,\ N_2 = 1250\times10^{-20}\,m^2/W,\ A_{eff} = 1.19\mu m^2$$

For shifting the MCW by $\Delta\lambda = 0.61nm,\ \delta n = 1.017\times10^{-3}$

$$P_{1.3\mu m} = \frac{A_{eff}\cdot\delta n}{N_2} = \frac{1.19\times10^{-12}\times1.017\times10^{-3}}{1250\times10^{-20}} = 97[W]$$

Table 7-14 summarizes the required optical pump power at 1.3μm to shift the MCW of 1.5496μm by an amount of the spectral width for wavelength-division demultiplexers based on ATCFs.

Table 7-14. The Required Optical Pump Power at 1.3μm to shift the MCW of 1.5496μm for Wavelength-Division Demultiplexers based on ATCFs

Power [KW]	GeO_2-doped	Litharge	Bismite	Tellurite	Chalcogenide
	10	1.33	0.092	0.7	0.097

As can be seen, the power requirements for the wavelength-division demultiplexers based on ATCFs turn out to be large as compared with other nonlinear fiber devices. The reason is that, because HNL glasses have much higher linear refractive indices, the rate of variation of the effective refractive indices in the small core is much smaller. As a result, the required δn for shifting the MCW, which is proportional to the optical pump power, becomes much larger. Finally, even for the case of chalcogenide glasses which have the highest linear refractive indices, it still resumes the relatively high power of 97W due to the highest δn, despite the smallest effective mode area and the largest nonlinear-index coefficient.

7.3.3. Relative Group Delay, Group-Velocity Dispersion, and Dispersion Slope

This section provides the ERI, the GERI, the GVD, and the DS of nonlinear fiber devices based on ATCFs. The RGD between the large and small cores for the constant coupling length shown in Table 7-13 is also provided as a function of wavelength. Furthermore, to investigate the applicable potentiality of optical time-division demultiplexers based on ATCFs, the RGD between the signal pulse at the MCW of 1.5496μm in the large core and the control pulse at 1.3μm in the small core for the device length (coupling length) were evaluated from Equation (6.13).

$$aL = 3\mu m,\ n_1 L = 1.4554,\ n_2 = 1.4441\ at\ 1.55\mu m,\ \lambda_{cutoff} L = 1.42\mu m$$

LITHARGE GLASSES in the Small Core

$$aS = 0.2254\mu m,\ n_1 S = 1.8017\,(at 1.55\mu m),\ \lambda_{cutoff} S = 0.63\mu m$$

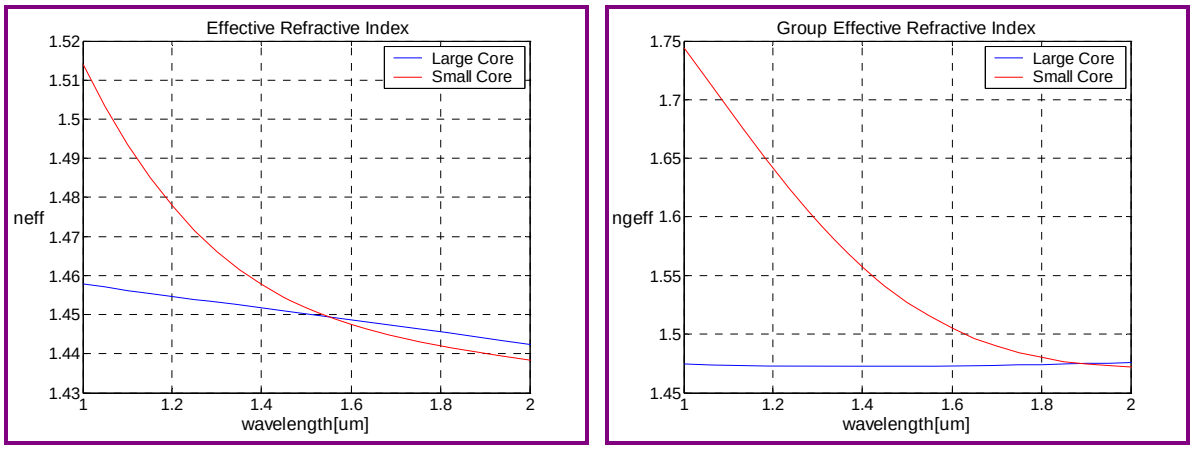

Figure 7-43. ERI and GERI When Litharge Glass is in the Small Core

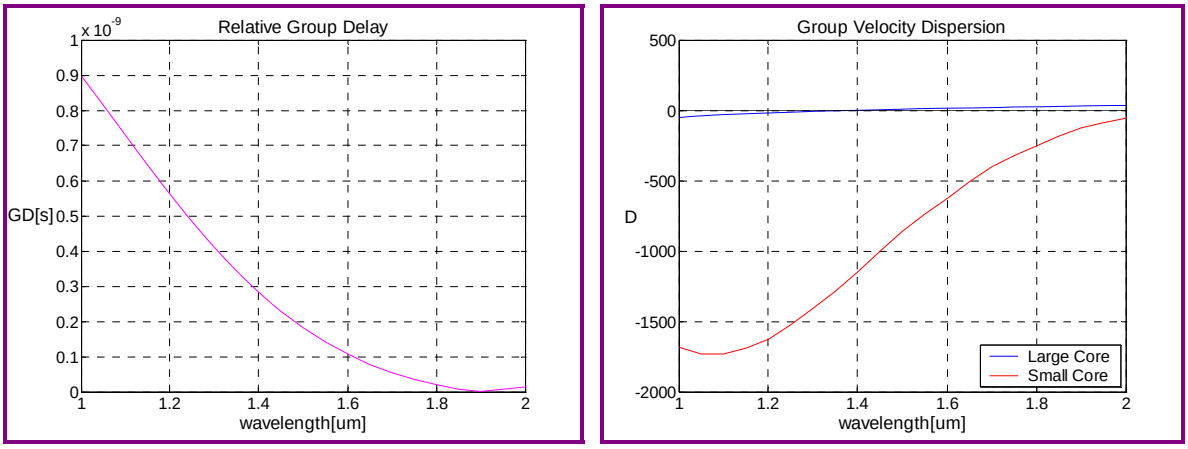

Figure 7-44. RGD and GVD When Litharge Glass is in the Small Core

The RGD between the signal pulse at the MCW of 1.5496μm in the large core and the control pulse at 1.3μm in the small core for the coupling length of 0.07m is 29ps, and the GVD and DS of the control pulse are -1405[ps/nm-km] and 2.36[ps/nm^2-km], respectively.

BISMITE GLASSES in the Small Core

$$aS = 0.164\mu m,\ n_1 S = 2.1009\,(at\,1.55\mu m),\ \lambda_{cutoff} S = 0.65\mu m$$

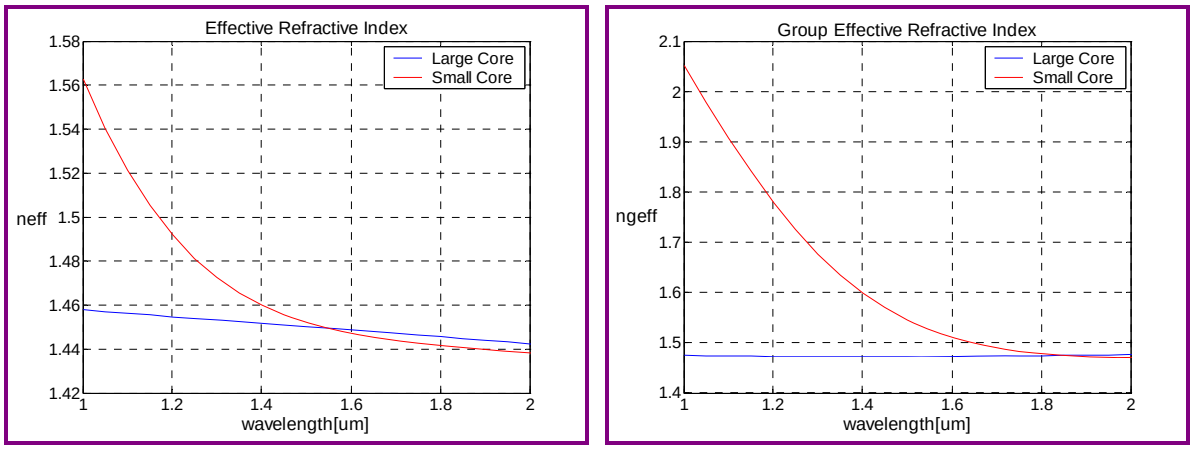

Figure 7-45. ERI and GERI When Bismite Glass is in the Small Core

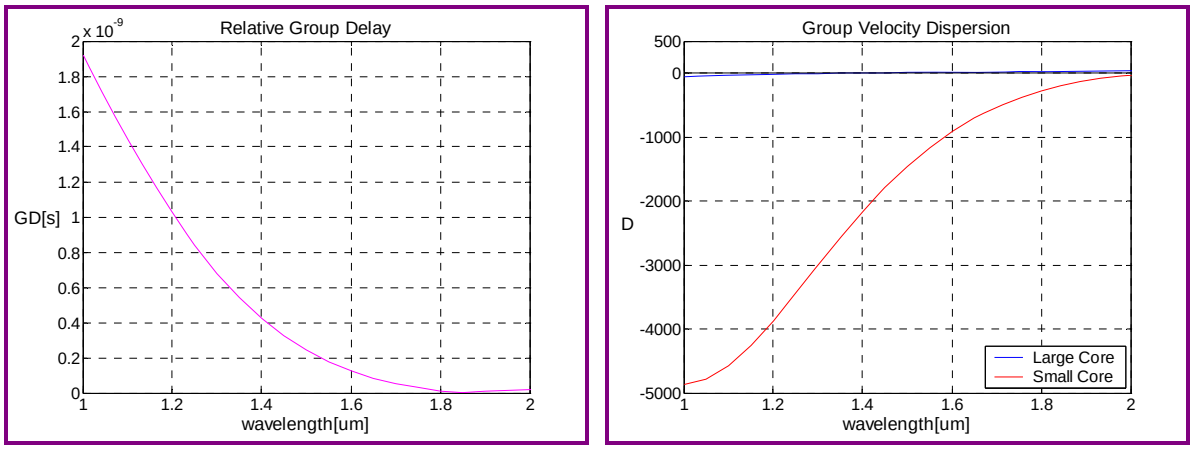

Figure 7-46. RGD and GVD When Bismite Glass is in the Small Core

The RGD between the signal pulse at the MCW of 1.5496μm in the large core and the control pulse at 1.3μm in the small core for the coupling length of 0.0647m is 44ps, and the GVD and DS of the control pulse are -3001[ps/nm-km] and 8.69[ps/nm^2-km], respectively.

TELLURITE GLASSES in the Small Core

$$aS = 0.174\mu m,\ n_1 S = 2.0278(at\,1.55\mu m),\ \lambda_{cutoff} S = 0.64\mu m$$

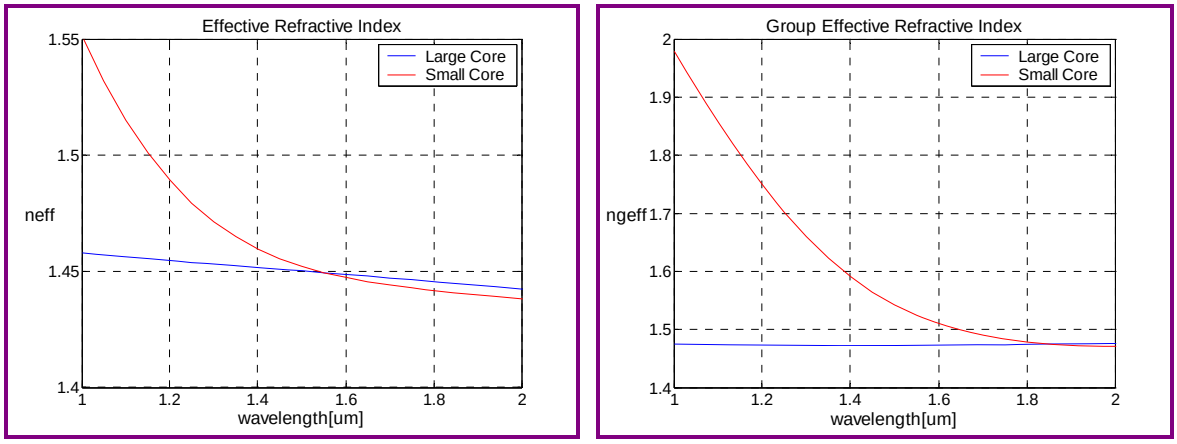

Figure 7-47. ERI and GERI When Tellurite Glass is in the Small Core

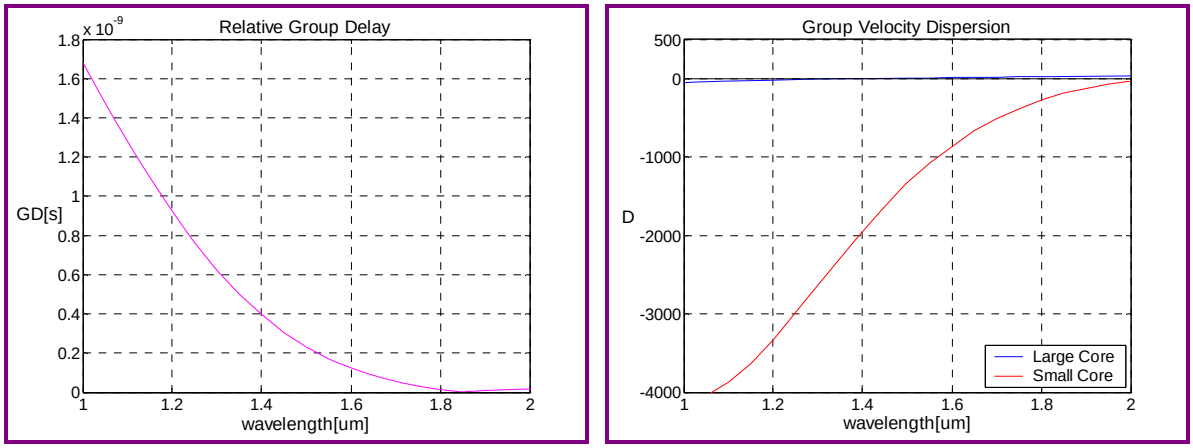

Figure 7-48. RGD and GVD When Tellurite Glass is in the Small Core

The RGD between the signal pulse at the MCW of 1.5496μm in the large core and the control pulse at 1.3μm in the small core for the coupling length of 0.0659m is 41ps, and the GVD and DS of the control pulse are -2632[ps/nm-km] and 7.06[ps/nm^2-km], respectively.

CHALCOGENIDE GLASSES in the Small Core

$$aS = 0.1203\mu m,\ n_1S = 2.7555\,(at\,1.55\mu m),\ \lambda_{cutoff}S = 0.74\mu m$$

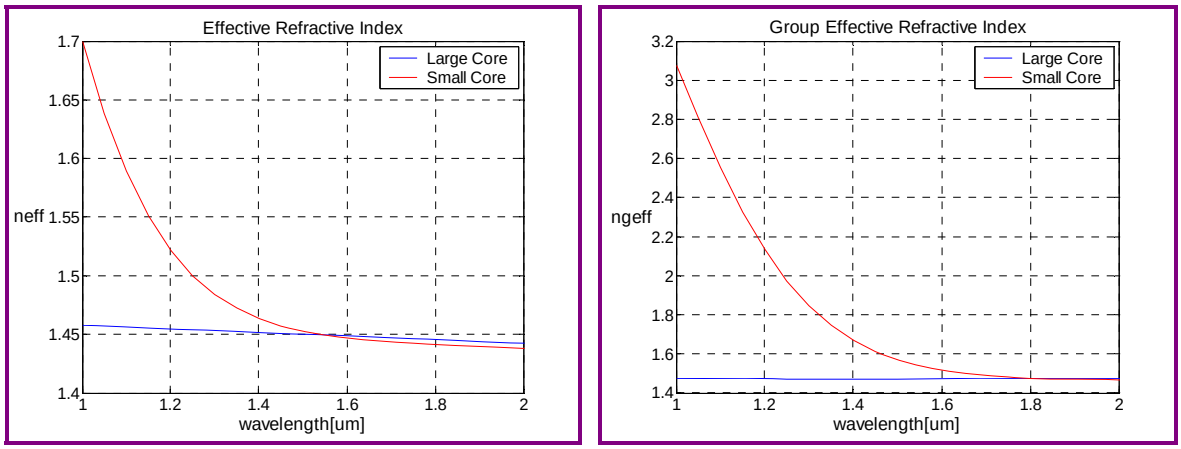

Figure 7-49. ERI and GERI When Chalcogenide Glass is in the Small Core

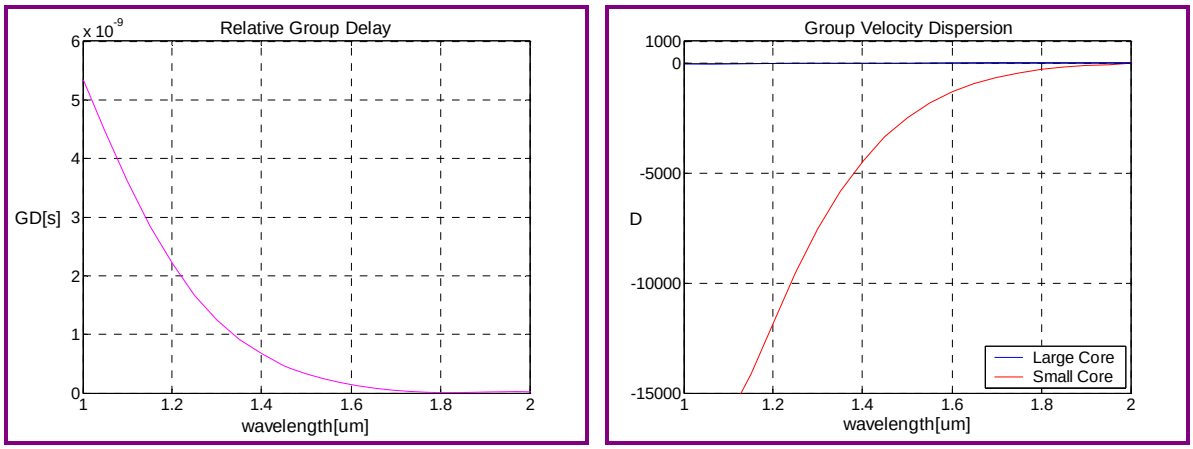

Figure 7-50. RGD and GVD When Chalcogenide Glass is in the Small Core

The RGD between the signal pulse at the MCW of 1.5496μm in the large core and the control pulse at 1.3μm in the small core for the coupling length of 0.0565m is 70ps, and the GVD and DS of the control pulse are -7513[ps/nm-km] and 37.08[ps/nm^2-km], respectively.

Table 7-15 summarizes the RGD, calculated from Equation (6.13), between the signal pulse at the MCW of 1.5496μm in the large core and the control pulse at 1.3μm in the small core for the device length shown in Table 7-13, and the GVD and DS of the control pulse at 1.3μm in the small core for different HNL glasses. The GVD and DS of the signal pulse at the MCW of 1.5496μm in the large core of slightly GeO_2-doped silica glass are 12[ps/nm-km] and 0.052[ps/nm^2-km], respectively.

Table 7-15. RGD between Signal at 1.5496μm in the Large Core and Control at 1.3μm in the Small Core, GVD at 1.3μm, and DS at 1.3μm for Nonlinear Fiber Devices based on ATCFs

Properties	Litharge	Bismite	Tellurite	Chalcogenide
RGD [ps]	29	44	41	70
GVD [ps/nm-km] at 1.3μm	-1405	-3001	-2632	-7513
DS [ps/nm^2-km] at 1.3μm	2.36	8.69	7.06	37.08

7.3.4. Walk-Off Length

Table 7-16 presents the walk-off length, calculated from Equation (6.15), between the signal pulse at the MCW of 1.5496μm in the large core and the control pulse at 1.3μm in the small core with 10ps pulse width for nonlinear fiber devices based on ATCFs.

Table 7-16. Walk-Off Length between Signal at 1.5496μm in the Large Core and Control at 1.3μm in the Small Core with 10ps Pulse Width for Nonlinear Fiber Devices based on ATCFs

Walk-Off Length [m]	Litharge	Bismite	Tellurite	Chalcogenide
	0.024	0.015	0.016	0.008

7.4. Nonlinear Fiber Devices based on LP_{01}-LP_{02} Mode Interference

7.4.1. Required Device Length

This section provides the required device length for nonlinear fiber devices based on LP_{01}-LP_{02} mode interference. For all nonlinear fiber devices constructed with different glasses, the same normalized frequency V of 5 at 1.55μm was selected for reasonable comparison. Thus, the devices support the LP_{01} and LP_{02} modes simultaneously at 1.55μm.

Followings are the required device lengths obtained from Equation (6.4) for the SPM-induced nonlinear phase shift of π. It is assumed that the signal operates at 1.55μm and the LP_{01} and LP_{02} modes of the signal have the same power of 1W.

For SPM-Induced Nonlinear Fiber Devices

based on LP_{01}-LP_{02} Mode Interference

$$\lambda_S = 1.55\mu m,\ P_S = P_{01} = P_{02} = 1W,\ V = 5(at\,1.55\mu m)$$

SILICA-CORE

$$n_{core} = 1.4554,\ N_2 = 2.5\times10^{-20}\,m^2/W\ \ at\,1.55\mu m$$

Silica-Clad Devices

$$n_{cladding} = 1.4441(at\,1.55\mu m),\ a = 6.81\mu m$$

$$n_{eff\_01} = 1.4536,\ n_{eff\_02} = 1.4465,\ A_{eff\_01} = 102.95\mu m^2,\ A_{eff\_02} = 107.41\mu m^2$$

$$L_\pi^{SPM} = \frac{1.55\times10^{-6}}{2\times2.5\times10^{-20}\times1\times\left|\frac{1}{102.95\times10^{-12}} - \frac{1}{107.41\times10^{-12}}\right|} = 77[Km]$$

Microstructure Devices

$$n_{cladding} = 1,\ a = 1.17\mu m$$

$$n_{eff\_01} = 1.3859,\ n_{eff\_02} = 1.0832,\ A_{eff\_01} = 2.97\mu m^2,\ A_{eff\_02} = 5.67\mu m^2$$

$$L_\pi^{SPM} = \frac{1.55\times10^{-6}}{2\times2.5\times10^{-20}\times1\times\left|\frac{1}{2.97\times10^{-12}} - \frac{1}{5.67\times10^{-12}}\right|} = 193[m]$$

LITHARGE-CORE

$$n_{core} = 1.8017,\ N_2 = 40\times10^{-20}\,m^2/W\ \ at\,1.55\,\mu m$$

Silica-Clad Devices

$$n_{cladding} = 1.4441(at\,1.55\,\mu m),\ a = 1.14\,\mu m$$

$$n_{eff\_01} = 1.7461,\ n_{eff\_02} = 1.5157,\ A_{eff\_01} = 2.85\,\mu m^2,\ A_{eff\_02} = 4.73\,\mu m^2$$

$$L_{\pi}^{SPM} = \frac{1.55\times10^{-6}}{2\times40\times10^{-20}\times1\times\left|\frac{1}{2.85\times10^{-12}} - \frac{1}{4.73\times10^{-12}}\right|} = 13.89[m]$$

Microstructure Devices

$$n_{cladding} = 1,\ a = 0.82\,\mu m$$

$$n_{eff\_01} = 1.6831,\ n_{eff\_02} = 1.1221,\ A_{eff\_01} = 1.51\,\mu m^2,\ A_{eff\_02} = 3.06\,\mu m^2$$

$$L_{\pi}^{SPM} = \frac{1.55\times10^{-6}}{2\times40\times10^{-20}\times1\times\left|\frac{1}{1.51\times10^{-12}} - \frac{1}{3.06\times10^{-12}}\right|} = 5.76[m]$$

Litharge-Clad Devices

$$n_{core} = 1.774,\ n_{cladding} = 1.728,\ a = 3.07\,\mu m$$

$$n_{eff\_01} = 1.7667,\ n_{eff\_02} = 1.7378,\ A_{eff\_01} = 20.89\,\mu m^2,\ A_{eff\_02} = 23.13\,\mu m^2$$

$$L_{\pi}^{SPM} = \frac{1.55\times10^{-6}}{2\times40\times10^{-20}\times1\times\left|\frac{1}{20.89\times10^{-12}} - \frac{1}{23.13\times10^{-12}}\right|} = 418[m]$$

BISMITE-CORE

$$n_{core} = 2.1009,\ N_2 = 1000 \times 10^{-20} m^2/W\ \ at 1.55\mu m$$

Silica-Clad Devices

$$n_{cladding} = 1.4441 (at 1.55\mu m),\ a = 0.81\mu m$$

$$n_{eff\_01} = 2.0007,\ n_{eff\_02} = 1.5641,\ A_{eff\_01} = 1.43\mu m^2,\ A_{eff\_02} = 2.72\mu m^2$$

$$L_{\pi}^{SPM} = \frac{1.55 \times 10^{-6}}{2 \times 1000 \times 10^{-20} \times 1 \times \left| \frac{1}{1.43 \times 10^{-12}} - \frac{1}{2.72 \times 10^{-12}} \right|} = 0.23[m]$$

Microstructure Devices

$$n_{cladding} = 1,\ a = 0.67\mu m$$

$$n_{eff\_01} = 1.9421,\ n_{eff\_02} = 1.1408,\ A_{eff\_01} = 1.01\mu m^2,\ A_{eff\_02} = 2.14\mu m^2$$

$$L_{\pi}^{SPM} = \frac{1.55 \times 10^{-6}}{2 \times 1000 \times 10^{-20} \times 1 \times \left| \frac{1}{1.01 \times 10^{-12}} - \frac{1}{2.14 \times 10^{-12}} \right|} = 0.15[m]$$

Bismite-Clad Devices

$$n_{core} = 2.22,\ n_{cladding} = 2.13,\ a = 1.97\mu m$$

$$n_{eff\_01} = 2.2057,\ n_{eff\_02} = 2.1492,\ A_{eff\_01} = 8.56\mu m^2,\ A_{eff\_02} = 10.01\mu m^2$$

$$L_{\pi}^{SPM} = \frac{1.55 \times 10^{-6}}{2 \times 1000 \times 10^{-20} \times 1 \times \left| \frac{1}{8.56 \times 10^{-12}} - \frac{1}{10.01 \times 10^{-12}} \right|} = 4.58[m]$$

TELLURITE-CORE

$$n_{core} = 2.0278,\ N_2 = 148\times10^{-20}\,m^2/W\ \ at\,1.55\mu m$$

Silica-Clad Devices

$$n_{cladding} = 1.4441(at\,1.55\mu m),\ a = 0.87\mu m$$

$$n_{eff\_01} = 1.9383,\ n_{eff\_02} = 1.5534,\ A_{eff\_01} = 1.64\mu m^2,\ A_{eff\_02} = 3.06\mu m^2$$

$$L_{\pi}^{SPM} = \frac{1.55\times10^{-6}}{2\times148\times10^{-20}\times1\times\left|\frac{1}{1.64\times10^{-12}} - \frac{1}{3.06\times10^{-12}}\right|} = 1.85[m]$$

Microstructure Devices

$$n_{cladding} = 1,\ a = 0.70\mu m$$

$$n_{eff\_01} = 1.8786,\ n_{eff\_02} = 1.1374,\ A_{eff\_01} = 1.10\mu m^2,\ A_{eff\_02} = 2.30\mu m^2$$

$$L_{\pi}^{SPM} = \frac{1.55\times10^{-6}}{2\times148\times10^{-20}\times1\times\left|\frac{1}{1.10\times10^{-12}} - \frac{1}{2.30\times10^{-12}}\right|} = 1.10[m]$$

Tellurite-Clad Devices

$$n_{core} = 2.028,\ n_{cladding} = 1.983,\ a = 2.90\mu m$$

$$n_{eff\_01} = 2.0209,\ n_{eff\_02} = 1.9926,\ A_{eff\_01} = 18.70\mu m^2,\ A_{eff\_02} = 20.48\mu m^2$$

$$L_{\pi}^{SPM} = \frac{1.55\times10^{-6}}{2\times148\times10^{-20}\times1\times\left|\frac{1}{18.70\times10^{-12}} - \frac{1}{20.48\times10^{-12}}\right|} = 113[m]$$

CHALCOGENIDE-CORE

$$n_{core} = 2.7555,\ N_2 = 1250 \times 10^{-20}\, m^2/W \ \ at 1.55\,\mu m$$

Silica-Clad Devices

$$n_{cladding} = 1.4441 (at 1.55\,\mu m),\ a = 0.53\,\mu m$$

$$n_{eff\_01} = 2.5633,\ n_{eff\_02} = 1.6321,\ A_{eff\_01} = 0.62\,\mu m^2,\ A_{eff\_02} = 1.27\,\mu m^2$$

$$L_{\pi}^{SPM} = \frac{1.55 \times 10^{-6}}{2 \times 1250 \times 10^{-20} \times 1 \times \left| \frac{1}{0.62 \times 10^{-12}} - \frac{1}{1.27 \times 10^{-12}} \right|} = 0.075[m]$$

Microstructure Devices

$$n_{cladding} = 1,\ a = 0.48\,\mu m$$

$$n_{eff\_01} = 2.5135,\ n_{eff\_02} = 1.1469,\ A_{eff\_01} = 0.54\,\mu m^2,\ A_{eff\_02} = 1.07\,\mu m^2$$

$$L_{\pi}^{SPM} = \frac{1.55 \times 10^{-6}}{2 \times 1250 \times 10^{-20} \times 1 \times \left| \frac{1}{0.54 \times 10^{-12}} - \frac{1}{1.07 \times 10^{-12}} \right|} = 0.068[m]$$

Chalcogenide-Clad Devices

$$n_{core} = 2.6,\ n_{cladding} = 2.443,\ a = 1.39\,\mu m$$

$$n_{eff\_01} = 2.5752,\ n_{eff\_02} = 2.4763,\ A_{eff\_01} = 4.23\,\mu m^2,\ A_{eff\_02} = 5.17\,\mu m^2$$

$$L_{\pi}^{SPM} = \frac{1.55 \times 10^{-6}}{2 \times 1250 \times 10^{-20} \times 1 \times \left| \frac{1}{4.23 \times 10^{-12}} - \frac{1}{5.17 \times 10^{-12}} \right|} = 1.44[m]$$

Table 7-17 summarizes the required device length with the same optical power in both modes of 1W for SPM-induced nonlinear fiber devices based on LP_{01}-LP_{02} mode interference when the signal which supports the LP_{01} and LP_{02} modes operates at 1.55μm.

Table 7-17. The Required Device Length with 1W Optical Power at 1.55μm for SPM-Induced Nonlinear Fiber Devices based on LP_{01}-LP_{02} Mode Interference

Device Length[m]	Silica	Litharge	Bismite	Tellurite	Chalcogenide
Silica-Cladding	77000	13.89	0.23	1.85	0.075
MSF	193	5.76	0.15	1.10	0.068
HNL Glass-Cladding	-	418	4.58	113	1.44

Followings are the required device lengths, obtained from Equation (6.5), for the XPM-induced nonlinear phase shift of π when the pump is much stronger than the signal. It is assumed that the signal operates at 1.55μm and almost all pump power of 1W is launched into the fundamental mode at 1.3μm.

For XPM-Induced Nonlinear Fiber Devices

based on LP_{01}-LP_{02} Mode Interference

$$\lambda_S = 1.55\mu m,\ \lambda_P = 1.3\mu m,\ P_P = 1W >> P_S,\ V = 5(at\,1.55\mu m)$$

SILICA-CORE

$$n_{core} = 1.4554,\ N_2 = 2.5\times10^{-20}\,m^2/W\ \ at\,1.55\mu m$$

Silica-Clad Devices

$$n_{cladding} = 1.4441(at\,1.55\mu m),\ a = 6.81\mu m$$

$$n_{eff\_01P} = 1.4541,\ A_{eff\_01S\_01P} = 100.21\mu m^2,\ A_{eff\_02S\_01P} = 139.45\mu m^2$$

$$L_\pi^{XPM} = \frac{1.55\times10^{-6}}{4\times2.5\times10^{-20}\times1\times\left|\frac{1}{100.21\times10^{-12}} - \frac{1}{139.45\times10^{-12}}\right|} = 5.5[Km]$$

Microstructure Devices

$$n_{cladding} = 1,\ a = 1.17\mu m$$

$$n_{eff\_01P} = 1.4047,\ A_{eff\_01S\_01P} = 2.85\mu m^2,\ A_{eff\_02S\_01P} = 4.23\mu m^2$$

$$L_\pi^{XPM} = \frac{1.55\times10^{-6}}{4\times2.5\times10^{-20}\times1\times\left|\frac{1}{2.85\times10^{-12}} - \frac{1}{4.23\times10^{-12}}\right|} = 135[m]$$

LITHARGE-CORE

$$n_{core} = 1.8017,\ N_2 = 40\times10^{-20}\,m^2/W\ \ at\,1.55\,\mu m$$

Silica-Clad Devices

$$n_{cladding} = 1.4441(at\,1.55\,\mu m),\ a = 1.14\,\mu m$$

$$n_{eff\_01P} = 1.7608,\ A_{eff\_01S\_01P} = 2.75\,\mu m^2,\ A_{eff\_02S\_01P} = 4.05\,\mu m^2$$

$$L_{\pi}^{XPM} = \frac{1.55\times10^{-6}}{4\times40\times10^{-20}\times1\times\left|\frac{1}{2.75\times10^{-12}} - \frac{1}{4.05\times10^{-12}}\right|} = 8.30[m]$$

Microstructure Devices

$$n_{cladding} = 1,\ a = 0.82\,\mu m$$

$$n_{eff\_01P} = 1.7162,\ A_{eff\_01S\_01P} = 1.44\,\mu m^2,\ A_{eff\_02S\_01P} = 2.16\,\mu m^2$$

$$L_{\pi}^{XPM} = \frac{1.55\times10^{-6}}{4\times40\times10^{-20}\times1\times\left|\frac{1}{1.44\times10^{-12}} - \frac{1}{2.16\times10^{-12}}\right|} = 4.19[m]$$

Litharge-Clad Devices

$$n_{core} = 1.774,\ n_{cladding} = 1.728,\ a = 3.07\,\mu m$$

$$n_{eff\_01P} = 1.7686,\ A_{eff\_01S\_01P} = 20.24\,\mu m^2,\ A_{eff\_02S\_01P} = 27.98\,\mu m^2$$

$$L_{\pi}^{XPM} = \frac{1.55\times10^{-6}}{4\times40\times10^{-20}\times1\times\left|\frac{1}{20.24\times10^{-12}} - \frac{1}{27.98\times10^{-12}}\right|} = 70.88[m]$$

BISMITE-CORE

$$n_{core} = 2.1009,\ N_2 = 1000 \times 10^{-20}\, m^2/W \ \ at\, 1.55\,\mu m$$

Silica-Clad Devices

$$n_{cladding} = 1.4441 (at\, 1.55\,\mu m),\ a = 0.81\,\mu m$$

$$n_{eff\_01P} = 2.0278,\ A_{eff\_01S\_01P} = 1.37\,\mu m^2,\ A_{eff\_02S\_01P} = 2.03\,\mu m^2$$

$$L_{\pi}^{XPM} = \frac{1.55 \times 10^{-6}}{4 \times 1000 \times 10^{-20} \times 1 \times \left| \frac{1}{1.37 \times 10^{-12}} - \frac{1}{2.03 \times 10^{-12}} \right|} = 0.16[m]$$

Microstructure Devices

$$n_{cladding} = 1,\ a = 0.67\,\mu m$$

$$n_{eff\_01P} = 1.9870,\ A_{eff\_01S\_01P} = 0.96\,\mu m^2,\ A_{eff\_02S\_01P} = 1.49\,\mu m^2$$

$$L_{\pi}^{XPM} = \frac{1.55 \times 10^{-6}}{4 \times 1000 \times 10^{-20} \times 1 \times \left| \frac{1}{0.96 \times 10^{-12}} - \frac{1}{1.49 \times 10^{-12}} \right|} = 0.11[m]$$

Bismite-Clad Devices

$$n_{core} = 2.22,\ n_{cladding} = 2.13,\ a = 1.97\,\mu m$$

$$n_{eff\_01P} = 2.2094,\ A_{eff\_01S\_01P} = 8.29\,\mu m^2,\ A_{eff\_02S\_01P} = 11.67\,\mu m^2$$

$$L_{\pi}^{XPM} = \frac{1.55 \times 10^{-6}}{4 \times 1000 \times 10^{-20} \times 1 \times \left| \frac{1}{8.29 \times 10^{-12}} - \frac{1}{11.67 \times 10^{-12}} \right|} = 1.11[m]$$

TELLURITE-CORE

$$n_{core} = 2.0278,\ N_2 = 148\times10^{-20}\,m^2/W\ \ at\,1.55\mu m$$

Silica-Clad Devices

$$n_{cladding} = 1.4441(at\,1.55\mu m),\ a = 0.87\mu m$$

$$n_{eff\_01P} = 1.9624,\ A_{eff\_01S\_01P} = 1.57\mu m^2,\ A_{eff\_02S\_01P} = 2.33\mu m^2$$

$$L_{\pi}^{XPM} = \frac{1.55\times10^{-6}}{4\times148\times10^{-20}\times1\times\left|\frac{1}{1.57\times10^{-12}} - \frac{1}{2.33\times10^{-12}}\right|} = 1.26[m]$$

Microstructure Devices

$$n_{cladding} = 1,\ a = 0.70\mu m$$

$$n_{eff\_01P} = 1.9207,\ A_{eff\_01S\_01P} = 1.05\mu m^2,\ A_{eff\_02S\_01P} = 1.61\mu m^2$$

$$L_{\pi}^{XPM} = \frac{1.55\times10^{-6}}{4\times148\times10^{-20}\times1\times\left|\frac{1}{1.05\times10^{-12}} - \frac{1}{1.61\times10^{-12}}\right|} = 0.79[m]$$

Tellurite-Clad Devices

$$n_{core} = 2.028,\ n_{cladding} = 1.983,\ a = 2.90\mu m$$

$$n_{eff\_01P} = 2.0227,\ A_{eff\_01S\_01P} = 18.09\mu m^2,\ A_{eff\_02S\_01P} = 24.95\mu m^2$$

$$L_{\pi}^{XPM} = \frac{1.55\times10^{-6}}{4\times148\times10^{-20}\times1\times\left|\frac{1}{18.09\times10^{-12}} - \frac{1}{24.95\times10^{-12}}\right|} = 17.23[m]$$

CHALCOGENIDE-CORE

$$n_{core} = 2.7555,\ N_2 = 1250\times10^{-20}\,m^2/W\ \ at\,1.55\mu m$$

Silica-Clad Devices

$$n_{cladding} = 1.4441(at\,1.55\mu m),\ a = 0.53\mu m$$

$$n_{eff\_01P} = 2.6172,\ A_{eff\_01S\_01P} = 0.59\mu m^2,\ A_{eff\_02S\_01P} = 0.89\mu m^2$$

$$L_{\pi}^{XPM} = \frac{1.55\times10^{-6}}{4\times1250\times10^{-20}\times1\times\left|\frac{1}{0.59\times10^{-12}} - \frac{1}{0.89\times10^{-12}}\right|} = 0.054[m]$$

Microstructure Devices

$$n_{cladding} = 1,\ a = 0.48\mu m$$

$$n_{eff\_01P} = 2.5834,\ A_{eff\_01S\_01P} = 0.51\mu m^2,\ A_{eff\_02S\_01P} = 0.91\mu m^2$$

$$L_{\pi}^{XPM} = \frac{1.55\times10^{-6}}{4\times1250\times10^{-20}\times1\times\left|\frac{1}{0.51\times10^{-12}} - \frac{1}{0.91\times10^{-12}}\right|} = 0.036[m]$$

Chalcogenide-Clad Devices

$$n_{core} = 2.6,\ n_{cladding} = 2.443,\ a = 1.39\mu m$$

$$n_{eff\_01P} = 2.5816,\ A_{eff\_01S\_01P} = 4.09\mu m^2,\ A_{eff\_02S\_01P} = 5.79\mu m^2$$

$$L_{\pi}^{XPM} = \frac{1.55\times10^{-6}}{4\times1250\times10^{-20}\times1\times\left|\frac{1}{4.09\times10^{-12}} - \frac{1}{5.79\times10^{-12}}\right|} = 0.432[m]$$

Table 7-18 summarizes the required device length with a pump power of 1W for XPM-induced nonlinear fiber devices based on LP_{01}-LP_{02} mode interference when the signal which supports the LP_{01} and LP_{02} modes operates at 1.55μm and the control which supports the fundamental mode operates at 1.3μm.

Table 7-18. The Required Device Length with 1W Pump Power for XPM-Induced Nonlinear Fiber Devices based on LP_{01}-LP_{02} Mode Interference(Signal at 1.55μm and Pump at 1.3μm)

Device Length[m]	Silica	Litharge	Bismite	Tellurite	Chalcogenide
Silica-Cladding	5500	8.30	0.16	1.26	0.054
MSF	135	4.19	0.11	0.79	0.036
HNL Glass-Cladding	-	70.88	1.11	17.23	0.432

7.4.2. Relative Group Delay, Group-Velocity Dispersion, and Dispersion Slope

Basically, the principle of mode interference is based on the phase-velocity difference between two modes. However, if nonlinear fiber devices based on mode interference are used for time-dependent applications such as optical time-division demultiplexing, group-velocity difference between two modes plays an important role in their performances. This section provides the ERI, the GERI, the GVD, and the DS of the LP_{01} and LP_{02} modes in the devices. In addition, graphs of the RGD between the LP_{01} and LP_{02} modes of the signal pulse at 1.55μm for the required device length of the SMP-induced devices are provided. In the graphs, although the required device length should be changed according to the wavelength, the same required device length for 1.55μm was used for all wavelengths to roughly see the extent and trend of the RGD. To assess the applicability of devices for time-dependent applications, values of the RGD between the modes of the SPM-induced and XPM-induced devices at 1.55μm signal for the required device length were also calculated.

SILICA-CORE

$$n_{core} = slightly\ GeO_2 - doped\ \ silica$$

Silica-Clad Devices

$$n_{cladding} = silica,\ a = 6.81\mu m$$

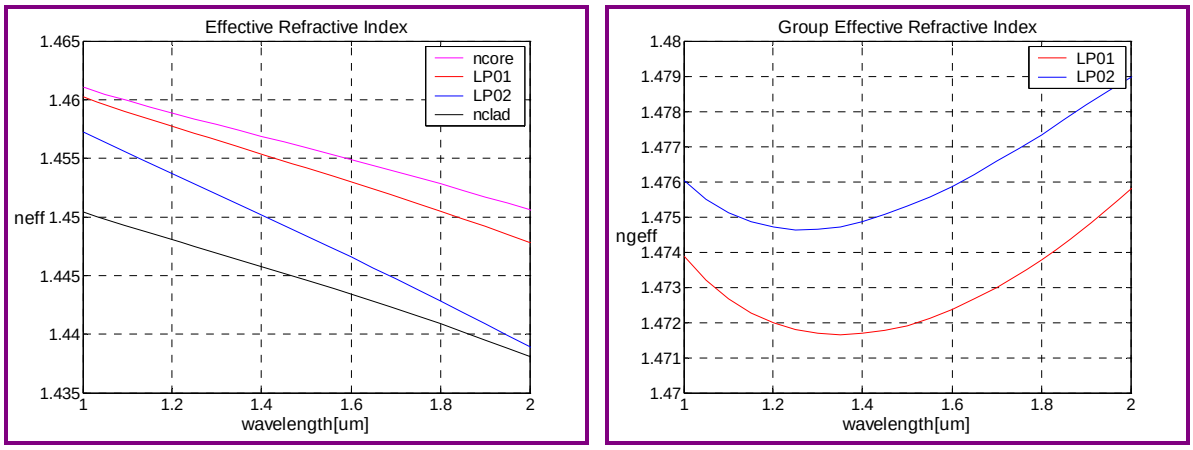

Figure 7-51. ERI and GERI of Silica-Core Silica-Clad Devices(LP_{01}-LP_{02} Mode)

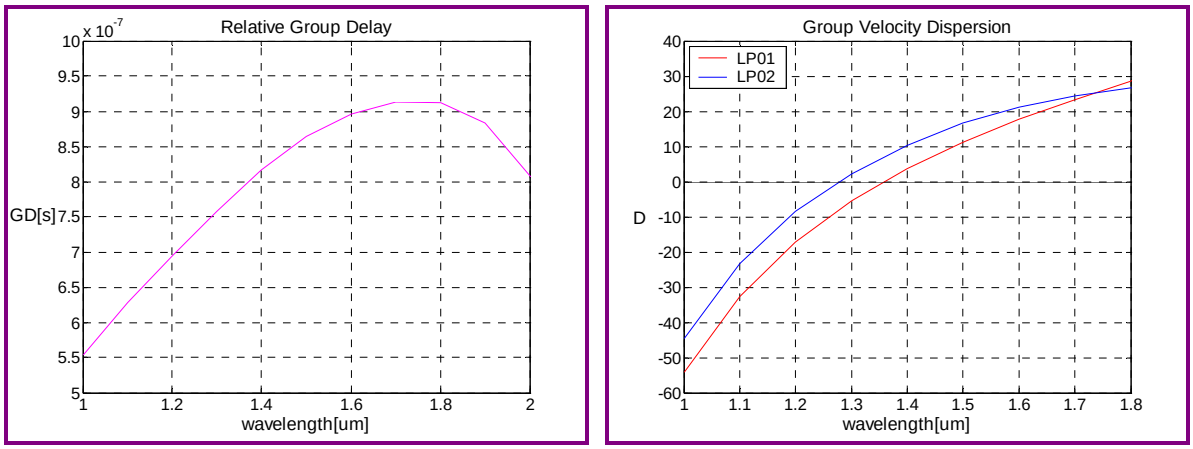

Figure 7-52. RGD and GVD of Silica-Core Silica-Clad Devices(LP_{01}-LP_{02} Mode)

The RGD between the LP_{01} and LP_{02} modes at 1.55μm for the device length of 77Km is 880ns. The GVDs are 14.33[ps/nm-km] and 18.93[ps/nm-km], and the DSs are 0.075[ps/nm^2-km] and 0.037[ps/nm^2-km], for the LP_{01} and LP_{02} modes at 1.55μm, respectively.

Microstructure Devices

$$n_{cladding} = air,\ a = 1.17\mu m$$

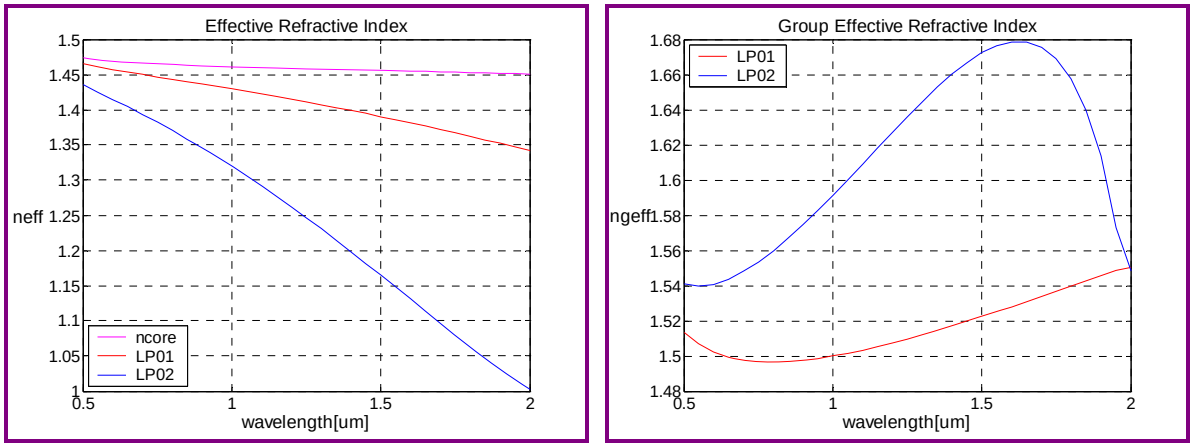

Figure 7-53. ERI and GERI of Silica-Core Microstructure Devices(LP_{01}-LP_{02} Mode)

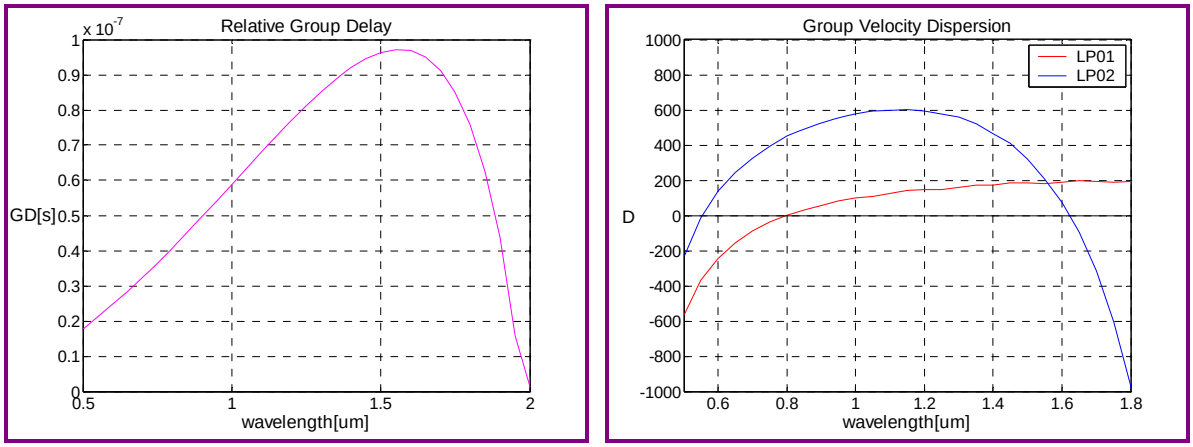

Figure 7-54. RGD and GVD of Silica-Core Microstructure Devices(LP_{01}-LP_{02} Mode)

The RGD between the LP_{01} and LP_{02} modes at 1.55μm for the device length of 193m is 97ns. The GVDs are 181[ps/nm-km] and 205[ps/nm-km], and the DSs are 0.027[ps/nm^2-km] and -2.452[ps/nm^2-km], for the LP_{01} and LP_{02} modes at 1.55μm, respectively.

LITHARGE-CORE

$$n_{core} = SF57$$

Silica-Clad Devices

$$n_{cladding} = silica,\ a = 1.14\mu m$$

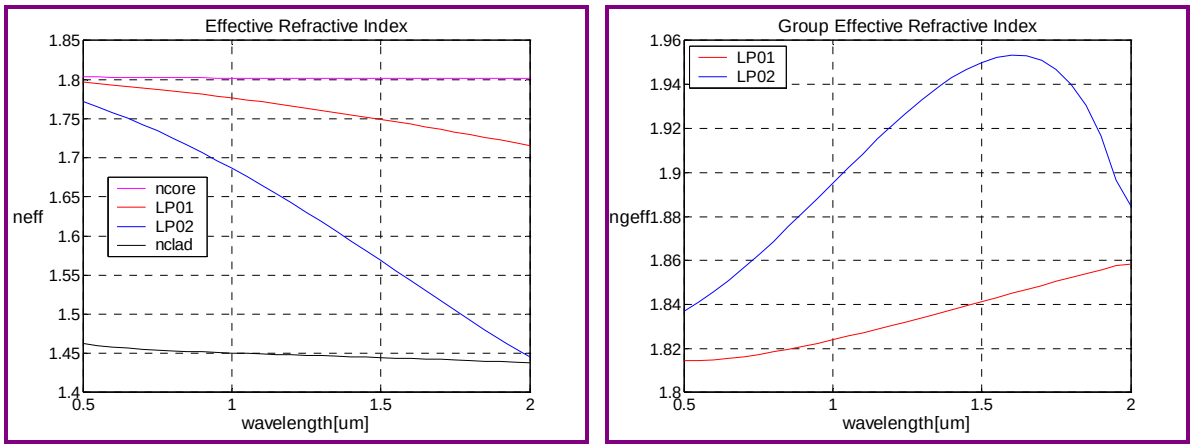

Figure 7-55. ERI and GERI of Litharge-Core Silica-Clad Devices(LP_{01}-LP_{02} Mode)

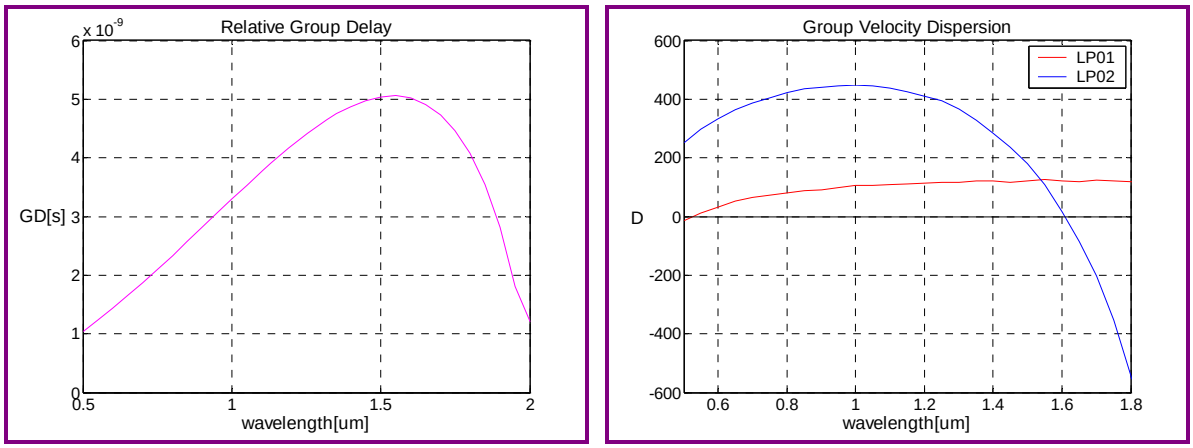

Figure 7-56. RGD and GVD of Litharge-Core Silica-Clad Devices(LP_{01}-LP_{02} Mode)

The RGD between the LP_{01} and LP_{02} modes at 1.55μm for the device length of 13.89m is 5.06ns. The GVDs are 126[ps/nm-km] and 110[ps/nm-km], and the DSs are -0.021[ps/nm^2-km] and -1.636[ps/nm^2-km], for the LP_{01} and LP_{02} modes at 1.55μm, respectively.

Microstructure Devices

$$n_{cladding} = air,\ a = 0.82\mu m$$

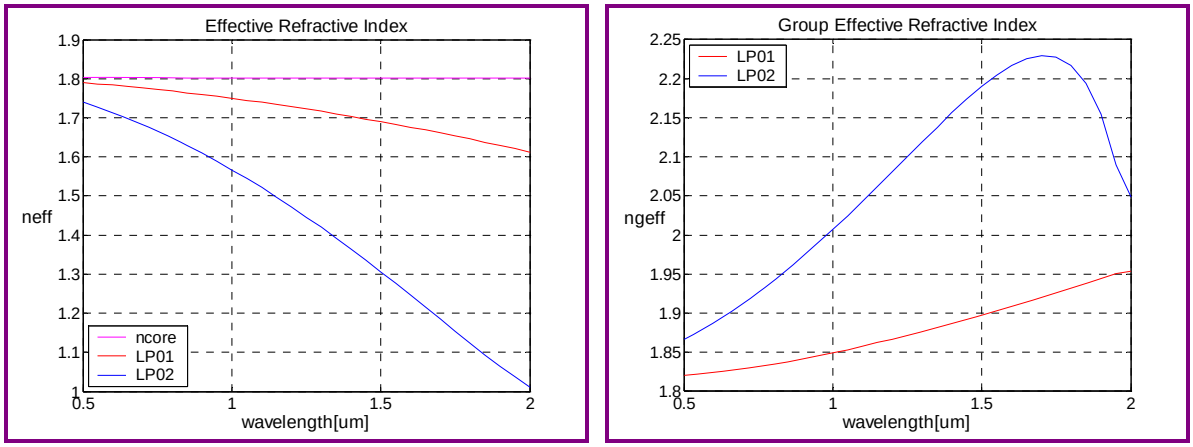

Figure 7-57. ERI and GERI of Litharge-Core Microstructure Devices(LP_{01}-LP_{02} Mode)

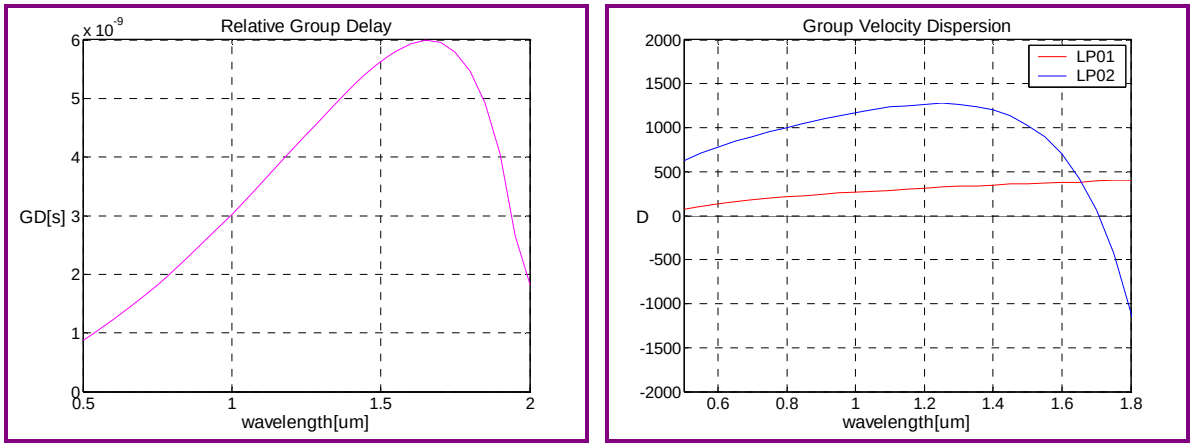

Figure 7-58. RGD and GVD of Litharge-Core Microstructure Devices(LP_{01}-LP_{02} Mode)

The RGD between the LP_{01} and LP_{02} modes at 1.55μm for the device length of 5.76m is 5.80ns. The GVDs are 369[ps/nm-km] and 899[ps/nm-km], and the DSs are 0.142[ps/nm^2-km] and -3.275[ps/nm^2-km], for the LP_{01} and LP_{02} modes at 1.55μm, respectively.

BISMITE-CORE

$$n_{core} = 55Bi_2O_3 \cdot 45B_2O_3$$

Silica-Clad Devices

$$n_{cladding} = silica,\ a = 0.81\mu m$$

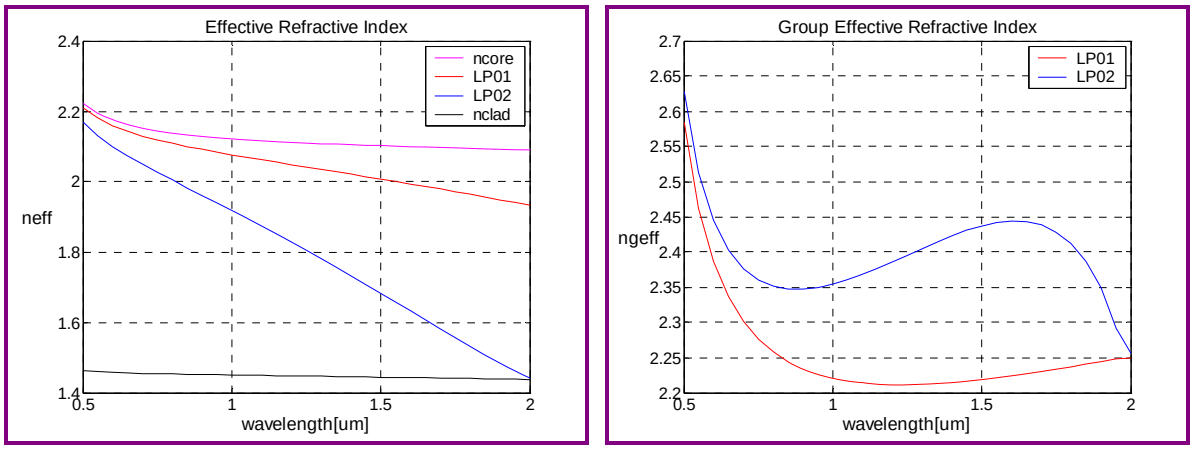

Figure 7-59. ERI and GERI of Bismite-Core Silica-Clad Devices(LP_{01}-LP_{02} Mode)

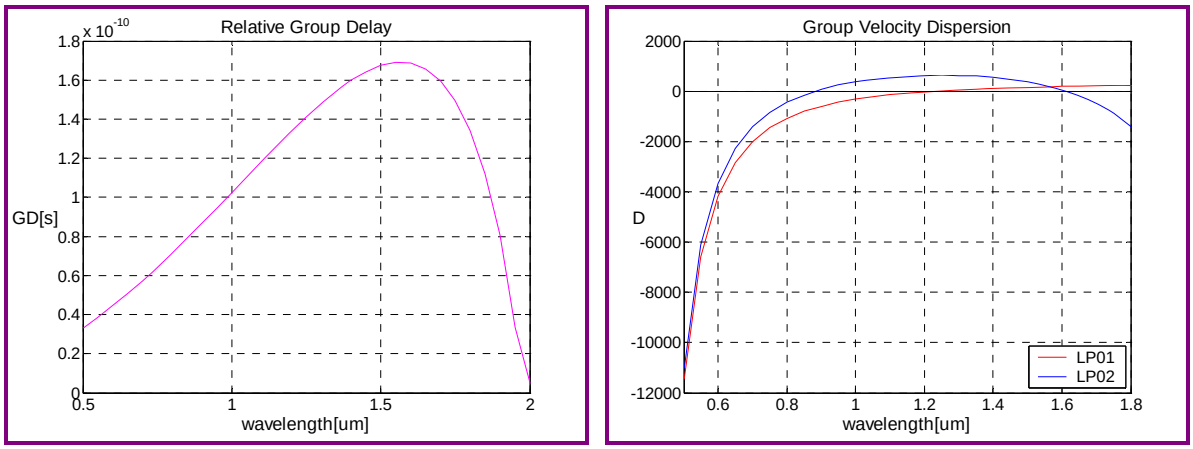

Figure 7-60. RGD and GVD of Bismite-Core Silica-Clad Devices(LP_{01}-LP_{02} Mode)

The RGD between the LP_{01} and LP_{02} modes at 1.55μm for the device length of 0.23m is 0.17ns. The GVDs are 173[ps/nm-km] and 237[ps/nm-km], and the DSs are 0.368[ps/nm^2-km] and -3.342[ps/nm^2-km], for the LP_{01} and LP_{02} modes at 1.55μm, respectively.

Microstructure Devices

$$n_{cladding} = air,\ a = 0.67\,\mu m$$

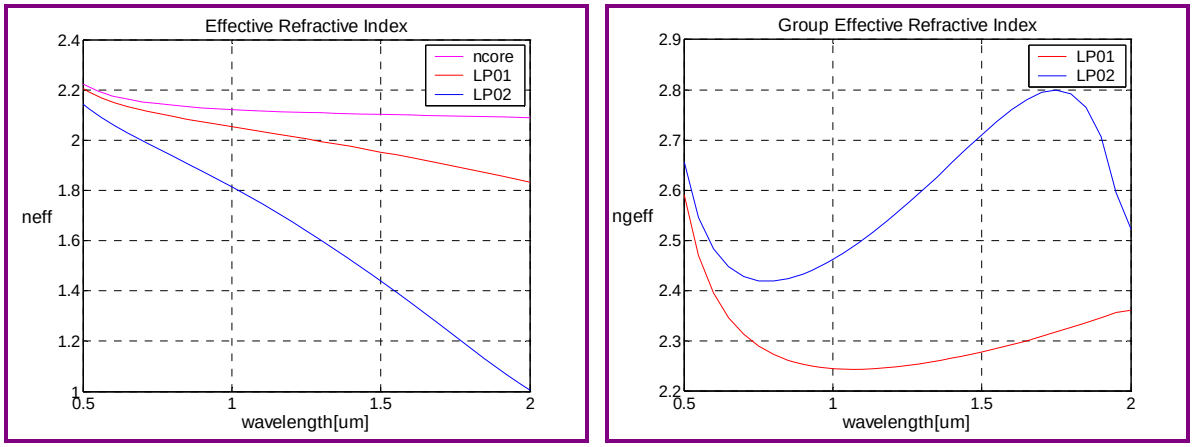

Figure 7-61. ERI and GERI of Bismite-Core Microstructure Devices(LP_{01}-LP_{02} Mode)

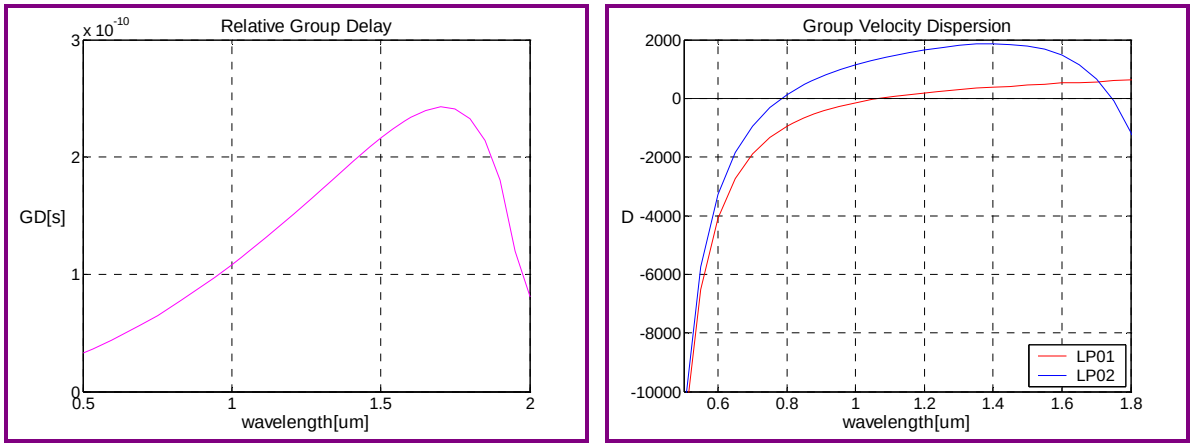

Figure 7-62. RGD and GVD of Bismite-Core Microstructure Devices(LP_{01}-LP_{02} Mode)

The RGD between the LP_{01} and LP_{02} modes at 1.55μm for the device length of 0.15m is 0.23ns. The GVDs are 493[ps/nm-km] and 1672[ps/nm-km], and the DSs are 0.673[ps/nm^2-km] and -3.305[ps/nm^2-km], for the LP_{01} and LP_{02} modes at 1.55μm, respectively.

TELLURITE-CORE

$$n_{core} = 75TeO_2 \cdot 25ZnO$$

Silica-Clad Devices

$$n_{cladding} = silica,\ a = 0.87\mu m$$

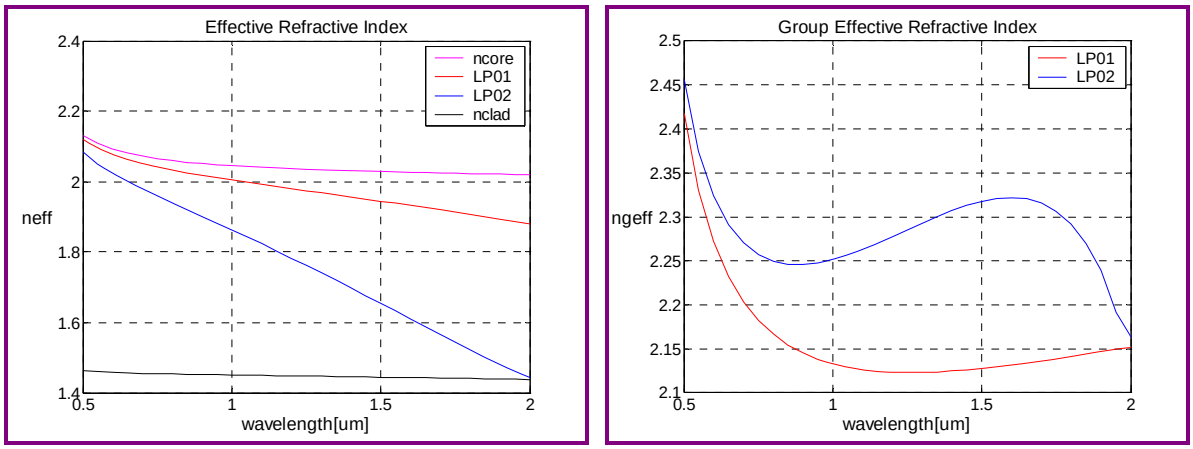

Figure 7-63. ERI and GERI of Tellurite-Core Silica-Clad Devices(LP_{01}-LP_{02} Mode)

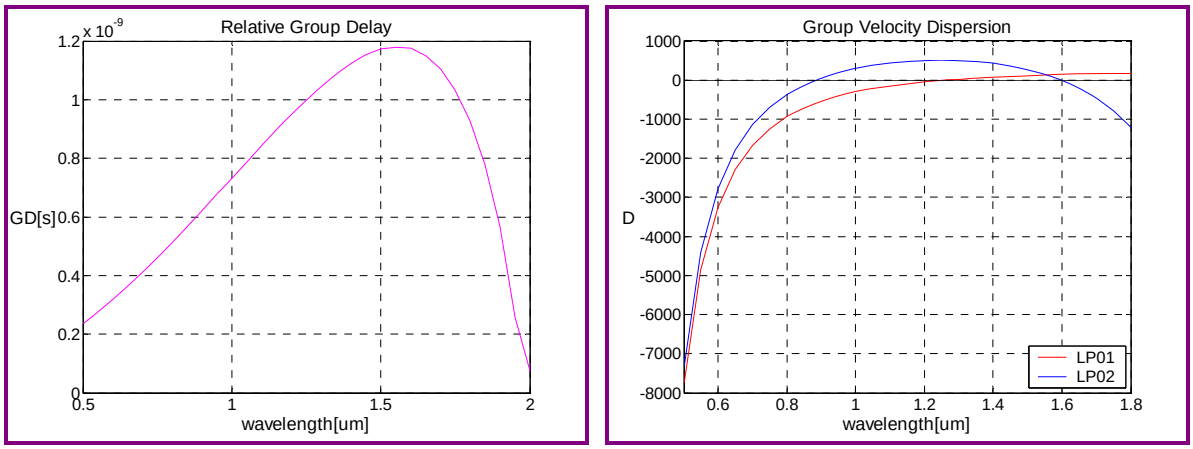

Figure 7-64. RGD and GVD of Tellurite-Core Silica-Clad Devices(LP_{01}-LP_{02} Mode)

The RGD between the LP_{01} and LP_{02} modes at 1.55μm for the device length of 1.85m is 1.18ns. The GVDs are 128[ps/nm-km] and 142[ps/nm-km], and the DSs are 0.267[ps/nm^2-km] and -2.733[ps/nm^2-km], for the LP_{01} and LP_{02} modes at 1.55μm, respectively.

Microstructure Devices

$$n_{cladding} = air,\ a = 0.70\mu m$$

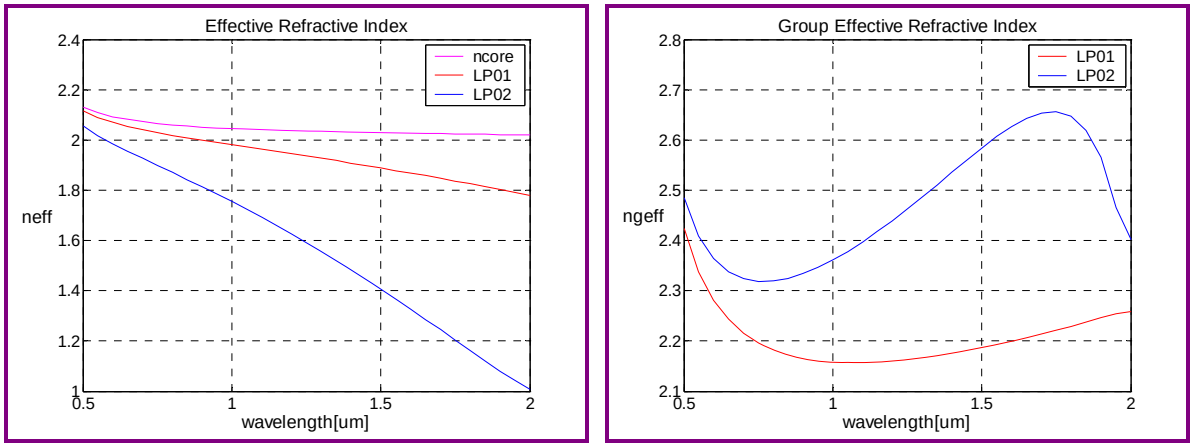

Figure 7-65. ERI and GERI of Tellurite-Core Microstructure Devices(LP_{01}-LP_{02} Mode)

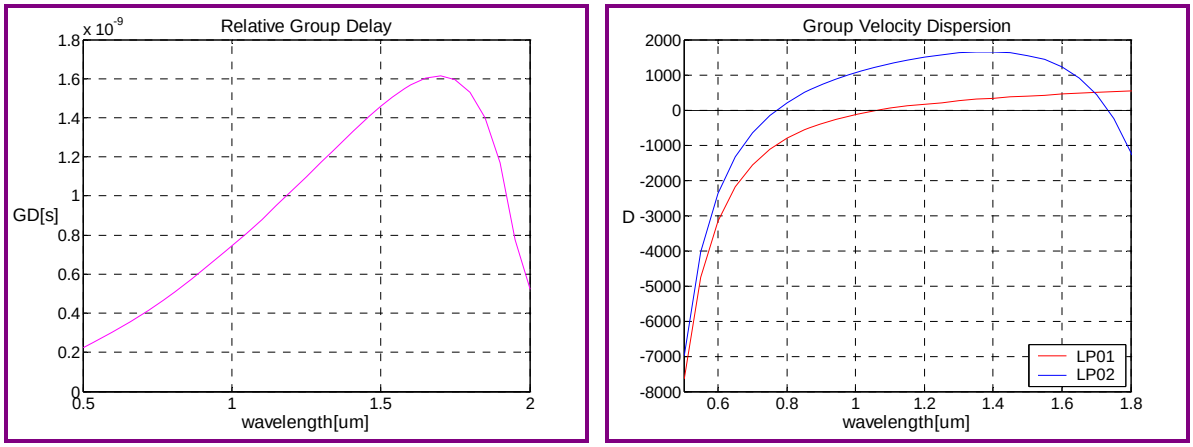

Figure 7-66. RGD and GVD of Tellurite-Core Microstructure Devices(LP_{01}-LP_{02} Mode)

The RGD between the LP_{01} and LP_{02} modes at 1.55μm for the device length of 1.10m is 1.52ns. The GVDs are 423[ps/nm-km] and 1427[ps/nm-km], and the DSs are 0.615[ps/nm^2-km] and -3.282[ps/nm^2-km], for the LP_{01} and LP_{02} modes at 1.55μm, respectively.

CHALCOGENIDE-CORE

$$n_{core} = 40As \cdot 60Se$$

Silica-Clad Devices

$$n_{cladding} = silica,\ a = 0.53\mu m$$

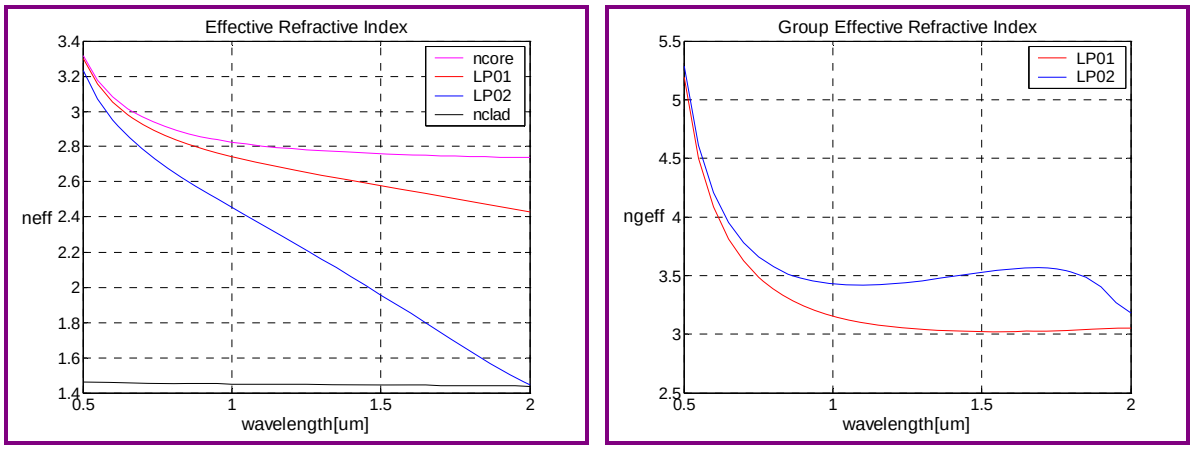

Figure 7-67. ERI and GERI of Chalcogenide-Core Silica-Clad Devices(LP_{01}-LP_{02} Mode)

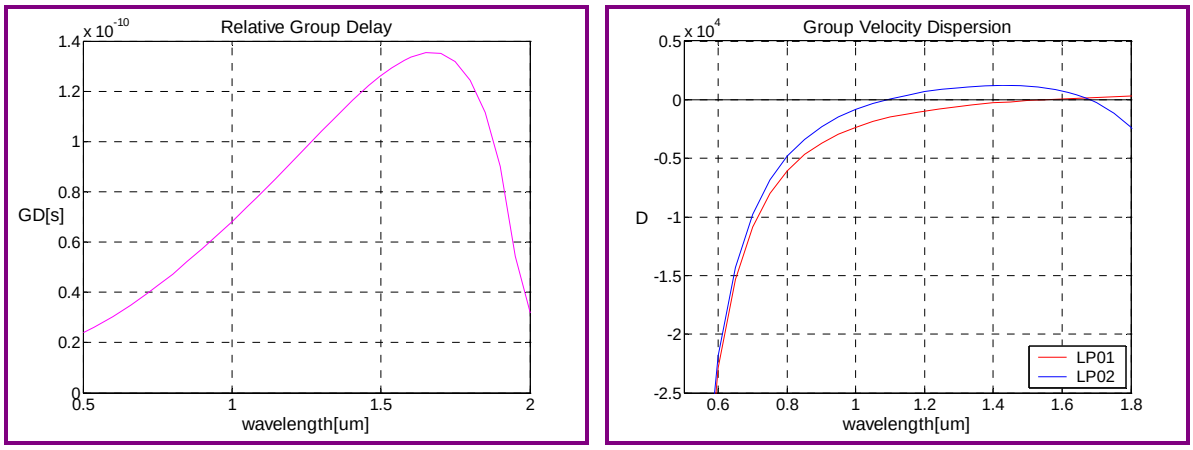

Figure 7-68. RGD and GVD of Chalcogenide-Core Silica-Clad Devices(LP_{01}-LP_{02} Mode)

The RGD between the LP_{01} and LP_{02} modes at 1.55μm for the device length of 0.075m is 0.13ns. The GVDs are -0.34[ps/nm-km] and 992[ps/nm-km], and the DSs are 1.591[ps/nm^2-km] and -4.067[ps/nm^2-km], for the LP_{01} and LP_{02} modes at 1.55μm, respectively.

Microstructure Devices

$$n_{cladding} = air,\ a = 0.48\mu m$$

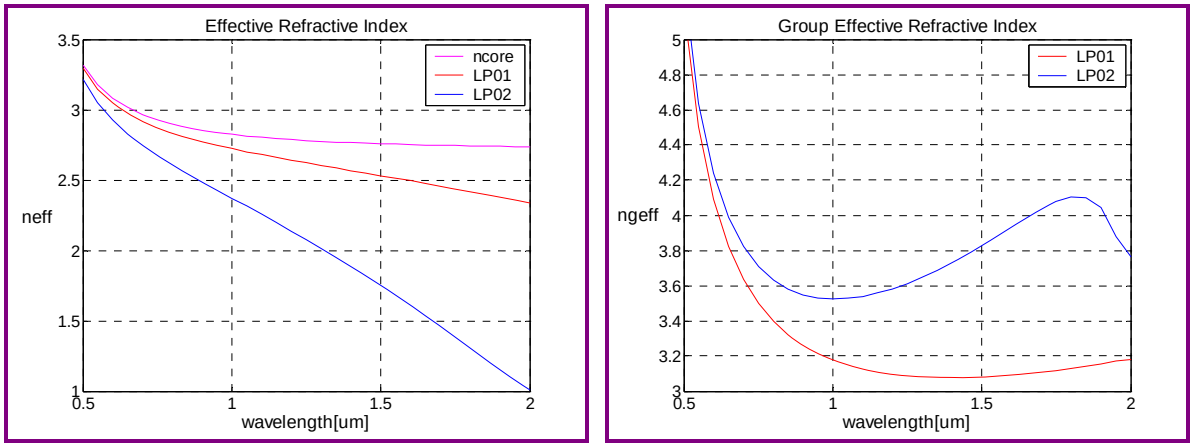

Figure 7-69. ERI and GERI of Chalcogenide-Core Microstructure Devices(LP_{01}-LP_{02} Mode)

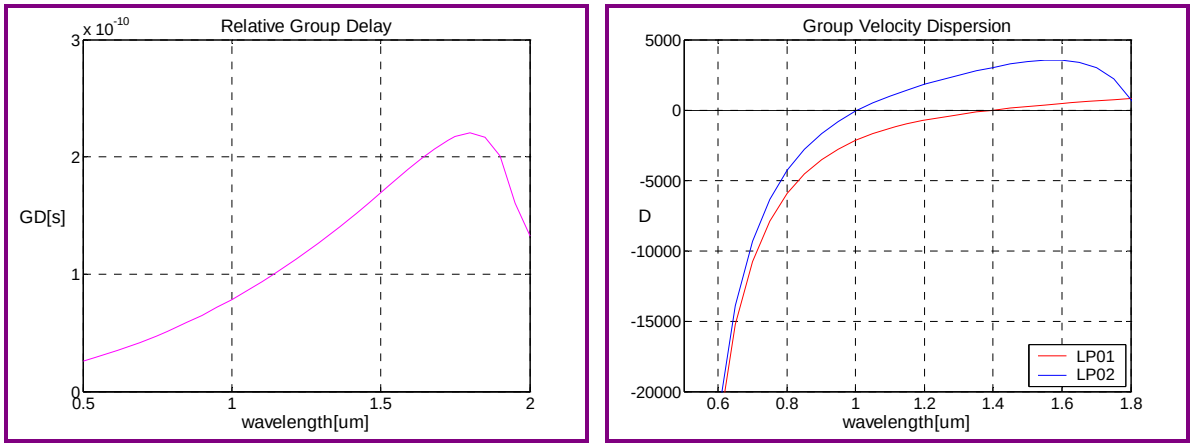

Figure 7-70. RGD and GVD of Chalcogenide-Core Microstructure Devices(LP_{01}-LP_{02} Mode)

The RGD between the LP_{01} and LP_{02} modes at 1.55μm for the device length of 0.068m is 0.18ns. The GVDs are 362[ps/nm-km] and 3542[ps/nm-km], and the DSs are 2.135[ps/nm^2-km] and 1.138[ps/nm^2-km], for the LP_{01} and LP_{02} modes at 1.55μm, respectively.

Table 7-19 summarizes the RGD, calculated from Equation (6.14), between the LP_{01} and LP_{02} modes of the signal pulse at 1.55μm for the required device length of SPM-induced devices and XPM-induced devices, shown in Tables 7-17 and 7-18, respectively. In addition, the GVD and the DS of the two modes at 1.55μm for nonlinear fiber devices based on LP_{01}-LP_{02} mode interference are provided.

Table 7-19. RGD between LP_{01} and LP_{02} Modes of Signal at 1.55μm, GVD at 1.55μm, and DS at 1.55μm for Nonlinear Fiber Devices based on LP_{01}-LP_{02} Mode Interference

Properties			Silica	Litharge	Bismite	Tellurite	Chalcogenide
RGD [ns] by SPM	S-clad		880	5.06	0.17	1.18	0.13
	MSF		97	5.80	0.23	1.52	0.18
RGD [ns] by XPM	S-clad		642	3.00	0.12	0.80	0.09
	MSF		68	4.20	0.17	1.10	0.10
GVD [ps/nm-km] at 1.55μm	S-clad	LP_{01}	14.33	126	173	128	-0.34
		LP_{02}	18.93	110	237	142	992
	MSF	LP_{01}	181	369	493	423	362
		LP_{02}	205	899	1672	1427	3542
DS [ps/nm^2-km] at 1.55μm	S-clad	LP_{01}	0.075	-0.021	0.368	0.267	1.591
		LP_{02}	0.037	-1.636	-3.342	-2.733	-4.067
	MSF	LP_{01}	0.027	0.142	0.673	0.615	2.135
		LP_{02}	-2.452	-3.275	-3.305	-3.282	1.138

7.4.3. Walk-Off Length

Table 7-20 presents the walk-off length, calculated from Equation (6.16), between the LP_{01} and LP_{02} modes of the signal pulse at 1.55μm with 10ps pulse width for nonlinear fiber devices based on LP_{01}-LP_{02} Mode Interference.

Table 7-20. Walk-Off Length between LP_{01} and LP_{02} Modes of Signal at 1.55μm with 10ps Pulse Width for Nonlinear Fiber Devices based on LP_{01}-LP_{02} Mode Interference

Walk-Off Length [m]	Silica	Litharge	Bismite	Tellurite	Chalcogenide
Silica-Cladding	0.86	0.0270	0.0140	0.0160	0.0058
MSF	0.02	0.0010	0.0066	0.0072	0.0038

7.5. Nonlinear Fiber Devices based on LP_{01}-LP_{11} Mode Interference

7.5.1. Required Device Length

This section provides the required device length for nonlinear fiber devices based on LP_{01}-LP_{11} mode interference. For all nonlinear fiber devices constructed with different glasses, the same normalized frequency V of 3.5 at 1.55μm was selected for reasonable comparison. Thus, the devices support only the LP_{01} and LP_{11} modes at 1.55μm.

Followings are the required device lengths obtained from Equation (6.6) for the SPM-induced nonlinear phase shift of π. It is assumed that the signal operates at 1.55μm and the LP_{01} and LP_{11} modes of the signal have the same power of 1W.

For SPM-Induced Nonlinear Fiber Devices

based on LP_{01}-LP_{11} Mode Interference

$$\lambda_S = 1.55\mu m,\ P_S = P_{01} = P_{11} = 1W,\ V = 3.5(at\,1.55\mu m)$$

SILICA-CORE

$$n_{core} = 1.4554,\ N_2 = 2.5\times10^{-20}\,m^2/W\ \ at\,1.55\mu m$$

Silica-Clad Devices

$$n_{cladding} = 1.4441(at\,1.55\mu m),\ a = 4.77\mu m$$

$$n_{eff\_01} = 1.4522,\ n_{eff\_11} = 1.4478,\ A_{eff\_01} = 60.45\mu m^2,\ A_{eff\_11} = 100.58\mu m^2$$

$$L_\pi^{SPM} = \frac{1.55\times10^{-6}}{2\times2.5\times10^{-20}\times1\times\left|\frac{1}{60.45\times10^{-12}} - \frac{1}{100.58\times10^{-12}}\right|} = 4.7[Km]$$

Microstructure Devices

$$n_{cladding} = 1,\ a = 0.82\mu m$$

$$n_{eff\_01} = 1.3263,\ n_{eff\_11} = 1.1341,\ A_{eff\_01} = 1.90\mu m^2,\ A_{eff\_11} = 2.97\mu m^2$$

$$L_\pi^{SPM} = \frac{1.55\times10^{-6}}{2\times2.5\times10^{-20}\times1\times\left|\frac{1}{1.90\times10^{-12}} - \frac{1}{2.97\times10^{-12}}\right|} = 164[m]$$

LITHARGE-CORE

$$n_{core} = 1.8017,\ N_2 = 40\times10^{-20}\, m^2/W\ \ at\, 1.55\,\mu m$$

Silica-Clad Devices

$$n_{cladding} = 1.4441 (at\, 1.55\,\mu m),\ a = 0.80\,\mu m$$

$$n_{eff\_01} = 1.7009,\ n_{eff\_11} = 1.5543,\ A_{eff\_01} = 1.75\,\mu m^2,\ A_{eff\_11} = 2.88\,\mu m^2$$

$$L_{\pi}^{SPM} = \frac{1.55\times10^{-6}}{2\times40\times10^{-20}\times1\times\left|\frac{1}{1.75\times10^{-12}} - \frac{1}{2.88\times10^{-12}}\right|} = 8.64[m]$$

Microstructure Devices

$$n_{cladding} = 1,\ a = 0.58\,\mu m$$

$$n_{eff\_01} = 1.5742,\ n_{eff\_11} = 1.2185,\ A_{eff\_01} = 1.02\,\mu m^2,\ A_{eff\_11} = 1.46\,\mu m^2$$

$$L_{\pi}^{SPM} = \frac{1.55\times10^{-6}}{2\times40\times10^{-20}\times1\times\left|\frac{1}{1.02\times10^{-12}} - \frac{1}{1.46\times10^{-12}}\right|} = 6.56[m]$$

Litharge-Clad Devices

$$n_{core} = 1.774,\ n_{cladding} = 1.728,\ a = 2.15\,\mu m$$

$$n_{eff\_01} = 1.7612,\ n_{eff\_11} = 1.7430,\ A_{eff\_01} = 12.39\,\mu m^2,\ A_{eff\_11} = 20.81\,\mu m^2$$

$$L_{\pi}^{SPM} = \frac{1.55\times10^{-6}}{2\times40\times10^{-20}\times1\times\left|\frac{1}{12.39\times10^{-12}} - \frac{1}{20.81\times10^{-12}}\right|} = 59.33[m]$$

BISMITE-CORE

$$n_{core} = 2.1009,\ N_2 = 1000 \times 10^{-20}\, m^2/W \ \ at\, 1.55\,\mu m$$

Silica-Clad Devices

$$n_{cladding} = 1.4441 (at\, 1.55\,\mu m),\ a = 0.57\,\mu m$$

$$n_{eff\_01} = 1.9147,\ n_{eff\_11} = 1.6375,\ A_{eff\_01} = 0.91\,\mu m^2,\ A_{eff\_11} = 1.43\,\mu m^2$$

$$L_{\pi}^{SPM} = \frac{1.55 \times 10^{-6}}{2 \times 1000 \times 10^{-20} \times 1 \times \left| \frac{1}{0.91 \times 10^{-12}} - \frac{1}{1.43 \times 10^{-12}} \right|} = 0.19[m]$$

Microstructure Devices

$$n_{cladding} = 1,\ a = 0.47\,\mu m$$

$$n_{eff\_01} = 1.7900,\ n_{eff\_11} = 1.2806,\ A_{eff\_01} = 0.71\,\mu m^2,\ A_{eff\_11} = 1.08\,\mu m^2$$

$$L_{\pi}^{SPM} = \frac{1.55 \times 10^{-6}}{2 \times 1000 \times 10^{-20} \times 1 \times \left| \frac{1}{0.71 \times 10^{-12}} - \frac{1}{1.08 \times 10^{-12}} \right|} = 0.16[m]$$

Bismite-Clad Devices

$$n_{core} = 2.22,\ n_{cladding} = 2.13,\ a = 1.38\,\mu m$$

$$n_{eff\_01} = 2.1949,\ n_{eff\_11} = 2.1596,\ A_{eff\_01} = 5.09\,\mu m^2,\ A_{eff\_11} = 8.62\,\mu m^2$$

$$L_{\pi}^{SPM} = \frac{1.55 \times 10^{-6}}{2 \times 1000 \times 10^{-20} \times 1 \times \left| \frac{1}{5.09 \times 10^{-12}} - \frac{1}{8.62 \times 10^{-12}} \right|} = 0.96[m]$$

TELLURITE-CORE

$$n_{core} = 2.0278,\ N_2 = 148\times10^{-20}\, m^2/W\ \ at\, 1.55\,\mu m$$

Silica-Clad Devices

$$n_{cladding} = 1.4441 (at\, 1.55\,\mu m),\ a = 0.61\,\mu m$$

$$n_{eff\_01} = 1.8625,\ n_{eff\_11} = 1.6179,\ A_{eff\_01} = 1.04\,\mu m^2,\ A_{eff\_11} = 1.64\,\mu m^2$$

$$L_{\pi}^{SPM} = \frac{1.55\times10^{-6}}{2\times148\times10^{-20}\times1\times\left|\frac{1}{1.04\times10^{-12}} - \frac{1}{1.64\times10^{-12}}\right|} = 1.49[m]$$

Microstructure Devices

$$n_{cladding} = 1,\ a = 0.49\,\mu m$$

$$n_{eff\_01} = 1.7371,\ n_{eff\_11} = 1.2663,\ A_{eff\_01} = 0.77\,\mu m^2,\ A_{eff\_11} = 1.15\,\mu m^2$$

$$L_{\pi}^{SPM} = \frac{1.55\times10^{-6}}{2\times148\times10^{-20}\times1\times\left|\frac{1}{0.77\times10^{-12}} - \frac{1}{1.15\times10^{-12}}\right|} = 1.22[m]$$

Tellurite-Clad Devices

$$n_{core} = 2.028,\ n_{cladding} = 1.983,\ a = 2.03\,\mu m$$

$$n_{eff\_01} = 2.0154,\ n_{eff\_11} = 1.9977,\ A_{eff\_01} = 11.03\,\mu m^2,\ A_{eff\_11} = 18.39\,\mu m^2$$

$$L_{\pi}^{SPM} = \frac{1.55\times10^{-6}}{2\times148\times10^{-20}\times1\times\left|\frac{1}{11.03\times10^{-12}} - \frac{1}{18.39\times10^{-12}}\right|} = 14.43[m]$$

CHALCOGENIDE-CORE

$$n_{core} = 2.7555,\ N_2 = 1250\times10^{-20}\,m^2/W\ \ at\,1.55\,\mu m$$

Silica-Clad Devices

$$n_{cladding} = 1.4441(at\,1.55\,\mu m),\ a = 0.37\,\mu m$$

$$n_{eff\_01} = 2.3839,\ n_{eff\_11} = 1.7932,\ A_{eff\_01} = 0.42\,\mu m^2,\ A_{eff\_11} = 0.60\,\mu m^2$$

$$L_{\pi}^{SPM} = \frac{1.55\times10^{-6}}{2\times1250\times10^{-20}\times1\times\left|\frac{1}{0.42\times10^{-12}} - \frac{1}{0.60\times10^{-12}}\right|} = 0.087[m]$$

Microstructure Devices

$$n_{cladding} = 1,\ a = 0.34\,\mu m$$

$$n_{eff\_01} = 2.2681,\ n_{eff\_11} = 1.4230,\ A_{eff\_01} = 0.39\,\mu m^2,\ A_{eff\_11} = 0.64\,\mu m^2$$

$$L_{\pi}^{SPM} = \frac{1.55\times10^{-6}}{2\times1250\times10^{-20}\times1\times\left|\frac{1}{0.39\times10^{-12}} - \frac{1}{0.64\times10^{-12}}\right|} = 0.062[m]$$

Chalcogenide-Clad Devices

$$n_{core} = 2.6,\ n_{cladding} = 2.443,\ a = 0.97\,\mu m$$

$$n_{eff\_01} = 2.5561,\ n_{eff\_11} = 2.4949,\ A_{eff\_01} = 2.52\,\mu m^2,\ A_{eff\_11} = 4.32\,\mu m^2$$

$$L_{\pi}^{SPM} = \frac{1.55\times10^{-6}}{2\times1250\times10^{-20}\times1\times\left|\frac{1}{2.52\times10^{-12}} - \frac{1}{4.32\times10^{-12}}\right|} = 0.375[m]$$

Table 7-21 summarizes the required device length with the same optical power in both modes of 1W for SPM-induced nonlinear fiber devices based on LP_{01}-LP_{11} mode interference when the signal which supports the LP_{01} and LP_{11} modes operates at 1.55μm.

Table 7-21. The Required Device Length with 1W Optical Power at 1.55μm for SPM-Induced Nonlinear Fiber Devices based on LP_{01}-LP_{11} Mode Interference

Device Length[m]	Silica	Litharge	Bismite	Tellurite	Chalcogenide
Silica-Cladding	4700	8.64	0.19	1.49	0.087
MSF	164	6.56	0.16	1.22	0.062
HNL Glass-Cladding	-	59.33	0.96	14.43	0.375

Followings are the required device lengths, obtained from Equation (6.7), for the XPM-induced nonlinear phase shift of π when the pump is much stronger than the signal. It is assumed that the signal operates at 1.55μm and almost all pump power of 1W is launched into the fundamental mode at 1.3μm.

For XPM-Induced Nonlinear Fiber Devices

based on LP_{01}-LP_{11} Mode Interference

$$\lambda_S = 1.55\mu m,\ \lambda_P = 1.3\mu m,\ P_P = 1W >> P_S,\ V = 3.5(at\,1.55\mu m)$$

SILICA-CORE

$$n_{core} = 1.4554,\ N_2 = 2.5\times10^{-20} m^2/W\ \ at\,1.55\mu m$$

Silica-Clad Devices

$$n_{cladding} = 1.4441(at\,1.55\mu m),\ a = 4.77\mu m$$

$$n_{eff\_01P} = 1.4530,\ A_{eff\_01S\_01P} = 57.69\mu m^2,\ A_{eff\_11S\_01P} = 99.76\mu m^2$$

$$L_\pi^{XPM} = \frac{1.55\times10^{-6}}{4\times2.5\times10^{-20}\times1\times\left|\frac{1}{57.69\times10^{-12}} - \frac{1}{99.76\times10^{-12}}\right|} = 2.1[Km]$$

Microstructure Devices

$$n_{cladding} = 1,\ a = 0.82\mu m$$

$$n_{eff\_01P} = 1.3598,\ A_{eff\_01S\_01P} = 1.76\mu m^2,\ A_{eff\_11S\_01P} = 2.96\mu m^2$$

$$L_\pi^{XPM} = \frac{1.55\times10^{-6}}{4\times2.5\times10^{-20}\times1\times\left|\frac{1}{1.76\times10^{-12}} - \frac{1}{2.96\times10^{-12}}\right|} = 67.29[m]$$

LITHARGE-CORE

$$n_{core} = 1.8017,\ N_2 = 40\times10^{-20} m^2/W\ \ at 1.55\mu m$$

Silica-Clad Devices

$$n_{cladding} = 1.4441 (at 1.55\mu m),\ a = 0.80\mu m$$

$$n_{eff\_01P} = 1.7261,\ A_{eff\_01S\_01P} = 1.65\mu m^2,\ A_{eff\_11S\_01P} = 2.83\mu m^2$$

$$L_{\pi}^{XPM} = \frac{1.55\times10^{-6}}{4\times40\times10^{-20}\times1\times\left|\frac{1}{1.65\times10^{-12}} - \frac{1}{2.83\times10^{-12}}\right|} = 3.83[m]$$

Microstructure Devices

$$n_{cladding} = 1,\ a = 0.58\mu m$$

$$n_{eff\_01P} = 1.6364,\ A_{eff\_01S\_01P} = 0.93\mu m^2,\ A_{eff\_11S\_01P} = 1.49\mu m^2$$

$$L_{\pi}^{XPM} = \frac{1.55\times10^{-6}}{4\times40\times10^{-20}\times1\times\left|\frac{1}{0.93\times10^{-12}} - \frac{1}{1.49\times10^{-12}}\right|} = 2.40[m]$$

Litharge-Clad Devices

$$n_{core} = 1.774,\ n_{cladding} = 1.728,\ a = 2.15\mu m$$

$$n_{eff\_01P} = 1.7642,\ A_{eff\_01S\_01P} = 11.76\mu m^2,\ A_{eff\_11S\_01P} = 20.59\mu m^2$$

$$L_{\pi}^{XPM} = \frac{1.55\times10^{-6}}{4\times40\times10^{-20}\times1\times\left|\frac{1}{11.76\times10^{-12}} - \frac{1}{20.59\times10^{-12}}\right|} = 26.57[m]$$

BISMITE-CORE

$$n_{core} = 2.1009,\ N_2 = 1000 \times 10^{-20}\, m^2/W \ \ at\, 1.55\,\mu m$$

Silica-Clad Devices

$$n_{cladding} = 1.4441 (at\, 1.55\,\mu m),\ a = 0.57\,\mu m$$

$$n_{eff\_01P} = 1.9631,\ A_{eff\_01S\_01P} = 0.85\,\mu m^2,\ A_{eff\_11S\_01P} = 1.42\,\mu m^2$$

$$L_{\pi}^{XPM} = \frac{1.55 \times 10^{-6}}{4 \times 1000 \times 10^{-20} \times 1 \times \left| \frac{1}{0.85 \times 10^{-12}} - \frac{1}{1.42 \times 10^{-12}} \right|} = 0.082[m]$$

Microstructure Devices

$$n_{cladding} = 1,\ a = 0.47\,\mu m$$

$$n_{eff\_01P} = 1.8775,\ A_{eff\_01S\_01P} = 0.64\,\mu m^2,\ A_{eff\_11S\_01P} = 0.98\,\mu m^2$$

$$L_{\pi}^{XPM} = \frac{1.55 \times 10^{-6}}{4 \times 1000 \times 10^{-20} \times 1 \times \left| \frac{1}{0.64 \times 10^{-12}} - \frac{1}{0.98 \times 10^{-12}} \right|} = 0.071[m]$$

Bismite-Clad Devices

$$n_{core} = 2.22,\ n_{cladding} = 2.13,\ a = 1.38\,\mu m$$

$$n_{eff\_01P} = 2.2009,\ A_{eff\_01S\_01P} = 4.84\,\mu m^2,\ A_{eff\_11S\_01P} = 8.54\,\mu m^2$$

$$L_{\pi}^{XPM} = \frac{1.55 \times 10^{-6}}{4 \times 1000 \times 10^{-20} \times 1 \times \left| \frac{1}{4.84 \times 10^{-12}} - \frac{1}{8.54 \times 10^{-12}} \right|} = 0.433[m]$$

TELLURITE-CORE

$$n_{core} = 2.0278,\ N_2 = 148\times10^{-20}\,m^2/W\ \ at\,1.55\,\mu m$$

Silica-Clad Devices

$$n_{cladding} = 1.4441(at\,1.55\,\mu m),\ a = 0.61\,\mu m$$

$$n_{eff\_01P} = 1.9051,\ A_{eff\_01S\_01P} = 0.97\,\mu m^2,\ A_{eff\_11S\_01P} = 1.64\,\mu m^2$$

$$L_{\pi}^{XPM} = \frac{1.55\times10^{-6}}{4\times148\times10^{-20}\times1\times\left|\frac{1}{0.97\times10^{-12}} - \frac{1}{1.64\times10^{-12}}\right|} = 0.62[m]$$

Microstructure Devices

$$n_{cladding} = 1,\ a = 0.49\,\mu m$$

$$n_{eff\_01P} = 1.8184,\ A_{eff\_01S\_01P} = 0.70\,\mu m^2,\ A_{eff\_11S\_01P} = 1.07\,\mu m^2$$

$$L_{\pi}^{XPM} = \frac{1.55\times10^{-6}}{4\times148\times10^{-20}\times1\times\left|\frac{1}{0.70\times10^{-12}} - \frac{1}{1.07\times10^{-12}}\right|} = 0.53[m]$$

Tellurite-Clad Devices

$$n_{core} = 2.028,\ n_{cladding} = 1.983,\ a = 2.03\,\mu m$$

$$n_{eff\_01P} = 2.0184,\ A_{eff\_01S\_01P} = 10.48\,\mu m^2,\ A_{eff\_11S\_01P} = 18.26\,\mu m^2$$

$$L_{\pi}^{XPM} = \frac{1.55\times10^{-6}}{4\times148\times10^{-20}\times1\times\left|\frac{1}{10.48\times10^{-12}} - \frac{1}{18.26\times10^{-12}}\right|} = 6.44[m]$$

CHALCOGENIDE-CORE

$$n_{core} = 2.7555,\ N_2 = 1250\times10^{-20}\,m^2/W\ \ at\,1.55\,\mu m$$

Silica-Clad Devices

$$n_{cladding} = 1.4441(at\,1.55\,\mu m),\ a = 0.37\,\mu m$$

$$n_{eff\_01P} = 2.4865,\ A_{eff\_01S\_01P} = 0.39\,\mu m^2,\ A_{eff\_11S\_01P} = 0.61\,\mu m^2$$

$$L_{\pi}^{XPM} = \frac{1.55\times10^{-6}}{4\times1250\times10^{-20}\times1\times\left|\frac{1}{0.39\times10^{-12}} - \frac{1}{0.61\times10^{-12}}\right|} = 0.034[m]$$

Microstructure Devices

$$n_{cladding} = 1,\ a = 0.34\,\mu m$$

$$n_{eff\_01P} = 2.4112,\ A_{eff\_01S\_01P} = 0.35\,\mu m^2,\ A_{eff\_11S\_01P} = 0.57\,\mu m^2$$

$$L_{\pi}^{XPM} = \frac{1.55\times10^{-6}}{4\times1250\times10^{-20}\times1\times\left|\frac{1}{0.35\times10^{-12}} - \frac{1}{0.57\times10^{-12}}\right|} = 0.028[m]$$

Chalcogenide-Clad Devices

$$n_{core} = 2.6,\ n_{cladding} = 2.443,\ a = 0.97\,\mu m$$

$$n_{eff\_01P} = 2.5666,\ A_{eff\_01S\_01P} = 2.39\,\mu m^2,\ A_{eff\_11S\_01P} = 4.28\,\mu m^2$$

$$L_{\pi}^{XPM} = \frac{1.55\times10^{-6}}{4\times1250\times10^{-20}\times1\times\left|\frac{1}{2.39\times10^{-12}} - \frac{1}{4.28\times10^{-12}}\right|} = 0.168[m]$$

Table 7-22 summarizes the required device length with a pump power of 1W for XPM-induced nonlinear fiber devices based on LP_{01}-LP_{11} mode interference when the signal which supports the LP_{01} and LP_{11} modes operates at 1.55μm and the control which supports the fundamental mode operates at 1.3μm.

Table 7-22. The Required Device Length with 1W Pump Power for XPM-Induced Nonlinear Fiber Devices based on LP_{01}-LP_{11} Mode Interference (Signal at 1.55μm and Pump at 1.3μm)

Device Length[m]	Silica	Litharge	Bismite	Tellurite	Chalcogenide
Silica-Cladding	2100	3.83	0.082	0.62	0.034
MSF	67.29	2.40	0.071	0.53	0.028
HNL Glass-Cladding	-	26.57	0.433	6.44	0.168

7.5.2. Relative Group Delay, Group-Velocity Dispersion, and Dispersion Slope

This section provides the ERI, the GERI, the GVD, and the DS of the LP_{01} and LP_{11} modes in the devices. In addition, graphs of the RGD between the LP_{01} and LP_{11} modes of the signal pulse at 1.55μm for the required device length of the SPM-induced devices are provided. Similarly, in the graphs, although the required device length should be changed according to the wavelength, the same required device length for 1.55μm was used for all wavelengths to roughly see the extent and trend of the RGD. To assess the applicability of devices for time-dependent applications, values of the RGD between the modes of the SPM-induced and XPM-induced devices at 1.55μm signal for the required device length were also calculated.

SILICA-CORE

$$n_{core} = slightly\ GeO_2 - doped\ \ silica$$

Silica-Clad Devices

$$n_{cladding} = silica,\ a = 4.77\,\mu m$$

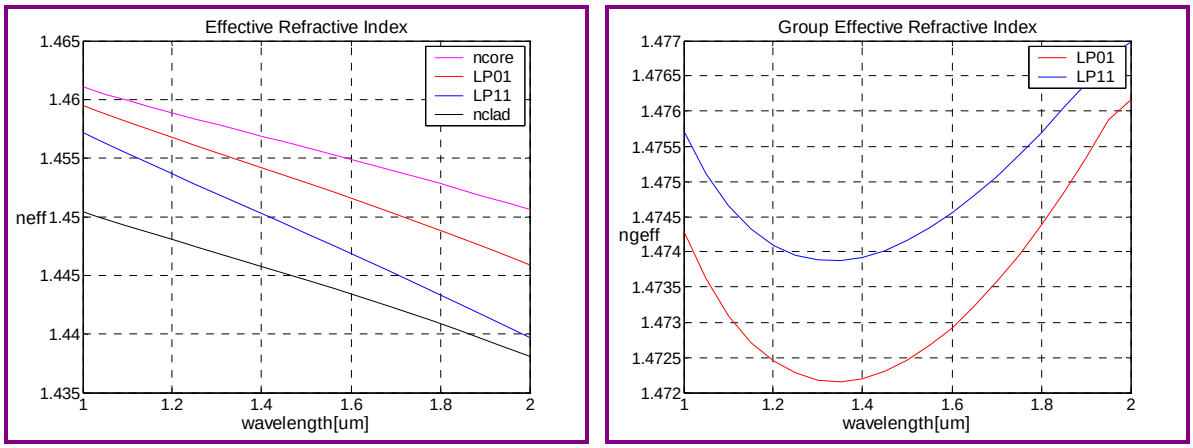

Figure 7-71. ERI and GERI of Silica-Core Silica-Clad Devices(LP_{01}-LP_{11} Mode)

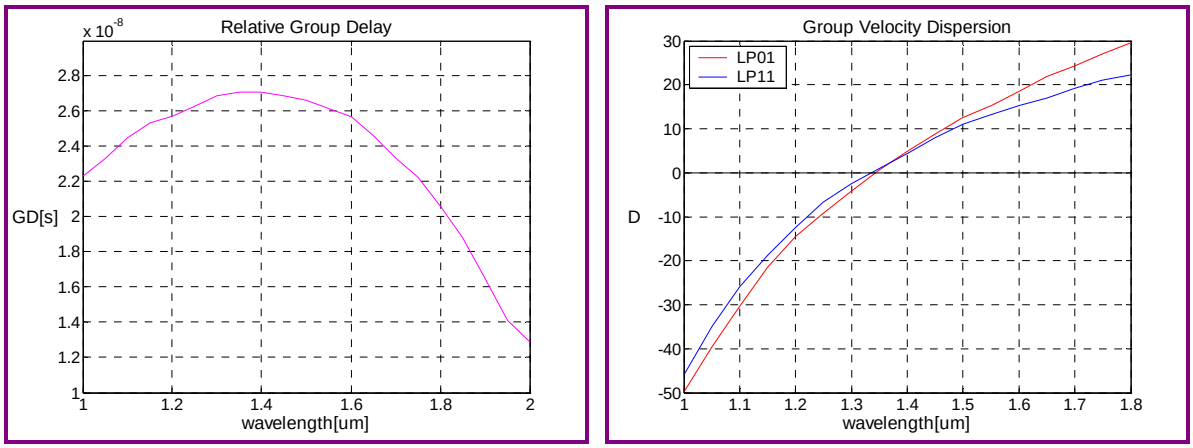

Figure 7-72. RGD and GVD of Silica-Core Silica-Clad Devices(LP_{01}-LP_{11} Mode)

The RGD between the LP_{01} and LP_{11} modes at 1.55μm for the device length of 4.7Km is 26ns. The GVDs are 15.33[ps/nm-km] and 13.26[ps/nm-km], and the DSs are 0.059[ps/nm^2-km] and 0.038[ps/nm^2-km], for the LP_{01} and LP_{11} modes at 1.55μm, respectively.

Microstructure Devices

$$n_{cladding} = air,\ a = 0.82\mu m$$

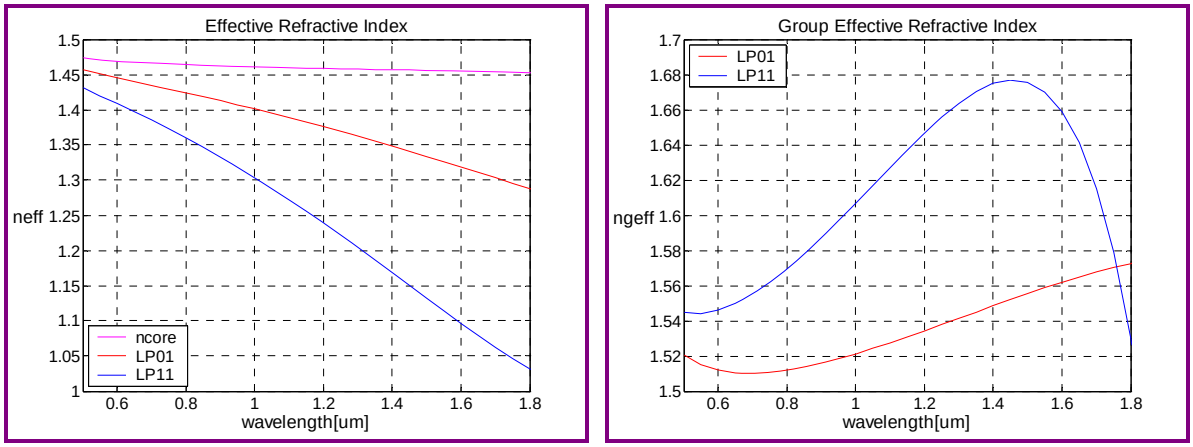

Figure 7-73. ERI and GERI of Silica-Core Microstructure Devices(LP_{01}-LP_{11} Mode)

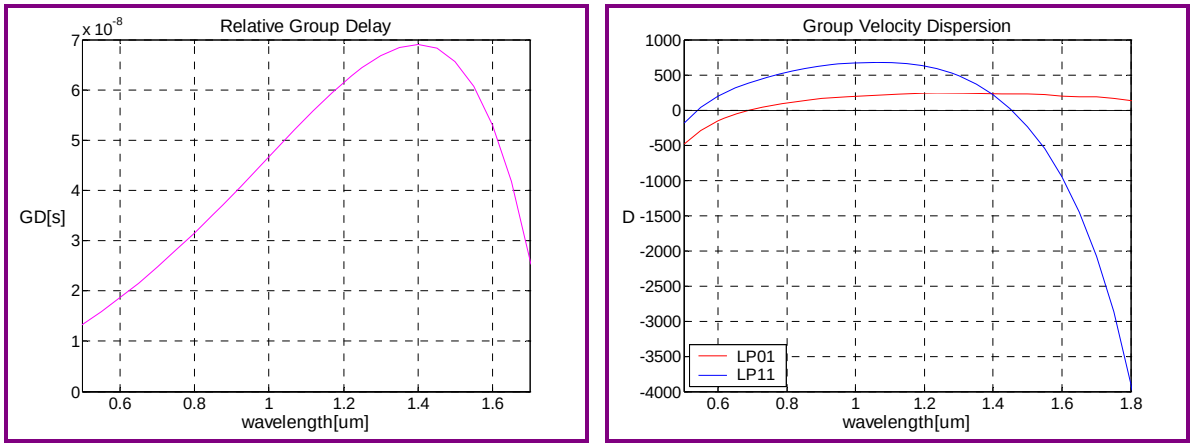

Figure 7-74. RGD and GVD of Silica-Core Microstructure Devices(LP_{01}-LP_{11} Mode)

The RGD between the LP_{01} and LP_{11} modes at 1.55μm for the device length of 164m is 61ns. The GVDs are 222[ps/nm-km] and -553[ps/nm-km], and the DSs are -0.277[ps/nm^2-km] and -7.103[ps/nm^2-km], for the LP_{01} and LP_{11} modes at 1.55μm, respectively.

LITHARGE-CORE

$$n_{core} = SF57$$

Silica-Clad Devices

$$n_{cladding} = silica,\ a = 0.80\mu m$$

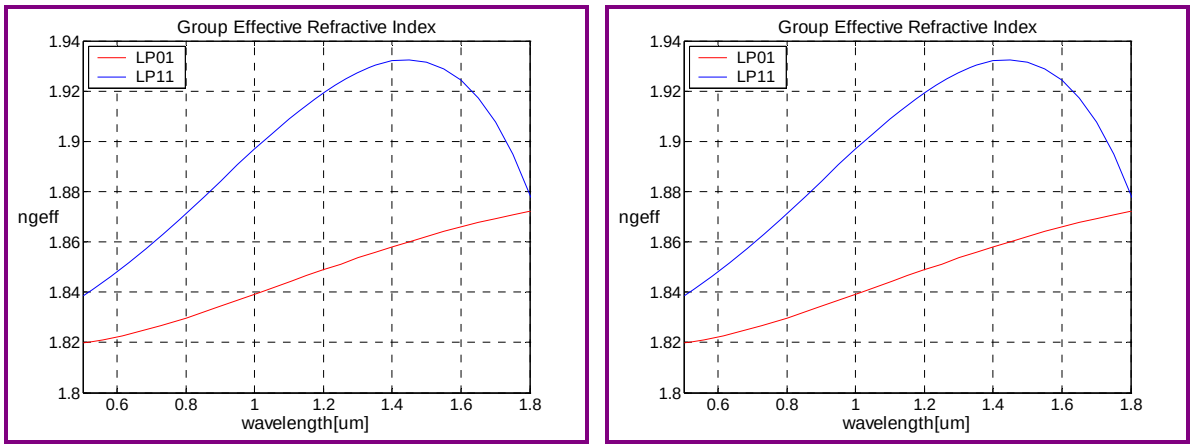

Figure 7-75. ERI and GERI of Litharge-Core Silica-Clad Devices(LP_{01}-LP_{11} Mode)

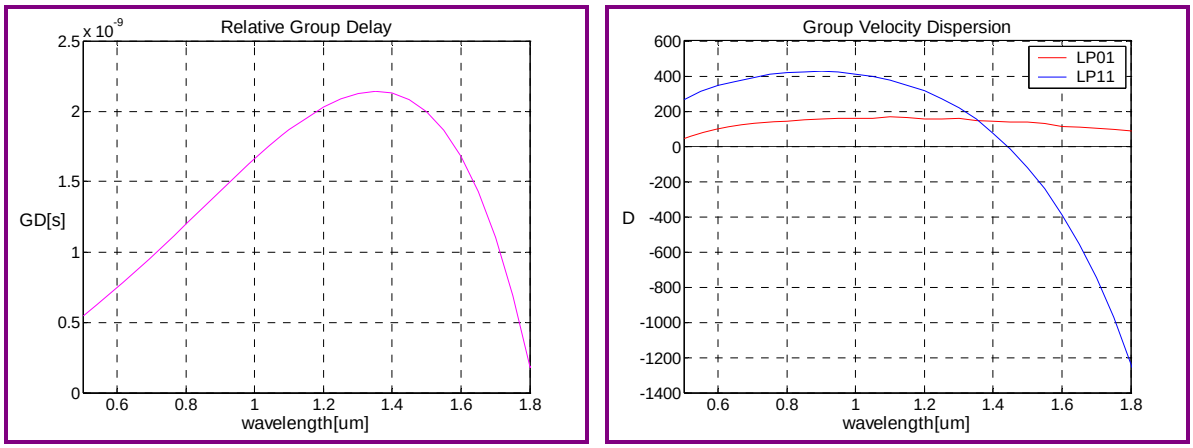

Figure 7-76. RGD and GVD of Litharge-Core Silica-Clad Devices(LP_{01}-LP_{11} Mode)

The RGD between the LP_{01} and LP_{11} modes at 1.55μm for the device length of 8.64m is 1.86ns. The GVDs are 131[ps/nm-km] and -242[ps/nm-km], and the DSs are -0.224[ps/nm^2-km] and -2.689[ps/nm^2-km], for the LP_{01} and LP_{11} modes at 1.55μm, respectively.

Microstructure Devices

$$n_{cladding} = air,\ a = 0.58\mu m$$

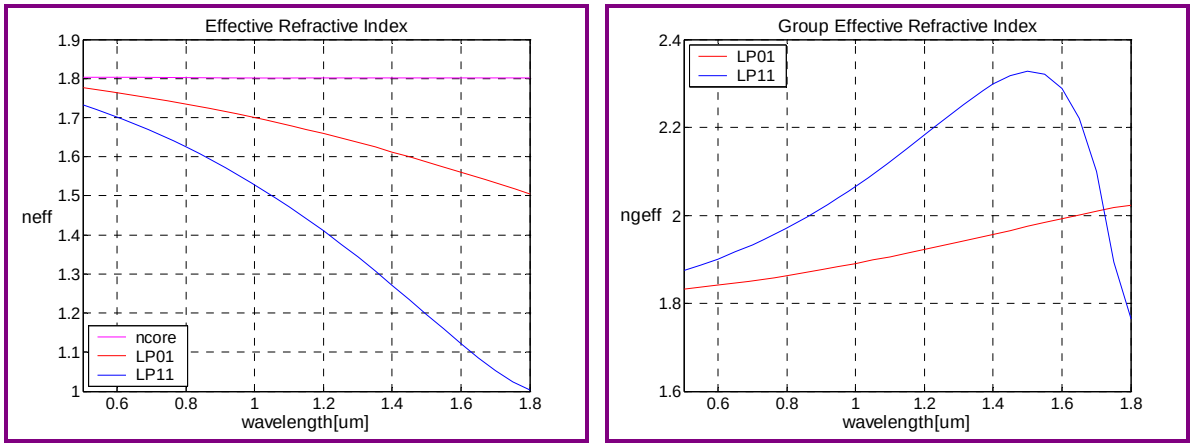

Figure 7-77. ERI and GERI of Litharge-Core Microstructure Devices(LP_{01}-LP_{11} Mode)

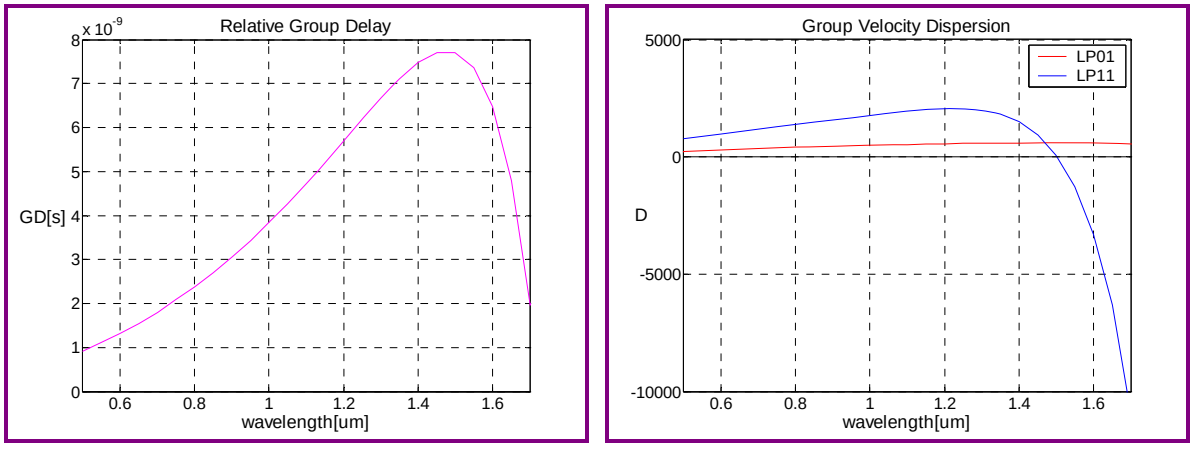

Figure 7-78. RGD and GVD of Litharge-Core Microstructure Devices(LP_{01}-LP_{11} Mode)

The RGD between the LP_{01} and LP_{11} modes at 1.55μm for the device length of 6.56m is 7.36ns. The GVDs are 596[ps/nm-km] and -1284[ps/nm-km], and the DSs are -0.076[ps/nm^2-km] and -33.769[ps/nm^2-km], for the LP_{01} and LP_{11} modes at 1.55μm, respectively.

BISMITE-CORE

$$n_{core} = 55Bi_2O_3 \cdot 45B_2O_3$$

Silica-Clad Devices

$$n_{cladding} = silica,\ a = 0.57\mu m$$

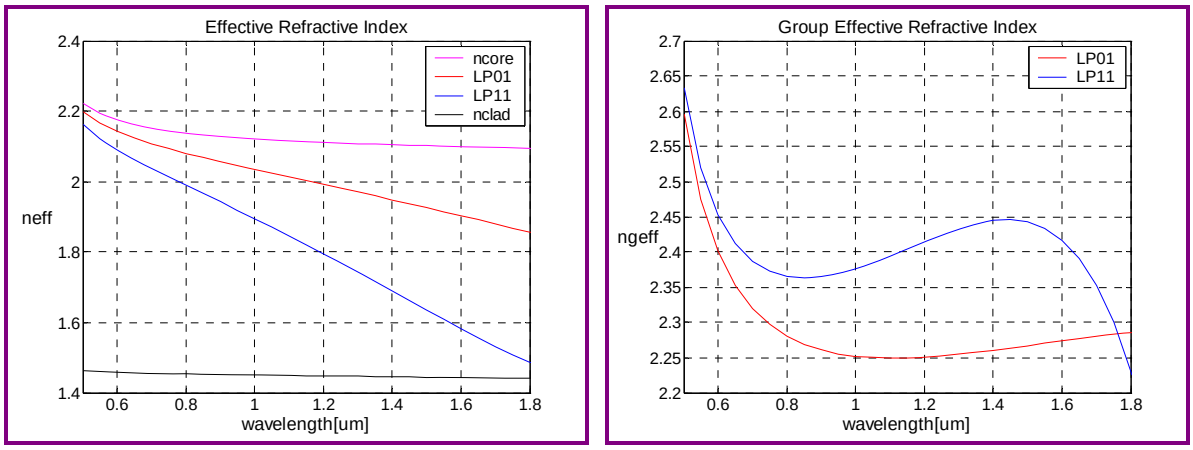

Figure 7-79. ERI and GERI of Bismite-Core Silica-Clad Devices(LP_{01}-LP_{11} Mode)

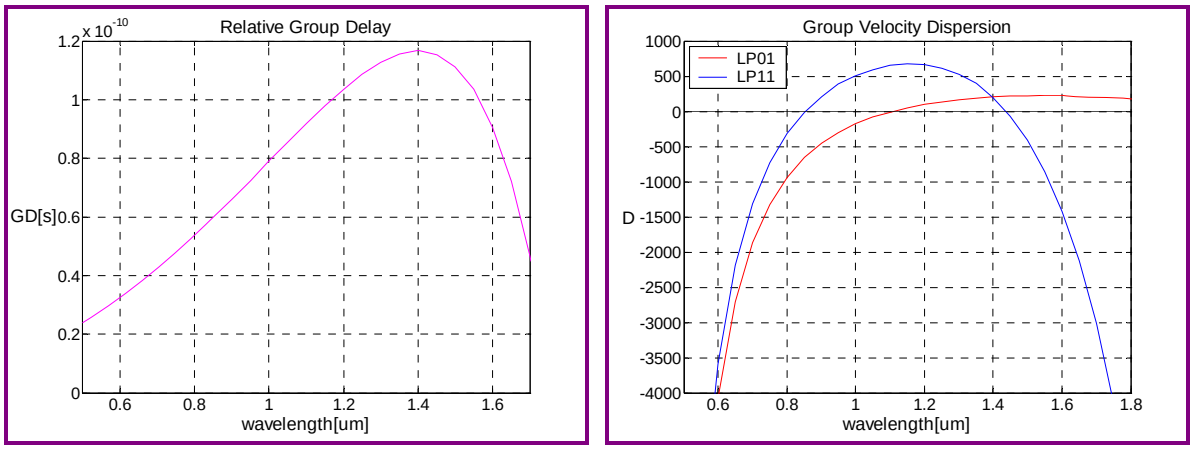

Figure 7-80. RGD and GVD of Bismite-Core Silica-Clad Devices(LP_{01}-LP_{11} Mode)

The RGD between the LP_{01} and LP_{11} modes at 1.55μm for the device length of 0.19m is 0.10ns. The GVDs are 229[ps/nm-km] and -858[ps/nm-km], and the DSs are 0.087[ps/nm^2-km] and -10.107[ps/nm^2-km], for the LP_{01} and LP_{11} modes at 1.55μm, respectively.

Microstructure Devices

$$n_{cladding} = air,\ a = 0.47\,\mu m$$

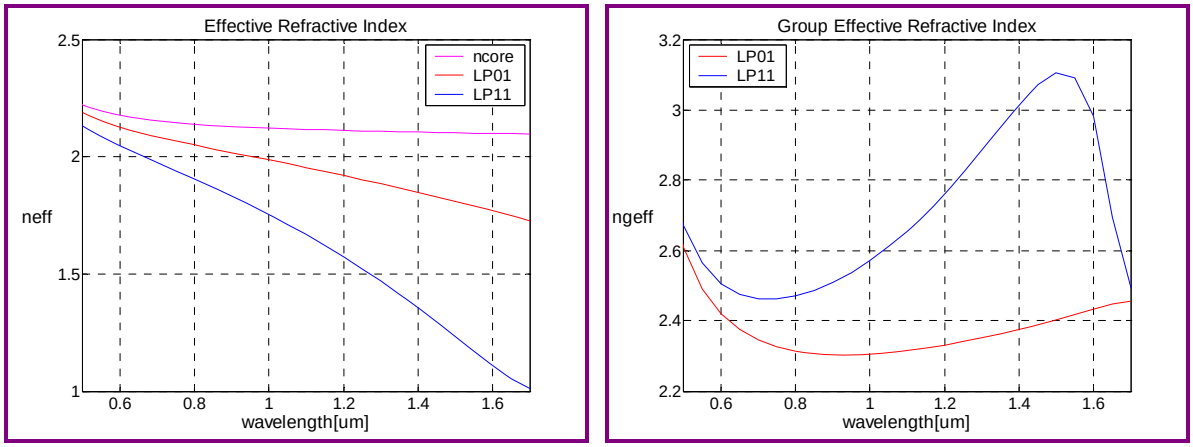

Figure 7-81. ERI and GERI of Bismite-Core Microstructure Devices(LP_{01}-LP_{11} Mode)

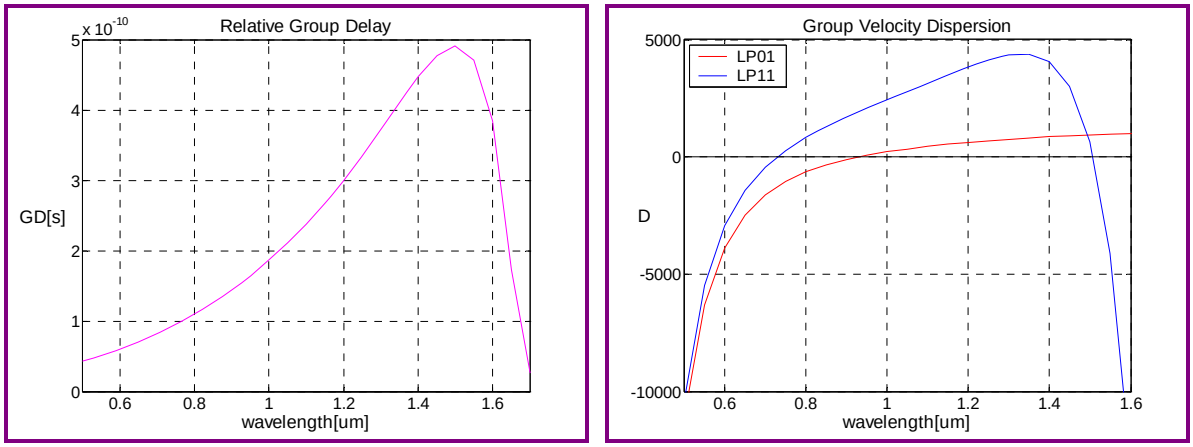

Figure 7-82. RGD and GVD of Bismite-Core Microstructure Devices(LP_{01}-LP_{11} Mode)

The RGD between the LP_{01} and LP_{11} modes at 1.55μm for the device length of 0.16m is 0.47ns. The GVDs are 978[ps/nm-km] and -4102[ps/nm-km], and the DSs are 0.626[ps/nm^2-km] and -139[ps/nm^2-km], for the LP_{01} and LP_{11} modes at 1.55μm, respectively.

TELLURITE-CORE

$$n_{core} = 75TeO_2 \cdot 25ZnO$$

Silica-Clad Devices

$$n_{cladding} = silica,\ a = 0.61\mu m$$

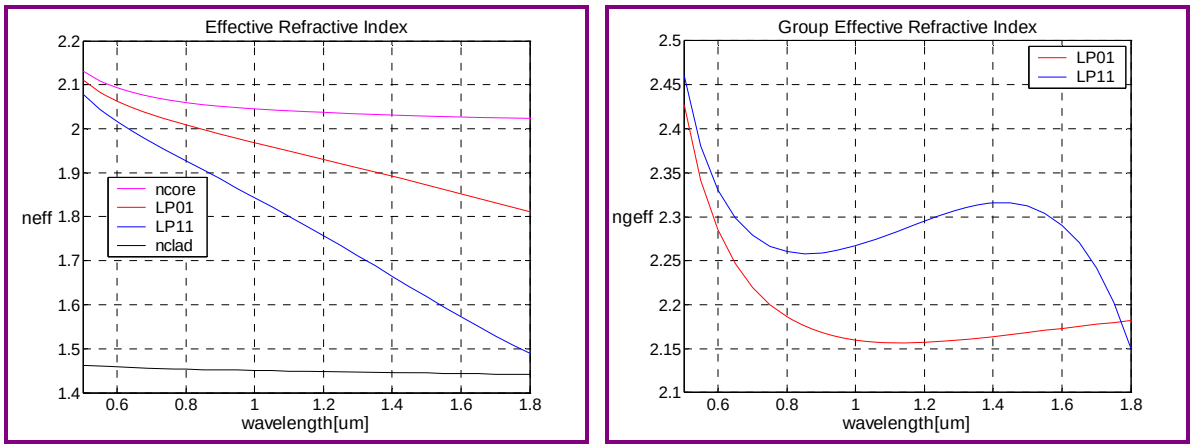

Figure 7-83. ERI and GERI of Tellurite-Core Silica-Clad Devices(LP_{01}-LP_{11} Mode)

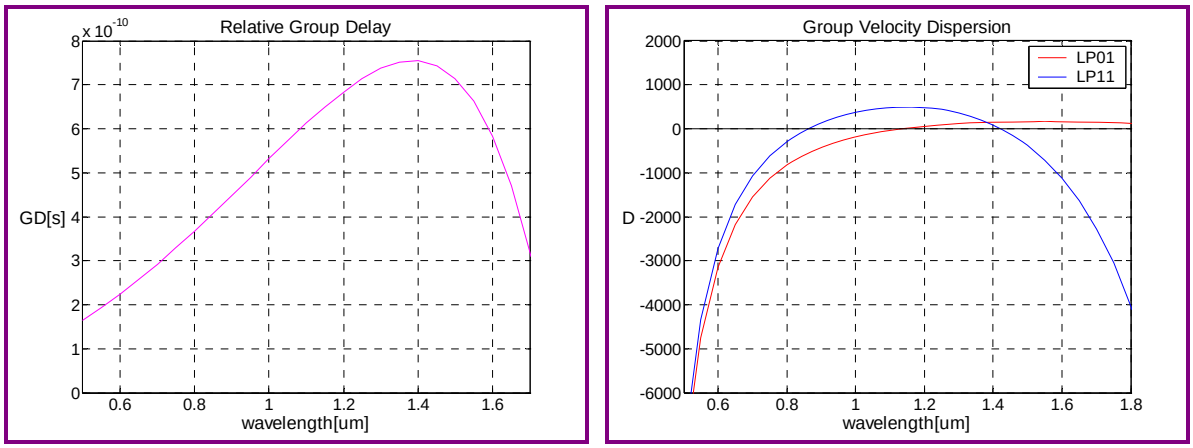

Figure 7-84. RGD and GVD of Tellurite-Core Silica-Clad Devices(LP_{01}-LP_{11} Mode)

The RGD between the LP_{01} and LP_{11} modes at 1.55μm for the device length of 1.49m is 0.66ns. The GVDs are 164[ps/nm-km] and -720[ps/nm-km], and the DSs are -0.027[ps/nm^2-km] and -7.488[ps/nm^2-km], for the LP_{01} and LP_{11} modes at 1.55μm, respectively.

Microstructure Devices

$$n_{cladding} = air,\ a = 0.49\mu m$$

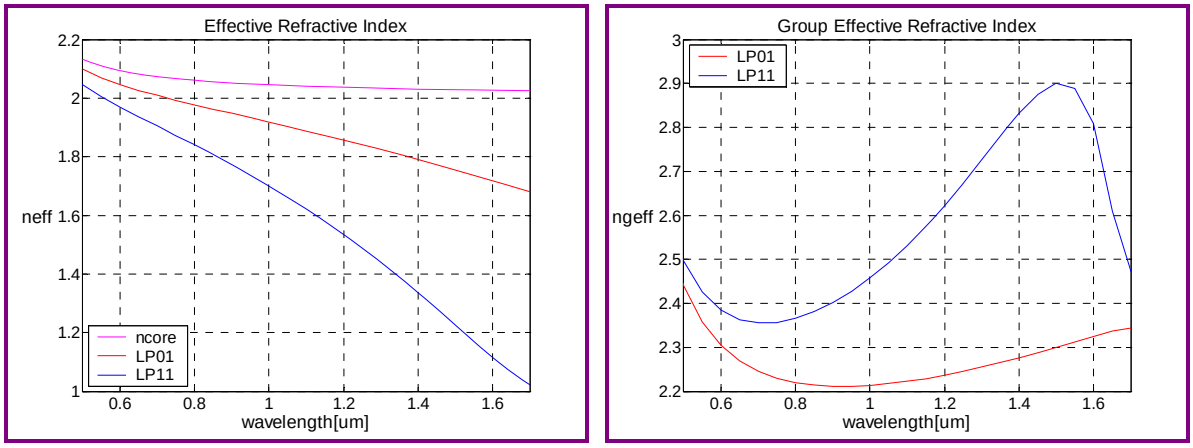

Figure 7-85. ERI and GERI of Tellurite-Core Microstructure Devices(LP_{01}-LP_{11} Mode)

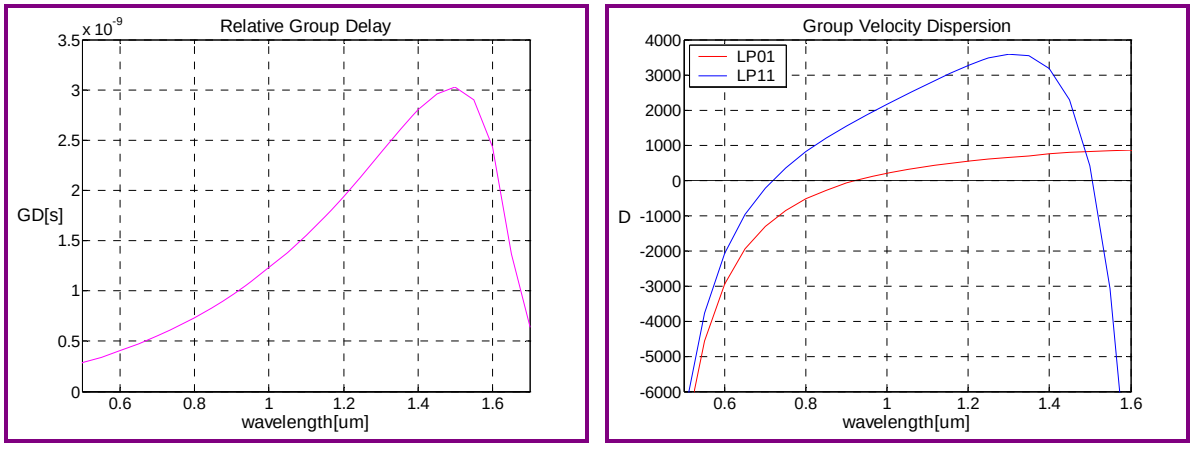

Figure 7-86. RGD and GVD of Tellurite-Core Microstructure Devices(LP_{01}-LP_{11} Mode)

The RGD between the LP_{01} and LP_{11} modes at 1.55μm for the device length of 1.22m is 2.89ns. The GVDs are 836 [ps/nm-km] and -3084[ps/nm-km], and the DSs are 0.413[ps/nm^2-km] and -97.353[ps/nm^2-km], for the LP_{01} and LP_{11} modes at 1.55μm, respectively.

CHALCOGENIDE-CORE

$$n_{core} = 40As \cdot 60Se$$

Silica-Clad Devices

$$n_{cladding} = silica,\ a = 0.37\mu m$$

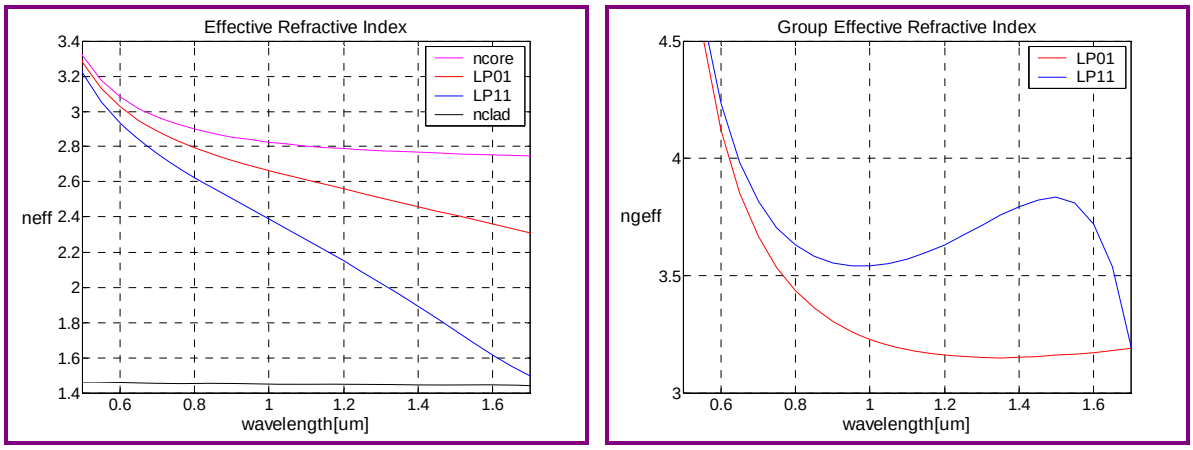

Figure 7-87. ERI and GERI of Chalcogenide-Core Silica-Clad Devices(LP_{01}-LP_{11} Mode)

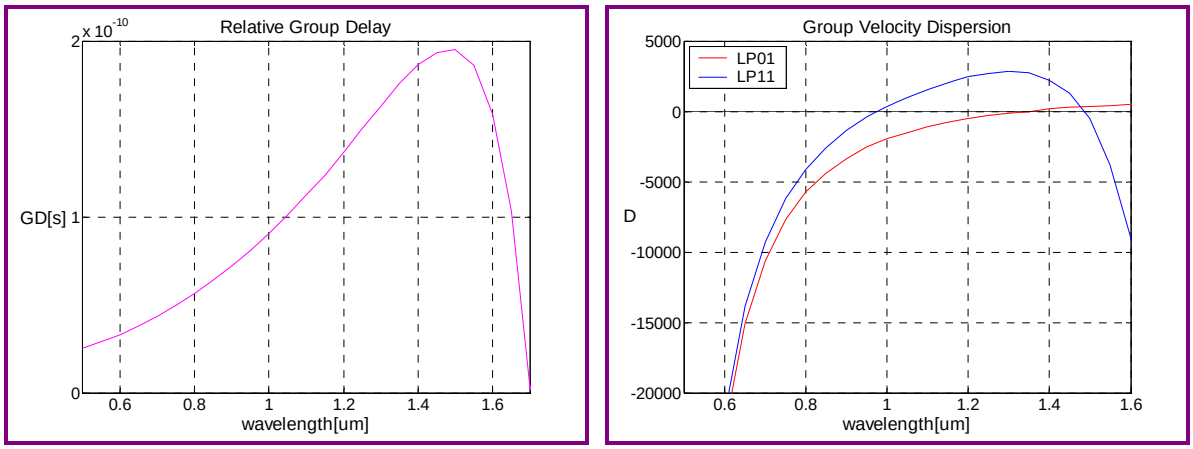

Figure 7-88. RGD and GVD of Chalcogenide-Core Silica-Clad Devices(LP_{01}-LP_{11} Mode)

The RGD between the LP_{01} and LP_{11} modes at 1.55μm for the device length of 0.087m is 0.19ns. The GVDs are 393[ps/nm-km] and -3807[ps/nm-km], and the DSs are 1.519[ps/nm^2-km] and -85.430[ps/nm^2-km], for the LP_{01} and LP_{11} modes at 1.55μm, respectively.

Microstructure Devices

$$n_{cladding} = air,\ a = 0.34\mu m$$

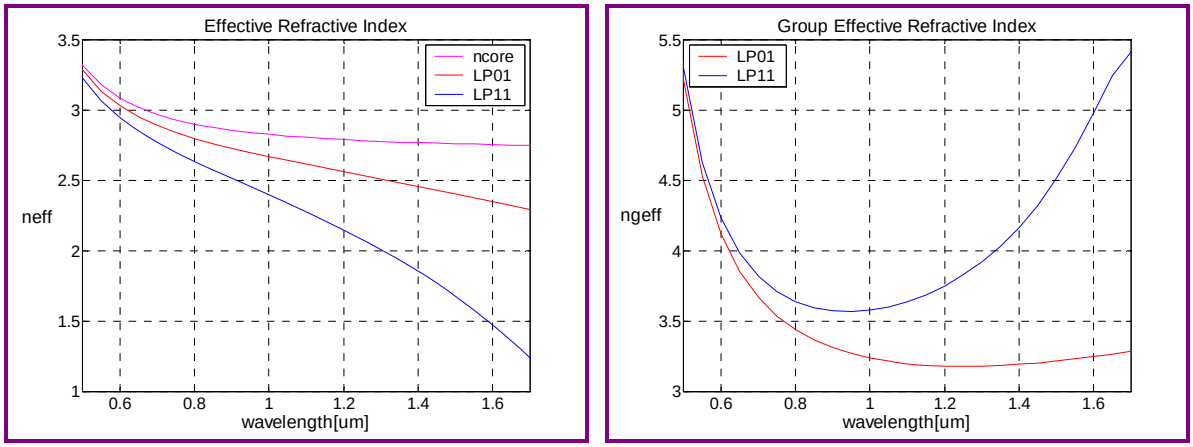

Figure 7-89. ERI and GERI of Chalcogenide-Core Microstructure Devices(LP_{01}-LP_{11} Mode)

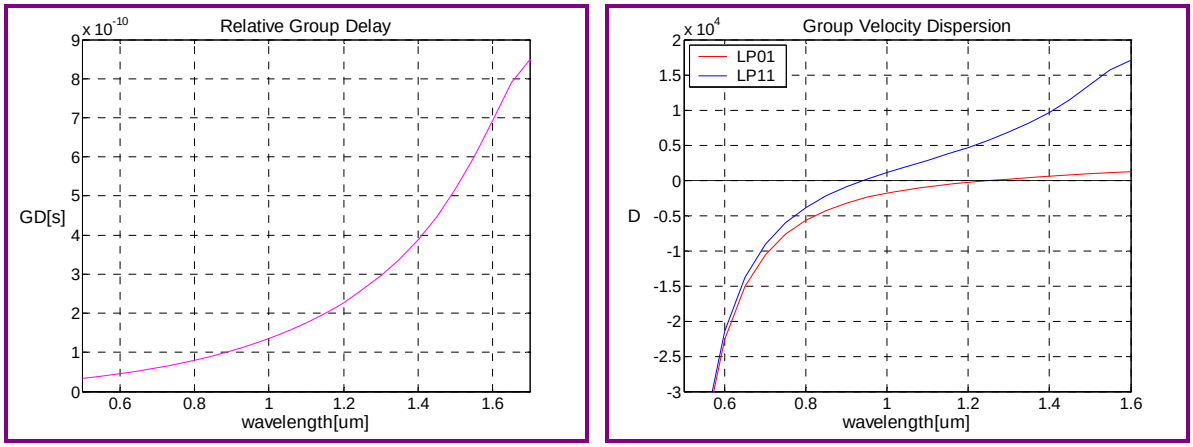

Figure 7-90. RGD and GVD of Chalcogenide-Core Microstructure Devices(LP_{01}-LP_{11} Mode)

The RGD between the LP_{01} and LP_{11} modes at 1.55μm for the device length of 0.062m is 0.60ns. The GVDs are 1067[ps/nm-km] and 15721[ps/nm-km], and the DSs are 2.956 [ps/nm^2-km] and 35.688[ps/nm^2-km], for the LP_{01} and LP_{11} modes at 1.55μm, respectively.

Table 7-23 summarizes the RGD, calculated from Equation (6.14), between the LP_{01} and LP_{11} modes of the signal pulse at 1.55μm for the required device length of SPM-induced devices and XPM-induced devices, shown in Tables 7-21 and 7-22, respectively. In addition, the GVD, and the DS of the two modes at 1.55μm for nonlinear fiber devices based on LP_{01}-LP_{11} mode interference are provided.

Table 7-23. RGD between LP_{01} and LP_{11} Modes of Signal at 1.55μm, GVD at 1.55μm, and DS at 1.55μm for Nonlinear Fiber Devices based on LP_{01}-LP_{11} Mode Interference

Properties			Silica	Litharge	Bismite	Tellurite	Chalcogenide
RGD [ns] by SPM	S-clad		26	1.86	0.10	0.66	0.19
	MSF		61	7.36	0.47	2.89	0.60
RGD [ns] by XPM	S-clad		11	0.83	0.05	0.28	0.07
	MSF		25	2.70	0.16	1.02	0.14
GVD [ps/nm-km] at 1.55μm	S-clad	LP_{01}	15.33	131	229	164	393
		LP_{11}	13.26	-242	-858	-720	-3807
	MSF	LP_{01}	222	596	978	836	1067
		LP_{11}	-553	-1284	-4102	-3084	15721
DS [ps/nm^2-km] at 1.55μm	S-clad	LP_{01}	0.059	-0.224	0.087	-0.027	1.519
		LP_{11}	0.038	-2.689	-10.107	-7.488	-85.430
	MSF	LP_{01}	-0.277	-0.076	0.626	0.413	2.956
		LP_{11}	-7.103	-33.769	-139	-97.353	35.688

7.5.3. Walk-Off Length

Table 7-24 presents the walk-off length, calculated from Equation (6.16), between the LP_{01} and LP_{11} modes of the signal pulse at 1.55μm with 10ps pulse width for nonlinear fiber devices based on LP_{01}-LP_{11} Mode Interference.

Table 7-24. Walk-Off Length between LP_{01} and LP_{11} Modes of Signal at 1.55μm with 10ps Pulse Width for Nonlinear Fiber Devices based on LP_{01}-LP_{11} Mode Interference

Walk-Off Length [m]	Silica	Litharge	Bismite	Tellurite	Chalcogenide
Silica-Cladding	1.80	0.0460	0.0180	0.0225	0.0047
MSF	0.027	0.0089	0.0045	0.0052	0.0020

7.6. Effects of Loss

The required device length in the previous sections was calculated without consideration of fiber losses. As shown in Equation (1.9), the effective length decreases as fiber losses increase. As a result, when fiber losses are present, the required device length should be increased to compensate for losses and thus maintain the same amount of nonlinear phase shift. Table 7-25 compares the required device length calculated without fiber losses and the effective length calculated with the best losses of actually fabricated fibers for the devices based on NOLMs.

Table 7-25. Comparison between the Required Device Length and Effective Length

Properties		Silica	Litharge	Bismite	Tellurite	Chalcogenide
Loss [dB/m]		0.0002	2	0.7	0.035	0.7
α[m^{-1}]		0.000046	0.46	0.16	0.0008	0.16
L[m]	Si-Clad	584	1.17	0.0271	0.2016	0.0118
	MSF	22	0.85	0.0256	0.1833	0.0115
L_{eff}[m]	Si-Clad	576	0.9	0.0270	0.2016	0.0118
	MSF	22	0.7	0.0255	0.1833	0.0115

As can be seen, the difference between the required device length and the effective length is almost zero except for the case of litharge glass devices. This is due to the extremely short device length despite of high losses of HNL glass fibers. For the case of litharge glass devices, the difference is noticeable owing to the much higher loss. As a result, the required device length for litharge glass devices should be slightly increased for achieving the same amount of nonlinear phase shift. However, it will not be a significant problem since the difference is small. Finally, even though nonlinear fiber devices constructed with HNL glasses have high losses, they do not cause any significant problems in the performance of the devices due to the extremely short device length.

CHAPTER 8.
CONCLUSIONS

SCOPE OF THE DISSERTATION

In this dissertation, the performance of nonlinear fiber devices constructed with the high-nonlinearity glasses of Litharge, Bismite, Tellurite, and Chalcogenide glasses have been evaluated to investigate the applicable potentiality of the ultrafast highly nonlinear fiber devices considering both the advantages and disadvantages of the high-nonlinearity glasses.

ADVANTAGES OF HIGH-NONLINEARITY GLASSES

High-nonlinearity glasses such as Litharge, Bismite, Tellurite, and Chalcogenide glasses have both high linear refractive indices and high nonlinear-index coefficients. Due to their high nonlinear-index coefficients, nonlinear fiber devices made of the high-nonlinearity glasses can have highly nonlinear properties. In addition, high linear refractive indices of the high-nonlinearity glasses enable higher index difference between the core and cladding of the devices, thus making it possible to develop smaller effective mode area. This also leads to increase of nonlinearities in the nonlinear fiber devices. Furthermore, if the high-nonlinearity glasses are used in microstructure fibers, the effective mode areas can be reduced further due to much higher index difference and thus, the nonlinearities of the devices can be increased much more. As a result, it is certain that one can increase the nonlinear properties of nonlinear fiber devices by introducing the high-nonlinearity glasses with high linear refractive index and high nonlinear-index coefficients.

Since nonlinearities of silica glasses are very small, conventional nonlinear fiber devices usually require either long length or high power for a sufficient nonlinear phase shift in order to achieve the desired nonlinear effects. The long length of fiber leads to the serious problems of pulse walk-off, pulse broadening, and polarization fluctuation. It is also certain that one can drastically reduce the required device length by introducing the high-nonlinearity glasses due to their high nonlinearities and thus can suppress the problems caused by the long length.

Moreover, the fabrication processes of high-nonlinearity glasses are easier because of their low melting temperatures and high glass stability. Also, they have wide transmission range from near-infrared to far-infrared.

DISADVANTAGES OF HIGH-NONLINEARITY GLASSES

However, the high-nonlinearity glasses have extremely high losses and group-velocity dispersions. This extremely high group-velocity dispersion can cause the deleterious effects of high relative group delay and rapid pulse walk-off between two pulses at different wavelengths, despite the short device length, due to the extremely high group-velocity difference. It also can cause huge pulse broadening and, moreover, the extremely high loss limits the performance of the devices. These problems can be major limiting factors for response time, switching bandwidth, and maximum transmittable bit-rate.

TYPES OF HIGH-NONLINEARITY GLASS FIBERS

In this dissertation, three types of high-nonlinearity glass fibers were considered. The first type is high-nonlinearity glass-core silica-clad fibers which have high index difference and small effective mode area, thus resulting in high nonlinearities. The second type is high-nonlinearity glass-core air-clad(microstructure) fibers. In microstructure fibers, because the cladding is effectively air, they can develop much higher index difference and much smaller effective mode area. These properties enable extremely small spot size and thus much higher nonlinearity for nonlinear applications.

Highly nonlinear fibers with lower-index cladding have usually been fabricated using similar glasses with slightly different compositions for both the core and cladding. The third type of fiber has a high-nonlinearity glass-core with a cladding of a similar glass. Such fibers have lower index differences and larger effective mode areas compared to the high-nonlinearity glass-core silica-clad fibers.

TYPES OF NONLINEAR FIBER DEVICES

The nonlinear fiber devices evaluated in this dissertation include (i)OTDM/WDM demultiplexers based on the optical Kerr effect, nonlinear optical loop mirrors, asymmetric twin-core fibers, or LP_{01}-LP_{11} mode interference, (ii)wavelength converters based on the optical Kerr effect or nonlinear optical loop mirrors, (iii)nonlinear noise filters based on LP_{01}-LP_{02} mode interference, and (iv)amplitude modulators and (v)nonlinear optical switches based on LP_{01}-LP_{11} mode interference. To evaluate the performance of these nonlinear fiber devices, the three types of fibers described above were considered. Then, the required device length, the required optical power, relative group delay, group-velocity dispersion, dispersion slope, walk-off length, and output pulse width(pulse broadening) were evaluated for individual nonlinear fiber devices.

RESULTS

It was found that the required lengths of nonlinear fiber devices based on the optical Kerr effect, nonlinear optical loop mirrors, and mode interference were drastically reduced for both the high-nonlinearity glass-core silica-clad and high-nonlinearity glass-core microstructure fiber devices. The required length for the chalcogenide glass-core microstructure fiber devices based on nonlinear optical loop mirrors was just 1.15cm with the control power of 1W for a phase shift of π, which is typically 1Km for conventional silica-core silica-clad fiber devices with the same conditions.

As expected, the required device lengths of high-nonlinearity glass-core high-nonlinearity glass-clad fiber devices were longer than those of the other two types of fiber devices, although they were much shorter than those of conventional silica-core silica-clad fiber devices. It is because they have lower index difference and larger effective mode area compared to the other two types of fibers. In addition, high-nonlinearity glass-core high-nonlinearity glass-clad fiber devices will have group-velocity dispersions dominated by their material dispersion, while the other two types of fibers exhibit the strong influence of waveguide dispersion.

As also expected, group-velocity dispersions and losses of nonlinear fiber devices constructed with high-nonlinearity glasses were far higher than those of conventional silica-core silica-clad fiber devices. However, the high group-velocity dispersion was found not to be a major problem for most practical applications in high bit-rate systems, since the strong nonlinearities of high-nonlinearity glasses allow the use of extremely short lengths of fiber for functional devices. In addition, published loss data from highly nonlinear fibers which have already been fabricated with high-nonlinearity glasses ensure that nonlinear fiber devices will perform properly with these short device lengths.

RESULTS FOR SPECIFIC NOLLINEAR FIBER DEVICES BASED ON THE OPTICAL KERR EFFECT AND NONLINEAR OPTICAL LOOP MIRRORS

With the extremely reduced device length, the evaluations of relative group delay between the control and signal pulses, walk-off length, and output control pulse width for the nonlinear fiber devices based on the optical Kerr effect and nonlinear optical loop mirrors proved that those devices constructed with any high-nonlinearity glasses with a signal at 1.55μm and control at 1.54μm will function properly without any problems despite extremely high group-velocity dispersion. Even with the worst conditions, the devices constructed with bismite and chalcogenide glasses still will function properly without any difficulties.

For the best performance of nonlinear fiber devices, the required device length should be short, the relative group delay between the control and signal pulses for the required device length should be small, the walk-off length for a given input pulse width should be long, and the input pulse should remain the same. To compare relative group delays, the worst case was chosen for signal wavelength of 1.55μm and control wavelengths over a range from 1.04μm to 1.6μm. When all these requirements were considered with the worst conditions, it turned out that the bismite-core microstructure fiber devices have the most reasonable properties for practical applications. Their relative group delay with the signal pulse at 1.55μm and the worst case of control pulse at 1.48μm for the required device lengths were just 1.31ps and 0.98ps for the cases of the optical Kerr effect and nonlinear optical loop mirror, respectively and the 10ps input control pulse remained almost the same after propagation. In addition, the walk-off length of 0.25m for the 10ps input pulse is about 8 times and 10 times longer than the required device length for the cases of the optical Kerr effect and nonlinear optical loop mirror, respectively.

Even though the chalcogenide-core silica-clad fiber devices developed better performances than bismite-core microstructure fiber devices, it seems impossible to use chalcogenide

glasses as core materials in silica-clad fibers due to the high melting temperature difference. As a result, the bismite-core microstructure devices can be the best candidate for the nonlinear fiber devices based on the optical Kerr effect and nonlinear optical loop mirrors.

At the same control wavelength, although the chalcogenide-core microstructure fiber devices developed the shortest device lengths, they showed larger relative group delay and shorter walk-off length than those of the chalcogenide-core silica-clad fiber devices. For all high-nonlinearity glasses, microstructure fiber devices developed larger relative group delay and shorter walk-off length than silica-clad fiber devices due to higher refractive index difference between the core and cladding of the microstructure fiber devices, leading to higher group effective refractive index difference between the two wavelengths.

ASYMMETRIC TWIN-CORE FIBERS

The asymmetric twin-core fiber is a narrow band filter where light is coupled only when the propagation constants of the two cores are identical. A large slope difference of the effective refractive indices between the two cores produces a narrower band spectral filter. In the asymmetric twin-core nonlinear devices, one of the cores is a high-nonlinearity glass, and a change in the effective refractive index of one of the cores will shift the maximum coupling wavelength.

For wavelength-division demultiplexers based on asymmetric twin-core fibers, the required optical pump power to shift the maximum coupling wavelength by one spectral width was 10KW for the case when GeO_2-doped glass was used in the small core. This power would be reduced to 92W if the small GeO_2-doped core was replaced with bismite glass. In addition, if bismite glass was used in the small core, the spectral width of the filter would be 0.65nm.

Chalcogenide glasses could also be used as the small core and would show performance similar to the bismite glasses. However, bismite glasses would be the best candidate for wavelength-division demultiplexers based on asymmetric twin-core fibers with silica-cladding due to the fabrication difficulties of chalcogenide-core silica-clad fibers.

The power requirements for the asymmetric twin-core nonlinear filter turn out to be large as compared with other nonlinear fiber devices. The reason is that because high-nonlinearity glasses have much higher linear refractive indices, the rate of variation of the effective refractive indices in the small core is much smaller. Therefore, the required δn for shifting the maximum coupling wavelength, which is proportional to the pump power, becomes much larger. Even for the case of chalcogenide glasses, the relatively high power of 97W is required despite the smallest effective mode area and the largest nonlinear-index coefficient.

For optical time-division demultiplexers based on asymmetric twin-core fibers, the group-velocity difference between the signal in the large core and the control in the small core was too large for the device to act properly. The relative group delays between the signal pulses in the large core at 1.55μm and the control pulses in the small core at 1.3μm for the calculated device lengths were high(tens of picoseconds) and the walk-off lengths between the signal and control pulses for 10ps input control pulses were shorter than the device lengths. Thus, it seems impractical to use nonlinear fiber devices based on asymmetric twin-core fibers for time-dependent applications such as optical time-division demultiplexers.

MODE INTERFERENCE BETWEEN LP_{01} AND LP_{02} MODES OR LP_{01} AND LP_{11} MODES

For the nonlinear fiber devices based on LP_{01}-LP_{02} mode interference, the required lengths of SPM-induced and XPM-induced devices were drastically reduced from 77Km and 5.5Km for silica-core silica-clad fiber devices to 0.068m and 0.036m for chalcogenide-core microstructure fiber devices, respectively. As a result, the chalcogenide-core microstructure fiber would be the best candidate for the nonlinear fiber devices based on LP_{01}-LP_{02} mode interference. In addition, for the nonlinear fiber devices based on LP_{01}-LP_{11} mode interference, the required lengths of SPM-induced and XPM-induced devices were shortened from 4.7Km and 2.1Km for silica-core silica-clad fiber devices to 0.062m and 0.028m for chalcogenide-core microstructure fiber devices, respectively. Thus, the chalcogenide-core microstructure

fiber would also be the best candidate for the nonlinear fiber devices based on LP_{01}-LP_{11} mode interference.

Basically, the principle of mode interference is based on phase-velocity difference between two modes. However, if nonlinear fiber devices based on mode interference are used for time-dependent applications such as optical time-division demultiplexing, group-velocity mismatch between two modes plays an important role in their performances. According to the results, group-velocity differences between the two modes were significantly large. The relative group delays between the two modes for the required device lengths were too high(a few nanoseconds) and the walk-off lengths between the two modes for 10ps input pulses were extremely shorter the required device lengths. As a result, time-dependent applications of highly nonlinear fiber devices based on mode interference may not be practical despite the extremely short device length.

APPLICATION OF HIGH CROUP-VELOCITY DISPERSION IN AN OPTICAL KERR WAVELENGTH-DIVISION DEMULTIPLEXER

In this dissertation, a new scheme of wavelength-division demultiplexing based on the optical Kerr effect has been proposed for the first time. The scheme utilizes the rapid pulse walk-off between a control pulse and undesired signal pulses, caused by the extremely high group-velocity dispersion of high-nonlinearity glasses. It was found that wavelength-division-multiplexed signal pulses with a narrow channel spacing can be demultiplexed in very short propagation. In calculations using S-LAH79 glasses in microstructure fibers, signal pulses with a spacing of 0.8nm were easily demultiplexed by a 10ps control pulse with a device length of just 2m. It is very probable that the required device length and(or) the channel spacing can be reduced further by using much higher nonlinearity glasses such as bismite and chalcogenide glasses with careful design of the parameters. This new scheme can turn the disadvantage of the extremely high group-velocity dispersion in high-nonlinearity glasses into an advantage of wavelength-division demultiplexing. It is highly likely to greatly increase the transmission capacity in optical communication systems by simultaneously demultiplexing optical time-division-multiplexed signals and wavelength-division-multiplexed signals with an optical Kerr effect-based demultiplexer.

OVERALL CONCLUSIONS

In conclusion, one can drastically reduce the required device length and suppress simultaneously the problems of pulse walk-off between the control and signal pulses, pulse broadening, and polarization fluctuation in nonlinear fiber devices by introducing high-nonlinearity glasses, without problems resulting from high group-velocity dispersion and losses. This makes it possible to have shorter control pulse widths, faster response time, broader switching bandwidth, and thus higher data transmission in optical communication systems. Thus, the high-nonlinearity glasses of litharge, bismite, tellurite, and chalcogenide glasses have potentials for nonlinear applications in highly nonlinear fiber devices. Among them, bismite-core silica(or air)-clad fiber and chalcogenide-core microstructure fiber devices have much higher potentials for the best performance and moreover, geometrical form birefringence of microstructure fibers can have fairly stable polarization properties.

Furthermore, the optical Kerr effect-based demultiplexers which can demultiplex optical time-division-multiplexed and wavelength-division-multiplexed signals simultaneously have high potentials of achieving unprecedented transmission capacities in future higher bit-rate optical communication systems.

DIRECTIONS FOR FUTURE WORK

Since highly nonlinear fibers have usually been fabricated with similar types of high-nonlinearity glasses for both the core and cladding, little information about fabrication of highly nonlinear fibers constructed with high-nonlinearity glass-core and silica(or air)-cladding exist. This work is expected to be a resource for the development of highly nonlinear fiber devices using high-nonlinearity glasses, especially for high-nonlinearity glass-core and silica(or air)-clad devices. The comparison between different types of high-nonlinearity glasses and different types of fibers, and the calculations of important factors such as relative group delay, walk-off length, and output pulse width should aid in the selection of high-nonlinearity materials for specific applications.

Refinement of fabrication techniques for highly nonlinear fibers using high-nonlinearity glasses discussed in this dissertation is an important task that should be investigated as part of the future work. This work needs to be extended to the fabrication of highly nonlinear fiber devices such as wavelength-division demultiplexers based on the optical Kerr effect and asymmetric twin-core fibers. In addition, efficient coupling of power into highly nonlinear fiber devices remains a challenging task. A satisfactory solution to this problem certainly constitutes a natural extension of this work which needs to be pursued vigorously.

APPENDIX A

Solutions of the Vector Wave Equations for Fiber Modes

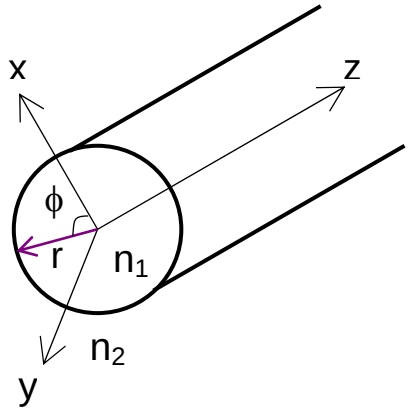

Figure A-1. Geometry and Coordinates of Optical Fibers

Figure A-1 shows the geometry and coordinates of optical fibers and the modal solutions for step-index fibers by vector wave analysis are derived from the following vector wave equation.

$$\nabla^2 \vec{E} = \frac{n^2}{c^2} \frac{\partial^2 \vec{E}}{\partial t^2}$$
$$\vec{E}(r, \phi, z, t) = \left[e_r \hat{a}_r + e_\phi \hat{a}_\phi + e_z \hat{a}_z \right] (r, \phi) e^{j(\omega t - \beta z)} \tag{A.1}$$

The solutions for the axial component of e_z and the two transverse components e_r and e_ϕ of the electric field are given by[243, 245]

$$e_z = AJ_\nu\left(\frac{Ur}{a}\right)\begin{bmatrix}\cos(\nu\phi)\\ \sin(\nu\phi)\end{bmatrix},\ r \le a \tag{A.2}$$

$$e_z = CK_\nu\left(\frac{Wr}{a}\right)\begin{bmatrix}\cos(\nu\phi)\\ \sin(\nu\phi)\end{bmatrix},\ r \ge a \tag{A.3}$$

$$e_r = -\frac{ja^2}{U^2}\left[A\left(\frac{\beta U}{a}\right)J_\nu'\left(\frac{Ur}{a}\right) + B\left(\frac{\nu\omega\mu_0}{r}\right)J_\nu\left(\frac{Ur}{a}\right)\right]\begin{bmatrix}\cos(\nu\phi)\\ \sin(\nu\phi)\end{bmatrix},\ r \le a \tag{A.4}$$

$$e_r = \frac{ja^2}{W^2}\left[C\left(\frac{\beta W}{a}\right)K_\nu'\left(\frac{Wr}{a}\right) + D\left(\frac{\nu\omega\mu_0}{r}\right)K_\nu\left(\frac{Wr}{a}\right)\right]\begin{bmatrix}\cos(\nu\phi)\\ \sin(\nu\phi)\end{bmatrix},\ r \ge a \tag{A.5}$$

$$e_\phi = -\frac{ja^2}{U^2}\left[A\left(\frac{\nu\beta}{r}\right)J_\nu\left(\frac{Ur}{a}\right) + B\left(\frac{U\omega\mu_0}{a}\right)J_\nu'\left(\frac{Ur}{a}\right)\right]\begin{bmatrix}-\sin(\nu\phi)\\ \cos(\nu\phi)\end{bmatrix},\ r \le a \tag{A.6}$$

$$e_\phi = \frac{ja^2}{W^2}\left[C\left(\frac{\nu\beta}{r}\right)K_\nu\left(\frac{Wr}{a}\right) + D\left(\frac{W\omega\mu_0}{a}\right)K_\nu'\left(\frac{Wr}{a}\right)\right]\begin{bmatrix}-\sin(\nu\phi)\\ \cos(\nu\phi)\end{bmatrix},\ r \ge a \tag{A.7}$$

and the solutions for the axial component of h_z and the two transverse components h_r and h_ϕ of the magnetic field are given by

$$h_z = BJ_\nu\left(\frac{Ur}{a}\right)\begin{bmatrix}\sin(\nu\phi)\\ -\cos(\nu\phi)\end{bmatrix},\ r \le a \tag{A.8}$$

$$h_z = DK_\nu\left(\frac{Wr}{a}\right)\begin{bmatrix}\sin(\nu\phi)\\ -\cos(\nu\phi)\end{bmatrix},\ r \ge a \tag{A.9}$$

$$h_r = -\frac{ja^2}{U^2}\left[A\left(\frac{\nu n_1^2 \omega\varepsilon_0}{r}\right)J_\nu\left(\frac{Ur}{a}\right) + B\left(\frac{\beta U}{a}\right)J_\nu'\left(\frac{Ur}{a}\right)\right]\begin{bmatrix}\sin(\nu\phi)\\ -\cos(\nu\phi)\end{bmatrix},\ r \le a \quad \text{(A.10)}$$

$$h_r = \frac{ja^2}{W^2}\left[C\left(\frac{\nu n_2^2 \omega\varepsilon_0}{r}\right)K_\nu\left(\frac{Wr}{a}\right) + D\left(\frac{\beta W}{a}\right)K_\nu'\left(\frac{Wr}{a}\right)\right]\begin{bmatrix}\sin(\nu\phi)\\ -\cos(\nu\phi)\end{bmatrix},\ r \ge a \quad \text{(A.11)}$$

$$h_\phi = -\frac{ja^2}{U^2}\left[A\left(\frac{Un_1^2 \omega\varepsilon_0}{a}\right)J_\nu'\left(\frac{Ur}{a}\right) + B\left(\frac{\nu\beta}{r}\right)J_\nu\left(\frac{Ur}{a}\right)\right]\begin{bmatrix}\cos(\nu\phi)\\ \sin(\nu\phi)\end{bmatrix},\ r \le a \quad \text{(A.12)}$$

$$h_\phi = \frac{ja^2}{W^2}\left[C\left(\frac{Wn_2^2 \omega\varepsilon_0}{a}\right)K_\nu'\left(\frac{Wr}{a}\right) + D\left(\frac{\nu\beta}{r}\right)K_\nu\left(\frac{Wr}{a}\right)\right]\begin{bmatrix}\cos(\nu\phi)\\ \sin(\nu\phi)\end{bmatrix},\ r \ge a \quad \text{(A.13)}$$

Applying the boundary conditions for only tangential components of e_z, h_z, e_ϕ, and h_ϕ, the characteristic equation can be derived as

$$\left(\eta_1 + \eta_2\right)\left(n_1^2\eta_1 + n_2^2\eta_2\right) - \left(\nu n_{eff}\right)^2\left(\frac{V}{UW}\right)^4 = 0 \quad \text{(A.14)}$$

where U, W, and V are the parameters defined in Equations (2.24), (2.25), and (2.26), respectively and

$$\eta_1 = \frac{J_\nu'(U)}{UJ_\nu(U)} \quad \text{(A.15)}$$

$$\eta_2 = \frac{K_\nu'(W)}{WK_\nu(W)} \quad \text{(A.16)}$$

When ν>=1, there are two types of $HE_{\nu m}$ and $EH_{\nu m}$ modes and all six components of the electromagnetic field are nonzero. When ν=0, these modes are analogous to the transverse-

electric(TE) and transverse-magnetic(TM) modes of a planar waveguide, since the axial electric-field component e_z=0 for TE modes and the axial magnetic-field component h_z=0 for TM modes.

In addition, three of coefficients A, B, C, and D in the field expression can be obtained in terms of a fourth one by using boundary conditions. After determining the effective refractive index from Equation (A.14), the mode patterns for the electric and magnetic fields can be obtained from Equations (A.2)-(A.7) and (A.8)-(A.13), respectively. Also, field magnitudes are obtained from

$$\left|\vec{E}\right| = \sqrt{\left|e_z\right|^2 + \left|e_r\right|^2 + \left|e_\phi\right|^2} \tag{A.17}$$

$$\left|\vec{H}\right| = \sqrt{\left|h_z\right|^2 + \left|h_r\right|^2 + \left|h_\phi\right|^2} \tag{A.18}$$

Using the weakly guiding approximation that $n_1 \approx n_{eff} \approx n_2$, the characteristic equation in Equation (A.14) can be simplified as

$$\eta_1 + \eta_2 = \pm\nu\left(\frac{V}{UW}\right)^2 \tag{A.19}$$

When ν=0,

$$\frac{UJ_0(U)}{J_1(U)} = -\frac{WK_0(W)}{K_1(W)}, \quad \mathrm{TE}_{\nu m}\ \&\ \mathrm{TM}_{\nu m} \tag{A.20}$$

and when ν >= 1,

$$\frac{UJ_{\nu}(U)}{J_{\nu+1}(U)} = -\frac{WK_{\nu}(W)}{K_{\nu+1}(W)}, \quad + \text{EH}_{\nu m} \tag{A.21}$$

$$\frac{UJ_{\nu-2}(U)}{J_{\nu-1}(U)} = -\frac{WK_{\nu-2}(W)}{K_{\nu-1}(W)}, \quad - \text{HE}_{\nu m} \tag{A.22}$$

Defining a new integer denoted as l, Equations (A.20)-(A.22) can be cast into the same formats as the characteristic equation obtained from the scalar wave analysis given in Equation (2.47). Therefore, these modes and the LP_{lm} modes have a relationship according to the following:

$$l = \begin{cases} 1 & TE_{0m},\ TM_{0m} \\ \nu + 1 & EH_{\nu m} \\ \nu - 1 & HE_{\nu m} \end{cases}$$

$$l = \begin{cases} 0 & HE_{1m} \\ 1 & TE_{0m},\ TM_{0m},\ HE_{2m} \\ >=2 & EH_{l-1m},\ HE_{l+1m} \end{cases}$$

When ν=1 and m=1, 2 in the vector wave analysis, they represent the fundamental HE_{11} mode(LP_{01} mode of the scalar wave analysis) and the HE_{12} mode(LP_{02} mode), respectively. In addition, the TE_{01}, TM_{01}, and HE_{21} modes in the vector wave analysis correspond to the LP_{11} mode in the scalar wave analysis. Table A-1 lists the first 12 LP modes and their corresponding vector degenerate modes[245].

Table A-1. Relationship between LP Modes and Degenerate Modes

V_{cutoff}	l	Degenerate Modes	LP_{lm} Modes
0	0	HE_{11}	LP_{01}
2.405	1	TE_{01}, TM_{01}, HE_{21}	LP_{11}
3.832	2	EH_{11}, HE_{31}	LP_{21}
3.832	0	HE_{12}	LP_{02}
5.136	3	HE_{21}, HE_{41}	LP_{31}
5.520	1	TE_{02}, TM_{02}, HE_{22}	LP_{12}
6.380	4	EH_{31}, HE_{51}	LP_{41}
7.016	2	EH_{12}, HE_{32}	LP_{22}
7.016	0	HE_{13}	LP_{03}
7.588	5	EH_{41}, HE_{61}	LP_{51}
8.417	3	EH_{22}, HE_{42}	LP_{32}
8.654	1	TE_{03}, TM_{03}, HE_{23}	LP_{13}

A.1. $LP_{01}(HE_{11})$ and $LP_{02}(HE_{12})$ Modes

For the $LP_{0m}(HE_{1m})$ modes, ν of the characteristic equation in Equation (A.14) is 1, and thus the characteristic equation becomes

$$\left(\eta_1+\eta_2\right)\left(n_1{}^2\eta_1+n_2{}^2\eta_2\right)-\left(n_{eff}\right)^2\left(\frac{V}{UW}\right)^4=0 \tag{A.23}$$

where

$$\eta_1=-\frac{1}{U^2}+\frac{J_0(U)}{UJ_1(U)} \tag{A.24}$$

$$\eta_2=-\frac{1}{W^2}-\frac{K_0(W)}{WK_1(W)} \tag{A.25}$$

From Equations (A.2)-(A.7), the solutions of the electric field with the axial component of e_z and the two transverse components of e_r and e_ϕ for the $LP_{0m}(HE_{1m})$ modes can be given by

$$e_z=AJ_1\left(\frac{Ur}{a}\right)\begin{bmatrix}\cos\phi\\ \sin\phi\end{bmatrix},\ r\le a \tag{A.26}$$

$$e_z=CK_1\left(\frac{Wr}{a}\right)\begin{bmatrix}\cos\phi\\ \sin\phi\end{bmatrix},\ r\ge a \tag{A.27}$$

$$e_r=-\frac{ja^2}{U^2}\left[A\left(\frac{\beta U}{a}\right)J_1{}'\left(\frac{Ur}{a}\right)+B\left(\frac{\omega\mu_0}{r}\right)J_1\left(\frac{Ur}{a}\right)\right]\begin{bmatrix}\cos\phi\\ \sin\phi\end{bmatrix},\ r\le a \tag{A.28}$$

$$e_r = \frac{ja^2}{W^2}\left[C\left(\frac{\beta W}{a}\right)K_1'\left(\frac{Wr}{a}\right) + D\left(\frac{\omega\mu_0}{r}\right)K_1\left(\frac{Wr}{a}\right)\right]\begin{bmatrix}\cos\phi\\ \sin\phi\end{bmatrix},\ r \geq a \quad \text{(A.29)}$$

$$e_\phi = -\frac{ja^2}{U^2}\left[A\left(\frac{\beta}{r}\right)J_1\left(\frac{Ur}{a}\right) + B\left(\frac{U\omega\mu_0}{a}\right)J_1'\left(\frac{Ur}{a}\right)\right]\begin{bmatrix}-\sin\phi\\ \cos\phi\end{bmatrix},\ r \leq a \quad \text{(A.30)}$$

$$e_\phi = \frac{ja^2}{W^2}\left[C\left(\frac{\beta}{r}\right)K_1\left(\frac{Wr}{a}\right) + D\left(\frac{W\omega\mu_0}{a}\right)K_1'\left(\frac{Wr}{a}\right)\right]\begin{bmatrix}-\sin\phi\\ \cos\phi\end{bmatrix},\ r \geq a \quad \text{(A.31)}$$

The electric field magnitudes of the $LP_{01}(HE_{11})$ and $LP_{02}(HE_{12})$ modes can be obtained for the core region($r \leq a$) and for the cladding region($r \geq a$) from Equations (A.26)-(A.31) and (A.17).

A.2. $LP_{11}(TE_{01}, TM_{01}, \text{and } HE_{21})$ Mode

The LP_{11} mode from scalar wave analysis corresponds to the three nearly degenerate TE_{01}, TM_{01}, and HE_{21} vector modes. When $\nu=0$, $\cos\nu\phi=1$ and $\sin\nu\phi=0$. Therefore, all field component become independent of ϕ.

For the $LP_{1m}(TE_{0m}$ and $TM_{0m})$modes, ν of the characteristic equation in Equation (A.14) is 0, and thus the characteristic equation becomes

$$\left(\eta_1 + \eta_2\right)\left(n_1^2\eta_1 + n_2^2\eta_2\right) = 0 \quad \text{(A.32)}$$

where

$$\eta_1 = -\frac{J_1(U)}{UJ_0(U)} \tag{A.33}$$

$$\eta_2 = -\frac{K_1(W)}{WK_0(W)} \tag{A.34}$$

The characteristic equation for the TE_{0m} modes is given by

$$\left(\eta_1 + \eta_2\right) = 0 \tag{A.35}$$

Since e_z=0 for the TE_{0m} mode, the solutions for the $LP_{1m}(TE_{0m})$ modes can be defined by h_z, h_r, and e_ϕ from Equations (A.8)-(A.9), (A.10)-(A.11), and (A.6)-(A.7), respectively as

$$h_z = -BJ_0\left(\frac{Ur}{a}\right),\ r \le a \tag{A.36}$$

$$h_z = -DK_0\left(\frac{Wr}{a}\right),\ r \ge a \tag{A.37}$$

$$h_r = \frac{ja^2}{U^2}\left[B\left(\frac{\beta U}{a}\right)J_0'\left(\frac{Ur}{a}\right)\right],\ r \le a \tag{A.38}$$

$$h_r = -\frac{ja^2}{W^2}\left[D\left(\frac{\beta W}{a}\right)K_0'\left(\frac{Wr}{a}\right)\right],\ r \ge a \tag{A.39}$$

$$e_\phi = -\frac{ja^2}{U^2}\left[B\left(\frac{U\omega\mu_0}{a}\right)J_0'\left(\frac{Ur}{a}\right)\right],\ r \le a \tag{A.40}$$

$$e_\phi = \frac{ja^2}{W^2}\left[D\left(\frac{W\omega\mu_0}{a}\right)K_0'\left(\frac{Wr}{a}\right)\right],\ r \ge a \tag{A.41}$$

The electric field magnitude of the $LP_{11}(TE_{01})$ mode can be obtained from Equations (A.40) and (A.41) as

$$\left|\vec{E}\right| = \left|e_{\phi}\right| \tag{A.42}$$

The characteristic equation for the TM_{0m} modes is given by

$$\left(n_1^{\,2}\eta_1 + n_2^{\,2}\eta_2\right) = 0 \tag{A.43}$$

Since $h_z=0$ for the TM_{0m} mode, the solutions for the $LP_{1m}(TM_{0m})$ modes can be defined by e_z, e_r, and h_ϕ from Equations (A.2)-(A.3), (A.4)-(A.5), and (A.12)-(A.13), respectively as

$$e_z = AJ_0\left(\frac{Ur}{a}\right),\ r \le a \tag{A.44}$$

$$e_z = CK_0\left(\frac{Wr}{a}\right),\ r \ge a \tag{A.45}$$

$$e_r = -\frac{ja^2}{U^2}\left[A\left(\frac{\beta U}{a}\right)J_0{}'\left(\frac{Ur}{a}\right)\right],\ r \le a \tag{A.46}$$

$$e_r = \frac{ja^2}{W^2}\left[C\left(\frac{\beta W}{a}\right)K_0{}'\left(\frac{Wr}{a}\right)\right],\ r \ge a \tag{A.47}$$

$$h_\phi = -\frac{ja^2}{U^2}\left[A\left(\frac{Un_1^{\,2}\omega\varepsilon_0}{a}\right)J_0{}'\left(\frac{Ur}{a}\right)\right],\ r \le a \tag{A.48}$$

$$h_\phi = \frac{ja^2}{W^2}\left[C\left(\frac{Wn_2^{\,2}\omega\varepsilon_0}{a}\right)K_0{}'\left(\frac{Wr}{a}\right)\right],\ r \ge a \tag{A.49}$$

The electric field magnitude of the $LP_{11}(TM_{01})$ mode can be obtained from Equations (A.44)-(A.47) as

$$\left|\vec{E}\right| = \sqrt{\left|e_z\right|^2 + \left|e_r\right|^2} \tag{A.50}$$

For the $LP_{1m}(HE_{2m})$ modes, ν of the characteristic equation in Equation (A.14) is 2, and thus the characteristic equation becomes

$$\left(\eta_1 + \eta_2\right)\left(n_1{}^2\eta_1 + n_2{}^2\eta_2\right) - \left(2n_{eff}\right)^2\left(\frac{V}{UW}\right)^4 = 0 \tag{A.51}$$

where

$$\eta_1 = -\frac{2}{U^2} + \frac{J_1(U)}{UJ_2(U)} \tag{A.52}$$

$$\eta_2 = -\frac{2}{W^2} - \frac{K_1(W)}{WK_2(W)} \tag{A.53}$$

From Equations (A.2)-(A.7), the solutions of the electric field with the axial component of e_z and the two transverse components of e_r and e_ϕ for the $LP_{1m}(HE_{2m})$ modes can be given by

$$e_z = AJ_2\left(\frac{Ur}{a}\right)\begin{bmatrix}\cos 2\phi \\ \sin 2\phi\end{bmatrix},\ r \le a \tag{A.54}$$

$$e_z = CK_2\left(\frac{Wr}{a}\right)\begin{bmatrix}\cos 2\phi \\ \sin 2\phi\end{bmatrix},\ r \ge a \tag{A.55}$$

$$e_r = -\frac{ja^2}{U^2}\left[A\left(\frac{\beta U}{a}\right)J_2'\left(\frac{Ur}{a}\right) + B\left(\frac{2\omega\mu_0}{r}\right)J_2\left(\frac{Ur}{a}\right)\right]\begin{bmatrix}\cos 2\phi \\ \sin 2\phi\end{bmatrix},\ r \le a \tag{A.56}$$

$$e_r = \frac{ja^2}{W^2}\left[C\left(\frac{\beta W}{a}\right)K_2'\left(\frac{Wr}{a}\right) + D\left(\frac{2\omega\mu_0}{r}\right)K_2\left(\frac{Wr}{a}\right)\right]\begin{bmatrix}\cos 2\phi \\ \sin 2\phi\end{bmatrix},\ r \ge a \tag{A.57}$$

$$e_\phi = -\frac{ja^2}{U^2}\left[A\left(\frac{2\beta}{r}\right)J_2\left(\frac{Ur}{a}\right) + B\left(\frac{U\omega\mu_0}{a}\right)J_2'\left(\frac{Ur}{a}\right)\right]\begin{bmatrix}-\sin 2\phi \\ \cos 2\phi\end{bmatrix},\ r \le a \tag{A.58}$$

$$e_\phi = \frac{ja^2}{W^2}\left[C\left(\frac{2\beta}{r}\right)K_2\left(\frac{Wr}{a}\right) + D\left(\frac{W\omega\mu_0}{a}\right)K_2'\left(\frac{Wr}{a}\right)\right]\begin{bmatrix}-\sin 2\phi \\ \cos 2\phi\end{bmatrix},\ r \ge a \tag{A.59}$$

The electric field magnitudes of the $LP_{11}(HE_{21})$ mode can be obtained from Equations (A.54)-(A.59) and Equation (A.17).

In this dissertation, the average values of the effective refractive indices and the effective mode areas from the three degenerate modes are used for the LP_{11} mode and the evaluation of the devices based on LP_{01}-LP_{11} mode interference.

BIBLIOGRAPHY

[1] Andrew R. Chraplyvy, "Limitations on Lightwave Communications Imposed by Optical Fiber Nonlinearities", Journal of Lightwave Technology, Vol.8, No.10, pp.1548-1557, 1990

[2] T. Morioka, M. Saruwatari, and A. Takada, "Ultrafast Optical Multi/Demultiplexer Utilizing Optical Kerr Effect in Polarization-Maintaining Single-Mode Fibers", Electronics Letters, Vol.23, No.9, pp.453-454, 1987

[3] Toshio Morioka and Masatoshi Saruwatari, "Ultrafast All-Optical Switching Utilizing the Optical Kerr Effect in Polarization-Maintaining Single-Mode Fibers", IEEE Journal on Selected Areas in Communications, Vol.6, No.7, pp.1186-1198, 1988

[4] T. Morioka, H. Takara, K. Mori, and M. Saruwatari, "Ultrafast Reflective Optical Kerr Demultiplexer Using Polarisation Rotation Mirror", Electronics Letters, Vol.28, No.6, pp.521-522, 1992

[5] J. K. Kim and R. H. Stolen, "All-Optical Kerr Wavelength-Division Demultiplexer Using Pulse Walk-Off by High Group Velocity Difference in Highly Nonlinear Photonic Crystal Fiber", OISE, SE06, C4, pp.143, 2004

[6] K. J. Blow, N. J. Doran, and B. P. Nelson, "Demonstration of the Nonlinear Fiber Loop Mirror as an Ultrafast All-Optical Demultiplexer", Electronics Letters, Vol.26, No.14, pp.962-964, 1990

[7] B. P. Nelson, K. J. Blow, P. D. Constantine, N. J. Doran, J. K. Lucek, I. W. Marshall, and K. Smith, "All-Optical Gbit/s Switching using Nonlinear Optical Loop Mirror", Electronics Letters, Vol.27, No.9, pp.704-705, 1991

[8] P. A. Andrekson, N. A. Olsson, J. R. Simpson, D. J. Digiovanni, P. A. Morton, T. Tanbun-Ek, R. A. Rogan, and K. W. Wecht, "64Gb/s All-Optical Demultiplexing with the Nonlinear Optical-Loop Mirror", IEEE Photonics Technology Letters, Vol.4, No.6, pp.644-647, 1992

[9] K. Uchiyama, H. Takara, T. Morioka, S. Kawanishi, and M. Saruwatari, "Effects of Control-Signal Pulse Walk-Off On BER Performance of Nonlinear Optical Loop Mirror Demultiplexer", Electronics Letters, Vol.29, No.15, pp.1313-1314, 1993

[10] K. Uchiyama, T. Morioka, M. Saruwatari, M. Asobe, and T. Ohara, "Error free all-optical demultiplexing using a chalcogenide glass fibre based nonlinear optical loop mirror", Electronics Letters, Vol.32, No.17, pp.1601-1602, 1996

[11] Kentaro Uchiyama, Toshio Morioka, Satoki Kawanishi, Hidehiko Takara, and Masatoshi Saruwatari, "Signal-to-Noise Ratio Analysis of 100Gb/s Demultiplexing Using Nonlinear Optical Loop Mirror", Journal of Lightwave Technology, Vol.15, No.2, pp.194-201, 1997

[12] Mark F. Arend, Michael L. Dennis, and Irl N. Duling III, Ekaterina A. Golovchenko, Alexei N. Pilipetskii, and Curtis R. Menyuk, "Nonlinear-optical loop mirror demultiplexer using a random birefringence fiber: comparison between simulation and experiments", Optics Letters, Vol.22, No.12, pp.886-888, 1997

[13] M. Nakazawa, E. Yoshida, T. Yamamoto, E. Yamada, and A. Sahara, "TDM signal channel 640Gbit/s transmission experiment over 60km using 400fs pulse train and walk-off free, dispersion flattened nonlinear optical loop mirror", Electronics Letters, Vol.34, No.9, pp.907-908, 1998

[14] T. Yamamoto, E. Yoshida, and M. Nakazawa, "Ultrafast nonlinear optical loop mirror for demultiplexing 640Gbit/s TDM signals", Electronics Letters, Vol.34, No.10, pp.1013-1014, 1998

[15] C. Y. Cheung, Z. Ghassemlooy, and G. Swift, "Bit-error-rate analysis for a 100-Gbit/s nonlinear optical loop mirror demultiplexer employing soliton control and signal pulses", Optics letters, Vol.24, No.24, pp.1817-1819, 1999

[16] Y. Liang, J. W. Lou, J. K. Anderson, J. C. Stocker, O. Boyraz, M. N. Islam, and D. A. Nolan, "Polarization-insensitive nonlinear optical loop mirror demultiplexer with twisted fiber", Optics Letters, Vol.24, No.11, pp.726-728, 1999

[17] Han Chuen Lim, Takahide Sakamoto, and kazuro Kikuchi, "Polarization-Independent Optical Demultiplexing by Conventional Nonlinear Optical Loop Mirror in a

Polarization-Diversity Loop Configuration", IEEE Photonics Technology Letters, Vol.12, No.12, pp.1704-1706, 2000

[18] Takahide Sakamoto, Han Chuen Lim, and Kazuro Kikuchi, "All-Optical Polarization-Insensitive Time-Division Demultiplexer Using a Nonlinear Optical Loop Mirror With a Pair of Short Polarization-Maintaining Fibers", IEEE Photonics Technology Letters, Vol.14, No.12, pp.1737-1739, 2002

[19] Hideyuki Sotobayashi, Chikara Sawaguchi, Yahei Koyamada, and Wataru Chujo, "Ultrafast walk-off free nonlinear optical loop mirror by a simplified configuration for 320-Gbit/s time-division multiplexing signal demultiplexing", Optics Letters, Vol.27, No.17, pp.1555-1557, 2002

[20] Andrei I. Siahlo, Leif K. Oxenlowe, Kim S. Berg, Anders T. Clausen, Peter A. Andersen, Christophe Peucheret, Andrea Tersigni, Palle Jeppesen, Kim P. Hansen, and Jacob R. Folkenberg, "A High-Speed Demultiplexer Based on a Nonlinear Optical Loop Mirror With a Photonic Crystal Fiber", IEEE Photonics Technology Letters, Vol.15, No.8, pp.1147-1149, 2003

[21] P.A. Andrekson, N. A. Olsson, J. R. Simpson, T. Tanbun-Ek, R. A. Logan, and M. Haner, "16Gbit/s All-Optical Demultiplexing Using Four-Wave Mixing", Electronics Letters, Vol.27, No.11, pp.922-924, 1991

[22] T. Morioka, S. Kawanishi, H. Takara, and M. Saruwatari, "Multiple-output, 100Gbit/s all-optical demultiplexer based on multichannel four-wave mixing pumped by a linearly-chirped square pulse", Electronics Letters, Vol.30, No.23, pp.1959-1960, 1994

[23] T. Morioka, S. Kawanishi, K. Uchiyama, H. Takara, and M. Saruwatari, "Polarisation-independent 100Gbit/s all-optical demultiplexer using four-wave mixing in a polarisation-maintaining fibre loop", Electronics Letters, Vol.30, No.7, pp.591-592, 1994

[24] T. Morioka, H. Takara, S. Kawanishi, T. Kitoh, and M. Saruwatari, "Error-free 500Gbit/s all-optical demultiplexing using low-noise, low-jitter supercontinuum short pulses", Electronics Letters, Vol.32, No.9, pp.833-834, 1996

[25] P. O. Hedekvist and P. A. Andrekson, “Demonstration of fibre four-wave mixing optical demultiplexing with 19dB parametric amplification”, Electronics Letters, Vol.32, No.9, pp.830-831, 1996

[26] H. Sotobayashi, W. Chujo, and T.Ozeki, “80Gbit/s simultaneous photonic demultiplexing based on OTDM-to-WDM conversion by four-wave mixing with supercontinuum light source”, Electronics Letters, Vol.37, No.10, pp.640-642, 2001

[27] T. Morioka, K. Mori, and M. Saruwatari, “Ultrafast Polarization-Independent Optical Demultiplexer Using Optical Carrier Frequency Shift Through Crossphase Modulation”, Electronics Letters, Vol.28, No.11, pp.1070-1072, 1992

[28] Bengt-Erik Olsson and Daniel J. Blumenthal, “All-Optical Demultiplexing Using Fiber Cross-Phase Modulation (XPM) and Optical Filtering”, IEEE Photonics Technology Letters, Vol.13, No.8, pp.875-877, 2001

[29] Jie Li, Bengt-Erik Olsson, Magnus Karlsson, and Peter A. Andrekson, “OTDM Demultiplexer Based on XPM-Induced Wavelength Shifting in Highly Nonlinear Fiber”, IEEE Photonics Technology Letters, Vol.15, No.12, pp.1770-1772, 2003

[30] Roger H. Stolen and John E. Bjorkholm, “Parametric Amplification and Frequency Conversion in Optical Fibers”, IEEE Journal of Quantum Electronics, Vol.QE-18, No.7, pp.1062-1072, 1982

[31] Ju Han Lee, Zulfadzli Yusoff, Walter Belardi, Morten Ibsen, Tanya M. Monro, and Davis J. Richardson, “A Tunable WDM Wavelength Converter Based on Cross-Phase Modulation Effects in Normal Dispersion Holey Fiber”, IEEE Photonics Technology Letters, Vol.15, No.3, pp.437-439, 2003

[32] Guo-Wei Lu, Lian-Kuan Chen, Chun-Kit Chan, and Chinlon Lin, “All-Optical Tunable Wavelength Conversion based on Cross-Polarization Modulation in Nonlinear Photonic Crystal Fiber”, Optical Fiber Communication Conference, 2005

[33] K. J. Blow, N. J. Doran, B. K. Nayar, and B. P. Nelson, “Two-wavelength operation of the nonlinear fiber loop mirror”, Optics Letters, Vol.15, No.4, pp.248-250, 1990

[34] Masahiko Jinno, "All Optical Signal Regularizing/Regeneration Using a Nonlinear Fiber Sagnac Interferometer Switch with Signal-Clock Walk-Off", Journal of Lightwave Technology, Vol.12, No.9, pp.1648-1659, 1994

[35] K. A. Rauschenbach, K. L. Hall, J. C. Livas, and G. Raybon, "All-Optical Pulse Width and Wavelength Conversion at 10Gb/s Using a Nonlinear Optical Loop Mirror", IEEE Photonics Technology Letters, Vol.6, No.9, pp.1130-1132, 1994

[36] K. Uchiyama, T. Morioka, and M. Saruwatari, "Polarization-independent wavelength conversion using nonlinear optical loop mirror", Electronics Letters, Vol.31, No.21, pp.1862-1863, 1995

[37] Christian Kolleck and Uwe Hempelmann, "All-Optical Wavelength Conversion of NRZ and RZ Signals Using a Nonlinear Optical Loop Mirror", Journal of Lightwave Technology, Vol.15, No.10, pp.1906-1913, 1997

[38] Jianjun Yu, Xueyan Zheng, Christophe Peucheret, Anders T. Clausen, Henrik N. Poulsen, and Palle Jeppesen, "40-Gb/s All-Optical Wavelength Conversion Based on a Nonlinear Optical Loop Mirror", Journal of Lightwave Technology, Vol.18, No.7, pp.1001-1006, 2000

[39] Jianjun Yu, Xueyan Zheng, Christophe Peucheret, Anders T. Clausen, Henrik N. Poulsen, and Palle Jeppesen, "All-Optical Wavelength Conversion of Short Pulses and NRZ Signals Based on a Nonlinear Optical Loop Mirror", Journal of Lightwave Technology, Vol.18, No.7, pp.1007-10017, 2000

[40] Takahide Sakamoto, Fumio Futami, Kazuro Kikuchi, Shinichi Takeda, Yasushi Sugaya, and Shigeki Watanabe, "All-Optical Wavelength Conversion of 500-fs Pulse Trains by Using Nonlinear-Optical Loop Mirror Composed of a Highly Nonlinear DSF", IEEE Photonics Technology Letters, Vol.13, No.5, pp.502-504, 2001

[41] Takahide Sakamoto and Kazuro Kikuchi, "Nonlinear Optical Loop Mirror With an Optical Bias Controller for Achieving Full-Swing Operation of Gate Switching", IEEE Photonics Technology Letters, Vol.16, No.2, pp.545-547, 2004

[42] Kyo Inoue and Hiromu Toba, "Wavelength Conversion Experiment Using Fiber Four-Wave Mixing", IEEE Photonics Technology Letters, Vol.4, No.1, pp.69-72, 1992

[43] K. Inoue, T. Hasegawa, K. Oda, and H. Toba, "Multichannel frequency conversion experiment using fibre four-wave mixing", Electronics Letters, Vol.29, No.19, pp.1708-1710, 1993

[44] T. Morioka, S. Kawanishi, and M. Saruwatari, "Tunable error-free optical frequency conversion of a 4ps optical short pulse over 25nm by four-wave mixing in a polarization-maintaining optical fibre", Electronics Letters, Vol.30, No.11, pp.884-885, 1994

[45] Jianjun Yu and Palle Jeppesen, "Wavelength conversion by use of four-wave mixing in a noble optical loop configuration", Optics Letters, Vol.25, No.6, pp.393-395, 2000

[46] O. Aso, Shin-ichi Arai, T. Yagi, M. Tadakuma, Y. Suzuki, and S. Namiki, "Broadband four-wave mixing generation in short optical fibers", Electronics Letters, Vol.36, No.8, pp.709-711, 2000

[47] Jonas Hansryd and Peter A. Andrekson, "Broad-Band Continuous-Wave-Pumped Fiber Optical Parametric Amplifier with 49-dB Gain and Wavelength-Conversion Efficiency", IEEE Photonics Technology Letters, Vol.13, No.3, pp.194-196, 2001

[48] David A. Chestnut, Christiano J. S. de Matos, and J. Roy Taylor, 'Raman-assisted fiber optical parametric amplifier and wavelength converter in highly nonlinear fiber", Journal of the Optical Society of America B, Vol.9, No.8, pp.1901-1904, 2002

[49] Ju Han Lee, Walter Belardi, Kentaro Furusawa, Periklis Petropoulos, Zulfadzli Yusoff, Tanya M. Monro, and David J. Richardson, "Four-Wave Mixing Based 10-Gb/s Tunable Wavelength Conversion Using a Holey Fiber With a High SBS Threshold", IEEE Photonics Technology Letters, Vol.15, No.3, pp.440-442, 2003

[50] Thomas V. Andersen, Karen Marie Hilligsoe, Carsten K. Nielsen, Jan Thogersen, K. P. Hansen, Soren R. Keiding, and Jakob J. Larsen, "Continuous-wave wavelength conversion in a photonic crystal fiber with two zero-dispersion wavelengths", Optics Express, Vol.12, No.17, pp.4113-4122, 2004

[51] K. K. Chow, C. Shu, Chinlon Lin, and A. Bjarklev, "Polarization-Insensitive Widely Tunable Wavelength Converter Based on Four-Wave Mixing in a Dispersion-Flattened Nonlinear Photonic Crystal Fiber", IEEE Photonics Technology Letters, Vol.17, No.3, pp.624-626, 2005

[52] Jianjun Yu, Yong-Kee Yeo, and Gee-Kung Chang, "Simultaneous wavelength conversion and format conversion for DPSK signal based on four-wave mixing in nonlinear fiber", Optical Fiber Communication Conference, 2005

[53] R. H. Stolen, J. Botineau, and A. ashkin, "Intensity discrimination of optical pulses with birefringent fibers", Optics Letters, Vol.7, No.10, pp.512-514, 1982

[54] Ken-ichi Kitayama, Yasuo Kimura, Katsunari Okamoto, and Shigeyuki Seikai, "Optical sampling using an all-fiber optical Kerr shutter", Applied Physics Letters, Vol.46, No.7, pp.623-625, 1985

[55] T. Morioka and M. Saruwatari, "Determination of nondiagonal component $n_{2B\perp}$ of nonlinear refractive index in polarization-maintaining fibers utilizing optical Kerr modulation scheme", Electronics Letters, Vol.23, pp.1330-1332, 1987

[56] R. V. Penty, I. H. White, and A. R. L. Travis, "Nonlinear, Two-Moded, Single-Fibre, Interferometric Switch", Electronics Letters, Vol.24, No.21, pp.1338-1339, 1988

[57] S. Usman Ahmed, Vincent A. Handerek, and Alan J. Rogers, "Characteristics and applications of birefringent-fiber Kerr-couplers", Applied Optics, Vol.33, No.3, pp.397-406, 1994

[58] J. Suzuki, K. Taira, Y. Fukuchi, Y. Ozeki, T. Tanemura, and K. Kikuchi, "All-optical time-division add-drop multiplexer using optical fiber Kerr shutter", Electronics Letters, Vol.40, No.7, pp.445-446, 2004

[59] S. M. Jensen, "The Nonlinear Coherent Coupler", IEEE Journal of Quantum Electronics, Vol.18, No.10, pp.1580-1583, 1982

[60] Yaron Silberberg and George I. Stegeman, "Nonlinear coupling of waveguide modes", Applied Physics Letters, Vol.50, No.13, pp.801-803, 1987

[61] F. Cuesta-Soto, A. Martinez, J. Garcia, F. Ramos, P. Sanchis, J. Blasco, and J. Marti, "All-optical switching structure based on a photonic crystal directional coupler", Optics Express, Vol.12, No.1, pp.161-167, 2004

[62] C. C. Yang, "All-optical ultrafast logic gates that use asymmetric nonlinear directional couplers", Optics Letters, Vol.16, No.21, pp.1641-1643, 1991

[63] Ladislav Mista Jr, Jaroslav Rehacek, and Jan Perina, "Phase properties of the asymmetric nonlinear coupler", Journal of Modern Optics, Vol.45, No.11, pp.2269-2279, 1998

[64] S. R. Friberg, Y. Silberberg, M. K. Oliver, M. J. Andrejco, M. A. Saifi, and P. W. Smith, "Ultrafast all-optical switching in a dual-core fiber nonlinear coupler", Applied Physics Letters, Vol.51, No.15, pp.1135-1137, 1987

[65] S. R. Friberg, A. M. Weiner, Y. Silberberg, B. G. Sfez, and P. S. Smith, "Femtosecond switching in a dual-core-fiber nonlinear coupler", Optics Letters, Vol.13, No.10, pp.904-906, 1988

[66] R. A. Betts, T. Tjugiarto, Y. L. Xue, and P. L. Chu, "Nonlinear Refractive Index in Erbium Doped Optical Fiber: Theory and Experiment", IEEE Journal of Quantum Electronics, Vol.27, No.4, pp.908-913, 1991

[67] Yijiang Chen, Allan W. Snyder, and David N. Payne, "Twin Core Nonlinear Couplers with Gain and Loss", IEEE Journal of Quantum Electronics, Vol.28, No.1, pp.239-245, 1992

[68] P. L. Chu and B. Wu, "Optical switching in twin-core erbium-doped fibers", Optics Letters, Vol.17, No.4, pp.255-257, 1992

[69] K. Z. Nobrega and A. S. B. Sombra, "Optimum self phase modulation profile for nonlinear transmission recovery in twin core optical couplers with loss", Optics Communications, Vol.151, No.1-3, pp.31-34, 1998

[70] Pedro M. Ramos and Carlos R. Paiva, "All-Optical Pulse Switching in Twin-Core Fiber Coupler with Intermodal Dispersion", IEEE Journal of Quantum Electronics, Vol.35, No.6, pp.983-989, 1999

[71] Jorge R. Costa, Pedro M. Ramos, Carlos R. Paiva, and Afonso M. Barbosa, "Numerical Study of Passive Gain Equalization With Twin-Core Fiber Coupler Amplifiers for WDM Systems", IEEE Journal of Quantum Electronics, Vol.37, No.12, pp.1553-1561, 2001

[72] Ken-ichi Kitayama and Yukinori Ishida, "Wavelength-selective coupling of two-core optical fiber: application and design", Journal of the Optical Society of America A, Vol.2, No.1, pp.90-94, 1985

[73] K. Z. Nobrega, M. G. da Silva, and A. S. B. Sombra, "Multistable all-optical switching behavior of the asymmetric nonlinear directional coupler", Optics Communications, Vol.173, No.1-6, pp.413-421, 2000

[74] Chinlon Lin and Rogers H. Stolen, "Backward Raman amplification and pulse steepening in silica fibers", Applied Physics Letters, Vol.29, No.7, pp.428-431, 1976

[75] Yasuhiro Aoki, "Properties of Fiber Raman Amplifiers and Their Applicability to Digital Optical Communication Systems", Journal of Lightwave Technology, Vol.6, No.7, pp.1225-1239, 1988

[76] Victor E. Perlin and Herbert G. Winful, "On Distributed Raman Amplification for Ultrabroad-band Long-Haul WDM Systems", Journal of Lightwave Technology, Vol.20, No.3, pp.409-416, 2002

[77] A. Mori, H. Masuda, K. Shikano, and M. Shimizu, "Ultra-Wide-Band Tellurite-Based Fiber Raman Amplifier", Journal of Lightwave Technology, Vol.21, No.5, pp.1300-1306, 2003

[78] C. V. Shank, R. L. Fork, R. Yen, R. H. Stolen, and W. J. Tomlinson, "Compression of femtosecond optical pulses", Applied Physics Letters, Vol.40, No.9, pp.761-763, 1982

[79] W. J. Tomlinson, R. H. Stolen, and C. V. Shank, "Compression of optical pulses chirped by self-phase modulation in fibers", Journal of the Optical Society of America B, Vol.1, No.2, pp.139-149, 1984

[80] W. H. Knox, R. L. Fork, M. C. Downer, R. H. Stolen, C. V. Shank, and J. A. Valdmanis, "Optical pulse compression to 8fs at a 5-kHz repetition rate", Applied Physics Letters, Vol.46, No.12, pp.1120-1121, 1985

[81] A. M. Weiner, J. P. Heritage, and R. H. Stolen, "Self-phase modulation and optical pulse compression influenced by stimulated Raman scattering in fibers", Journal of the Optical Society of America B, Vol.5, No.2, pp.364-372, 1988

[82] Jamal T. Manassah, "Pulse compression of an induced-phase-modulation weak signal", Optics Letters, Vol.13, No.9, pp.755-757, 1988

[83] E. M. Dianov, Luben M. Ivanov, Pavel V. Mamyshev, and A. M. Prokhorov, "Efficient Compression of High-Energy Laser Pulses", IEEE Journal of Quantum Electronics, Vol.25, No.4, pp.828-835, 1989

[84] Govind P. Agrawal, P. L. Baldeck, and R. R. Alfano, "Optical wave breaking and pulse compression due to cross-phase modulation in optical fibers", Optics Letters, Vol.14, No.2, pp.137-139, 1989

[85] Joshua E. Rothenberg, "Intrafiber visible pulse compression by cross-phase modulation in a birefringent optical fiber", Optics Letters, Vol.15, No.9, pp.495-497, 1990

[86] Q. Z. Wang, P. P. Ho, and R. R. Alfano, "Degenerate cross-phase modulation for pulse compression and amplification of ultrashort laser pulses", Optics Letters, Vol.15, No.18, pp.1023-1025, 1990

[87] R. A. Betts, S. J. Frisken, C. A. Telford, and P. S. Atherton, "All-Optical Pulse Compression Using Amplifying Sagnag Loop", Electronics Letters, Vol.27, No.10, pp.858-860, 1991

[88] A. D. Ellis and D. M. Patrick, "All Laser Diode Compression of 5GHz Picosecond Pulses Using Cross-Phase Modulation in Optical Fibre", Electronics Letters, Vol.29, No.2, pp.149-150, 1993

[89] Satoki Kawanishi, "Ultrahigh-Speed Optical Time-Division-Multiplexed Transmission Technology Based on Optical Signal Processing", IEEE Journal of Quantum Electronics, Vol.34, No.11, pp.2064-2079, 1998

[90] Michael J. Yadlowsky, Evelyn M. Deliso, and Valeria L. Da Silva, "Optical Fibers and Amplifiers for WDM Systems", Proceedings of the IEEE, Vol.85, No.11, pp.1765-1779, 1997

[91] Fumiaki Miyaji, Kiyoharu Tadanaga, and Sumio Sakka, "Third harmonic generation from MOx-PbO-GaO1.5 ternary glasses", Applied Physics Letters, Vol.60, No.17, pp.2060-2061, 1992

[92] Q. F. Zhou, Q. Q. Zhang, L. Y. Zhang, and X. Yao, "Optical properties of sol-gel derived lead titanate nanocrystallites in silica glass", Materials Letters, Vol.54, No.1, pp.21-24, 2002

[93] L. C. Hwang, S. C. Lee, and T. C. Wen, "Nonlinear absorption and refraction in lead glasses: enhanced by the small metal particle dispersions", Optics Communications, Vol.228, No.4-6, pp.373-380, 2003

[94] M. A. Newhouse, D. L. Weidman, and D. W. Hall, "Enhanced-nonlinearity single-mode lead silicate optical fiber", Optics Letters, Vol.15, No.21, pp.1185-1187, 1990

[95] J. R. Lincoln, C. J. Mackechnie, J. Wang, W. S. Brocklesby, R. S. Deol, A. Pearson, D. C. Hanna, and D. N. Payne, "New Class of Fiber Laser Based on Lead-Germanate Glasses", Electronics Letters, Vol.28, No.11, pp.1021-1022, 1992

[96] K. M. Kiang, K. Frampton, T. M. Monro, R. Moore, J. Tucknott, D. W. Hewak, D. J. Richardson, and H. N. Rutt, "Extruded singlemode non-silicate glass holey optical fibres", Electronics Letters, Vol.38, No.12, pp.546-547, 2002

[97] T. M. Monro, K. M. Kiang, J. H. Lee, K. Frampton, Z. Yusoff, R. Moore, J. Tucknott, D. W. Hewak, H. N. Rutt, and D. J. Richardson, "High nonlinearity extruded single-mode holey fibers", Optical Fiber Communication Conference, FA1-1, 2002

[98] V. V. Ravi Kanth Kumar, A. K. George, W. H. Reeves, J. C. Knight, P. St. J. Russell, F. G. Omenetto, and A. J. Taylor, "Extruded soft glass photonic crystal fiber for ultrabroad supercontinuum generation", Optics Express, Vol.10, No.25, pp.1520-1525, 2002

[99] P. Petropoulos, T. M. Monro, H. Ebendorff-Heidepriem, K. Frampton, R. C. Moore, H. N. Rutt, and D. J. Richardson, "Soliton-self-frequency-shift effects and pulse compression in an anomalously dispersive high nonlinearity lead silicate holey fiber", Optical Fiber Communication Conference, PD3-1, 2003

[100] P. Petropoulos, H. Ebendorff-Heidepriem, V. Finazzi, R. C. Moore, K. Frampton, D. J. Richardson, and T. M. Monro, "Highly nonlinear and anomalously dispersive lead silicate glass holey fibers", Optics Express, Vol.11, No.26, pp.3568-3573, 2003

[101] X. Feng, A. K. Mairaj, D. W. Hewak, and T. M. Monro, "Towards high-index glass based monomode holey fibre with large mode area", Electronics Letters, Vol.40, No.3, pp.167-168, 2004

[102] Takuya Suemura, Morimasa Ohtani, Ryuji Morita, and Mikio Yamashita, "Femtosecond Refractive-Index Nonlinearities in a Flint Glass Single-Mode Fiber",

Japanese Journal of Applied Physics Part 2-Letters, Vol.36, No.10A, pp.1307-1310, 1997

[103] Naoki Sugimoto, Hirohisa Kanbara, Seiji Fujiwara, Koichiro Tanaka, and Kazuyuki Hirao, "Ultrafast response of third-order optical nonlinearity in glasses containing Bi_2O_3", Optics Letters, Vol.21, No.20, pp.1637-1639, 1996

[104] Naoki Sugimoto, Hirohisa Kanbara, Seiji Fujiwara, Koichiro Tanaka, Yutaka Shimizugawa, and Kazuyuki Hirao, "Third-order optical nonlinearities and their ultrafast response in Bi_2O_3-B_2O_3-SiO_2 glasses", Journal of the Optical Society of America B, Vol.16, No.11, pp.1904-1908, 1999

[105] Jianhu Yang, Shixun Dai, Nengli Dai, Shiqing Xu, Lei Wen, Lili Hu, and Zhonghong Jiang, "Effects of Bi_2O_3 on the spectroscopic properties of erbium-doped bismuth silicate glasses, Journal of the Optical Society of America B, Vol.20, No.5, pp.810-815, 2003

[106] P. Becker, "Thermal and optical properties of glasses of the system Bi_2O_3-B_2O_3", Crystal Research and Technology, Vol.38, No.1, pp.74-82, 2003

[107] A. Agarwal, V. P. Seth, S. Sanghi, P. Gahlot, and S. Khasa, "Mixed alkali effect in optical properties of lithium-potassium bismuth borate glass system", Materials Letters, Vol.58, No.5, pp.694-698, 2004

[108] Tomoharu Hasegawa, Tatsuo Nagashima, and Naoki Sugimoto, "Z-scan study of third-order optical nonlinearities in bismuth-based glasses", Optics Communications, IN PRESS, 2005

[109] Isabella-Ioana, Hartmut Hesse, and Klaus Betzler, "Optical properties of bixmuth borate glasses", Optical Materials, Vol.26, No.3, pp.235-237, 2004

[110] K. Kikuchi and K. Taira, "Highly-nonlinear Bismuth Oxide-based glass fibers for all-optical signal processing", Optical Fiber Communication Conference, ThY6, 2002

[111] S. Ohara, N. Sugimoto, K. Ochiai, H. Hayashi, Y. Fukasawa, T. Hirose, and M. Reyes, "Extra-Broadband and Highly Efficient Short Length Bi_2O_3-based EDF", Optical Fiber Communication Conference, FB8, 2003

[112] N. Sugimoto, T. Nagashima, T. Hasegawa, S. Ohara, K. Taira, and K. Kikuchi, "Bismuth-based optical fiber with nonlinear coefficient of 1360$W^{-1}km^{-1}$", Optical Fiber Communication Conference, PDP26, 2004

[113] Juliet T. Gopinath, Hanfei M. Shen, Hideyuki Sotobayashi, Erich P. Ippen, Tomoharu Hasegawa, Tatsuo Nagashima, and Naoki Sugimoto, "Highly nonlinear bismuth-oxide fiber for smooth supercontinuum generation at 1.5μm", Optics Express, Vol.12, No.23, pp.5697-5702, 2004

[114] H. Ebendorff-Heidepriem, P. Petropoulos, V. Finazzi, K. Frampton, R. C. Moore, D. J. Richardson, and T. M. Monro, "Highly nonlinear bismuth-oxide-based glass holey fiber", Optical Fiber Communication Conference, ThA4, 2004

[115] H. Ebendorff-Heidepriem, P. Petropoulos, S. Asimakis, V. Finazzi, R. C. Moore, K. Frampton, F. Koizumi, D. J. Richardson, and T. M. Monro, "Bismuth glass holey fibers with high nonlinearity", Optics Express, Vol.12, No.21, pp.5082-5087, 2004

[116] S. Set, M. Jablonski, T. Kotake, K. Furuki, M. Tojo, Y. Tanaka, N. Sugimoto, and K. Kikuchi, "Low Nonlinearity Bismuth Oxide-based Erbium-doped Fiber Amplifiers for Short Pulse Amplification", Optical Fiber Communication Conference, FB7, 2003

[117] P. Petropoulos, H. Ebendorff-Heidepriem, T. Kogure, K. Furusawa, V. Finazzi, T. M. Monro, and D. J. Richardson, "A spliced and connectorized highly nonlinear and anomalously dispersive bismuth-oxide glass holey fiber", Conference on Lasers and Electro-Optics, CTuD, 2004

[118] Hideyuki Sotobayashi, Juliet T. Gopinath, Elisabeth M. Koontz, Leslie A. Kolodziejski, and Erich P. Ippen, "Wavelength tunable passively mode-locked bismuth oxide-based erbium-doped fiber laser", Optics Communications, Vol.237, No.4-6, pp.399-403, 2004

[119] H. Burger, K. Kneipp, H. Hobert, W. Vogel, V. Kozhukharov, and S. Neov, "Glass formation, properties and structure of glasses in the TeO_2-ZnO system", Journal of Non-Crystalline Solids, Vol.151, No.1-2, pp.134-142, 1992

[120] Hiroyuki Nasu, Jun Matsuoka, and Kanichi Kamiya, "Second- and third-order optical non-linearity of homogeneous glasses", Journal of Non-Crystalline Solids, Vol.178, pp.23-30, 1994

[121] A. Berthereau, Y. Le Luyer, R. Olazcuaga, G. Le Flem, M. Couzi, L. Canioni, P. Segonds, L. Sarger, and A. Ducasse, "Nonlinear optical properties of some tellurium(IV) oxide glasses", Materials Research Bulletin, Vol.29, No.9, pp.933-941, 1994

[122] Raul F. Cuevas, Luiz C. Barbosa, Ana M. de Paula, Yudong Liu, Victor C.S. Reynoso, Oswaldo L. Alves, Norberto Aranha, and Carlos L. Cesar, "Preparation and characterization of Tellurite based glass: Li_2O-TiO_2-TeO_2 system", Journal of Non-Crystalline Solids, Vol.191, No.1-2, pp.107-114, 1995

[123] Zhengda Pan and Steven H. Morgan, "Raman spectra and thermal analysis of a new lead-tellurium-germanate glass system", Journal of Non-Crystalline Solids, Vol.210, No.2-3, pp.130-135, 1997

[124] Sae-Hoon Kim and Toshinobu Yoko, "Nonlinear Optical Properties of TeO_2-Based Glasses: MOx-TeO_2 (M = Sc, Ti, V, Nb, Mo, Ta, and W) Binary Glasses", Journal of the American Ceramic Society, Vol.78, No.4, pp.1061-1065, 1995

[125] S. Cenk, B. Demirata, M. L. Ovecoglu, and G. Ozen, "Thermal properties and optical transition probabilities of Tm^{3+} doped TeO_2-WO_3 glasses, Spectrochimica Acta Part A, Vol.57, No.12, pp.2367-2372, 2001

[126] C. Duverger, M. Bouazaoui, and S. Turrell, "Raman spectroscopic investigations of the effect of the doping metal on the structure of binary tellurium-oxide glasses", Journal of Non-Crystalline Solids, Vol.220, No.2-3, pp.169-177, 1997

[127] M. A. P. Silva, Y. Messaddeq, S. J. L. Ribeiro, M. Poulain, F. Villain, and V. Briois, "Structural studies on TeO_2-PbO glasses", Journal of Physics and Chemistry of Solids, Vol.62, No.6, pp.1055-1060, 2001

[128] C. Jiang, J. Zhang, H. Mao, and F. Gan, "Formation, properties and structures of TeO_2-GeO_2-Nb_2O_5-BaO glasses", Glass Technology, Vol.39, No.6, pp.200-203, 1998

[129] T. Kosuge, Y. Benino, V. Dimitrov, R. Sato, and T. Komatsu, "Thermal stability and heat capacity changes at the glass transition in K_2O-WO_3-TeO_2 glasses", Journal of Non-Crystalline Solids, Vol.242, No.2-3, pp.154-156, 1998

[130] Sae-Hoon Kim, "Nonlinear optical properties of TeO_2-based glasses: Li(Na and K)$_2$O-TeO_2 binary glasses", Journal of Materials Research, Vol.14, No.3, pp.1074-1083, 1999

[131] R. Akagi, K. Handa, N. Ohtori, A. C. Hannon, M. Tatsumisago, and N. Umesaki, "High-temperature structure of K2O-TeO2 glasses", Journal of Non-Crystalline Solids, Vol.256&257, pp.111-118, 1999

[132] M. D. O'Donnell, C. A. Miller, D. Furniss, V. K. Tikhomirov, and A. B. Seddon, "Fluorotellurite glasses with improved mid-infrared transmission", Journal of Non-Crystalline Solids, Vol.331, No.1-3, pp.48-57, 2003

[133] Robert Stegeman, Ladislav Jankovic, Hongki Kim, Clara Rivero, George Stegeman, Kathleen Richardson, Peter Delfyett, Yu Guo, Alfons Schulte, and Thierry Cardinal, "Tellurite Glasses with peak absolute Raman gain coefficients up to 30 times that of fused silica", Optics Letters, Vol.28, No.13, pp.1126-1128, 2003

[134] Gorachand Ghosh, "Sellmeier-Coefficients and Chromatic Dispersions for Some Tellurite Glasses", Journal of the American Ceramic Society, Vol.78, No.10, pp.2828-2830, 1995

[135] Takao Sekiya, Norio Mochida, Atsushi Ohtsuka, and Mamoru Tonokawa, "Raman spectra of $MO_{1/2}$-TeO_2 (M = Li, Na, K, Rb, Cs, and Tl) glasses", Journal of Non-Crystalline Solids, Vol.144, pp.128-144, 1992

[136] Takao Sekiya, Norio Mochida, Atsushi Ohtsuka, and Ayako Soejima, "Raman spectra of $BO_{3/2}$-TeO_2 glasses", Journal of Non-Crystalline Solids, Vol.151, No.3, pp.222-228, 1992

[137] Sae-Hoon Kim, Toshinobu Yoko, and Sumio Sakka, "Linear and Nonlinear Optical Properties of TeO_2 Glass", Journal of the American Ceramic Society, Vol.76, No.10, pp.2486-2490, 1993

[138] M. A. Khaled, H. Elzahed, S. A. Fayek, and M. M. El-Ocker, "Optical absorption, infrared and differential thermal analysis studies of borotellurite glass containing nickel", Materials Chemistry and Physics, Vol.37, No.4, pp.329-332, 1994

[139] Takao Sekiya, Norio Mochida, and Atsushi Ohtsuka, "Raman spectra of MO-TeO_2 (M = Mg, Sr, Ba, and Zn) glasses", Journal of Non-Crystalline Solids, Vol.168, No.1-2, pp.106-114, 1994

[140] Masahiro Tatsumisago, Sang-Ki Lee, Tsutomu Minami, and Yoshiyuki Kowada, "Raman spectra of TeO2-based glasses and glassy liquids: local structure change with temperature in relation to fragility of liquid", Journal of Non-Crystalline Solids, Vol.177, pp.154-163, 1994

[141] T. Komatsu, H. G. Kim, and H. Mohri, "Raman scattering study on local structures of Te^{4+} and Nb^{5+} in $LiNbO_3$-TeO_2 glasses", Journal of Materials Science Letters, Vol.15, No.23, pp.2026-2029, 1996

[142] M. R. Sahar, A. K. Jehbu, and M. M. Karim, "TeO_2-ZnO-$ZnCl_2$ glasses for IR transmission", Journal of Non-Crystalline Solids, Vol.213&214, pp.164-167, 1997

[143] K. Muruganandam and M. Seshsayee, "Structural study of $LiPO_3$-TeO_2 glasses", Journal of Non-Crystalline Solids, Vol.222, pp.131-136, 1997

[144] E. B. Araujo, J. A. Eiras, and A. C. Hernandes, "Studies on tellurite glasses using differential thermal analysis", Journal of Materials Science Letters, Vol.18, No.10, pp.793-795, 1999

[145] Fabia C. Cassanjes, Younes Messaddeq, Luiz F. C. de Oliveira, Lilia C. Courrol, Laecio Gomes, and J. L. Ribeiro, "Raman scattering, differential scanning calorimetry and Nd^{3+} spectroscopy in alkali niobium tellurite glasses", Journal of Non-Crystalline Solids, Vol.247, No.1-3, pp.58-63, 1999

[146] G. Vijaya Prakash, D. Narayana Rao, and A. K. Bhatnagar, "Linear optical properties of niobium-based tellurite glasses", Solid State Communications, Vol.119, No.1, pp.39-44, 2001

[147] D. K. Durga, P. Yadagiri Reddy, and N. Veeraiah, "Optical absorption and thermoluminescence properties of ZnF_2-MO-TeO_2 (MO = As_2O_3, Bi_2O_3, and P_2O_5) glasses doped with chromium ions", Journal of Luminescence, Vol.99, No.1, pp.53-60, 2002

[148] Junjie Zhang, Jianbei Qiu, and Yoji Kawamoto, "New oxyfluorotellurite glass: thermal analysis and structural analysis by means of Raman scattering", Materials Letters, Vol.55, No.1-2, pp.77-82, 2002

[149] A. Abd El-Moneim, "DTA and IR absorption spectra of vanadium tellurite glasses", Materials Chemistry and Physics, Vol.73, No.2-3, pp.318-322, 2002

[150] Shaoxiong Shen, Mira Naftaly, and Animesh Jha, "Tungsten-tellurite-a host glass for broadband EDFA", Optics Communications, Vol.205, No.1-3, pp.101-105, 2002

[151] P. Charton, P. Thomas, and P. Armand, "Raman and crystallization of TeO_2-Sb_2O_4 glasses", Journal of Non-Crystalline Solids, Vol.321, No.1-2, pp.81-88, 2003

[152] S. Marjanovic, J. Toulouse, H. Jain, C. Sandmann, V. Dierolf, A. R. Kortan, N. Kopylov, and R. G. Ahrens, "Characterization of new erbium-doped tellurite glasses and fibers", Journal of Non-Crystalline Solids, Vol.322, No.1-3, pp.311-318, 2003

[153] P. Charton and P. Armand, "X-ray absorption and Raman characterizations of TeO_2-Ga_2O_3 glasses", Journal of Non-Crystalline Solids, Vol.333, No.3, pp.307-315, 2004

[154] J. S. Wang, E. M. Vogel, and E. Snitzer, "Tellurite glass: a new candidate for fiber devices", Optical Materials, Vol.3, No.3, pp.187-203, 1994

[155] V. V. Ravi Kanth Kumar, A. K. George, J. V. Knight, and P. St. J. Russell, "Tellurite photonic crystal fiber", Optics Express, Vol.11, No.20, pp.2641-2645, 2003

[156] A. Mori, H. Masuda, K. Shikano, and M. Shimizu, "Ultra-Wide-Band Tellurite-Based Fiber Raman Amplifier", Journal of Lightwave Technology, Vol.21, No.5, pp.1300-1305, 2003

[157] A. Mori, K. Kobayashi, M. Yamada, T. Kanamori, K. Oikawa, Y. Nishida, and Y. Ohishi, "Low noise broadband tellurite-based Er^{3+}-doped fiber amplifiers", Electronics Letters, Vol.34, No.9, pp.887-888, 1998

[158] Yasutake Ohishi, Atsushi Mori, Makoto Yamada, Hirotaka Ono, Yoshiki Nishida, and Kiyoshi Oikawa, "Gain characteristics of tellurite-based erbium-doped fiber amplifiers for 1.5-μm broadband amplification", Optics Letters, Vol.23, No.4, pp.274-276, 1998

[159] M. Yamada, A. Mori, H. Ono, K. Kobayashi, T. Kanamori, and Y. Ohishi, "Broadband and gain-flattened Er3+-doped tellurite fibre amplifier constructed using a gain equaliser", Electronics Letters, Vol.34, No.4, pp.370-371, 1998

[160] Atsushi Mori, Tadashi Sakamoto, Kenji Kobayashi, Koji Shikano, Kiyoshi Oikawa, Koichi Hoshino, Terutoshi Kanamori, Yasutake Ohishi, and Makoto Shimizu, "1.58-μm Broad-Band Erbium-Doped Tellurite Fiber Amplifier", Journal of Lightwave Technology, Vol.20, No.5, pp.822-827, 2002

[161] E. R. M. Taylor, L. N. Ng, J. Nilsson, R. Caponi, A. Pagano, M. Potenza, and B. Sordo, "Thulium-Doped Tellurite Fiber Amplifier", IEEE Photonics Technology Letters, Vol.16, No.3, pp.777-779, 2004

[162] J. S. Wang, D. P. Machewirth, F. Wu, E. Snitzer, and E. M. Vogel, "Neodymiun-doped tellurite single-mode fiber laser", Optics Letters, Vol.19, No.18, pp.1448-1449, 1994

[163] K. Petkov, and P.J.S. Ewen, "Photoinduced changes in the linear and nonlinear optical properties of chalcogenide glasses", Journal of Non-Crystalline Solids, Vol.249, No.2-3, pp.150-159, 1999

[164] T. Cardinal, K.A. Richardson, H. Shim, A. Schulte, R. Beatty, K. Le Foulgoc, C. Meneghini, J.F. Viens, and A. Villeneuve, "Non-linear optical properties of chalcogenide glasses in the system As-S-Se", Journal of Non-Crystalline Solids, Vol.256&257, pp.353-360, 1999

[165] G. Lenz, J. Zimmermann, T. Katsufuji, M. E. Lines, H. Y. Hwang, S. Spalter, R. E. Slusher, S.-W. Cheong, J. S. Sanghera, and I. D. Aggarwal, "Large Kerr effect in bulk Se-based chalcogenide glasses", Optics Letters, Vol.25, No.4, pp.254-256, 2000

[166] F. Smektala, C. Quemard, V. Couderc, and A. Barthelemy, "Non-linear optical properties of chalcogenide glasses measured by Z-scan", Journal of Non-Crystalline Solids, Vol.274, No.1-3, pp.232-237, 2000

[167] J. M. Harbold, F. O. Ilday, F. W. Wise, J. S. Sanghera, V. Q. Nguyen, L. B. Shaw, and I. D. Aggarwal, "Highly nonlinear As-S-Se glasses for all-optical switching", Optics Letters, Vol.27, No.2, pp.119-121, 2002

[168] J. Requejo-Isidro, A. K. Mairaj, V. Pruneri, D. W. Hewak, M. C. Netti, and J. J. Baumberg, "Self refractive non-linearities in chalcogenide based glasses", Journal of Non-Crystalline Solids, Vol.317, No.3, pp.241-246, 2003

[169] J. Troles, F. Smektala, G, Boudebs, and A. Monteil, "Third order nonlinear optical characterization of new chalcogenide glasses containing lead iodine", Optical Materials, Vol.22, No.4, pp.335-343, 2003

[170] Kazuhiko Ogusu, Jun Yamasaki, Shinpei Maeda, Michihiko Kitao, and Makoto Minakata "Linear and nonlinear optical properties of Ag-As-Se chalcogenide glasses for all-optical switching", Optics Letters, Vol.29, No.3, pp.265-267, 2004

[171] Hideki Kobayashi, Hirohisa Kanbara, and Masanori Koga, Ken'ichi Kubodera, "Third-order nonlinear optical properties of As2S3 chalcogenide glass", Journal of Applied Physics, Vol.74, No.6, pp.3683-3687, 1993

[172] M. F. Churbanov, "High-purity chalcogenide glasses as materials for fiber optics", Journal of Non-Crystalline Solids, Vol.184, pp.25-29, 1995

[173] A. B. Seddon, "Chalcogenide glasses: a review of their preparation, properties, and applications", Journal of Non-Crystalline Solids, Vol.184, pp.44-50, 1995

[174] K. A. Cerqua-Richardson, J. M. McKinley, B. Lawrence, S. Joshi, and A. Villeneuve, "Comparison of nonlinear optical properties of sulfide glasses in bulk and thin film form", Optical Materials, Vol.10, No.2, pp.155-159, 1998

[175] D. Tonchev and S. O. Kasap, "Thermal properties of $Sb_xSe_{(100-x)}$ glasses studied by modulated temperature differential scanning calorimetry", Journal of Non-Crystalline Solids, Vol.248, No.1, pp.28-36, 1999

[176] A. H. Khafagy, M. S. Abo-Ghazala, M. M. El-Zaidia, and A. A. El-Shourbagy, "Structural and thermal properties of $Se_{85}S_{15-x}Sb_x$ glassy system", Journal of Non-Crystalline Solids, Vol.278, No.1-3, pp.119-127, 2000

[177] Takeshi Usuki, Osamu Uemura, Shigemoto Konno, Yasuo Kameda, and Masaki Sakurai, "Structural and physical properties of Ag-As-Te glasses", Journal of Non-Crystalline Solids, Vol.273-295, pp.799-805, 2001

[178] A. Zakery and S. R. Elliott, "Optical properties and applications of chalcogenide glasses: a review", Journal of Non-Crystalline Solids, Vol.330, No.1-3, pp.1-12, 2003

[179] Terutoshi Kanamori, Yukio Terunuma, Shiro Takahashi, and Tadashi Miyashita, "Chalcogenide Glass Fibers for Mid-Infrared Transmission", Journal of Lightwave Technology, Vol.LT-2, No.5, pp.607-613, 1984

[180] Masaki Asobe, Ken'ichi Suzuki, Terutoshi Kanamori, and Ken'ichi Kubodera, "Nonlinear refractive index measurement in chalcogenide-glass fibers by self-phase modulation", Applied Physics Letters, Vol.60, No.10, pp.1153-1154, 1992

[181] M. Asobe, H. Itoh, T. Miyazawa, and T. Kanamori, "Efficient and ultrafast all-optical switching using high Δn, small core chalcogenide glass fiber", Electronics Letters, Vol.29, No.22, pp.1966-1968, 1993

[182] Masaki Asobe, Terutoshi Kanamori, and Ken'ichi Kubodera, "Applications of Highly Nonlinear Chalcogenide Glass Fibers in Ultrafast All-Optical Switches", IEEE Journal of Quantum Electronics, Vol.29, No.8, pp.2325-2332, 1993

[183] Masaki Asobe, Hideki Kobayashi, and Hiroki Itoh, "Laser-diode-driven ultrafast all-optical switching by using highly nonlinear chalcogenide glass fiber", Optics Letters, Vol.18, No.13, pp.1056-1058, 1993

[184] Masaki Asobe, Terutoshi Kanamori, Kazunori Naganuma, and Hiroki Itoh, and Toshikuni Kaino, "Third-order nonlinear spectroscopy in As_2S_3 chalcogenide glass fibers", Journal of Applied Physics, Vol.77, No.11, pp.5518-5523, 1995

[185] Jas S. Sanghera and Ishwar D. Aggarwal, "Development of chalcogenide glass fiber optics at NRL", Journal of Non-Crystalline Solids, Vol.213&214, pp.63-67, 1997

[186] D. J. Bardy, T. Schweizer, J. Wang, and D. W. Hewak, "Minimum loss predictions and measurements in gallium lanthanum sulphide based glasses and fibre", Journal of Non-Crystalline Solids, Vol.242, No.2-3, pp.92-98, 1998

[187] R. Mossadegh, J. S. Sanghera, D. Schaafsma, B. J. Cole, V. Q. Nguyen, R. E. Miklos, and I. D. Aggarwal, "Fabrication of Single-Mode Chalcogenide Optical Fiber", Journal of Lightwave Technology, Vol.16, No.2, pp.214-217, 1998

[188] J. Kobelke, J. Kirchhof, M. Scheffler, and A. Schwuchow, "Chalcogenide glass single mode fibers - preparation and properties, Journal of Non-Crystalline Solids, Vol.256&257, pp.226-231, 1999

[189] T. M. Monro, Y. D. West, D. W. Hewak, N. G. R. Broderick, and D. J. Richardson, "Chalcogenide holey fibres", Electronics Letters, Vol.36, No.24, pp.1998-2000, 2000

[190] P. A. Thielen, L. B. Shaw, P. C. Pureza, V. Q. Nguyen, J. S. Sanghera, and I. D. Aggarwal, "Small-core As-Se fiber for Raman amplification", Optics Letters, Vol.28, No.16, pp.1406-1408, 2003

[191] Richart E. Slusher, Gadi Lenz, Juan Hodelin, Jasbinder Sanghera, L. Brandon Shaw, and Ishwar D. Aggarwal, "Large Raman gain and nonlinear phase shifts in high-purity As2Se3 chalcogenide fibers", Journal of the Optical Society of America B, Vol.21, No.6, pp.1146-1155, 2004

[192] Junji Nishii, Toshiharu Yamashita, and Takashi Yamagishi, "Chalcogenide glass fiber with a core-cladding structure", Applied Optics, Vol.28, No.23, pp.5122-5127, 1989

[193] Masaki Asobe, Terutoshi Kanamori, and Kenichi Kubodera, "Ultrafast All-Optical Switching Using Highly Nonlinear Chalcogenide Glass Fiber", IEEE Photonics Technology Letters, Vol.4, No.4, pp.362-365, 1992

[194] M. Asobe, T. Ohara, I. Yokohama, and T. Kaino, "Low power all-optical switching in a nonlinear optical loop mirror using chalcogenide glass fibre", Electronics Letters, Vol.32, No.15, pp.1396-1397, 1996

[195] Masaki Asobe, "Nonlinear Optical Properties of Chalcogenide Glass Fibers and Their Application to All-Optical Switching", Optical Fiber Technology, Vol.3, No.2, pp.142-148, 1997

[196] T. Schweizer, B. N. Samson, R. C. Moore, D. W. Hewak, and D. N. Payne, "Rare-earth doped chalcogenide glass fibre laser", Electronics Letters, Vol.33, No.5, pp.414-416, 1997

[197] Govind P. Agrawal, *Nonlinear Fiber Optics*, Academic Press, 3rd edition, 2001

[198] George I Stegeman and Roger H. Stolen, "Waveguides and fibers for nonlinear optics", Journal of the Optical Society of America B, Vol.6, No.4, pp.652-662, 1989

[199] R. H. Stolen and Chinlon Lin, "Self-phase-modulation in silica optical fibers", Physics Review A, Vol.17, No.4, pp.1448-1453, 1978

[200] M. N. Islam, L. F. Mollenauer, R. H. Stolen, J. R. Simpson, and H. T. Shang, "Cross-phase modulation in optical fibers", Optics Letters, Vol.12, No.8, pp.625-627, 1987

[201] M. Jinno and T. Matsumoto, "Ultrafast all-optical logic operations in a nonlinear Sagnac interferometer with two control beams", Optics Letters, Vol.16, No.4, pp.220-222, 1991

[202] J. D. Moores, K. Bergman, H. A. Haus, and E. P. Ippen, "Optical switching using fiber ring reflectors", Journal of the Optical Society of America B, Vol.8, No.3, pp.594-601, 1991

[203] Joshua E. Rothenberg, "Complete all-optical switching of visible picosecond pulses in birefringent fiber", Optics Letters, Vol.18, No.10, pp.796-798, 1993

[204] P. L. Baldeck, R. R. Alfano, and Govind P. Agrawal "Induced-frequency shift of copropagating ultrafast optical pulses", Applied Physics Letters, Vol.52, No.23, pp.1939-1941, 1988

[205] Masahiko Jinno, "Pump-induced frequency shifting of switched pulses in an interferometric all-optical switch", Optics Letters, Vol.18, No.9, pp.726-728, 1993

[206] R. H. Stolen, E. P. Ippen, and A. R. Tynes, "Raman Oscillation in Glass Optical Waveguide", Applied Physics Letters, Vol.20, No.2, pp.62-64, 1972

[207] R. H. Stolen and E. P. Ippen, "Raman Gain in Glass Optical Waveguides", Applied Physics Letters, Vol.22, No.6, pp.276-278, 1973

[208] R. H. Stolen and Clinton Lee, "Development of the stimulated Raman spectrum in single-mode silica fibers", Journal of the Optical Society of America B, Vol.1, No.4, pp.652-657, 1984

[209] E. P. Ippen and R. H. Stolen, "Stimulated Brillouin scattering in optical fibers", Applied Physics Letters, Vol.21, No.11, pp.539-541, 1972

[210] R. H. Stolen, J. E. Bjorkholm, and A. Ashkin, "Phase-matched three-wave mixing in silica fiber optical waveguides", Applied Physics Letters, Vol.24, No.7, pp.308-310, 1974

[211] Rogers H. Stolen, "Phase-Matched-Stimulated Four-Photon Mixing in Silica-Fiber Waveguides", IEEE Journal of Quantum Electronics, Vol.QE-11, No.3, pp.100-103, 1975

[212] G. Cappellini and S. Trillo, "Third-order three-wave mixing in single-mode fibers: exact solutions and spatial instability effects", Journal of the Optical Society of America B, Vol.8, No.4, pp.824-838, 1991

[213] Kyo Inoue, "Four-Wave Mixing in an Optical Fiber in the Zero-Dispersion Wavelength Range", Journal of Lightwave Technology, Vol.10, No.11, pp.1553-1561, 1992

[214] Jay E. Sharping, Macro Fiorentino, Ayodeji Coker, Prem Kumar, and Robert S. Windeler, "Four-wave mixing in microstructure fiber", Optics Letters, Vol.26, No.14, pp.1048-1050, 2001

[215] R. H. Stolen, M. A. Bosch, and Chinlon Lin, "Phase matching in birefringent fibers", Optics Letters, Vol.6, No.5, pp.213-215, 1981

[216] Marvin J. Weber, CRC *Handbook of Laser Science and Technology supplement 2: Optical Materials*, CRC Press, 1995

[217] Bach and Neuroth, *The Properties of Optical Glass*, Springer, 1995

[218] Norman N. Boling, Alexander J. Glass, and Adelbert Owyoung, "Empirical Relationships for Predicting Nonlinear Refractive Index Changes in Optical Solids", IEEE Journal of Quantum Electronics, Vol.QE-14, No.8, pp.601-608, 1978

[219] M. E. Lines, "Oxide glasses for fast photonic switching: A Comparative Study", Journal of Applied Physics, Vol.69, No.10, pp.6876-6884, 1991

[220] D Milam and M. J. Weber, "Measurement of nonlinear refractive-index coefficients using time-resolved interferometry: Application to optical materials for high-power neodymium lasers", Journal of Applied Physics, Vol.47, No.6, pp.2497-2501, 1976

[221] K. S. Kim, R. H. Stolen, W. A. Reed, and K. W. Quoi, "Measurement of the nonlinear index of silica-core and dispersion-shifted fibers", Optics Letters, Vol.19, No.4, pp.257-259, 1994

[222] Roger H. Stolen, William A. Reed, Kwang S. Kim, and G. T. Harvey, "Measurement of the Nonlinear Refractive Index of Long Dispersion-Shifted Fibers by Self-Phase

Modulation at 1.55μm", Journal of Lightwave Technology, Vol.16, No.6, pp.1006-1012, 1998

[223] Govind P. Agrawal, *Fiber-Optic Communication Systems*, Wiley-Interscience, 3rd edition, 2002

[224] R. H. Stolen, V. Ramaswamy, P. Kaiser, and W. Pleibel, "Linear polarization in birefringence single-mode fibers", Applied Physics Letters, Vol.33, No.8, pp.699-701, 1978

[225] R. H. Stolen and A. Ashkin, "Optical Kerr effect in glass waveguide", Applied Physics Letters, Vol.22, No.6, pp.294-296, 1973

[226] J. M. Dziedzic, R. H. Stolen, and A. Ashkin, "Optical Kerr effect in long fibers", Applied Optics, Vol.20, No.8, pp.1403-1406, 1981

[227] N. J. Doran and David Wood, "Nonlinear-optical loop mirror", Optics Letters, Vol.13, No.1, pp.56-58, 1988

[228] M. A. Arbore, M. J. F. Digonnet, and R. H. Pantell, "Analysis of the insertion loss and Extinction Ratio of Two-Mode Fiber interferometric Devices", Academic Press, Inc., Optical Fiber Technology 2, pp.400-407, 1996

[229] John W. Arkwright, Pak L. Cu, and T. Tjugiarto, "Variable Demultiplexing Using a Twin-Core Fiber Mach-Zehnder Interferometer", IEEE Photonics Technology Letters, Vol.5, No.10, pp.1216-1218, 1993

[230] B. Wu and P. L. Chu, "Narrow-bandpass filter with gain by use of twin-core rare-earth-doped fiber", Optics Letters, Vol.18, No.22, pp.1913-1915, 1993

[231] J. W. Arkwright, B. Gillhoff, S. J. Hewlett, J. D. Love, P. M. Allen, P. L. Chu, T. W. Whitbread, B. Wu, G. R. Atkins, S. B. Poole, M. G. Sceats, and D. A. Thorncraft, "Optical-to-Electrical Wavelength Demultiplexing Detector: Design, Fabrication, and Analysis", Journal of Lightwave Technology, Vol.14, No.4, pp.534-541, 1996

[232] John W. Arkwright, Simon J. Hewlett, Graham R. Atkins, and Bin Wu, "High-Isolation Demultiplexing in Bend-Tuned Twin-Core Fiber", Journal of Lightwave Technology, Vol.14, No.7, pp.1740-1745, 1996

[233] Remigius Zengerle and Ottokar G. Leminger, "Wavelength-Selective Directional Coupler Made of Nonidentical Single-Mode Fibers", Journal of Lightwave Technology, Vol.4, No.7, pp.823-827, 1986

[234] Remigius Zengerle and Ottokar G. Leminger, "Narrow-Band Wavelength-Selective Directional Couplers Made of Dissimilar Single-Mode Fibers", Journal of Lightwave Technology, Vol.5, No.9, pp.1196-1198, 1987

[235] Katsumi Morishita, "Wavelength-selective optical-fiber directional couplers using dispersive materials", Optics Letters, Vol.13, No.2, pp.158-160, 1988

[236] Chul-Jong Chung and Ahmad Safaai-Jazi, "Narrow-Band Spectral Filter Made of W-Index and Step-Index Fibers", Journal of Lightwave Technology, Vol.10, No.1, pp.42-45, 1992

[237] Adrian Ankiewicz, Zi Hua Wang, and Gang-Ding Peng, "Analysis of narrow bandpass filter using coupler with Bragg grating in transmission", Optics Communications, Vol.156, No.1-3, pp.27-31, 1998

[238] B. Ortega and L. Dong, "Characteristics of Mismatched Twin-Core Fiber Spectral Filters", IEEE Photonics Technology Letters, Vol.10, No.7, pp.991-993, 1998

[239] B. Ortega and L. Dong, "Selective Fused Couplers Consisting of a Mismatched Twin-Core Fiber and a Standard Optical Fiber", Journal of Lightwave Technology, Vol.17, No.1, pp.123-128, 1999

[240] Honglin An, Brian Ashton, and Simon Fleming, "Long-period-grating-assisted optical add-drop filter based on mismatched twin-core photosensitive-cladding fiber", Optics Letters, Vol.29, No.4, pp.343-345, 2004

[241] Kunimasa Saitoh, Yuichiro Sato, and Masanori Koshiba, "Coupling characteristics of dual-core photonic crystal couplers", Optics Express, Vol.11, No.24, pp.3188-3195, 2003

[242] Ajoy Ghatak and K. Thyagarajan, *Introduction to Fiber Optics*, Cambridge University Press, Appendix E, 1998

[243] A. W. Snyder and J. D. Love, *Optical Waveguide Theory*, New York: Chapman and Hall, 1983

[244] Cheng Wen Wu, Shuh-Tai Lu, Tzong-Lin Wu, and Hung-Chun Chang, "All-Fiber Brewster Windows Made with Extremely Weakly Fused Asymmetric Coupler", IEEE Photonics Technology Letters, Vol.7, No.9, pp.1054-1056, 1995

[245] John A. Buck, *Fundamentals of Optical Fibers*, Wiley-Interscience, 1995

[246] R. J. Black, A. Henault, S. Lacroix, and M. Cada, "Structural Consideration for Bimodal Nonlinear Optical switching", IEEE Journal of Quantum Electronics, Vol.26, No.6, pp.1081-1088, 1990

[247] Tinko A. Eftimov and Wojtek J. Bock, "Sensing with a LP_{01}-LP_{02} Intermodal Interferometer", Journal of Lightwave Technology, Vol.11, No.12, pp.2150-2156, 1993

[248] Arun Kumar, Rajeev Jindal, Ravi K. Varshney, and Sangeet K. Sharma, "A Fiber-Optic Temperature Sensor Based on LP_{01}-LP_{02} Mode Interference", Optical Fiber Technology, Vol.6, pp.83-90, 2000

[249] Arun Kumar, Nitin K. Goel, and R. K. Varshney, "Studies on a Few-Mode Fiber-Optic Strain Sensor Based on LP_{01}-LP_{02} Mode Interference", Journal of Lightwave Technology, Vol.19, No.3, pp.358-362, 2001

[250] D. Kominsky and R. Stolen, "High-nonlinearity glasses in holey fibers", OISE, SE02-04, 2000

[251] H. G. Park, C. C. Pohalski, and B. Y. Kim, "Optical Kerr switch using elliptical-core two-mode fiber", Optics Letters, Vol.13, No.9, pp.776-778, 1988

[252] Youngchul Chung, Jong Chang Yi, Sun Ho Kim, and Sang Sam Choi, "Analysis of a Tunable Multichannel Two-Mode-Interference Wavelength Division Multiplexer/ Demultiplexer", Journal of Lightwave Technology, Vol.7, No.5, pp.766-777, 1989

[253] Wojtek J. Bock and Tinko A. Eftimov, "Simultaneous Hydrostatic Pressure and Temperature Measurement Employing an LP_{01}-LP_{11} Fiber-Optic Polarization-Sensitive Intermodal Interferometer", IEEE Transactions on Instrumentation and Measurement, Vol.43, No.2, pp.337-340, 1994

[254] C. F. Janz, M. R. Paiam, B. P. Keyworth, and J. N. Broughton, "Bent Waveguide Couplers for (De)Multiplexing of Arbitrary Broadly-Separated Wavelengths Using

Two-Mode Interference", IEEE Photonics Technology Letters, Vol.7, No.9, pp.1037-1039, 1995

[255] Kwang Yong Song, In Kag Hwang, Seok Hyun Yun, and Byoung Yoon Kim, "High Performance Fused-Type Mode-Selective Coupler Using Elliptical Core Two-Mode Fiber at 1550nm", IEEE Photonics Technology Letters, Vol.14, No.4, pp.501-503, 2002

[256] Victor Mizrahi, K. W. DeLong, G. I. Stegeman, M. A. Saifi, and M. J. Andrejco, "Two-photon absorption as a limitation to all-optical switching", Optics Letters, Vol.14, No.20, pp.1140-1142, 1989

[257] Masahiko Jinno, "Effects of Group Velocity Dispersion on Self/Cross-Phase Modulation in a Nonlinear Sagnac Interferometer Switch", Journal of Lightwave Technology, Vol.10, No.8, pp.1167-1178, 1992

[258] Pictures from Blaze Photonics website: http://www.blazephotonics.com

[259] J. C. Knight, T. A. Birks, R. F. Cregan, P. St. J. Russell, and J. -P. de Sandro, "Photonic crystals as optical fibres-physics and applications", Optical Materials, Vol.11, No.20, pp.143-151, 1999

[260] J. C. Knight, J. Arriaga, T. A. Birks, A. Ortigosa-Blanch, W. J. Wadsworth, and P. St. J. Russell, "Anomalous Dispersion in Photonic Crystal Fiber", IEEE Photonics Technology Letters, Vol.12, No.7, pp.807-809, 2000

[261] T. A. Birks, J. C. Knight, and P. St. J. Russell, "Endlessly single-mode photonic crystal fiber", Optics Letters, Vol.22, No.13, pp.961-963, 1997

[262] G. Bouwmans, F. Luan, J. C. Knight, P. St. J. Russell, L. Farr, B. J. Mangan, and H. Sabert, "Properties of a hollow-core photonic bandgap fiber at 850nm wavelength", Optics Express, Vol.11, No.14, pp.1613-1620, 2003

[263] N. G. R. Broderick, T. M. Monro, P. J. Bennett, and D. J. Richardson, "Nonlinearity in holey optical fibers: measurement and future opportunities", Optics Letters, Vol.24, No.20, pp.1395-1397, 1999

[264] J. C. Knight, T. A. Birks, R. F. Cregan, P. St. J. Russell, and J. -P. de Sandro, "Large mode area photonic crystal fibre", Electronics Letters, Vol.34, No.13, pp.1347-1348, 1998

[265] N. A. Mortensen, M. D. Nielsen, J. R. Folkenberg, A. Petersson, and H. R. Simonsen, "Improved large-mode-area endlessly single-mode photonic crystal fibers", Optics Letters, Vol.28, No.6, pp.393-395, 2003

[266] W. H. Reeves, J. C. Knight, P. St. J. Russell, and P. J. Roberts, "Demonstration of ultra-flattened dispersion in photonic crystal fibers", Optics Express, Vol.10, No.14, pp.609-613, 2002

[267] A. Ferrando, E. Silvestre, J. J. Miret, and P. Andres, "Nearly zero ultraflattened dispersion in photonic crystal fibers", Optics Letters, Vol.25, No.11, pp.790-792, 2000

[268] M. J. Gander, R. McBride, J. D. C. Jones, D. Mogilevtsev, T. A. Kirks, J. C. Knight, and P. St. J. Russell, "Experimental measurement of group velocity dispersion in photonic crystal fiber", Electronics Letters, Vol.35, pp.63-64, 1999

[269] T. A. Birks, D. Mogilevtsev, J. C. Knight, and P. St. J. Russell, "Dispersion Compensation Using Single-Material Fibers", IEEE Photonics Technology Letters, Vol.11, No.6, pp.674-676, 1999

[270] Federica Poli, Annamaria Cucinotta, Matteo Fuochi, Stefano Selleri, and Luca Vincetti, "Characterization of microstructured optical fibers for wideband dispersion compensation", Journal of the Optical Society of America A, Vol.20, No.10, pp.1958-1962, 2003

[271] Theis P. Hansen, Jes Broeng, Stig E. B. Libori, Erik Knudsen, Anders Bjarklev, Jacob Riis Jensen, and Harald Simonsen, "Highly Birefringent Index-Guiding Photonic Crystal Fibers", IEEE Photonics Technology Letters, Vol.13, No.6, pp.588-590, 2001

[272] K. P. Hansen, A. Petersson, J. R. Folkenberg, M. Albertsen, and A. Bjarklev, "Birefringence-induced splitting of the zero-dispersion wavelength in nonlinear photonic crystal fibers", Optics Letters, Vol.29, No.1, pp.14-16, 2004

[273] A. Ortigosa-Blanch, J. C. Knight, W. J. Wadsworth, J. Arriaga, B. J. Mangan, T. A. Birks, and P. St. J. Russell, "Highly birefringent photonic crystal fibers", Optics Letters, Vol.25, No.18, pp.1325-1327, 2000

[274] G. Vienne, Y. Xu, C. Jakobsen, H. J. Deyerl, T. P. Hansen, B. H. Larsen, J. B. Jensen, T. Sorensen, M. Terrel, Y. Huang, R. Lee, N. A. Mortensen, J. Broeng, H. Simonsen, A.

Bjarklev, and A. Yariv, "First demonstration of air-silica Bragg fiber", Optical Fiber Communication Conference, PDP25, 2004

[275] B. J. Mangan, L. Farr, A. Langford, P. J. Roberts, D. P. Williams, F. Couny, M. Lawman, M. Mason, S. Coupland, R. Flea, H. Sabert, T. A. Birks, J. C. Knight, and P. St. J. Russell, "Low loss(1.7dB/km) hollow core photonic bandgap fiber", Optical Fiber Communication Conference, PDP24, 2004

[276] Jinendra K. Ranka, Robert S. Windeler, and Andrew J. Stentz, "Visible continuum generation in air-silica microstructure optical fibers with anomalous dispersion at 800nm", Optics Letters, Vol.25, No.1, pp.25-27, 2000

[277] William J. Wadsworth, Arturo Ortigosa-Blanch, Jonathan C. Knight, Tim A. Birks, T. -P. Martin Man, and Philip St. J. Russell, "Supercontinuum generation in photonic crystal fibers and optical fiber tapers: a novel light source", Journal of the Optical Society of America B, Vol.19, No.9, pp.2148-2155, 2002

[278] Stephane Coen, Alvin Hing Lun Chau, Rainer Leonhardt, John D. Harvey, Jonathan C. Knight, William J. Wadsworth, and Philip St. J. Russell, "Supercontinuum generation by stimulated Raman scattering and parametric four-wave mixing in photonic crystal fibers", Journal of the Optical Society of America B, Vol.19, No.4, pp.753-764, 2002

[279] Z. Yusoff, J. H. Lee, W. Belardi, T. M. Monro, P. C. Teh, and D. J. Richardson, "Raman effects in a highly nonlinear holey fiber: amplification and modulation", Optics Letters, Vol.27, No.6, pp.424-426, 2002

[280] R. Tang, J. Lasri, P. Devgan, J. E. Sharping, and P. Kumar, "Microstructure-fibre-based optical parametric amplifier with gain slope of ~200dB/W/km in the telecom range", Electronics Letters, Vol.39, No.2, pp.195-196, 2003

[281] Fiorenzo G. Omenetto, Antoinette J. Taylor, Mark D. Moores, Jesus Arriaga, Jonathan C. Knight, William J. Wadsworth, and Philip St. J. Russell, "Simultaneous generation of spectrally distinct third harmonics in a photonic crystal fiber", Optics Letters, Vol.26, No.15, pp.1158-1160, 2001

[282] Jay E. Sharping, Marco Fiorentino, Prem Kumar, and Robert S. Windeler, "All-Optical Switching Based on Cross-Phase Modulation in Microstructure fiber", IEEE Photonics Technology Letters, Vol.14, No.1, pp.77-79, 2002

[283] W. J. Wadsworth, J. C. Knight, A. Ortigosa-Blanch, J. Arriaga, E. Silvestre, and P. St. J. Russell, "Soliton effects in photonic crystal fibers at 850nm", Electronics Letters, Vol.36, No.1, pp.53-55, 2000

[284] Stephen R. Friberg and Peter W. Smith, "Nonlinear Optical Glasses for Ultrafast Optical Switches", IEEE Journal of Quantum Electronics, Vol.23, No.12, pp.2089-2094, 1987

[285] Raouf A.H. EI-Mallawany, *Tellurite Glasses Handbook: Physical properties and data*, CRC Press, 2002

[286] M. E. Lines, "Scattering losses in optic fiber materials. I. A new parametrization", Journal of Applied Physics, Vol.55, No.11, pp.4052-4057, 1984

[287] M. E. Lines, "Scattering losses in optic fiber materials. II. Numerical Estimates", Journal of Applied Physics, Vol.55, No.11, pp.4058-4063, 1984

[288] S. H. Wemple, J. D. Gabbe, and G. D. Boyd, "Refractive-index behavior of ternary chalcopyrite semiconductors", Journal of Applied Physics, Vol.46, No.8, pp.3597-3605, 1975

VITA

Jong-Kook Kim was born in Jeonju, Korea on September 4, 1969. He graduated from Jeonju High School in 1988. He received his B.E. degree in Electrical Engineering from Chung-Ang University, Seoul, Korea in 1994. From January 1994 to August 1997, he worked as a research engineer at the research institute of Ssangyong Motor Company, Korea where he was involved in development of laser-based safety devices for advanced safety vehicles.

He earned his M.E. degree in Electrical Engineering from Chung-Ang University, Seoul, Korea in 1999. During his Master's degree, his main research was focused on development of optical measurement systems for characterization of MEMS devices. From March 2000 to June 2001, he served as a part-time instructor at Kaywon and Yeojoo Universities, Korea.

In August 2001, he joined the Ph.D. program at the Electrical and Computer Engineering Department of Virginia Polytechnic Institute and State University, Blacksburg, VA. His main research interests include analysis of the properties of highly nonlinear fibers, highly nonlinear fiber fabrication, and ultrafast nonlinear fiber devices for higher data transmission in optical communication systems. He earned his Ph.D. degree in August 2005 from Virginia Polytechnic Institute and State University.